Alma Mater Studiorum - Università di Bologna

DOTTORATO DI RICERCA IN

FISICA

Ciclo 35

Settore Concorsuale: 02/A1 - FISICA SPERIMENTALE DELLE INTERAZIONI FONDAMENTALI

Settore Scientifico Disciplinare: FIS/01 - FISICA SPERIMENTALE

STUDY OF THE CALORIMETRIC PERFORMANCE OF A LIQUID ARGON DETECTOR BASED ON A NOVEL OPTICAL IMAGING CONCEPT

Presentata da: Valerio Pia

Coordinatore Dottorato

Michele Cicoli

Supervisore

Nicoletta Mauri

Esame finale anno 2023

Abstract

DUNE is a next-generation long-baseline neutrino oscillation experiment. It aims to measure the still unknown δ_{CP} violation phase and the sign of Δm^2_{13}, which defines the neutrino mass ordering. DUNE will exploit a Far Detector composed of four multi-kiloton LArTPCs, and a Near Detector (ND) complex located close to the neutrino source at Fermilab.

The SAND detector at the ND complex is designed to perform on-axis beam monitoring, constrain uncertainties in the oscillation analysis and perform precision neutrino physics measurements. SAND includes a 0.6 T super-conductive magnet, an electromagnetic calorimeter, a 1-ton liquid Argon detector - GRAIN - and a modular, low-density straw tube target tracker system. GRAIN is an innovative LAr detector where neutrino interactions can be reconstructed using only the LAr scintillation light imaged by an optical system based on Coded Aperture masks and lenses - a novel approach never used before in particle physics applications. In this thesis, a first evaluation of GRAIN track reconstruction and calorimetric capabilities was obtained with an optical system based on Coded Aperture cameras. A simulation of $\nu_\mu + Ar$ interactions with the energy spectrum expected at the future Fermilab Long Baseline Neutrino Facility (LBNF) was performed. The performance of SAND was evaluated, combining the information provided by all its sub-detectors, on the selection of $\nu_\mu + Ar \rightarrow \mu^- + p$ sample and on the neutrino energy reconstruction.

Contents

Introduction

Since their discovery in 1998, neutrino oscillations have been investigated by a multitude of experiments (with solar, atmospheric, accelerator, and reactor neutrinos) leading to the measurement of several parameters ruling this phenomenon. Open questions still remain, like the neutrino mass ordering and the CP violation in the leptonic sector. In this context, the Deep Underground Neutrino Experiment (DUNE), currently being built, aims to determine both the leptonic CP violation phase and the neutrino mass ordering. In addition DUNE will carry out a rich program extending from the detection of core-collapse neutrinos to the search for nucleon decay and other beyond the Standard Model searches.

DUNE will be a dual-site experiment, with a Far Detector (FD) located 1300 km away from the neutrino source and a Near Detector (ND) at Fermilab. The Far Detector will exploit four multi-kiloton Liquid Argon Time Projection Chambers (LArTPC) 1500 m underground. The Near Detector will be a complex of three different detectors designed to perform all the measurements needed to constrain the systematic uncertainty in the analysis of neutrino oscillations at the FD. At the same time, the ND will pursue a search for new physics, like light dark matter candidates and heavy neutrinos. To fulfill its purpose, the same Far Detector target (liquid Argon) is needed, coupled to a high-resolution high-granularity detector. Moreover, to cope with the high event interaction rates at the near site, detectors with a much faster time response than LArTPCs are required.

The SAND detector at the ND complex includes a LAr subdetector - GRAIN - exploiting a novel concept never implemented in a particle physics experiment. GRAIN is based on the detection of the scintillation light produced in liquid Argon by charged particles to provide event information on a nanosecond timescale. The approach adopted in this thesis is based on the Coded Aperture Technique, largely applied in the X-ray and gamma astronomy. This method overcomes the limited light collection of the pinhole camera by substituting it with an array of holes which obey precise location and size rules (e.g. Hadamard masks). A matrix of SiPMs is located on the focal plane to collect the scintillation light.

Particles produced in the neutrino interactions are not fully contained in GRAIN, therefore event reconstruction will rely on the combined reconstruction of GRAIN

and of the other components of SAND. The main tasks of GRAIN are to unambiguously locate the neutrino interaction in the liquid argon and contribute to the event reconstruction and the determination of the neutrino energy.

In this thesis work, preliminary studies exploiting the Coded Aperture Cameras were performed, evaluating the GRAIN capabilities to reconstruct the track of secondary particles produced in neutrino interaction in argon. A detailed simulation of the liquid Argon scintillation, of the light propagation and its collection was developed. The reconstruction capabilities were first evaluated by comparing the simulation results with the results obtained by a small-scale prototype, exploiting one single Coded Aperture camera. A GRAIN-like configuration was then simulated, and preliminary considerations on the use of the coded aperture mask technique were inferred. The performances of the whole SAND apparatus were also evaluated by simulating $\nu_\mu + Ar$ interactions with the expected energy spectrum at LBNF, and by studying the selection capability of charged-current quasi-elastic events in the $\nu_\mu + Ar \rightarrow \mu^- + p + X$ channel. GRAIN was used first as a passive target, and then as a homogeneous calorimeter. To do so, the deposited energy inside the argon volume was reconstructed starting from the photons detected by multiple Coded Aperture cameras, and exploiting the results of a calibration process of the whole argon volume.

This thesis is organized as follows: Chapter 1 provides an overview of the theoretical and experimental state of the art on neutrino mixing. The design and physics program of the DUNE experiment is presented in Chapter 2, while Chapter 3 will detail the SAND detector and its components. Chapter 4 is dedicated to a detailed description of the liquid Argon properties, together with the effect that impurities and doping have on them. The last chapters of this thesis are dedicated to the description of the simulation and reconstructions. Chapter 5 provides information on the full simulation framework. Chapter 6 details the Coded Aperture Technique and the track reconstruction performances of both the GRAIN-like scenario and of the prototype. Lastly, Chapter 7 describes all the steps performed to evaluate the selection performance of SAND, including a detailed description of the calibration process and the reconstruction of the energy deposited in argon.

Chapter 1

Neutrino Oscillations

Neutrinos are the most elusive among known particles. They are colorless and chargeless fermions and they interact only with charged fermions and massive gauge bosons through weak interactions. In the last decades, neutrino physics has advanced quickly and dramatically thanks to a remarkable suite of experiments and theoretical works that have made it possible to reach the current knowledge on their properties. In the Standard Model of particle physics neutrinos and antineutrinos are distinct and massless particles, and their helicity is always left-handed for the neutrinos and right-handed for the antineutrinos. These properties are well explained by the two-component model of neutrinos. The main point of this model is the massless nature of neutrinos, which implies a permanent chirality state, equal to the helicity, for both neutrinos and antineutrinos. However, in the last decades, neutrino oscillations have shown that neutrino masses differ from zero and that the Standard Model must be extended.

1.1 Flavor and Mass

In the Standard Model there are three different generations of leptons, each one composed of a charged fermion (electron, muon, or tauon) and a corresponding massless neutrino, electron-, muon- and tau-neutrinos, coupling with them via weak current.

In the Standard Model neutrinos are massless particles but the phenomenon of neutrino oscillations has given proof of non-zero neutrino mass whose absolute value is still unknown.

Different methods are used to estimate the absolute neutrino mass: cosmological studies, search for neutrinoless-double β-decay and direct measurements based on the kinematics of single β-decay.

For what concerns the single β-decay, the most stringent results on the effective

Experiment	Limit	CL
KATRIN	< 0.8 eV	90%
Troitsk	< 2.05 eV	95%
Mainz	< 2.3 eV	95%

Table 1.1: Upper bounds on the $\bar{\nu}_e$ mass obtained by the Troitsk and Mainz experiments.

electron anti-neutrino mass were obtained by the KATRIN experiment[1], which set an upper limit of 0.8 eV (90% CL). Other results wew obtained by the Troitsk[2] and Mainz[3] experiments, and are reported in Table 1.1.

Results obtained using cosmological data, such as the ones from the WMAP and Planck experiments, provide an upper limit on the sum of ν_e, ν_μ, and ν_τ masses. Such results are model dependent and, in the ΛCDM Standard Cosmological Model, typical values are: $\sum_i m_i < (0.11 - 0.54)$ eV[4].

The Standard Model is not able to account for neutrino masses; moreover, unlike other fermions, neutrinos do not carry electric or color charge. This opens the possibility that neutrinos can be their own anti-particles. A fermion with such property is known as Majorana fermion while, in the other case, is known as Dirac fermion.

Describing neutrinos as Dirac particles, the mass term of the Dirac equation can be written as:

$$\mathcal{L} = m_D(\bar{\psi}_L\psi_R + \bar{\psi}_R\psi_L) \qquad \text{with} \quad \bar{\psi}_R\psi_L = (\bar{\psi}_L\psi_R)^\dagger \tag{1.1}$$

where both a left- and a right-handed Dirac neutrino and anti-neutrino are needed to produce it. Up to date, there is no experimental evidence of the existence of a right-handed neutrino. Hence, either the right-handed neutrino does not interact weakly or there is some other mass term to take into account.

A different approach is to make use of the charge-conjugation matrix $\mathcal{C}$ to rewrite the Dirac equation in terms of left-handed fields only, in which the fields can be written as:

$$\psi = \psi_L + \psi_R = \psi_L + \psi_L^c. \tag{1.2}$$

From Eq. 1.2 it is possible to see how the charge-conjugate of the Majorana field is the field itself or that a Majorana particle is its own anti-particle:

$$\psi^c = (\psi_L + \psi_L^c)^c = \psi_L^c + \psi_L = \psi. \tag{1.3}$$

Because of the use of the charge conjugation operator the only particle suitable to be a Majorana particle is the neutrino, the only neutral fermion in the Standard

Model. For a Majorana particle, it is now possible to rewrite the mass term using only left-handed component of the field:

$$\mathcal{L}_L^M = -\frac{1}{2} m \bar{\psi}_L^c \psi_L. \tag{1.4}$$

Today, there are no observations able to claim whether neutrinos are Dirac or Majorana particles and this is one of the main open questions on their nature.

1.2 Neutrino oscillations

The idea of neutrino-antineutrino oscillation was first suggested by Pontecorvo in 1957, following the analogy with the kaon-antikaon oscillations. Ten years later in 1967, Pontecorvo proposed the neutrino flavour oscillations, then presented in the modern formalism by Gribov and himself[5].

Neutrino oscillations are a phenomenon made possible by the lepton flavour mixing and the existence of a non-zero neutrino mass[6]. Similar to the quark sector, there is a non exact correspondence between the weak gauge eigenstates and the mass eigenstates. In this scenario, the three known flavour states (ν_e, ν_μ, ν_τ) are a linear superimposition of the mass eigenstates (ν_1, ν_2, ν_3):

$$\begin{pmatrix} \nu_e \\ \nu_\mu \\ \nu_\tau \end{pmatrix} = U_{PMNS} \begin{pmatrix} \nu_1 \\ \nu_2 \\ \nu_3 \end{pmatrix} \tag{1.5}$$

where ν_e, ν_μ, and ν_τ are left-handed neutrino flavour eigenstates, coupling via charged weak current with electrons, muons and taus, respectively. U_{PMNS} is the mixing matrix relating the unitary transformation between the flavour and mass eigentstates, known as the Pontecorvo-Maki-Nagakawa-Sakata (PMNS) matrix, and ν_1, ν_2, ν_3 are the left-handed mass eigenstates with masses m_1, m_2, m_3. Eq. 1 can be rewritten in a reduced form as:

$$|\nu_\alpha\rangle = \sum_j U_{\alpha j} |\nu_j\rangle \qquad \alpha = e, \nu, \tau \qquad j = 1, 2, 3 \tag{1.6}$$

Much like the CKM matrix, the PMNS matrix is a unitary matrix which satisfies unitary relations:

$$UU^\dagger = U^\dagger U = 1 \tag{1.7}$$

$$\sum_i U_{\alpha i} U_{\beta i}^* = \delta_{\alpha,\beta} \qquad (\alpha, \beta = e, \mu, \tau) \tag{1.8}$$

$$\sum_\alpha U_{\alpha i}^* U_{\alpha j} = \delta_{i,j} \qquad (i, j = 1, 2, 3) \tag{1.9}$$

A 3×3 unitary matrix can be parametrized using 3 angles and 6 phases, of which some are unphysical. Applying a phase rotation to the fields as $\Psi \to e^{i\phi}\Psi$, three phases can be absorbed. If neutrinos are Dirac particles, it is possible to apply the same transformation eliminating two other phases, leaving just one physical phase. If neutrinos are Majorana particles, the last rephasing is not possible, and three phases are required. Based on this, one can write the PMNS matrix as the product of three rotations, of which one depends on the phase δ_{CP}, and a phases' matrix P:

$$\begin{aligned} U &= \begin{pmatrix} 1 & 0 & 0 \\ 0 & c_{23} & s_{23} \\ 0 & -s_{23} & c_{23} \end{pmatrix} \begin{pmatrix} c_{13} & 0 & s_{13}e^{-i\delta_{CP}} \\ 0 & 1 & 0 \\ -s_{13}e^{-i\delta_{CP}} & 0 & c_{13} \end{pmatrix} \begin{pmatrix} c_{12} & s_{12} & 0 \\ -s_{12} & c_{12} & 0 \\ 0 & 0 & 1 \end{pmatrix} P \\ &= \begin{pmatrix} c_{13}c_{12} & c_{13}s_{12} & s_{13}e^{-i\delta_{CP}} \\ -s_{12}c_{23} - c_{12}s_{23}s_{13}e^{i\delta_{CP}} & c_{12}c_{23} - s_{12}s_{23}s_{13}e^{i\delta_{CP}} & s_{23}c_{13} \\ s_{12}s_{23} - c_{12}c_{23}s_{13}e^{i\delta_{CP}} & -c_{12}s_{23} - s_{12}c_{23}s_{13}e^{i\delta_{CP}} & c_{23}c_{13} \end{pmatrix} P \end{aligned} \quad (1.10)$$

where c_{jk} and s_{jk} represent respectively $\cos\theta_{jk}$ and $\sin\theta_{jk}$, and $\mathbf{P}$ is the unit matrix $\mathbf{1}$ in the Dirac case, or a diagonal matrix containing the two Majorana phases in the Majorana case. In the latter case, different equivalent conventions are commonly used in the literature:

$$P_{Majorana} = \begin{pmatrix} e^{i\alpha_1} & 0 & 0 \\ 0 & e^{i\alpha_2} & 0 \\ 0 & 0 & 1 \end{pmatrix}, \begin{pmatrix} 1 & 0 & 0 \\ 0 & e^{i\phi_2} & 0 \\ 0 & 0 & e^{i(\phi_3+\delta_{CP})} \end{pmatrix}, \begin{pmatrix} e^{i\rho} & 0 & 0 \\ 0 & 1 & 0 \\ 0 & 0 & e^{i\sigma} \end{pmatrix} \quad (1.11)$$

In Eq. 1.10 and 1.11, $\delta_{CP} \in [0, 2\pi[$ is usually called Dirac phase, while all the other phases in Eq. 1.11 are known as Majorana phases, and are usually restricted to the range $[0, \pi[$. Both Dirac and Majorana phases are involved in different physics phenomenon: Majorana phases appear in lepton number violating procesess, such as the double beta decay. Dirac phase enters in neutrino oscillations, as it gives rise to an asymmetry between neutrino and antineutrino oscillations in vacuum.

The neutrino oscillation phenomenon can be schematically described by a three steps process: the production of a pure flavor state from a charged current process, the propagation of the neutrino through vacuum or matter, and the detection of a different flavor again via a charged current interaction.

One common process used to generate neutrinos is the decay of charged pions: $\pi^+ \to \mu^+\nu_\mu$. From this, a coherent superimposition of mass eigenstates, determined by Eq. 1.6, is obtained:

$$|\nu_{(t=0)}\rangle = |\nu_\alpha\rangle = \sum_j U^*_{\alpha j}|\nu_j\rangle \quad (1.12)$$

After production, each mass eigenvalues evolution is determined by its own phase factor $e^{-iE_i t}$, with $E_i = \sqrt{p^2 + m_i^2}$ being the energy of the i-th mass eigenstate. The superimposition of the mass eigenstates is not coherent anymore, and the state is not a pure flavour one:

$$|\nu(t)\rangle = \sum_j U^*_{\alpha j} e^{-iE_i t} |\nu_j\rangle = \sum_i U^*_{\alpha j} e^{-iE_i t} \sum_\beta U_{\beta j} |\nu_\beta\rangle \tag{1.13}$$

When detected, the probability amplitude for the produced flavour to have oscillated into a different flavour is given by $\langle \nu_\beta | \nu(t) \rangle$, which yield, at a specific time t, an oscillation probability

$$P(\nu_\alpha \to \nu_\beta) = |\langle \nu_\beta | \nu(t) \rangle|^2 = \left| \sum_j U_{\beta j} U^*_{\alpha j} e^{-iE_i t} \right|^2 \tag{1.14}$$

Equation 1.14 can be rewritten expanding $E_i = \sqrt{p^2 + m_i^2} \simeq p + m_i^2/(2E)$ (using $E \simeq p$ as neutrinos are ultra-relativistic) as[7]:

$$\begin{aligned} P(\nu_\alpha \to \nu_\beta) = \delta_{\alpha\beta} &- 4 \sum_{i<j} \mathrm{Re}[U_{\alpha i} U^*_{\beta i} U^*_{\alpha j} U_{\beta j}] \sin^2 \left(\frac{\Delta m^2_{ji} L}{4E} \right) \\ &+ 2 \sum_{i<j} \mathrm{Im}[U_{\alpha i} U^*_{\beta i} U^*_{\alpha j} U_{\beta j}] \sin \left(\frac{\Delta m^2_{ji} L}{2E} \right) \end{aligned} \tag{1.15}$$

where $\Delta m^2_{ji} \equiv m^2_j - m^2_i$ is the squared masses difference between two mass eigenstates, and $L \sim ct$ is the traveled distance by the neutrino. It is possible to extract different properties of neutrino oscillations from Eq 1.15: the oscillation phenomenon requires the neutrino to have a non-degenerate mass ($\Delta m^2_{ji} \neq 0$) and a non-trivial flavor mixing ($U \neq \mathbf{1}$). It is also visible how the oscillation probability depends on three mixing angles $\theta_{12}, \theta_{23}, \theta_{13}$ and on two independent squared-masses differences. Usually the two differences are chosen to be Δm^2_{21} and Δm^2_{31}, with Δm^2_{32} being determined as $\Delta m^2_{32} = \Delta m^2_{31} - \Delta m^2_{21}$. Eq. 1.15 also shows how the oscillation probability depends only on the Dirac phase, while the Majorana phases cancel out. This is expected since neutrino oscillation is a total lepton number conserving process while the Majorana nature of neutrinos can manifest only in total lepton number violation processes, such as the neutrinoless double beta decay.

The probability 1.15 is valid regardless of the process generating neutrinos and different values of L/E can be used to investigate different Δm^2 regimes, defining two main experimental ranges. The different types of experiments are thus classified depending on the value of L/E, which determines their sensitivity

to Δm^2, defined as the value of Δm^2 for which:

$$\frac{\Delta m^2 L}{2E} \sim 1. \tag{1.16}$$

Commonly, neutrino oscillation experiments are subdivided in two categories:

- Short-baseline (SBL) experiments. These experiments exploit neutrinos produced in nuclear reactors or in particle accelerators by the decay of pions, kaons and muons. In these experiments the source-detector distance is usually short, $\mathcal{O}(10\text{m} \div 1\text{km})$. The range of L/E and the sensitivity of these experiments go from

  $$\frac{L}{E} \lesssim 10 \text{ m/MeV} \Longrightarrow \Delta m^2 \gtrsim 0.1 \text{ eV}^2 \tag{1.17}$$

  for the reactor experiments, to

  $$\frac{L}{E} \lesssim 1 \text{ km/GeV} \Longrightarrow \Delta m^2 \gtrsim 1 \text{ eV}^2 \tag{1.18}$$

  for the accelerator ones;

- Long-baseline (LBL) and atmospheric experiments. Likewise the SBL experiments, the neutrino sources used in these experiments could be nuclear reactors and accelerators but the source-detector distance is some order of magnitude larger. Despite different values of L/E for reactor and accelerator LBL experiments, their sensitivity is similar and is

  $$\begin{array}{ll} \text{Reactors:} & L/E \lesssim 10^3 \text{ m/MeV} \\ \text{Accelerators:} & L/E \lesssim 10^3 \text{ km/GeV} \end{array} \Longrightarrow \Delta m^2 \gtrsim 10^{-3} \text{ eV}^2. \tag{1.19}$$

  A different value can be reached with atmospheric neutrino experiments, for which L ranges from 20 km, for neutrinos coming from the upper atmosphere, to $\sim 10^4$ km, for neutrinos coming through the other side of the Earth. For these experiments thus, the sensitivity to Δm^2 is

  $$\frac{L}{E} \lesssim 10^4 \text{ km/GeV} \Longrightarrow \Delta m^2 \gtrsim 10^{-4} \text{ eV}^2. \tag{1.20}$$

Neutrino oscillations experiments can also be divided in appearance and disappearance experiments. This subdivision is based on the type of measurements performed:

- Appearance experiments. They measure the transition from the neutrino's flavor produced by the source and the other ones.

- Disappearance experiments. They measure the survival probability of the neutrino flavor produced by the source.

1.2.1 Two-flavour effective approximation

A good approximation, used for decades in many experimental situations, can be obtained neglecting the subleading terms in Eq. 1.15. Doing so, one obtains a two flavour oscillation probability described by a single mixing angle θ and a single Δm^2:

$$P(\nu_\alpha \to \nu_\beta) = P(\bar{\nu}_\alpha \to \bar{\nu}_\beta) = \sin^2 2\theta \sin^2\left(\frac{\Delta m^2 L}{4E}\right). \tag{1.21}$$

Equation 1.21 was used in particular in solar and atmospheric neutrino experiments

The dominant effects of neutrino oscillations in atmospheric neutrino experiments are usually described in a framework where $\Delta m^2_{21} L/E \ll 1$, usually aproximated by setting $\Delta m^2_{21} = 0$ in the three flavour formula 1.15. With this approximation, the oscillation appearance probability becomes[8]:

$$P(\nu_\alpha \to \nu_\beta) = \sin^2 2\theta^{eff}_{\alpha\beta} \sin^2\left(\frac{\Delta m^2_{31} L}{4E}\right), \;\; \sin^2 2\theta^{eff}_{\alpha\beta} \equiv 4|U_{\alpha 3} U_{\beta 3}|^2, \;\; (\beta \neq \alpha) \tag{1.22}$$

while for the oscillation disappearance probability one has:

$$P(\nu_\alpha \to \nu_\alpha) = 1 - \sin^2 2\theta^{eff}_{\alpha\alpha} \sin^2\left(\frac{\Delta m^2_{31} L}{4E}\right), \;\; \sin^2 2\theta^{eff}_{\alpha\alpha} \equiv 4|U_{\alpha 3}|^2(1 - |U_{\alpha 3}|^2) \tag{1.23}$$

For instance, the probability of muon neutrino disappearance is:

$$P(\nu_\mu \to \nu_\mu) \simeq 1 - \sin^2 2\theta_{23} \sin^2\left(\frac{\Delta m^2_{31} L}{4E}\right). \tag{1.24}$$

Equation 1.24 describes the dominant oscillations in atmospheric neutrinos and it's the origin of the terminology 'atmosferic mixing angle', θ_{atm} and 'atmospheric' Δm^2' for θ_{23} and Δm^2_{31} respectively. In the approximation where $\Delta m^2_{31} L/E \gg 1$ and $\Delta m^2_{21} L/E \gtrapprox 1$, electron neutrinos are dominated by Δm^2_{21} instead of Δm^2_{31}. Oscillations disappearence probability becomes:

$$P(\nu_e \to \nu_e) = P(\bar{\nu}_e \to \bar{\nu}_e) \simeq 1 - \sin^2 2\theta_{12} \sin^2\left(\frac{\Delta m^2_{21} L}{4E}\right). \tag{1.25}$$

This formula applies to low-energy solar neutrinos and justify the popular use of 'solar mixing angle' terminology for θ_{12} and 'solar Δm^2' for Δm^2_{21}.

With the increased precision of experiments, these formulas must be corrected for three-flavour effects not taken into account in the two-flavour approximation.

1.2.2 Three-flavour effect and CP violation

In the parametrization of the PMNS matrix seen in Sec. 1.2, the mixing between ν_1 and ν_3 depends on the CP-violation phase δ_{CP}. The presence of a non-zero CP violation term results in an asymmetry in the neutrino versus antineutrino oscillations $\Delta P_{\alpha\beta} = P(\nu_\alpha \to \nu_\beta) - P(\bar{\nu}_\alpha \to \bar{\nu}_\beta)$. It is possible to write this quantity as[9]:

$$\Delta P_{\alpha\beta} = \pm 16 J \sin\left(\frac{\Delta m^2_{21} L}{4E}\right) \sin\left(\frac{\Delta m^2_{31} L}{4E}\right) \sin\left(\frac{\Delta m^2_{32} L}{4E}\right), \tag{1.26}$$

$$J \equiv \mathrm{Im}[U_{e1} U^*_{\mu 1} U^*_{e2} U_{\mu 2}] \tag{1.27}$$

with a + and a - sign when (α, β, γ) is an even and odd permutation of (e, μ, τ) respectively. The measure of the CP violation from the Dirac phase is expressed by the quantity J, called Jarlskog invariant[10]:

$$J = \frac{1}{8} \cos\theta_{13} \sin 2\theta_{12} \sin 2\theta_{13} \sin 2\theta_{23} \sin\delta_{CP}. \tag{1.28}$$

From this equation it is possible to extract the necessary conditions to have CP violation in neutrino oscillation: all three mixing angle θ_{ij} must be non zero, the δ_{CP} phase must be different from 0 and π and the three sqared mass differences must be non vanishing:

$$\begin{gathered} \theta_{ij} \neq 0, \;\; \delta_{CP} \neq 0, \pi \\ m_1 \neq m_2, \;\; m_2 \neq m_3, \;\; m_3 \neq m_1. \end{gathered} \tag{1.29}$$

From Eq. 1.26 it is possible to extract even more information about CP violation. Due to the unitarity of the PMNS matrix, neutrino oscillations do not depend on the oscillation channel:

$$\mathrm{Im}[U_{e1} U^*_{\mu 1} U^*_{e2} U_{\mu 2}] = -\mathrm{Im}[U_{e1} U^*_{\tau 1} U^*_{e2} U_{\tau 2}] = \mathrm{Im}[U_{\mu 1} U^*_{\tau 1} U^*_{\mu 2} U_{\tau 2}] \tag{1.30}$$

from which one obtains $\Delta P_{e\mu} = -\Delta P_{e\tau} = \Delta P_{\mu\tau}$. Moreover, it can be obvserved how only experiments sensitive to oscillations governed by Δm^2_{21} can observe the CP violation effect. Tipical experimental conditions are such that $\Delta m^2_{31} L/E \sim 1$ and $\Delta m^2_{21} L/E \ll 1$. Equation 1.15 can thus be simplified as:

$$\Delta P_{\alpha\beta} \simeq \pm 16 J \sin\left(\frac{\Delta m^2_{21} L}{4E}\right) \sin^2\left(\frac{\Delta m^2_{31} L}{4E}\right) \tag{1.31}$$

Usually, experiments sensitive to oscillations governed by Δm^2_{21} consist of long baseline of hundreds of kilometers, high intensity neutrino beams and large detectors. These conditions add the complication of disentangling the effect of the CP

violation from the effect of the neutrino interaction with matter. The latter effect affects the $\nu_\mu - \nu_e$ channel, relevant for long baseline neutrino experiments, and is the source of an asymmetry between neutrino and antineutrino oscillation.

In vacuum, one can write the full $\nu_\mu \to \nu_e$ oscillation probability as:

$$\begin{aligned} P(\nu_\mu \to \nu_e) \simeq & \sin^2\theta_{23}\sin^2 2\theta_{13}\sin^2\left(\frac{\Delta m^2_{31}L}{4E}\right) \\ & + \cos^2\theta_{23}\sin^2 2\theta_{12}\sin^2\left(\frac{\Delta m^2_{21}L}{4E}\right) \\ & + \frac{1}{2}\cos\theta_{13}\sin 2\theta_{12}\sin 2\theta_{13}\sin 2\theta_{23}\cos\delta_{CP}\sin\left(\frac{\Delta m^2_{21}L}{4E}\right)\sin\left(\frac{\Delta m^2_{31}L}{2E}\right) \\ & - \cos\theta_{13}\sin 2\theta_{12}\sin 2\theta_{13}\sin 2\theta_{23}\sin\delta_{CP}\sin\left(\frac{\Delta m^2_{21}L}{4E}\right)\sin^2\left(\frac{\Delta m^2_{31}L}{4E}\right) \end{aligned} \tag{1.32}$$

where the first term is the Δm^2_{31}-driven oscillation terms, the second one is the one driven by Δm^2_{21}, while the third and fourth terms involve both Δm^2_{31} and Δm^2_{21} and are CP-even and CP-odd respectively. One can obtain the formula for the $\bar{\nu}_\mu - \bar{\nu}_e$ oscillation probability by switching the sign of δ_{CP} in Eq. 1.32. The CP violation in the $\nu_\mu - \nu_e$ channel can then be quantified by measuring the CP asymmetry parameter:

$$A_{\mu e} \equiv \frac{P(\nu_\mu \to \nu_e) - P(\bar{\nu}_\mu \to \bar{\nu}_e)}{P(\nu_\mu \to \nu_e) + P(\bar{\nu}_\mu \to \bar{\nu}_e)} \simeq -\frac{\cos\theta_{23}\sin 2\theta_{12}}{\sin\theta_{23}\sin\theta_{13}}\sin\left(\frac{\Delta m^2_{21}L}{4E}\right)\sin\delta_{CP} \tag{1.33}$$

1.2.3 Neutrino propagation in matter

When neutrinos propagate in matter, their propagation can be modified by the coherent forward weak charged-current (CC) and neutral-current (NC) scattering from particles they encounter along the way[11]. This effect, known as MSW effect, generates changes in the oscillation probability in matter compared to the ones in vacuum and has origin from the fact that ν_e are the only neutrinos that can take part both in CC and NC elastic interactions with electrons, while ν_μ and ν_τ can only have NC interactions with electrons

Neutrino's propagation in matter is descibed by a Schrodinger-like equation:

$$i\frac{d}{dt}\left|\nu(t)\right\rangle = \mathcal{H}\left|\nu(t)\right\rangle \tag{1.34}$$

with $|\nu(t)\rangle$ being the neutrino state vector at time t, and $\mathcal{H}$ the total Hamiltonian in matter:

$$\mathcal{H} = \mathcal{H}_0 + \mathcal{H}_1, \quad \mathcal{H}_1\left|\nu_\alpha\right\rangle = V_\alpha\left|\nu_\alpha\right\rangle \tag{1.35}$$

where H_0 is the free kinetic part describing the neutrino propagation in vacuum, and V is the potential induced by the neutrino interactions with the medium[12].

Equation 1.34 can be rewritten in the flavour eigenstate basis:

$$i\frac{d}{dt}\nu_\beta(t) = \sum_\gamma H_{\beta\gamma}\nu_\gamma(t) \quad \beta,\gamma = e,\mu,\tau \tag{1.36}$$

where $\mathcal{H}_{\beta\gamma} \equiv \langle\nu_\beta|\,\mathcal{H}\,|\nu_\gamma\rangle$ are the elements of the Hamiltonian matrix in the flavour basis, while $\nu_\beta(t) \equiv \langle\nu_\beta|\nu(t)\rangle$ is the probability amplitude of having a neutrino in the state $|\nu_\beta\rangle$ at the time t. From here, it is possible to obtain the probability that a neutrino generated with an α flavor is found to have a different flavor β after the time t: $P(\nu_\alpha \to \nu_\beta; t) = |\nu_\beta(t)|^2$.

It is possible to express the vacuum Hamiltonian in the flavor basis as:

$$H_0 = \frac{1}{2E}U\mathrm{Diag}(m_1^2, m_2^2, m_3^2)U^\dagger = \frac{M_\nu^\dagger M_\nu}{2E} \tag{1.37}$$

where M_ν is the neutrino mass matrix in the flavour basis. The V potential is induced by the coherent scattering of neutrinos on electrons in the medium. As ordinary matter is composed of just electrons, it receives contributions from both the W and the Z bosons, with the first present only for electron neutrinos as ordinary matter does not contain muons and taus, and the latter being identical for all the neutrino flavours. The V potential can be expressed as:

$$V_{\alpha\beta} = V_\alpha\delta_{\alpha\beta} = (V_{CC,\alpha} + V_{NC,\alpha})\,\delta_{\alpha\beta} \tag{1.38}$$

with:

$$V_{CC,\alpha} = \begin{cases} \sqrt{2}\,G_F n_e(x) & \alpha = e \\ 0 & \alpha = \mu,\tau \end{cases}, V_{NC,\alpha} = -\frac{G_F}{\sqrt{2}}\,n_n(x) \quad (\alpha = e,\mu,\tau)\,. \tag{1.39}$$

In the equation above, G_F is the Fermi constant and $n_e(x)$, $n_n(x)$ are the electron and neutron densities in the medium, which depend on the spatial position x. One can now write the matter Hamiltonian for neutrinos:

$$H_{\beta\gamma} = \frac{1}{2E}\sum_i U_{\beta i}U_{\gamma i}^* m_i^2 + V_{CC,\beta}\delta_{\beta\gamma} \tag{1.40}$$

This implies that in matter, the vacuum mass eigenstates are replaced by the so called matter eigenstates, related to the flavour eigenstates by the mixing matrix in matter U_m:

$$H = U_m \begin{pmatrix} E_1^m & 0 & 0 \\ 0 & E_2^m & 0 \\ 0 & 0 & E_3^m \end{pmatrix} U_m^\dagger, \begin{pmatrix} |\nu_e\rangle \\ |\nu_\mu\rangle \\ |\nu_\tau\rangle \end{pmatrix} = U_m^* \begin{pmatrix} |\nu_1^m\rangle \\ |\nu_2^m\rangle \\ |\nu_3^m\rangle \end{pmatrix} \tag{1.41}$$

Here, E_i^m are the eigenvalues of the matter Hamiltonian H, called the energy levels in matter. The amplitude of probability to find the neutrino in the matter eigenstate $|\nu_i^m\rangle$ at the time t, $\nu_i^m(t) = \langle\nu_i^m|\nu(t)\rangle$, is related to the amplitude of probability $\nu_\beta(t)$ to find it in the flavour eigenstate $|\nu_\beta\rangle$ by the mixing matrix in matter:

$$\nu_\beta(t) = \sum_i (U_m)_{\beta i}\nu_i^m(t). \tag{1.42}$$

The neutrino oscillations in matter further depend on the matter density and whether it is constant or not. For a description of neutrino propagation in a non uniform medium, one can look at [13]. For a uniform density medium, $n_e(x) = n_e = \text{const}$, the Hamiltonian doesn't change during the neutrino propagation and the matter eigenstates $|\nu_i^m\rangle$, the energy levels E_i^m, and the mixing matrix U_m are not time dependent. From Eq. 1.36 and Eq. 1.42 it is possible to derive the oscillation probability in matter:

$$P_m(\nu_\alpha \to \nu_\beta) = |\nu_\beta(t)|^2 = \left|\sum_i (U_m)_{\beta i}\,\nu_i^m(t)\right|^2 = \left|\sum_i (U_m)_{\beta i}(U_m)^*_{\alpha i}e^{-iE_i^m t}\right|^2 \tag{1.43}$$

In long-baseline neutrino oscillation experiments where the matter effect can't be neglected, the $\nu_\mu \to \nu_e$ oscillation probability defined in Eq. 1.32 becomes[14][15]:

$$\begin{aligned}
P(\nu_\mu \to \nu_e) \simeq\ & \sin^2\theta_{23}\frac{\sin^2 2\theta_{13}}{(A-1)^2}\sin^2\left[(A-1)\Delta_{31}\right] \\
& + \alpha^2\cos^2\theta_{23}\frac{\sin^2 2\theta_{12}}{A^2}\sin^2(A\Delta_{31}) \\
& + \alpha\frac{\cos\theta_{13}\sin 2\theta_{12}\sin 2\theta_{13}\sin 2\theta_{23}\cos\delta_{CP}}{A(1-A)}\cos\Delta_{31}\sin(A\Delta_{31})\sin\left[(1-A)\Delta_{31}\right] \\
& - \alpha\frac{\cos\theta_{13}\sin 2\theta_{12}\sin 2\theta_{13}\sin 2\theta_{23}\sin\delta_{CP}}{A(1-A)}\sin\Delta_{31}\sin(A\Delta_{31})\sin\left[(1-A)\Delta_{31}\right]
\end{aligned} \tag{1.44}$$

where

$$\alpha \equiv \Delta m^2_{21}/\Delta m^2_{31} \tag{1.45}$$

$$\Delta_{31} \equiv \Delta m^2_{31}L/4E \tag{1.46}$$

$$A \equiv 2VE/\Delta m^2_{31} = 2\sqrt{2}\,G_F n_e E/\Delta m^2_{31}. \tag{1.47}$$

Similarly to Eq. 1.32, the first term describes the Δm^2_{31}-driven oscillations, usually studied in the so called 1-3 sector. The second term is driven by Δm^2_{21}, whose oscillations are investigated in the "solar" or 1-2 sector. This term is suppressed because of the small value of the α parameter.

Experiment	L [Km]	E [GeV]	A
T2K	295	0.6	0.046
NOνA	800	1.6	0.12
DUNE	1300	2.6	0.20

Table 1.2: Matter effect parameter for current and next long baseline experiments.

The third term is the CP-violating term. It depends on the Jarlskog invariant J and impacts the leading term in the neutrino oscillation probability by a $\pm 30\%$ variation for $\delta_{CP} = \mp\pi/2$.

The last term is the CP conserving part, useful to resolve degeneracies as it depends on the δ_{CP} phase in a different way compared to the third term. The A parameter includes matter effects: it changes sign in the case of antineutrinos as the matter potential V becomes -V. From Eq. 1.44 one can see that the matter effect depends also on Δm^2_{31} and thus on the neutrino mass ordering (Sec. 1.3). Thus, the matter effect either enhance or suppress the neutrino oscillation probability $P(\nu_\mu \rightarrow \nu_e)$ or the antineutrino one $P(\bar{\nu}_\mu \rightarrow \bar{\nu}_e)$ depending on the true mass ordering. Values of the matter parameter for different experiments, baseline and energies are shown in Table 1.2.

As noted in Sec. 1.2.2 the oscillation probability for neutrino and antineutrino is either enhanced or suppressed by the size of CP violation. Figure 1.1 shows $P(\nu_\mu \rightarrow \nu_e)$ oscillation probability with the contribution from all terms in Eq. 1.44 as a function of the neutrino energy and for a specific value of L. Figure 1.2 shows the electron (anti) neutrino appearance probability at a fixed L/E ratio, enhancing the interplay between the terms in Eq. 1.44. The CP-violating and conserving terms modulate the probability along the ellipse, while the matter effect manifests in a translation of the ellipse, enhancing either the neutrino or antineutrino oscillation probability.

1.2.4 Experimental results

The current knowledge of the three-neutrino framework's parameters came from a wide range of experiments. They are usually subdivided based on the parameters they are most sensitive to, which depend of the different values of L/E of each experiment. A common subdivision is as follow:

- Solar neutrino experiments, sensitive to $\sin^2\theta_{12}$ and Δm^2_{21};
- Reactor neutrino experiments, sensitive to θ_{13};
- Atmospheric neutrino experiment, sensitive to $\sin^2\theta_{23}$ and Δm^2_{31};

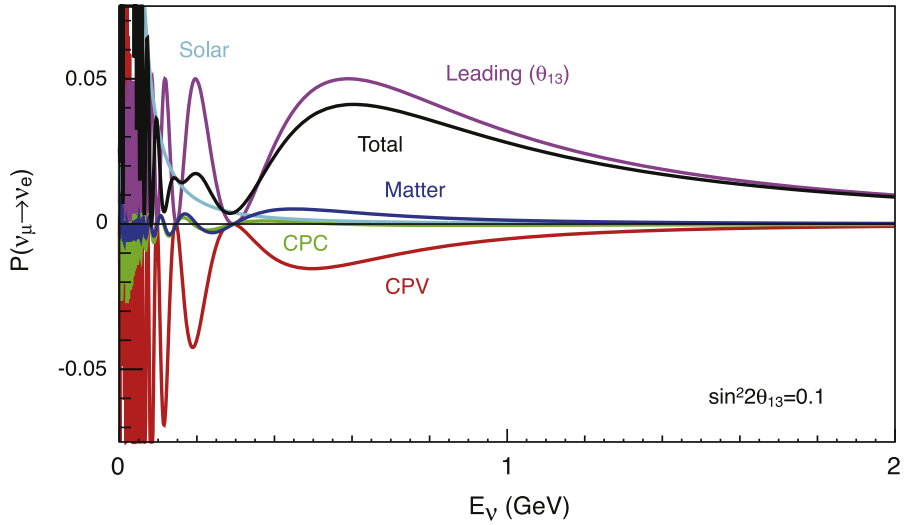

Figure 1.1: Oscillation probability as a function of the energy for the Hyper-Kamiokande experiment. L = 295 km, $\sin^2 2\theta_{13} = 0.1$, $\delta_{CP} = \pi/2$. Each term of Eq. 1.32 is shown separately[16].

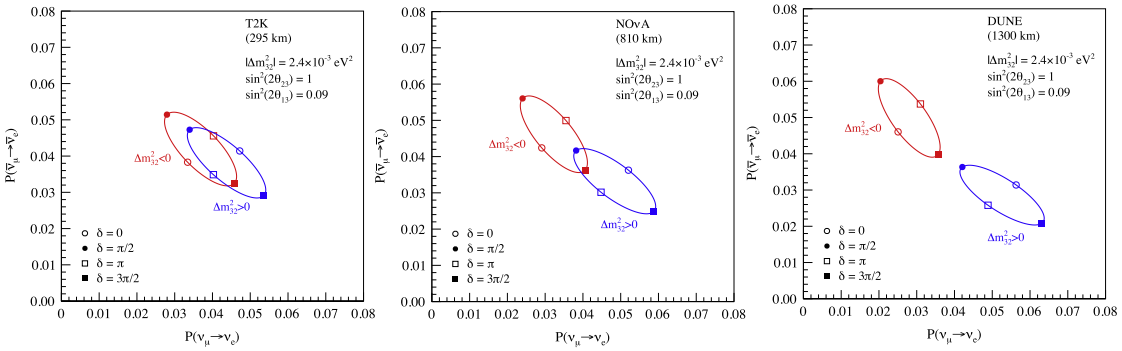

Figure 1.2: Oscillation probability for neutrinos and antineutrinos for normal (blue) and inverted (red) mass ordering for the current and next long baseline neutrino oscillation experiments[7][17].

- Long-baseline accelerator experiment, sensitive to $\sin^2\theta_{23}$, Δm^2_{31} and θ_{13}.

The solar sector The first results obtained detecting solar neutrinos were obtained by a series of radiochemicals experiments between 1968 and 2007: Homestake chlorine experiment[18], the Soviet-American Gallium Experiment (SAGE)[19], the Gallium Experiment (Gallex)[20], and the Gallium Neutrino Observatory (GNO)[21]. These experiments measure the solar neutrino flux by exploiting the capture of electron neutrinos on Chlorine or Gallium. The results were all in agreement, suggesting a deficit in the detected electron neutrino flux produced by the Sun, compared to the models[22].

Other experiments used a different approach to study solar neutrinos. A neutrino interaction in water produces Cherenkov light, with photons emitted in a cone shape centered on the secondary particles momentum. In the reaction $\nu e^- \to \nu e^-$, the scattered electron is emitted preferentially in the direction of the neutrino. Detecting the Cherenkov photons, it is then possible to verify the solar origin of the neutrinos and perform a solar flux measurement. This idea was used by the 2.14 kt water Cherenkov Kamioka Nucleon Decay Experiment (Kamiokande, 1987-1995)[23] in Japan and later on by the still running Super-Kamiokande[24], a 50 kt water Cherenkov detector. Both experiments provided results in agreement with a large suppresstion of the expected neutrino flux. The final result of the Kamiokande experiments is[25]:

$$\Phi(^8B) = [2.80 \pm 0.19\ (\text{stat.}) \pm 0.33\ (\text{sys.})] \times 10^6 \text{cm}^{-2}\text{s}^{-1} \tag{1.48}$$

while the latest update from the Super-Kamiokande experiments is[26]:

$$\Phi(^8B) = [2.308 \pm 0.020\ (\text{stat.}) \pm 0.040\ (\text{sys.})] \times 10^6 \text{cm}^{-2}\text{s}^{-1} \tag{1.49}$$

.

Both the radiochemical and the water Cherenkov experiments were not able to distinguish a deficit in the electron neutrino flux due to a wrong SSM prediction and a deficit due to neutrino oscillations. The definitive answer to the origin of the reduced neutrino flux was given by Sudbury Neutrino Observatory (SNO)[27] in Canada, a Cherenkov detector located 2 km below ground, containing 1 kt of heavy water and sensitive to three different channels:

$$\begin{aligned} &\text{Elastic Scattering:} && \nu_e e \to \nu_e e \\ &\text{Charged Current:} && \nu_e + d \to e^- + p + p \\ &\text{Neutral Current:} && \nu_f + d \to \nu_f + n + p \quad \nu_f = \nu_e, \nu_\mu, \nu_\tau. \end{aligned} \tag{1.50}$$

SNO was able to measure the total solar neutrinos flux, independently from their flavour[28]:

$$\phi_{NC}(\nu_{active}) = [5.25 \pm 0.16\ (\text{stat.})^{+0.11}_{-0.13}\ (\text{syst.})] \times 10^6\ \text{cm}^{-2}\text{s}^{-1} \tag{1.51}$$

in agreement with the expected flux, and the flux of electron neutrino:

$$\Phi_{CC}(\nu_e) = (0.301 \pm 0.033)\phi_{NC}(\nu_{active}). \tag{1.52}$$

The results obtained by SNO were clear: the total neutrino flux was in agreement with the one expected from solar models, while the electron neutrino flux had a deficit, confirming the results obtained by the other experiments and proving that along their way from the Sun to the Earth neutrinos can oscillate. Lastly, the Borexino experiment[29], a 278 t liquid scintillator detector installed in the Gran Sasso Laboratory (Italy) running since 2007, measured both the ^{7}Be electron neutrino flux and the pep flux. The measured values are as follow[30][31]:

$$\phi(^7Be) = (3.10 \pm 0.15) \times 10^9 \text{ cm}^{-2}\text{s}^{-1} \tag{1.53}$$
$$\phi(pep) = (1.6 \pm 0.3) \times 10^8 \text{ cm}^{-2}\text{s}^{-1} \tag{1.54}$$

where the Be neutrino flux is again around 62% of the SSM predicted flux.

All these measurements, together with an important contribution by the KamLAND experiment[32], allowed to measure both $\tan^2\theta_{12}$ and Δm^2_{21}. KamLAND is a 1 kt liquid scintillator experiment able to detect $\bar{\nu}_e$ produced in nuclear reactor through the reaction $\bar{\nu}_e p \to ne^+$. Due to the antineutrino energy having a peak at about 3-4 MeV, KamLAND can provide precise measurement of the same oscillation parameters of solar neutrino experiments.

The results of KamLAND can be well described in the two-flavour neutrino oscillation scenario, described by Eq. 1.21, where $\theta = \theta_{12}$ and $\Delta m^2 = \Delta m^2_{21}$. Solar neutrino experiments and KamLAND measurements agreed and the combined results, shown in Fig. 1.3, are:

$$\Delta m^2_{21} = (7.53 \pm 0.18) \times 10^{-5} \text{ eV}^2 \tag{1.55}$$
$$\tan^2\theta_{12} = 0.44 \pm 0.03. \tag{1.56}$$

The atmospheric sector The first indication of neutrino oscillation in the atmospheric sector was given by the Kamiokande experiment, measuring a deficit in the detected ν_μ rate compared to the expected one. Similar deficits were observed by the the Irvine–Michigan–Brookhaven (IMB)[34] experiment. A clear explanation for the source of this deficit was given in 1998 by the Super-Kamiokande experiment, and confirmed by the Monopole, Astrophysics and Cosmic Ray Observatory (MACRO)[35] and Soudan-2[36] experiments. Exploiting the behavior of the neutrino-nucleus interactions, where the produced lepton direction is correlated to the neutrino direction, Super-Kamiokande was able to provide results on the distribution of zenith angle for ν_μ and ν_e based on 33 kton year of exposure. Moreover, the traveled distance of the detected neutrinos could vary from some

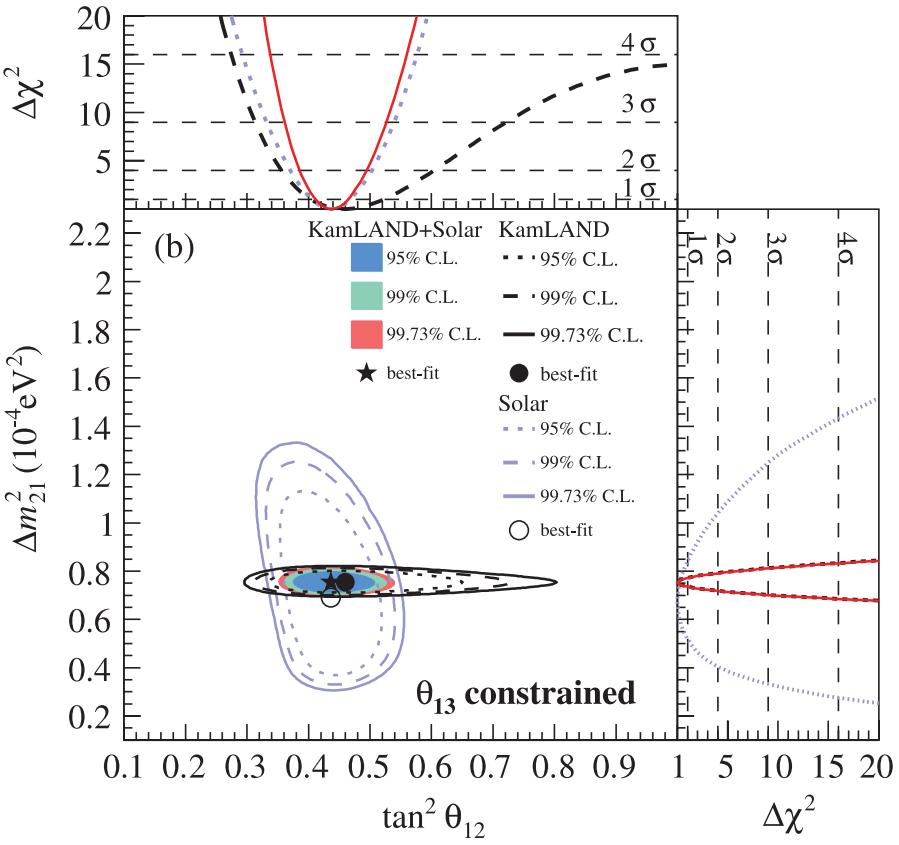

Figure 1.3: Allowed region at different C.L. for the neutrino oscillation parameters from solar data, KamLAND and a combined fit[33].

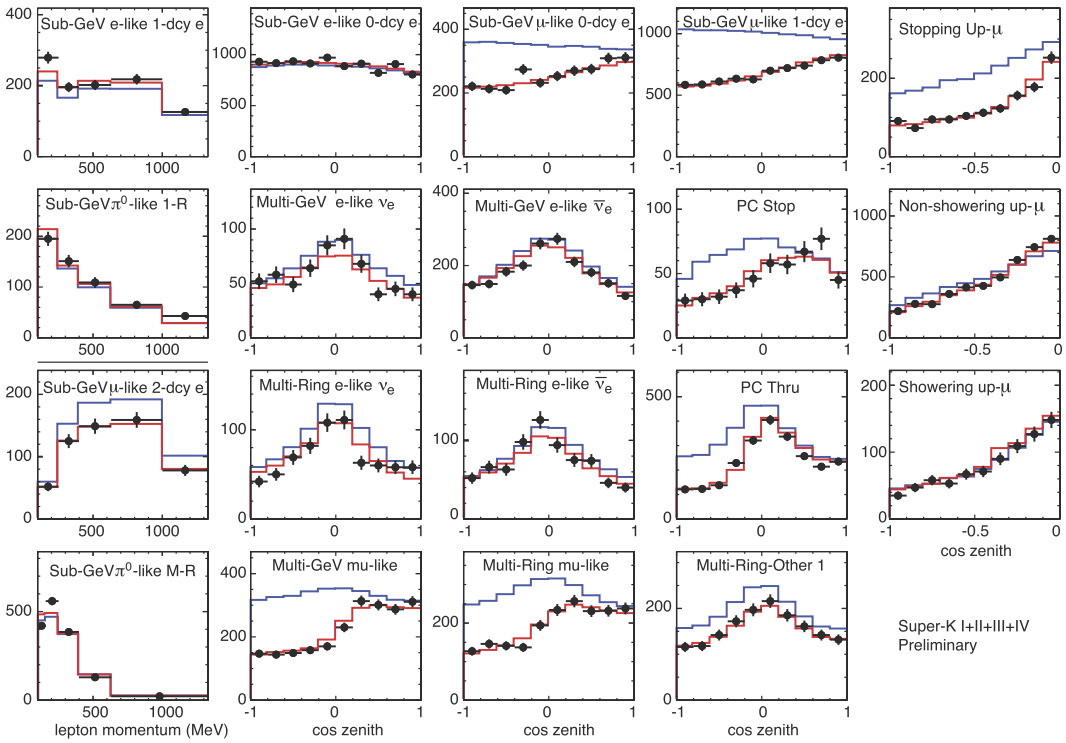

Figure 1.4: Momentum and zenith angle distributions for atmospheric neutrinos detected by the Super-Kamiokande experiments. Blue histograms correspond to the unoscillated expected distributions while the red ones are the results of data fit assuming neutrino oscillation. Data are represented by points with error bars[37].

tents of km for the down-going neutrinos, to about 12000 km for up-going ones, allowing the measurement of a large span of L/E scenarios. The results obtained by Super-Kamiokande can be understood again in the two neutrinos scenario described by Eq. 1.21, where $\theta = \theta_{23}$ and $\Delta m^2 = \Delta m^2_{31}$. Figure 1.4 shows these results, where it is possible to see the strong disappearance of ν_μ for up-going neutrinos. From these results, a first estimation of the atmospheric parameters can be extracted: as the survival probability for up-going neutrinos is close to 0.5, and Eq. 1.21 approaches $1 - 1/2 \sin^2 2\theta_{23}$ for high value of L, the mixing angle must be close to the $\pi/4$ maximal value. Moreover, as the neutrino disappearance starts for neutrino of about 1 GeV near the horizontal zenith angle, corresponding to a baseline of about 400 km, the Δm^2_{31} must be close to 10^{-3}eV^2. In more recent years the ANTARES[38] and IceCube[39] experiments have contributed to the study of atmospheric neutrino oscillations. Atmospheric neutrinos are detected via the Cherenkov light emitted by muons produced in nu-mu CC interactions. Figure 1.5 shows the results obtained by IceCube with data collected between 2012 and 2015, while Fig. 1.6 shows the allowed regions in the $\sin^2\theta_{23} - \Delta m^2_{32}$ plane obtained by

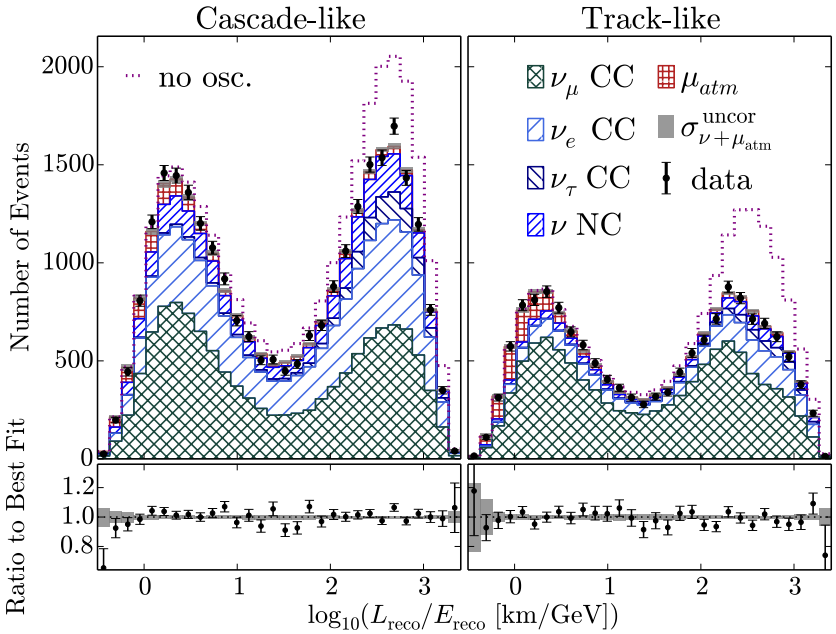

Figure 1.5: Distribution of the atmospheric neutrinos measured by the IceCube experiment as a function of L/E. The "no oscillation" scenario is represented by the dotted red line, while the best fit for the oscillated distribution is represented by the stacked hatched histograms. The ratio between the collected data and the data best fit is also shown in the bottom part of the plots. The two peaks represent the down-going and up-going trajectories. A strong suppression of the up-going events is visible due to oscillations[40].

IceCube, compared to results from other experiments[40].

Long-baseline experiment results Since the discovery of oscillations in the atmospheric neutrino sector, neutrino oscillation experiments have been performed using accelerator neutrino beams. The first two experiments probing the ν_μ disappearance oscillation channel in the same region explored by atmospheric neutrinos were KEK-to-Kamioka (K2K)[44] and the Main Injector Neutrino Oscillation Search (MINOS)[45] experiments. K2K measured the disappearance of ν_μ between 1999 and 2004. The final K2K results found that at 99.9985% confidence (4.3 σ) there had been a disappearance of muon neutrinos. Fitting the data under the oscillation hypothesis, the best fit for the difference of the squared masses between muon neutrinos and tau neutrinos was $\Delta m^2 = 2.8 \times 10^{-3}$ eV^2[46]. This result is in good agreement with the previous Super-Kamiokande result[47], and the later MINOS result[48]. MINOS reported the results obtained with the measurements

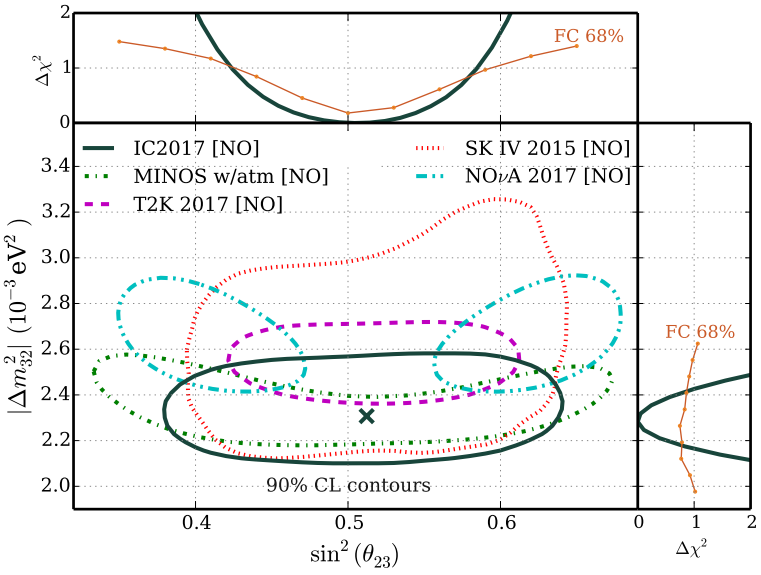

Figure 1.6: IceCube 90% contours in the $\sin^2\theta_{23} - \Delta m^2_{32}$ plane along with that of other experiments[40][41][42][43].

of the $\nu_\mu \to \nu_\mu$ oscillation combined with 37.88 kton-year of cosmic data:

$$NO \quad \begin{array}{l} |\Delta m^2_{32} = [2.28 - 2.46] \times 10^{-3}\text{eV}^2 \text{ (68\% C.L.)} \\ \sin^2 2\theta_{23} = 0.35 - 0.65 \text{ (90\% C.L.)} \end{array} \tag{1.57}$$

$$IO \quad \begin{array}{l} |\Delta m^2_{32} = [2.32 - 2.53] \times 10^{-3}\text{eV}^2 \text{ (68\% C.L.)} \\ \sin^2 2\theta_{23} = 0.34 - 0.675 \text{ (90\% C.L.)} \end{array} \tag{1.58}$$

The OPERA experiment[49] provided the ultimate confirmation of the neutrino oscillation phenomenon by discovering the appearance of ν_τ in the ν_μ neutrino beam from CERN to the Gran Sasso Laboratory The appearance of ten tau neutrinos was reported over an expected background 2 events, corresponding to 6.1 σ significance level observation.

The latest results were obtained by the current ongoing LBL neutrino experiments: T2K and NOνA. Initially, measurements of θ_{23} from the two experiments were in conflict: T2K observed a reduced number of ν_μ and $\bar{\nu}_\mu$ compared to the expected rate if no oscillations were present. The measured oscillation parameters are compatible with a maximal θ_{23} mixing angle, both for neutrino and antineutrinos. On the other hand, the results obtained in the same ν_μ disappearance channel by NOνA excluded the maximal mixing angle at 2.5σ, as visible in Fig.1.6.

Both experiments also published results of oscillation analysis in the electron neutrino appearance channel. T2K measured an excess of neutrino candidates

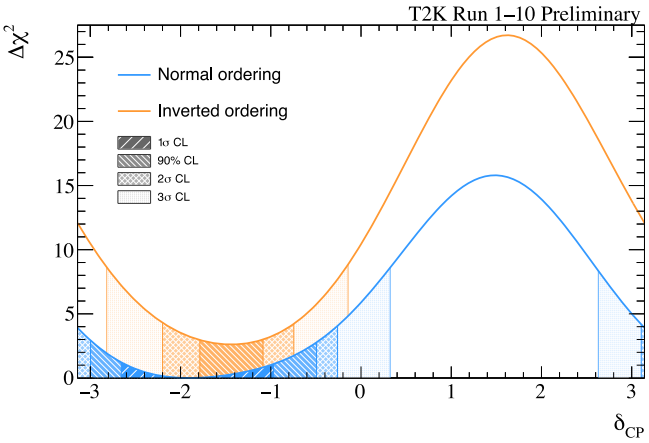

Figure 1.7: Contraint on δ_{CP} for normal and inverted mass ordering. Different CL regions are shown as vertical bands[50].

and a smaller number of antineutrino ones. These results are in agreement with a value of δ_{CP} close to $-\pi/2$ which enhances the neutrino oscillation probability and suppresses the antineutrino one (Fig. 1.7).

Similarly, NOνA released results on the electron neutrino appearance, observing an excess of neutrino candidates. A joint analysis of both the appearance and disappearance channels has been performed. Due to the value of θ_{23} found by the NOνA experiment being non-maximal, there are two degenerate best fit points in both the normal and inverted ordering. Despite these differences, the latest joint analysis showed a consistency of the results, with the 1σ regions in the $\sin^2\theta_{23}-\delta_{CP}$ from both experiments touching each other, indicating a statistically consistency always greater than 1.7σ[51]. The results of the joint analysis are visible in figure 1.8.

Short baseline sector The 1-3 sector of the PMNS matrix is governed by the Δm^2_{31} squared masses difference and the θ_{13} mixing angle. The neutrino survival probability can be described in the two neutrino flavour approximation (Eq. 1.25). With a neutrino energy of about 4 MeV, a baseline of 1 or 2 km offers a good probe for the θ_{13} mixing angle. Reactor based short-baseline experiments have measured θ_{13} exploiting the antineutrino induced inverse beta-decay (IBD) in Gadolinium doped liquid scintillators. A first upper limit on θ_{13} was set by the Chooz experiment[52]:

$$\sin^2 2\theta_{13} < 0.17 \text{ at } 90\% \text{ C.L for } \Delta m^2_{31} = 2.4 \times 10^{-3} \text{ eV}^2. \tag{1.59}$$

The determination of θ_{13} was achieved by next generation experiments: Double Chooz[52] in France, RENO[53] in South Korea and Daya Bay[54] in China.

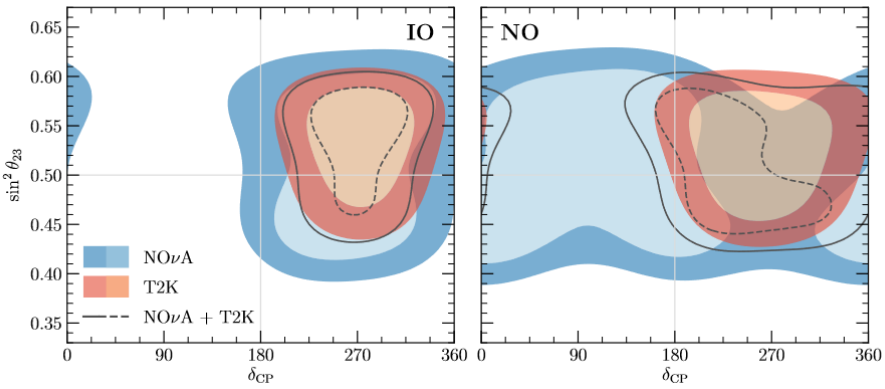

Figure 1.8: 1σ and 2σ allowed region in the $\delta_{CP} - \sin^2\theta_{23}$ plane for the T2K (red) and NOνA (blue) experiments and their combination[51].

Experiment	$\sin^2 2\theta_{13}$
Daya Baya	$0.0841 \pm 0.0027 \pm 0.0019$
RENO	$0.082 \pm 0.009 \pm 0.006$
Double Chooz	0.088 ± 0.033

Table 1.3: Best-fit values of $\sin^2 2\theta_{13}$ obtained by the Daya Bay[55], RENO[57] and Double Chooz[56] experiments.

These experiments use two or more identical detectors at different distances from the nuclear reactor plant. They also exploit the IBD process to detect reactor antineutrinos. Comparing the rate of neutrino interaction at different locations these experiments measured the θ_{13} mixing angle with incredible accuracy. The most constrained measurement is that from Daya Bay (Fig. 1.9)[55], with results from Double Chooz[56] and RENO[57] agreeing with Daya Bay's one but with larger uncertainties. Table 1.3 summarizes the best-fit value of θ_{13} for all the experiments.

1.3 Mass Ordering

In the minimal scenario experimental results require the mixing between the three flavour neutrinos of the standard model, thus neutrino oscillations depend on two independent squared-masses differences: Δm^2_{21} and Δm^2_{31}. In Sec. 1.2.4 it was shown that Δm^2_{21} was measured by solar neutrino experiments. Thanks to the

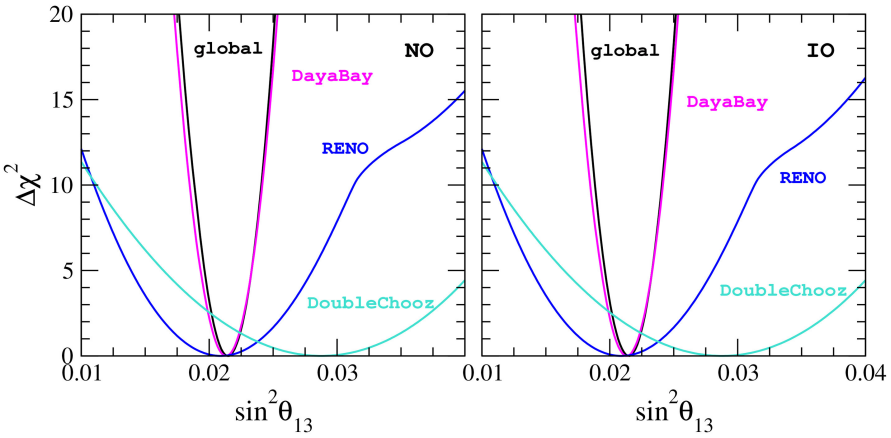

Figure 1.9: Profile of $\Delta\chi^2$ as a function of $\sin^2\theta_{13}$ from global data analysis (black line) and from separate analysis of reactor experiments for both the normal (left) and inverted (right) mass ordering[58].

matter effect of neutrino travelling through the Sun, the sign of the Δm^2_{21} splitting could be determined. The same is not possible for Δm^2_{31} measured by atmospheric neutrino experiments, because in that case matter effects are negligible. Until now the sign of Δm^2_{31} is unknown. As a consequence, two different neutrino mass ordering are possible based on the sign of Δm^2_{31}:

- spectrum with normal ordering (NO):

$$m_1 < m_2 < m_3 \tag{1.60}$$
$$\Delta m^2_{31} > 0 \tag{1.61}$$
$$\Delta m^2_{21} > 0 \tag{1.62}$$

- spectrum with inverted ordering (IO):

$$m_3 < m_1 < m_2 \tag{1.63}$$
$$\Delta m^2_{31} < 0 \tag{1.64}$$
$$\Delta m^2_{21} > 0 \tag{1.65}$$

These two possibilities are shown in Fig. 1.10, where a graphical representation of the flavour content of each mass eigenstate is provided within the 0 to 2π range of the unknown δ_{CP} phase. Given the known mass splitting provided by neutrino oscillation experiments, one can define the lower bound on the sum of the neutrino

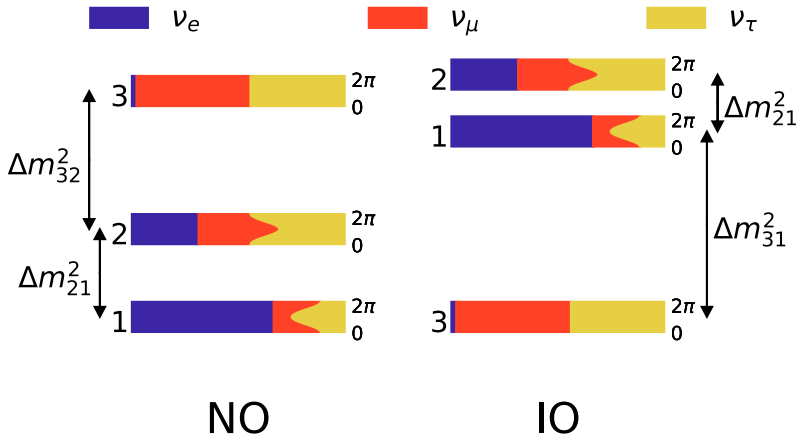

Figure 1.10: Probability of finding the $\alpha = \nu_e, \nu_\mu, \nu_\tau$ neutrino flavor in the i-th neutrino mass eigenstate for different values of the CP-violating phase, δ_{CP}, for the normal and inverted neutrino mass ordering[59].

masses for both the normal and inverted ordering:

$$\sum m_\nu^{NO} = m_1 + \sqrt{m_1^2 + \Delta m_{21}^2} + \sqrt{m_1^2 + \Delta m_{31}^2} \tag{1.66}$$

$$\sum m_\nu^{IO} = m_3 + \sqrt{m_3^2 + |\Delta m_{31}^2|} + \sqrt{m_3^2 + |\Delta m_{31}^2| + \Delta m_{21}^2} \tag{1.67}$$

The present global fit obtained from long-baseline experiments (NOνA, MINOS, T2K), reactor neutrino experiments (Daya Bay, RENO, Double Chooz) and solar neutrino experiments (SNO, Super-Kamiokande, Borexino), shows a preference (small significance) towards the normal mass ordering. The latest global analysis disfavors the inverted ordering by $\Delta\chi^2 = 2.7$ (1.6σ)[51].

1.4 Global fits in the 3 active neutrinos framework

Different groups performed a global fit of the neutrino oscillation results in the scenario of three active neutrino[51][60] The latest results are summarised in Table 1.4 and shown in figures 1.11 and 1.12. As of today, the octant of θ_{23} and of δ_{CP} remain to be determined.

With the values obtained from the latest fits, it is possible to determine the 3σ

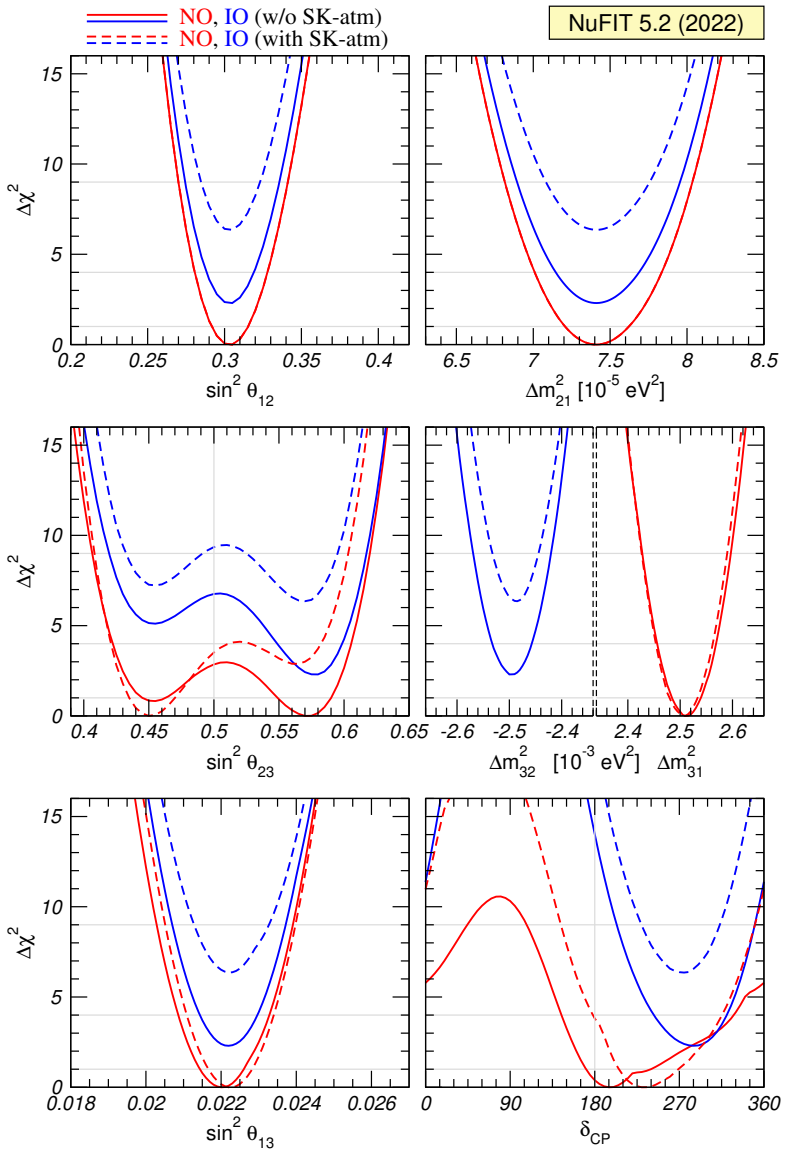

Figure 1.11: Global 3ν oscillation analysis. The red (blue) curves are for Normal (Inverted) Ordering. The solid (dashed) lines are obtained without (with) the inclusion of SK-atm χ^2 data[61].

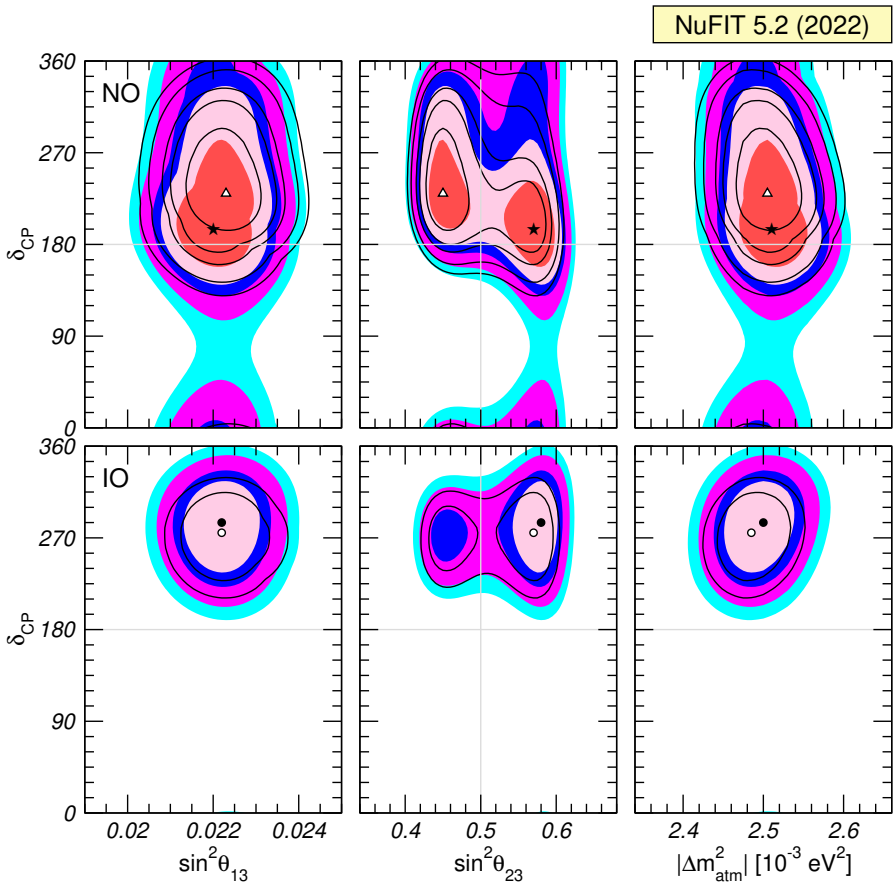

Figure 1.12: Allowed regions from the global analysis after minimizing with respect to all undisplayed parameters. The upper (lower) panel corresponds to IO (NO). Colored regions (black contour curves) are obtained without (with) the inclusion of the tabulated SK-atm χ^2 data. The different contours correspond to the two-dimensional allowed regions at 1σ, 2σ,and 3σ CL[61].

NuFIT 5.2 (2022)

		Normal Ordering (best fit)		Inverted Ordering ($\Delta\chi^2 = 2.3$)	
		bfp $\pm 1\sigma$	3σ range	bfp $\pm 1\sigma$	3σ range
without SK atmospheric data	$\sin^2\theta_{12}$	$0.303^{+0.012}_{-0.011}$	$0.270 \to 0.341$	$0.303^{+0.012}_{-0.011}$	$0.270 \to 0.341$
	$\theta_{12}/^\circ$	$33.41^{+0.75}_{-0.72}$	$31.31 \to 35.74$	$33.41^{+0.75}_{-0.72}$	$31.31 \to 35.74$
	$\sin^2\theta_{23}$	$0.572^{+0.018}_{-0.023}$	$0.406 \to 0.620$	$0.578^{+0.016}_{-0.021}$	$0.412 \to 0.623$
	$\theta_{23}/^\circ$	$49.1^{+1.0}_{-1.3}$	$39.6 \to 51.9$	$49.5^{+0.9}_{-1.2}$	$39.9 \to 52.1$
	$\sin^2\theta_{13}$	$0.02203^{+0.00056}_{-0.00059}$	$0.02029 \to 0.02391$	$0.02219^{+0.00060}_{-0.00057}$	$0.02047 \to 0.02396$
	$\theta_{13}/^\circ$	$8.54^{+0.11}_{-0.12}$	$8.19 \to 8.89$	$8.57^{+0.12}_{-0.11}$	$8.23 \to 8.90$
	$\delta_{\rm CP}/^\circ$	197^{+42}_{-25}	$108 \to 404$	286^{+27}_{-32}	$192 \to 360$
	$\frac{\Delta m^2_{21}}{10^{-5}\ \text{eV}^2}$	$7.41^{+0.21}_{-0.20}$	$6.82 \to 8.03$	$7.41^{+0.21}_{-0.20}$	$6.82 \to 8.03$
	$\frac{\Delta m^2_{3\ell}}{10^{-3}\ \text{eV}^2}$	$+2.511^{+0.028}_{-0.027}$	$+2.428 \to +2.597$	$-2.498^{+0.032}_{-0.025}$	$-2.581 \to -2.408$
		Normal Ordering (best fit)		Inverted Ordering ($\Delta\chi^2 = 6.4$)	
		bfp $\pm 1\sigma$	3σ range	bfp $\pm 1\sigma$	3σ range
with SK atmospheric data	$\sin^2\theta_{12}$	$0.303^{+0.012}_{-0.012}$	$0.270 \to 0.341$	$0.303^{+0.012}_{-0.011}$	$0.270 \to 0.341$
	$\theta_{12}/^\circ$	$33.41^{+0.75}_{-0.72}$	$31.31 \to 35.74$	$33.41^{+0.75}_{-0.72}$	$31.31 \to 35.74$
	$\sin^2\theta_{23}$	$0.451^{+0.019}_{-0.016}$	$0.408 \to 0.603$	$0.569^{+0.016}_{-0.021}$	$0.412 \to 0.613$
	$\theta_{23}/^\circ$	$42.2^{+1.1}_{-0.9}$	$39.7 \to 51.0$	$49.0^{+1.0}_{-1.2}$	$39.9 \to 51.5$
	$\sin^2\theta_{13}$	$0.02225^{+0.00056}_{-0.00059}$	$0.02052 \to 0.02398$	$0.02223^{+0.00058}_{-0.00058}$	$0.02048 \to 0.02416$
	$\theta_{13}/^\circ$	$8.58^{+0.11}_{-0.11}$	$8.23 \to 8.91$	$8.57^{+0.11}_{-0.11}$	$8.23 \to 8.94$
	$\delta_{\rm CP}/^\circ$	232^{+36}_{-26}	$144 \to 350$	276^{+22}_{-29}	$194 \to 344$
	$\frac{\Delta m^2_{21}}{10^{-5}\ \text{eV}^2}$	$7.41^{+0.21}_{-0.20}$	$6.82 \to 8.03$	$7.41^{+0.21}_{-0.20}$	$6.82 \to 8.03$
	$\frac{\Delta m^2_{3\ell}}{10^{-3}\ \text{eV}^2}$	$+2.507^{+0.026}_{-0.027}$	$+2.427 \to +2.590$	$-2.486^{+0.025}_{-0.028}$	$-2.570 \to -2.406$

Table 1.4: Three-flavor oscillation parameters from global data as of November 2022[61] for both the Normal and Inverted orderings. The results shown in the upper (lower) section are obtained without (with) the inclusion of the atmospheric neutrinos results provided by the Super-Kamiokande collaboration.

range of the PMNS matrix entries[61]:

$$|U|_{3\sigma}^{\text{w/o SK-atm}} = \begin{pmatrix} 0.803 - 0.845 & 0.514 - 0.578 & 0.142 - 0.155 \\ 0.233 - 0.505 & 0.460 - 0.693 & 0.630 - 0.779 \\ 0.262 - 0.525 & 0.473 - 0.702 & 0.610 - 0.762 \end{pmatrix} \tag{1.68}$$

$$|U|_{3\sigma}^{\text{w/ SK-atm}} = \begin{pmatrix} 0.803 - 0.845 & 0.514 - 0.578 & 0.143 - 0.155 \\ 0.244 - 0.498 & 0.502 - 0.693 & 0.632 - 0.768 \\ 0.272 - 0.517 & 0.473 - 0.672 & 0.623 - 0.761 \end{pmatrix} \tag{1.69}$$

as well as the value of the Jarlskog maximum value[51]:

$$J_{CP}^{max} = 0.0332 \pm 0.0008(\pm 0.0019) \;\; 1\sigma(3\sigma) \tag{1.70}$$

1.5 Experimental anomalies beyond the PMNS model

Despite most of the existing results can be accommodated in the three neutrino oscillation framework, there are some experimental data - so called neutrino oscillation anomalies - which do not fit in the global picture :

- The Liquid Scintillator Neutrino Detector (LSND), measured an excess in the short-baseline transition $(\bar{\nu}_\mu)\nu_\mu \rightarrow (\bar{\nu_e})\nu_e$ at 3.8 σ level, corresponding to $\Delta m^2 \sim 1\text{eV}^2$[62], giving origin to the so called short-baseline neutrino anomaly.

- The MiniBooNE experiment at FNAL, built to verify the LSND's results, measured an excess of ν and $\bar{\nu}$ studying a beam of mostly ν_μ and $\bar{\nu}_\mu$. With a significance level of 4.7σ[63], the result of MiniBooNE was in agreement with the one from LSND.

- By using re-evaluated reactor neutrino fluxes, the mean ratio R of observed over expected events for different reactor experiments was found to be $R = 0.94 \pm 0.02$, giving origin to the Reactor Antineutrino Anomaly (RAA)[64].

- The calibration of the GALLEX and SAGE experiments with radioactive sources a lower rate of events than expected was measured with a significance level of 3σ[65].

All these anomalies possibly hint at the presence of oscillations of the three active neutrinos in (at least) a fourth (sterile) neutrino state with $\Delta m^2 \sim 1$ eV^2.

1.5.1 3+1 neutrino oscillation probabilities

In the 3+1 neutrino model, a gauge singlet ν_s is added to the standard neutrino sector. This state, with a mass of O (1 eV) does not have weak interactions The 3x3 PMNS matrix to a 4x4 matrix $U_{\alpha i}$, with $\alpha = e, \mu, \tau, s$ and $i = 1, 2, 3, 4$. Here $\alpha = s$ and $i = 4$ represent the additional sterile eigenstate and the additional mass eigenstate. For scenarios in which $\Delta m^2_{41} \gg |\Delta m^2_{31}|, \Delta m^2_{21}$, both the Δm^2_{31}- and Δm^2_{21}-driven oscillation can be neglected, and the neutrino oscillations can be approximated as follow[66]:

$$P(\nu_e \to \nu_e) \simeq 1 - 4\,|U_{e4}|^2\left(1 - |U_{e4}|^2\right)\sin^2\left(\frac{\Delta m^2_{41} L}{4E_\nu}\right) \tag{1.71}$$
$$\equiv 1 - \sin^2\left(2\theta_{ee}\right)\sin^2\left(\frac{\Delta m^2_{41} L}{4E_\nu}\right),$$
$$P(\nu_\mu \to \nu_\mu) \simeq 1 - 4\,|U_{\mu 4}|^2\left(1 - |U_{\mu 4}|^2\right)\sin^2\left(\frac{\Delta m^2_{41} L}{4E_\nu}\right) \tag{1.72}$$
$$\equiv 1 - \sin^2\left(2\theta_{\mu\mu}\right)\sin^2\left(\frac{\Delta m^2_{41} L}{4E_\nu}\right),$$
$$P(\nu_\mu \to \nu_e) \simeq 4\,|U_{\mu 4}|^2\,|U_{e4}|^2\sin^2\left(\frac{\Delta m^2_{41} L}{4E_\nu}\right)$$
$$\equiv \sin^2\left(2\theta_{\mu e}\right)\sin^2\left(\frac{\Delta m^2_{41} L}{4E_\nu}\right). \tag{1.73}$$

where the three new mixing angles are introduced and are defined as:

$$\sin^2 2\theta_{ee} = 4|U_{e4}|^2(1 - |U_{e4}|^2) \tag{1.74}$$
$$\sin^2 2\theta_{\mu\mu} = 4|U_{\mu 4}|^2(1 - |U_{\mu 4}|^2) \tag{1.75}$$
$$\sin^2 2\theta_{\mu e} = 4|U_{\mu 4}|^2|U_{e4}|^2. \tag{1.76}$$

Equations 1.71 imply that ν_e disappearance, ν_μ disappearance, and $\nu_\mu \to \nu_e$ appearance must occur at the same L/E, and also that the neutrino oscillations in the 3+1 scenario are relevant for L/E $\simeq$ m/MeV or km/GeV. The 3+1 neutrino oscillation model can thus be tested and constrained by a combination of different experiments, combining appearance and disappearance dataset. The current status of the experimental results for the eV-scale sterile neutrino is ambiguous: a strong preference toward a 3+1 model is found by many different groups, at the same time, a large inconsistency between the dataset is also present. This is due to the large mixing required to explain the LSND and MiniBooNE anomalies, which also implies a large disappearance probability of muon neutrino, in contrast with data. As cited in the previous section, three different channel

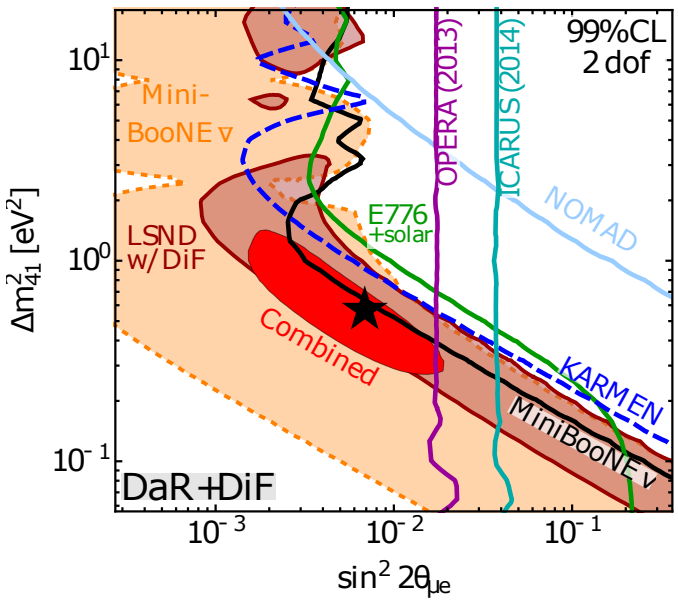

Figure 1.13: Preferred regions for several $\nu_\mu \to \nu_e$ appearance experiments in the 3+1 scenario at 99% CL for two degrees of freedom[71].

can be studied to verify the 3+1 neutrino model: ν_e appearance, ν_e disappearance, and ν_μ appearance. Referring to Eq. 1.71, the ν_e appearance is driven by $\sin^2 2\theta_{\mu e}$ and the experiments OPERA[67] and ICARUS[68] contrained its value to be $\sin^2 2\theta_{\mu e} < 0.015$. This results implies the MiniBooNE and LSND anomalies to be $2 \times 10^{-3} \leqslant \sin^2 2\theta_{\mu e} \leqslant 0.015$ with Δm^2_{41} greater than 0.3 eV^2. The NOMAD[69] and KARMEN[70] experiments also suppressed oscillation probabilities for large mixing angles and values of Δm^2_{41} grater than 1.5 eV^2 (Fig. 1.13). The ν_e disappearance channel is probed by short-baseline reactor experiments.

The joint analysis of results from different reactor experiments put the best-fit point at $\Delta m^2_{14} = 2.41 \pm 0.03$ and $\sin^2 2\theta_{ee} = 0.08 \pm 0.03$[72]. Figure 1.14 shows both the comparison of the exclusion limits on sterile neutrino oscillations and an allowed region obtained by the RENO and NEOS experiments and the exclusion regions obtained by the DANSS[73] and combined RENO+NEOS[74] experiments. Recently, the Neutrino-4 experiment released the results obtained from the analysis of data collected at different distances (6 to 12 m) from a very powerful (100 MW) SM-3 research reactor at Dmitrovgrad (Russia). A 2.7σ significance on the sterile neutrino signal was reported, with the best-fit point being $\Delta m^2_{14} = 7.3 \pm 1.17$ and $\sin^2 2\theta_{ee} = 0.36 \pm 0.12$[72]. This result is in tension with other short-baseline reactor experiments. The ν_μ disappearance channel data show no deviation from the three active neutrino framework. The MicroBooNE experiment recently published no excess of ν_e data. The results are thus consistent with

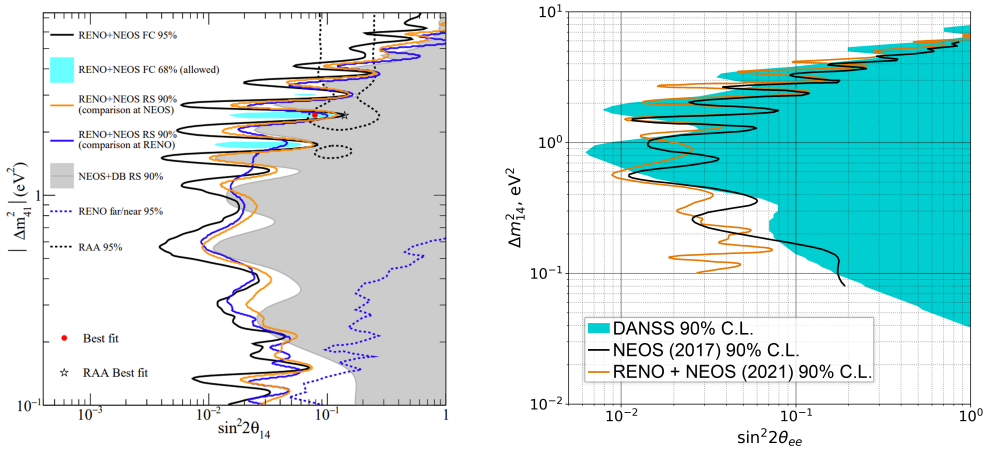

Figure 1.14: Left: Exclusion limits and allowed regions obtained with the NEOS and RENO experiments. The black dotted line shows the 95% allowed region from the RAA. Right: 90% CL exlusion limits obtained from the DANSS experiment (cyan) and from the NEOS+RENO[74] joint analysis[72].

the nominal ν_e rate expected. Figure 1.15 shows the exclusion limits obtained by MicrooBooNE in $\Delta m^2_{41} - \sin^2 2\theta_{\mu e}$ and $\Delta m^2_{41} - \sin^2 2\theta_{ee}$ plane while. Figure 1.16 shows the comparison with MicroBooNE results with the RAA + Neutrino-4 allowed regions (bottom) and with the LSND results (top).

1.6 Summary and Prospects

Recent years have marked a significant advancement in our understanding of neutrino physics with crucial questions remaining:

- Determination of the sign of Δm^2_{31} to assess the neutrino mass ordering;
- Measurement of the δ_{CP} in the leptonic sector;
- Determination of the nature of massive neutrinos (Dirac or Majorana);
- Measurement of the absolute scale of neutrino mass;
- Understand the short-baseline neutrino oscillation anomalies.

To answer these questions data from a wide range of experiments are needed, from long-baseline neutrino oscillation, to neutrinoless double beta decay, cosmological data, and short-baseline experiments.

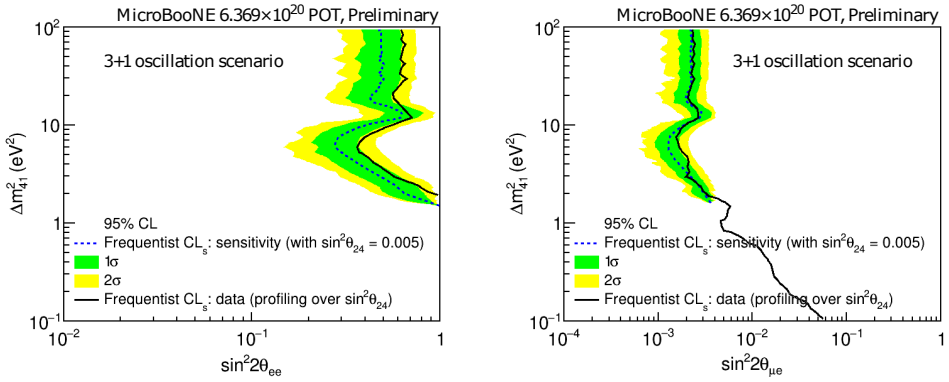

Figure 1.15: Left: 95% CL exclusion limits in the $\Delta m^2_{41} - \sin^2 2\theta_{ee}$ space obtained by the MicroBooNE experiment. Green and yellow bands represent the 1 and 2 sigma regions respectively. Right: 95% CL exclusion limits in the $\Delta m^2_{41} - \sin^2 2\theta_{\mu e}$ space obtained by the MicroBooNE experiment. Green and yellow bands represent the 1 and 2 sigma regions respectively. [75]

In the long-baseline domain, the Deep Underground Neutrino Experiment (DUNE) is a next-generation experiment aiming to determine the neutrino mass ordering and measure the $delta_{CP}$ violation phase but with a larger program including the search for the sterile neutrinos.

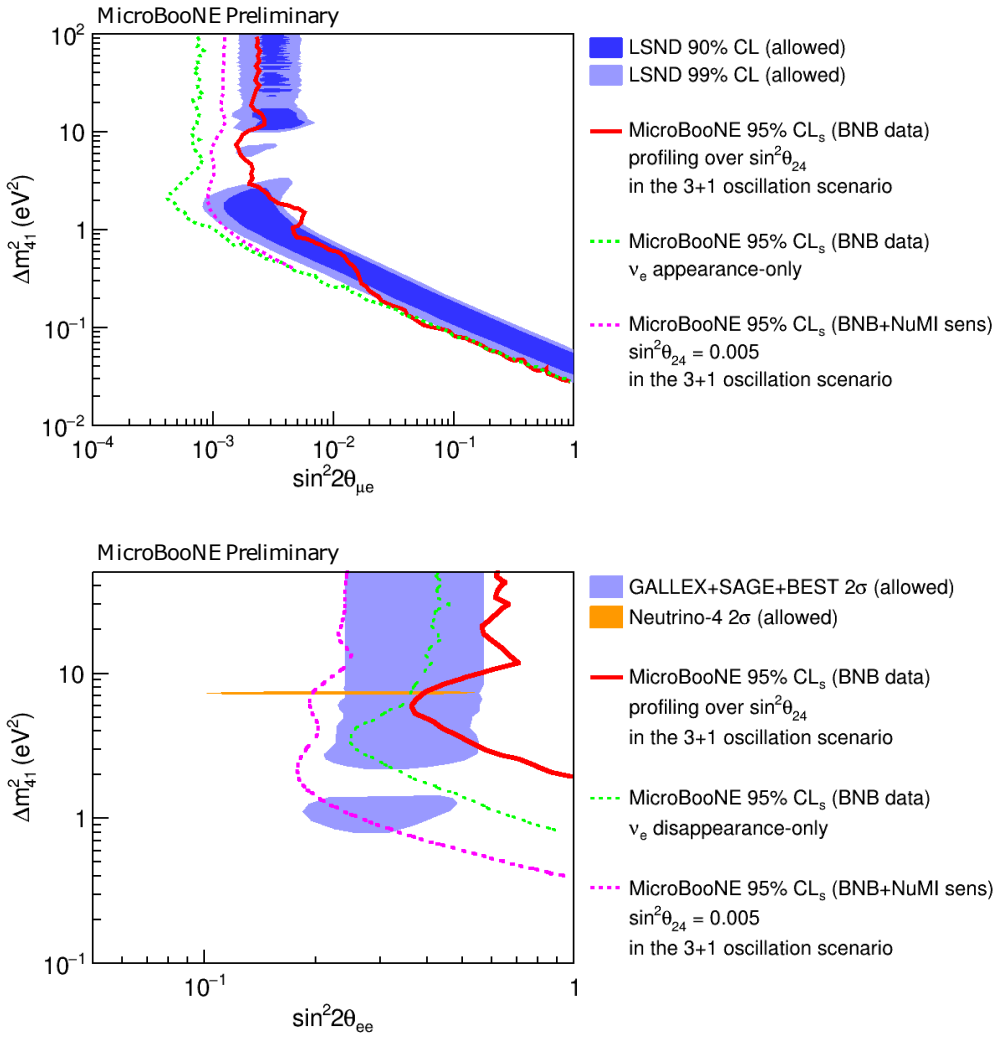

Figure 1.16: Top: 95% CL exclusion limits in the $\Delta m^2_{41} - \sin^2 2\theta_{ee}$ space obteined by the MicroBooNE experiment (red line) compared with the 2σ allowed regions from the GALLEX+SAGE+BEST (blue) and the Neutrino-4 experiments (orange). Green and magenta dotted lines represent the 95% Cl exlusion limit in the ν_e appearance channel only and the 95% CL sensitivity when data from both the BNB and NuMI beam are combined, respectively. Bottom: 95% CL exclusion limits in the $\Delta m^2_{41} - \sin^2 2\theta_{\mu e}$ space obteined by the MicroBooNE experiment (red line) compared with the 90% and 99% CL allowed regions from the LSND experiment[75].

Chapter 2

The Deep Underground Neutrino Experiment

DUNE is a next generation, long-baseline neutrino oscillation experiment, currently being built in the United States. DUNE will feature two experimental sites: a Near Detector complex at Fermilab, Illinois, and a Far Detector site at the Sanford Underground Research Facility (SURF) in South Dakota, 1.5 km underground and 1300 km from Fermilab. DUNE will pursue a broad science program that includes open questions in neutrino physics, search for proton decay, study of neutrinos from core-collapse supernovas, solar neutrinos and other BSM searches. The design of the DUNE detector is detailed in Sec 2.1, and the DUNE science program is introduced in Sec 2.2.

2.1 DUNE design

To pursue its primary physics goals, which are the determination the neutrino mass ordering and of the PMNS CP-violation phase, DUNE will exploit:

- the world most intense wide band (anti)neutrino beam
- a multi kiloton far detector based on liquid argon time projection chambers
- a near detector able to constrain systematic uncertainties to unprecedented levels.

In its starting phase (Phase I) DUNE will achieve some of the early physics goals using 1.2 MW proton beam, two far detector modules - 20 kt LAr fiducial mass - and a temporary configuration of the near detector complex. To completely carry out its scientific program however, DUNE will require (Phase II) an upgraded neutrino beam (2.4 MW) and its complete experimental apparatus: four far detector

Parameter	Phase I	Phase II	Impact
FD mass	20 kt fiducial	40 kt fiducial	FD statistics
Beam power	up to 1.2 MW	2.4 MW	FD statistics
ND config	ND-LAr, TMS, SAND	ND-LAr, ND-GAr, SAND	Syst. constraints

Table 2.1: Detail on the two-phased approach to DUNE.

modules (at least 40 kt fiducial mass) and a near detector in its final configuration. The main features of Phase I and Phase II are reported in Table 2.1 and discussed in the following.

2.1.1 Neutrino beam

The neutrino beam will be provided by the Long Baseline Neutrino Facility (LBNF), at Fermilab. LBNF is based on the Proton Improvement Plan II (PIP-II)[76] delivering an up to 1.2 MW proton beam from Fermilab's Main Injector, later upgradeable to 2.4 MW, with energy ranging between 60 and 120 GeV. The accelerated proton beam is left to impinge on a graphite fixed target. Secondary particles, mainly $\pi^{\pm}, K^{\pm}$, are focused by magnetic horns and left to decay in 194 m long pipe mainly in $\mu^{\pm}$ and $\nu_{\mu}/\bar{\nu}_{\mu}$. At the end of the decay pipe an absorber removes most of the muons in the beam leaving only ν_{μ}, with a small contamination of ν_e and $\bar{\nu}_e$ produced by the decay of kaons and muons.

By selecting the horn magnetic field polarity it is possible to focus only positive (or negative) particles, The two-operation modes of the horn are usually referred to as Forward Horn Current (FHC) and Reverse Horn Current (RHC) yielding a neutrino or an antineutrino beam, respectively. The horns will select a range of neutrino energies with a peak at about 2-3 GeV and up to about 10 GeV,covering the first two oscillation maxima, an exclusive feature of the DUNE experiment[77]. In Figure 2.1 the unoscillated (anti)neutrino fluxes from 120 GeV proton beam are shown, and in Table 2.2 the beam main parameters are listed.

2.1.2 DUNE Far Detector

The final design of the Far Detector is to have four LArTPC modules, each one having 17.5 kton mass. For DUNE Phase I, only two modules, FD1 and FD2, are planned. The other modules, FD3 and FD4, will be operational in Phase II.

Modules FD1 and FD2 are both LAr TPCs, each exploiting different technologies. The first module is a single-phase horizontal-drift LArTPC. Its design

Parameter	Value
Energy	120 GeV
POT	7.5×10^{13}
Spill duration	9.6 μs
POT per year	1.1×10^{21}
Cycle Time	1.2 s
Beam Power	1.2 MW
$\Delta p/p$	11×10^{-4} 99%
Beam divergence (x,y)	(15,17) μrad

Table 2.2: Main parameters of the Phase I neutrino beam[78].

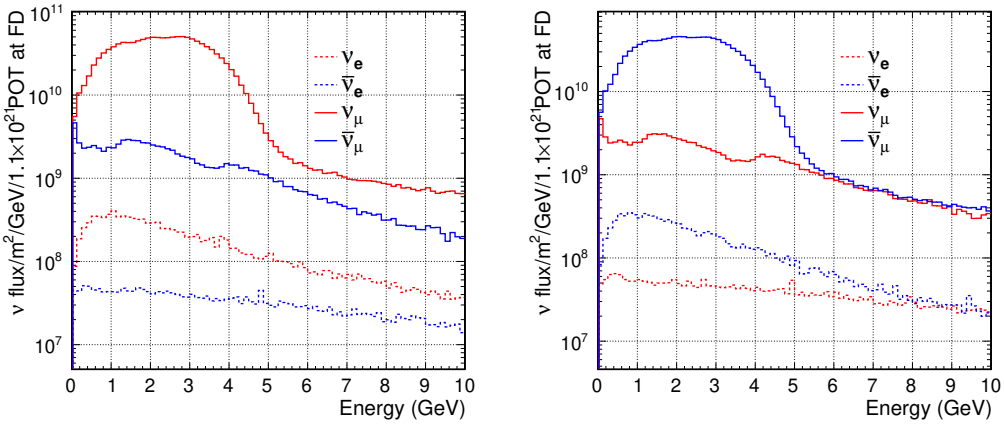

Figure 2.1: Expected unoscillated fluxes at the Far Detector for both muons and electron neutrino with horns working in FHC (left) and RHC (right)[77].

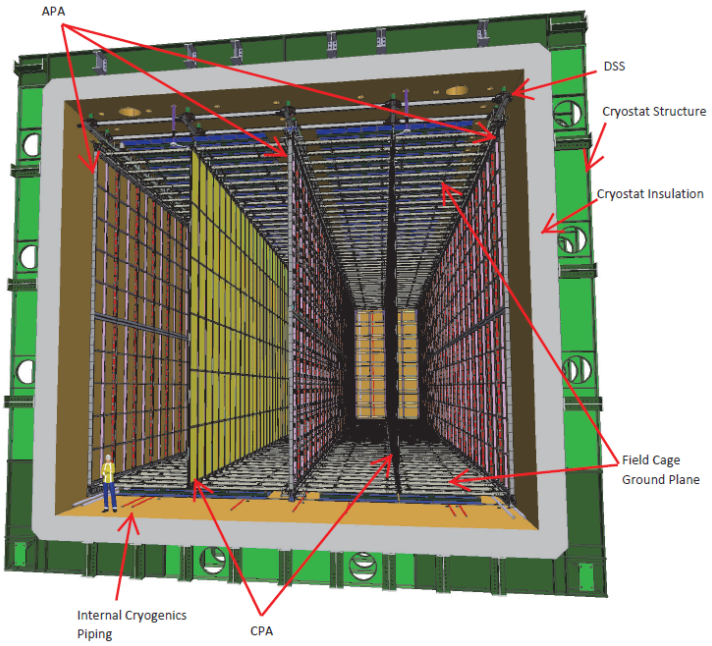

Figure 2.2: Drawing of the Horizontal Drift Far Detector Module 1, showing alternating APAs, CPAs, the detector support system, the cryostat and cryogenics distribution[79].

was tested and validated at CERN with the ProtoDUNE-SP detector, a prototype about 20 times smaller than FD1. The second module, FD2, will be a single-phase LArTPC implementing a vertical drift. The design of the third and fourth modules is yet to be defined.

Horizontal Drift LArTPC

The DUNE FD1 single-phase horizontal drift LArTPC[79] will be housed in a cryostat of 65.8 m × 17.8 m × 18.9 m. Its total mass will be 17.5 kt, with a fiducial mass of at least 10 kt. The design of the first Far Detector module is shown in Fig. 2.2. Its inner volume is divided in four drift regions by alternating anode plane assemblies (APAs) and cathode plane assemblies (CPAs). Each region is 58.2 m long, 3.5 m wide and 12.0 m high, with a constant electric field of 511 V/cm produced by biasing the cathode planes at -180 kV. Ionization electrons drift horizontally toward the anode planes.

The anode walls are made of 50 APAs each, arranged in a 2×25 grid, for a total of 150 APAs. Each APA measures 6.2 m by 2.32 m and is composed of three layers of active wires and ten photon detectors. The wires are arranged to form a grid and are used to collect drift electrons produced in the argon ionization.

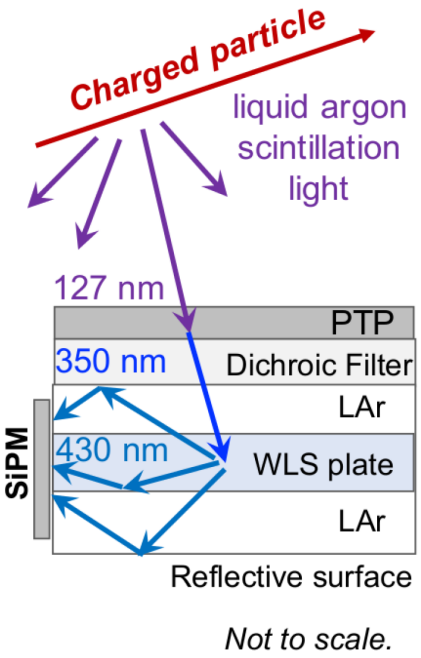

Figure 2.3: Sketch of the working principle of an X-Arapuca[80].

Photon detectors, so-called X-ARAPUCAs[80], are used to collect the scintillation light which provides timing information of the events. They exploit a dichroic short-pass filter to shift the wavelength of the scintillation photons and trap them in a closed box. A SiPM placed inside the box collects the shifted light (Fig. 2.3). The current signal from the APA wires and the timing information from the X-ARAPUCAs are used to reconstruct the events. The readout electronic of a single pair of APAs composing the wall is placed at the top of the upper module and at the bottom of the lower one, as shown in Fig. 2.4. The cathode walls are composed of 25 wide and 2 high CPAs, for a total of 100 CPA. The remaining open sides of the TPC are surrounded by a Field Cage which ensures an electric field uniformity better than 1% throughout the active volume.

Vertical Drift LArTPC

The FD Module 2 is a vertical drift LArTPC[82]; a schematic drawing of the detector is shown in Fig. 2.5. In this design, the cathode is suspended mid-height of the module, with electrons drifting vertically toward anodes placed at the bottom and top of the detector. Differently from the horizontal design, the anodes are made of perforated printed circuit boards (PCBs), avoiding deformations when hung horizontally. One anode is composed of two PCBs, the first of which has

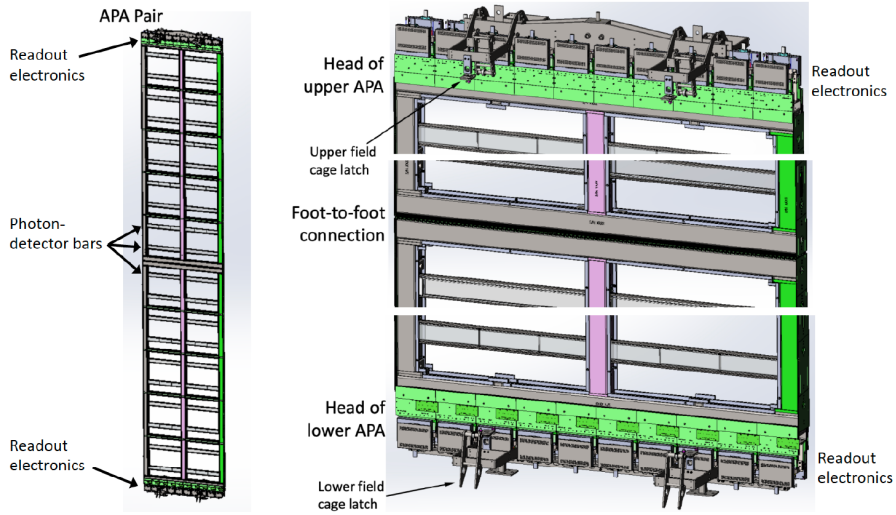

Figure 2.4: Left: one unit of the APA wall, composed by two APAs linked together. Right: zoomed view of the top and bottom ends of the left figure showing the readout electronics of the APAs[81].

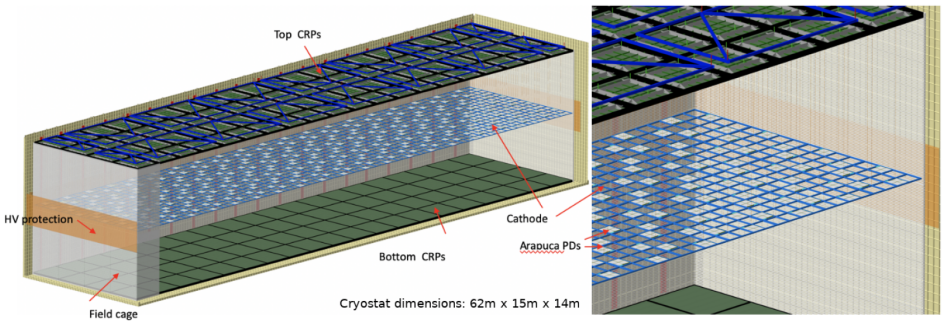

Figure 2.5: Sketch of the full vertical drift module, with a zoomed view of the mounting of the photo-sensors[82].

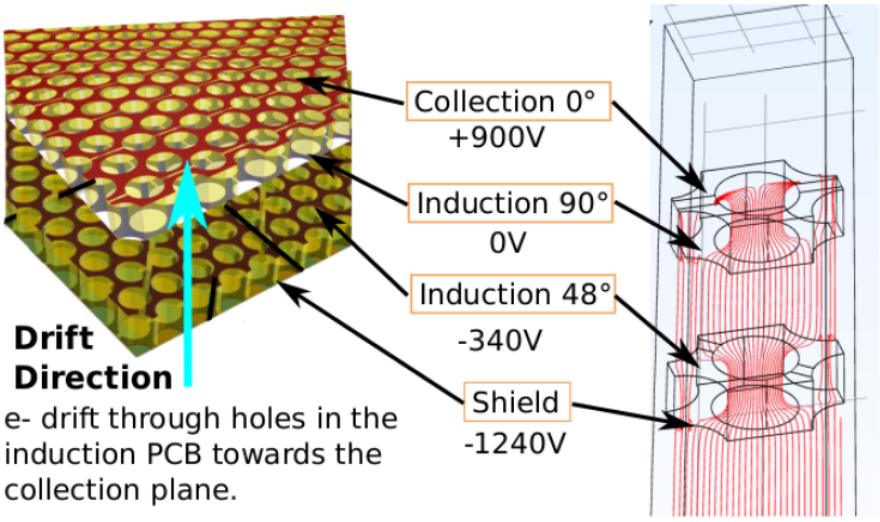

Figure 2.6: Structure of the PCB (left) and electric field simulation between two holes of the anode planes[82].

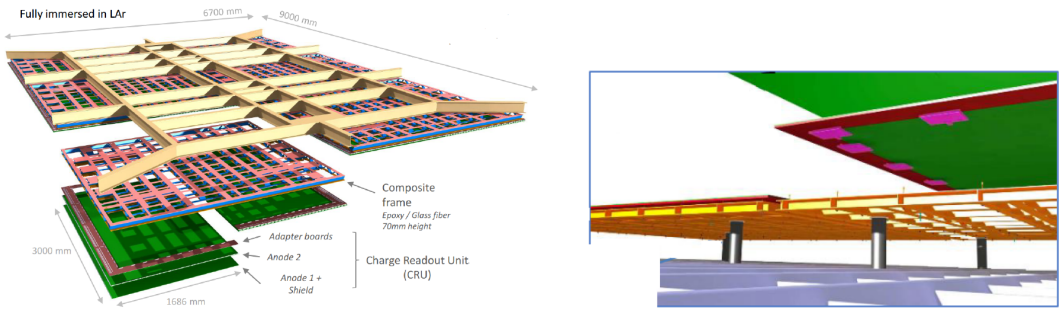

Figure 2.7: Schematic view of the top (left) and bottom (right) charge readout plane of both anodes in the vertical drift module[82].

a shielding plane and the first induction plane, with holes through which the electrons drift towards the second PCB, which has the second induction plane and the collection plane (Fig. 2.6). The two anodes are mounted on charge readout planes, which differ between the top and bottom anodes. The top one is a stainless steel frame that hangs from kevlar wires, with an adjustable position to achieve a deformation of the frame of less than 10 mm over 3 m. The bottom one is held by feet directly posed on the cryostat floor. The readout electronics also differ between anodes, with the top one being installed in the chimney of the cryostat, and the bottom one installed under the support frame (Fig. 2.7). As for the horizontal drift module, the argon scintillation light is collected by a photon detection system (PDS) and which provides trigger and time information of events.

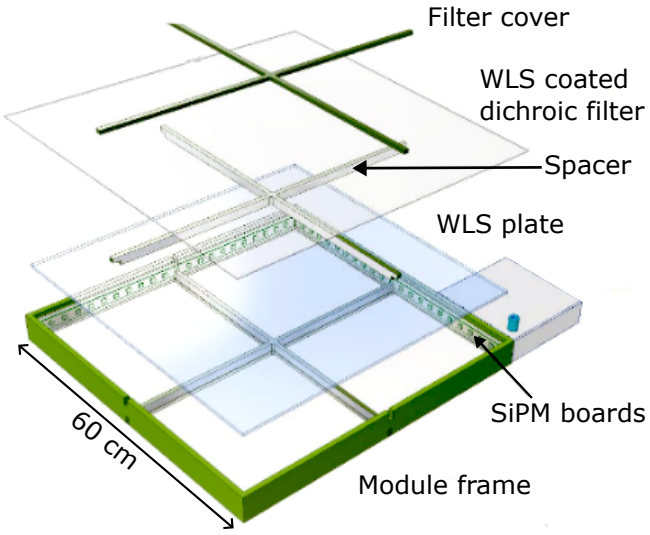

Figure 2.8: Drawing of an x-ARAPUCA detector for the vertical drift module[82].

The PDS is placed along the walls of the cryostat and on the cathode surface. Its design, shown in Fig. 2.8, is a revised version of the first module. It consists of $60 \times 60\text{cm}^2$ tiles equipped with 80 or 160 SiPMs. An X-Arapuca light trap is used to enhance the light collection. A "Power over Fiber " technique is used to power the SiPMs inside the cryostat without affecting the electric field: a high-power photonic laser module and a photovoltaic power converter are placed inside the cryostat and close to the photo-sensors.

2.1.3 Near Detector

The Near Detector complex[83] will be located about 600 m from the source of the neutrino beam. It includes three primary detectors: ND-LAr, the Temporary Muon Spectrometer -TMS- in DUNE I phase, to be replaced by the gaseous Ar TPC - ND-GAr- in DEUNE Phase II, and the System of on-Axis Neutrino Detection - SAND. Both ND-LAr and TMS/ND-GAr are on rails to move off-axis with respect to the direction of the beam, while SAND will stay fixed on-axis position. The program to take data at off-axis positions is usually referred to as Precision Reaction-Independent Spectrum Measurement-PRISM.)[83]. As already introduced, the ND will measure the neutrino beam near the production point, before oscillations take place. It also provides constraints on the systematic uncertainties and inputs for the neutrino interaction model. A brief description of ND-LAr , TMS and ND-GAr will be given in the following. A more detailed description of SAND and its components is provided in the next section. In Figure 2.9 the ND detectors in on- and off-axis positions are shown.

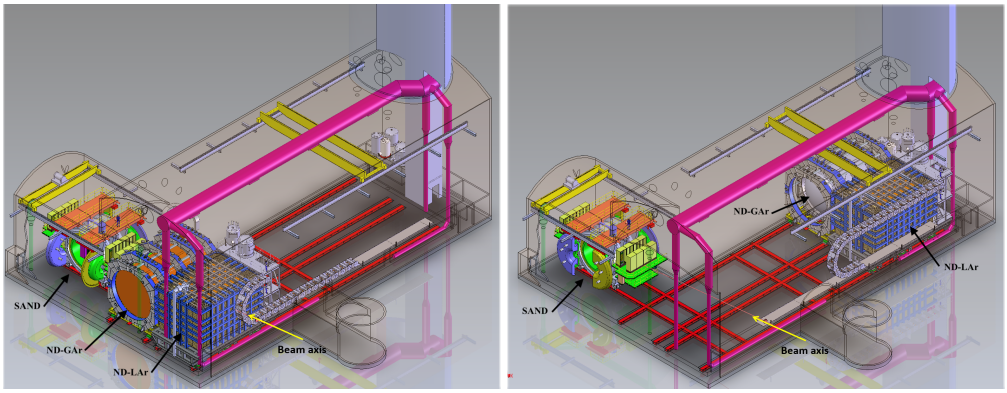

Figure 2.9: 3D view of the DUNE Near Detector hall: (left) all detectors are in on-axis position; (right) ND-LAr and ND-GAr are in an off-axis position, and SAND remaining on axis(right)[83].

ND-LAr

The ND-LAr is a LArTPC implementing an original design to cope with the large event pileup from the intense neutrino flux at the near site[83]. It will consist of multiple small size TPC modules, optically isolated from each other and with individual pixelated readouts able to provide precise timing information. Current design features a 5×7 matrix of modules. The reduced size of single TPC modules allows smaller drift distances and readout times, which help in reducing the event overlap. Reconstructed information from each TPC is then combined to provide the complete event reconstruction. The ND-LAr will have a fiducial mass of 67 tons, with a total active volume of $5 \times 7 \times 3$ m^3, and it is expected to detect $10^8 \nu_\mu$ events per year. Figure 2.10 shows an illustration of the detector, with the detail of one array of modules.

ND-GAr

The ND-GAr will be a high-pressure gaseous argon TPC (HPgTPC) surrounded by an electromagnetic calorimeter within a 0.5 T magnetic field. It will provide muon momentum and charge reconstruction for events not contained within the ND-LAr volume. In addition with a fiducial volume of $\sim$1 ton, ND-GAr will detect about $1.6 \times 10^{-6} \nu_\mu$ CC events per year at on-axis position providing an independent sample of neutrino interactions on argon. These events can be studied with a very low momentum threshold for charged particles, excellent tracking resolution, nearly uniform angular coverage and systematic uncertainties that differ from those of the liquid detectors. Similarly to ND-LAr, ND-GAr will perform PRISM measurements of off-axis spectra.

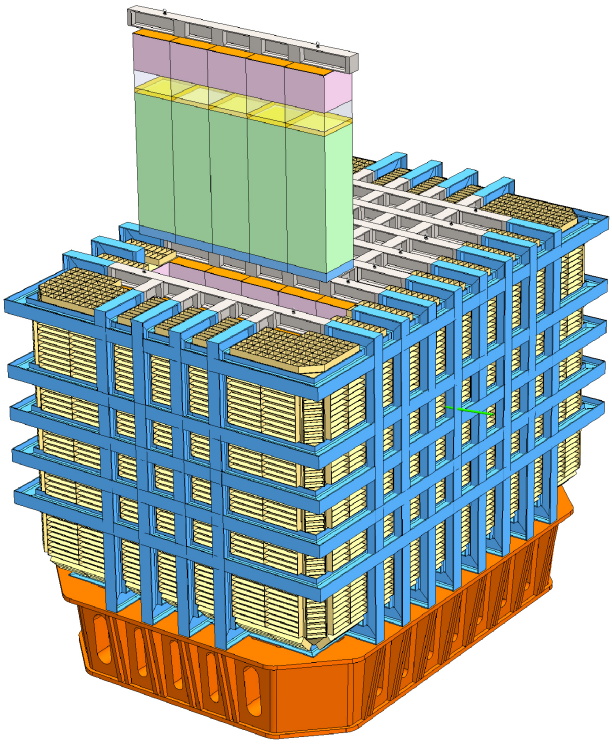

Figure 2.10: Sketch of the ND-LAr detector, with details one of the seven lines of five modules[83].

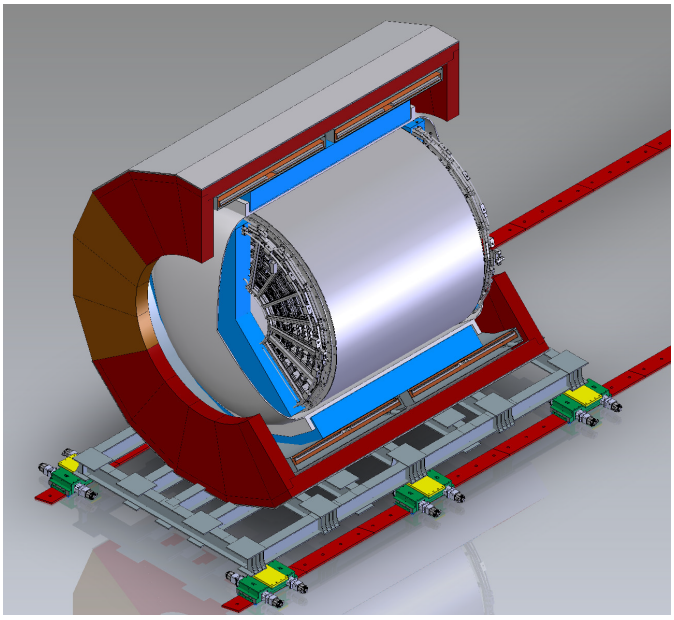

Figure 2.11: Schematic of ND-GAr showing the HPgTPC, its pressure vessel, the ECAL, the magnet, and the return iron[83].

As already mentioned ND-GAr is foreseen to operate during DUNE Phase II. In Phase I it will be replaced by the Temporary Muon Spectrometer (TMS). The design of TMS is based on magnetized steel planes interleaved with scintillator strips to provide muon momentum resolution up to 5%.

SAND

The System for on-Axis Neutrino Detection (SAND) will be the only ND detector permanently at an on-axis position. SAND will monitor the flux of neutrinos going to the FD, and perform a rich neutrino physics program. Its design is largely based on the reuse of the magnet and electromagnetic calorimeter (ECAL) of the KLOE experiment. The inner volume of the ECAL is instrumented with a target/tracking system and a small volume of liquid Argon. A detailed description of the SAND detector and its main physics goals is given in the next Chapter.

2.2 DUNE Scientific Program

DUNE has multiple scientific goals; the main one is a comprehensive program of neutrino oscillation measurements aimed at determining the value of the δ_{CP} violating phase, the neutrino mass ordering, the octant of θ_{23} and test the 3-flavour mixing paradigm. On top of this, DUNE will perform searches for physics Beyond

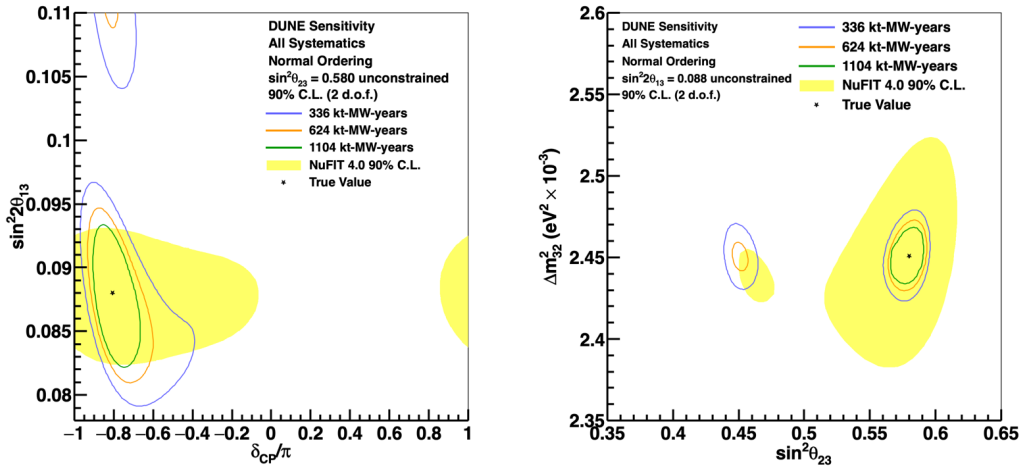

Figure 2.12: 90 % C.L. regions in the $\sin^2 2\theta_{13} - \delta_{CP}$ plane (left) and $\sin^2 \theta_{23} - \Delta m^2_{32}$ plane (right) for three different values of exposure and same running time for neutrino and antineutrino modes. The yellow regions represent the 90% C.L region of the NuFIT global fit[84].

the Standard Model (BSM) such as searches for proton decay, measurements of neutrinos produced in core-collapse supernovas, of atmospheric and solar neutrinos.
The design of the detector will allow an additional research program both at the Near and at the Far Detector. Examples are the search for dark-matter candidates, non-standard interactions, CPT violation, sterile neutrinos, heavy neutral leptons, tau neutrino appearance. Moreover, the Near Detector will allow precise measurements of neutrino interaction cross-sections and studies of nuclear effects.

2.2.1 Neutrino oscillation physics program

The sensitivity to oscillation parameters has been evaluated with full, end-to-end simulation, reconstruction and event selection. Both Far and Near detectors geometries, flux uncertainties, and neutrino interaction model have been included in the analysis[84]. The results demonstrate that DUNE will be able to make precise measurements of the parameters governing long-baseline neutrino oscillations, simultaneously and without the need of external constraints. This is visible in Fig. 2.12, where the 90% CL regions in the $\sin^2 2\theta_{13} - \delta_{CP}$ and $\sin^2 \theta_{23} - \Delta m^2_{32}$ planes are shown for 7, 10, and 15 years of running. The results are compared with the current world data global fit and show how DUNE will eventually be able to solve possible degeneracies in the results and constrain the parameters. By disentangling matter effects from the CP violation effects, the neutrino mass ordering

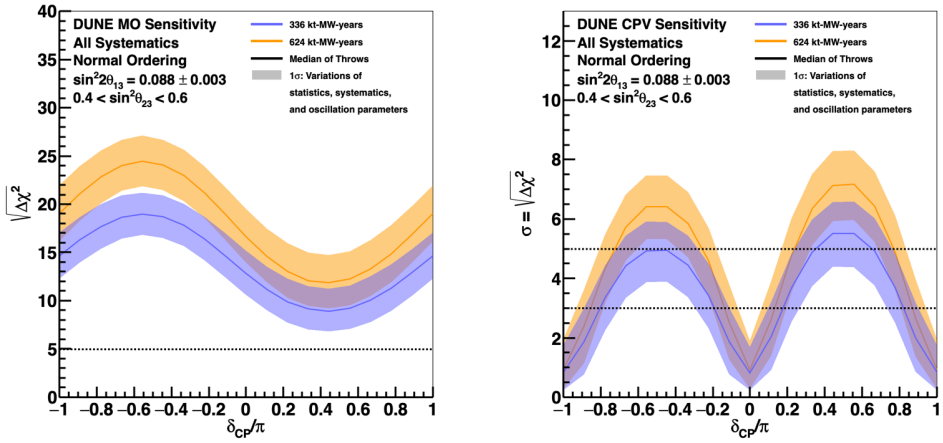

Figure 2.13: Sensitivity, with the Phase II Near Detector, to the neutrino mass ordering (left) and the CP violation (right) for different values of exposure as a function of the true δ_{CP} value. Solid lines represent the median sensitivity, while the colored band represents 68% of variations of statistics, systematics, and oscillation parameters[86].

will be determined. The disentangling is possible exploiting one of DUNE's main key strength, i.e. its 1300 km long baseline. Because of that the experiment is sensitive to matter effects which, recalling Sec. 1.2.3, lead to a large asymmetry in neutrino and antineutrino oscillation probabilities, and whose sign depends on the neutrino mass ordering. At a distance of 1300 km from the neutrino source, this asymmetry is estimated around ±40%. This value is larger than the maximal asymmetry generated by the δ_{CP} phase (described in Sec. 1.2.2) allowing to determine with high confidence both the mass ordering and δ_{CP}[85][84].
The expected sensitivity to the neutrino mass ordering and CP violation as a function of the value of δ_{CP} is shown in Fig. 2.13 for different exposures. Figure 2.14 shows the sensitivity to the same parameters as a function of the exposure for a fixed value of δ_{CP}. From the left plot of Fig. 2.13, it is visible how DUNE will be able to determine the mass ordering with a 5σ confidence level independently from the value of δ_{CP} and with an exposure of 100 kt-MW-years, corresponding to about 3 years of data. The same CL can be obtained with even shorter exposure times, depending on the values of other oscillation parameters. This is shown in the left plot of Fig. 2.14, where the sensitivity is greatly affected by the value of δ_{CP} and by external constrain in θ_{13}. In the best case scenario, a 5σ CL could be obtained in less than one year of data taking. With $\delta_{CP} = -\pi/2$, corresponding to maximal CP violation, 3σ and 5σ CLs will be achieved with 100 or 350 kt-MW-year exposure, respectively. For non-maximal CP violation, a 5σ sensitivity can be obtained for half the values of δ_{CP} with 10 years of data, while about 13 years

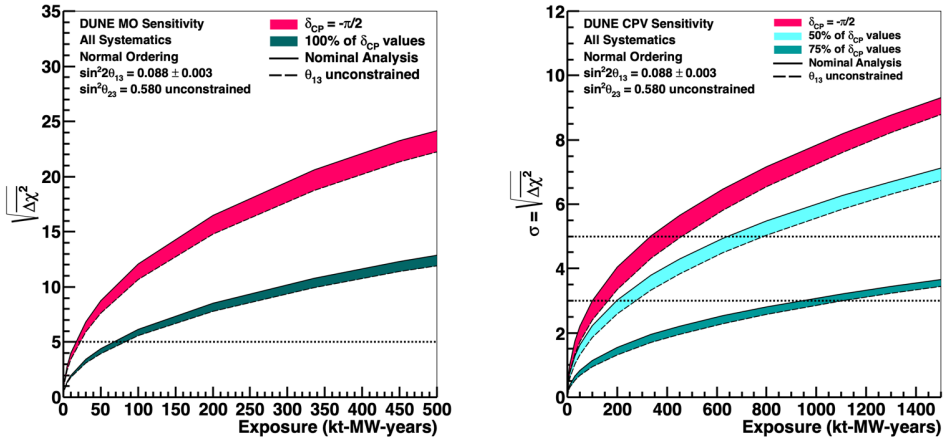

Figure 2.14: Sensitivity, with the Phase II Near Detector, to the neutrino mass ordering (left) and the CP violation (right) as a function of the exposure in kt-MW-years. The width of the bands represents the difference between the nominal analysis (solid line), which uses the external constraint from reactor antineutrino experiments on $\sin^2_{13}$, and an analysis without this constraint (dotted line)[86].

are needed to obtain a 3σ CL for 75% δ_{CP} values[86]. This is shown in the right plot of Fig. 2.14, where the effect of the θ_{13} constraint is visible again.
The $\nu_\mu \to \nu_\mu$ oscillation probability is sensitive to $\sin^2 2\theta_{23}$, while $\nu_\mu \to \nu_e$ probability depends on $\sin^2 \theta_{23}$: measuring both channels DUNE can probe both octant and maximal mixing of θ_{23}. The sensitivity to the θ_{23} octant is shown in Fig. 2.15 as a function of the true value of $\sin^2 \theta_{23}$ for 10 and 15 years of exposure.

To perform these precise measurements DUNE will rely on a high control of systematic uncertainties, achieved mainly thanks to the Near Detector measurements. The sensitivities presented in this section were thus estimated by implementing a sophisticated treatment of systematic uncertainties which includes contributions from both Far and Near detectors. The importance of the Near Detector measurements will be discussed later in Chapter 3.

2.2.2 Low energy

The large mass of the DUNE Far Detector will enable the detection of low energy neutrinos in the range from ∼5 MeV to a few tens of MeV, which is of particular interest for the detection of electron neutrinos from galactic core-collapse supernovas. As these events are expected to occur few times per century, it is reasonable that one will happen during the experiment lifetime. The neutrino signal coming from a core-collapse supernova evolves with time, starting with a sharp burst of mainly ν_e, corresponding to the *neutronization* phase of the core-collapse. This

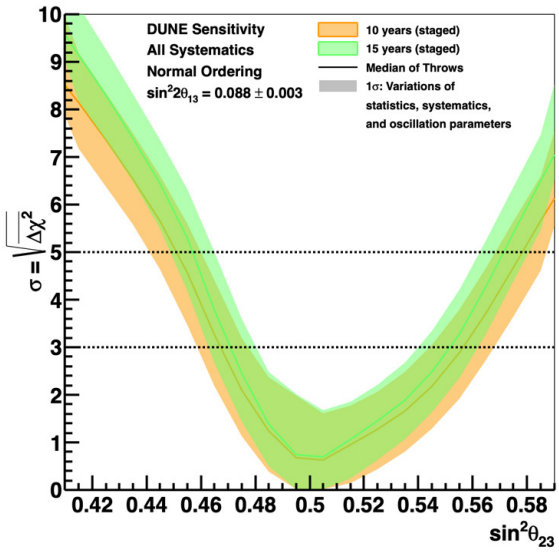

Figure 2.15: Sensitivity to the θ_{23} octant determination as a function of $\sin^2\theta_{23}$ for ten (orange) and fifteen (green) years of exposure for the normal neutrino mass ordering[84].

is then followed by the *accretion* and the *cooling* phases, lasting several hundreds of milliseconds and about 10 seconds respectively. The neutrino composition in these phases changes to be divided almost equally between all the flavors of neutrino and antineutrinos (Fig. 2.16). Being able to study the neutrino signal could then provide information about the collapse, the star progenitor, the explosion but also information on neutrino properties. DUNE will be sensitive mostly to the charged current of electron neutrinos and antineutrinos exploiting the absorption of $\nu_e/\bar{\nu_e}$ on Argon:

$$\nu_e + {}^{40}Ar \rightarrow e^- + {}^{40}K^* \tag{2.1}$$

for which the observable is a short electron track eventually followed by gamma-ray and other secondary particle signatures generated by the deexcitation of the K*. The capability of detecting such interaction is exclusive to the DUNE experiment. Independently from the model of supernova burst, DUNE is expected to observe about 3000 neutrino events from a collapse at 10 kpc, and will be able to determine the parameters describing the electron neutrinos spectrum (Fig. 2.17). On top of this, reconstructing the direction of the neutrinos, DUNE will be able to provide information on the supernova position in the sky, helping the world-wide multi-messanger astronomy effort[77][89]. Additionally, it could study the neutrino flavour oscillation probabilities in the supernova burst, which are strongly modified by the kinematics of the burst itself. Core-collapse supernova signals are

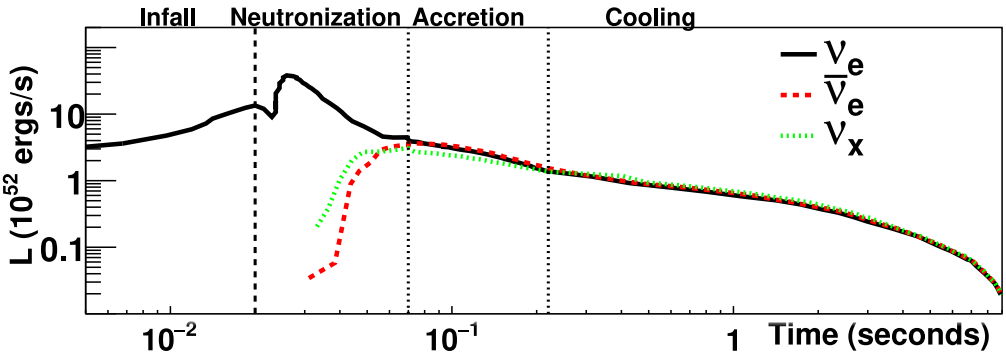

Figure 2.16: Luminosity as a function of time for the model in [87] of an electron-capture supernova. ν_x represents $\nu_e, \nu_\mu, \bar{\nu}_\mu$ and ν_τ. The vertical dashed line at 0.02 seconds indicates the time of core bounce, and the vertical lines indicate different eras in the supernova evolution[77].

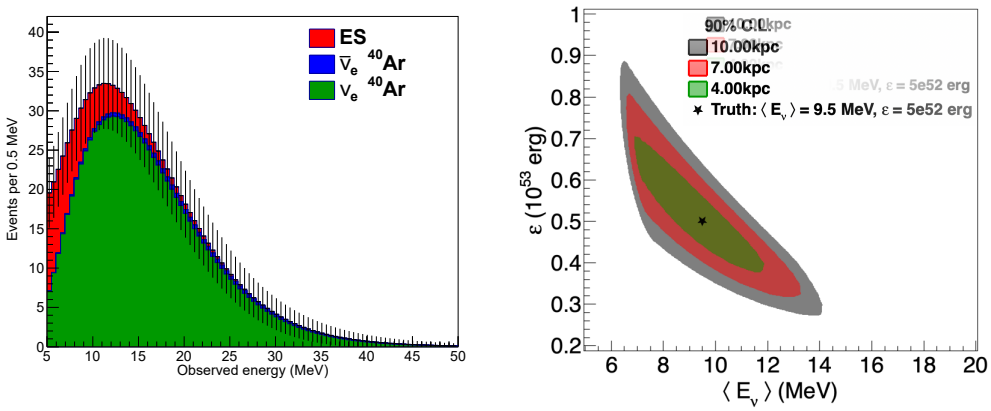

Figure 2.17: Left: Expected measured spectrum as a function of observed energy for the model in [88] with no flavor transformation. Right: Sensitivity regions in $(\langle E_\nu \rangle, \epsilon)$ for the ν_e spectrum for three different supernova distances. Both plots are obtained for the full 40kt fiducial mass at the far detector[86].

also strongly dependent on the neutrino mass ordering, with the normal ordering strongly suppressing the expected signal[90]. Combining DUNE own long-baseline mass ordering measurements, it could then be possible to extract astrophysical knowledge from the supernova burst signal. While challenging due to radioactive background of the argon, solar neutrinos will also be detectable in DUNE, providing significant improvements in the Δm^2_{21} measurement, and in the measurement of *hep* and ^{8}B solar neutrinos fluxes[91].

2.2.3 Physics Beyond the Standard Model

Thanks to a strong reduction of background events due to the underground location of the Far Detectors, DUNE will be sensitive to nucleon decay and other rare processes, enanching the possibility to perform Beyond the Standarf Model (BSM) searches. As described in Sec. 1.5, multiple anomalies in the three neutrino flavor paradigm led to a rich and diverse program of experiments to search for sterile neutrinos. Thanks to both the long baseline of the FD and the short one of the ND, DUNE will be able to probe a broad range of possible sterile neutrino mass splittings by looking for the disappearance of charged-current and neutral-current neutrino interactions. The long baseline of the experiment, combined with a wide-band neutrino beam, also allows to be sensitive to Non-Standard Interaction (NSI). Such interactions affect neutrinos propagating through the Earth and, if the involved parameters are large enough, they will modify the data collected by the experiment[92]. DUNE will thus be sensitive to NSI probes, largely improving the current bounds. At the Far Detector, extensive studies exploiting atmospheric neutrinos will be carried out. Thanks to a wide range of L/E values, an high sensitivity to matter effect and to both neutrino squared mass differences, atmospheric neutrinos will provide promising opportunities to study BSM effects.

On top of this, DUNE will perform an extensive program of searches for dark matter candidates, both at the Near and Far detectors. At the ND, thanks to the intense neutrino beam, it is expected to have a large production of low-mass dark matter (LDM)[93]. As LDM in the beamline are produced with a boost, the ND will be able to distinguish DM candidates to intrinsic radioactive impurities, allowing DUNE to access mass ranges usually not reachable. This capability will be further enhanced by the PRISM measurements, able to constrain neutrino background from the Standard Model. ND-GAr and SAND will also provide additional sensitivity to Heavy Neutral Lepton (HNL), for which the signal scales with the volume of the detector, in opposition to the background interactions, which instead scale with the detector mass. Far Detector DM searches include instead studies on boosted dark matter(BDM) signals produced by sources such as the galactic halo and dwarf spheroidal galaxies[94].

DUNE will also be sensitive to baryon number violating processes, such as

proton decay in the channel $p \to K^+\bar{\nu}$ or the neutron decay into a charged lepton plus meson, $n \to e^- K^+$. Sensitivities have been studied from simulations and, expecting a signal efficiency of 30%, a lower limit on the proton lifetime of 1.3×10^{34} years is foreseen. A more comprehensive description of the BSM searches just described is available in [95].

Chapter 3

SAND

SAND will be the only detector at the DUNE ND complex to be permanently in an on-axis position. The SAND physics program is discussed in Sec. 3.1, while in Sec. 3.2 the different components of the detector are detailed.

3.1 Physics program

The number of events for a specific process X, both at the Far and Near Detectors, can be written as:

$$N_X(E_{rec}) = \int_{E_\nu} dE_\nu \Phi(E_\nu) P_{osc}(E_\nu) \sigma_X(E_\nu) R_{phys}(E_\nu, E_{vis}) R_{det}(E_\nu, E_{rec}) \quad (3.1)$$

where Φ is the incoming (anti)neutrino flux, σ_X is the cross-section for the process X on the given nuclear target, R_{phys} is the physics response function introduced by the nuclear smearing, and R_{det} is the detector response function (acceptance) for the visible final state particles. E_ν and E_{rec} are the true and the reconstructed neutrino energies, respectively. As the main terms of Eq. 3.1 are folded together, it is necessary to unfold them. This is not possible exploiting just a single detector or a single target material. In addition, when performing neutrino oscillation analysis, different interaction processes have to be considered since 25% are quasi-elastic interactions (QES), 42% are resonances (RES), and 33% are deep inelastic scattering (DIS). Current uncertainties in neutrino-nucleus cross sections are too large to meet DUNE analysis requirements. The effect of different values of systematic uncertainties can be seen in Fig. 3.1, where it is visible how small changes greatly increase the exposure needed to achieve a 5σ discovery. SAND has been designed to contribute in constraining systematic unceratinties.

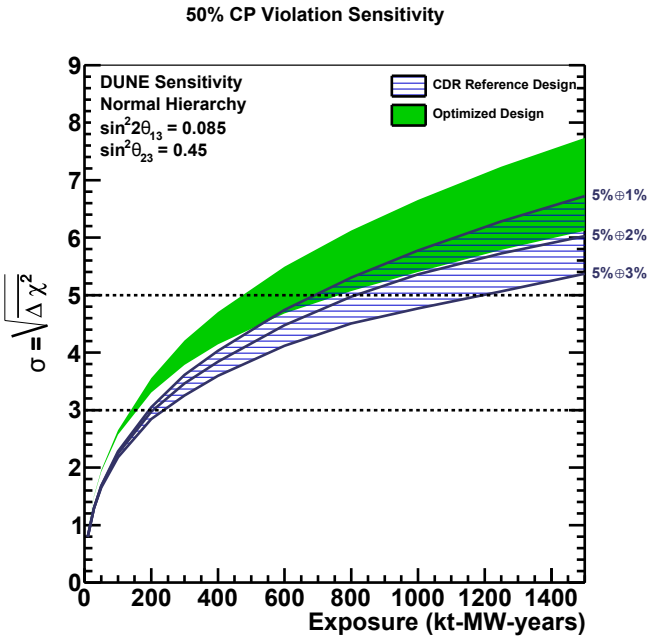

Figure 3.1: Impact of systematic uncertainties on the expected sensitivity to the determination of the CP violation. The dashed blue band and the green band plot represent the reference and optimized design of the beam respectively[96].

3.1.1 Systematics uncertainties constrains

SAND will perform on-axis flux measurements, providing accurate discrimination of the absolute $\nu_\mu, \bar{\nu}_\mu$ and relative $\nu_\mu, \bar{\nu}_\mu, \nu_e, \bar{\nu}_e$ fluxes. This will be possible exploiting different and complementary neutrino processes, including:

- absolute ν_μ flux from elastic $\nu e \to \nu e$
- relative ν_μ flux vs E_ν from $\nu p \to \mu^- p \pi^+$ on H selecting only samples with neutrino energy < 0.5 GeV
- absolute $\bar{\nu}_\mu$ flux and relative $\bar{\nu}_\mu$ flux vs E_ν from $\bar{\nu} p \to \mu^+ n$ QE
- ratio of $\bar{\nu}_\mu/\nu_\mu$ vs E_ν from coherent π^-/π^+ on C inside the CH_2 and graphite targets.
- ratio of ν_e/ν_μ and $\bar{\nu}_e/\bar{\nu}_\mu$ vs E_ν from $\nu(\bar{\nu})$ CC interaction on H

SAND will also provide constraints on the nuclear smearing (R_{phys}) thanks to the liquid argon target integrated with the inner straw tube tracker. This is needed as events interacting on heavy nuclear target, such as the argon nucleus, are affected by final-state nuclear effects, resulting in a significant missing transverse

momentum and smearing in the transverse plane kinematics. Referring to Eq. 3.1, by measuring the flux three terms -$\sigma_X R_{phys}$, and R_{det}- are still convoluted. The unfolding of $\sigma_X R_{phys}$ is possible when detecting neutrino interaction in the same detector, but on different targets, so that R_{det} does not change between measurements. Moreover, the possibility to have an Hydrogen target in SAND (see Sec. 3.2), makes it possible to accurately measure the neutrino cross section, as $R^H_{phys} \equiv 1$. The unfolding of the neutrino energy E_ν then only depends on R_{det}, which can be defined by $\delta p/p$. Performing measurements on Argon and on Hydrogen, one can constrain the product $\sigma_X R_{phys}$ in argon. To constrain R_{phys} separately, one can define a set of kinematic variables sensitive to nuclear smearing. The comparison of the interactions on H and on Ar will allow the determination of nuclear smearing effects with the neutrino spectrum at the ND, which differs from the one at the FD. With $\sigma_X R_{phys}$ on Argon determined, and the constraint on R_{phys}, it is possible to perform a comparison with ND-LAr data. This will allow in return to validate the unfolding of R_{det} in liquid Argon, and thus validate the predictions from the Near Detector before the extrapolation to the Far Detector.

3.1.2 Precision measurements and new physics

Thanks to the high statistics available at the Near Detector complex, together with high-precision measurements, SAND will be able to pursue an independent program of precision measurements and searches for new physics, such as:

- improved measurement of the weak mixing angle, $\sin^2\theta_W$, by exploiting the ratio on NC and CC neutrino DIS interactions $R \equiv \sigma^{NC}_\nu/\sigma^{CC}_\nu$. Thanks to the high resolution of the STT, the systematic uncertainties are much reduced compared to the previous measurements. Moreover, the STT has a high efficiency in the identification of ν_e CC interactions and in the separation of NC and CC interactions by kinematic analysis. The R measurements will be dominated by theoretical systematic uncertainties[97][98][99]. Overall, a total relative uncertainty on the value of $\sin^2\theta_W$ of 0.35% is expected when exploiting νN DIS interactions. An alternative measurement of $\sin^2\theta_W$ can be obtained by measuring NC $\nu_\mu e$ elastic scattering. This channel is unaffected by the nuclear model uncertainties but will be limited by the small cross-section of the process, leading to low statistics. With this measurement, the value of $\sin^2\theta_W$ can be extracted from the ratio $R_{\nu e}(Q^2) \equiv \sigma(\bar{\nu}_\mu e \to \bar{\nu}_\mu e)/\sigma(\nu_\mu e \to \nu_\mu e)$[100]. Performing measurements in this channel will also allow testing the running of $\sin^2\theta_W$, as the two measurements have largely different momentum transfer scales.

- Thanks to the availability of $\nu(\bar{\nu})$-H interactions, precision test of isospin rules can be possible, as the Adler sum rules, $S_A = 0.5\int_0^1 dx/x(F_2^{\bar{\nu}p} - F_2^{\nu p}) =$

I_p[101], which was limited by low statistics in its most recent measurement. S_A value can be measured as a function of the momentum transfer Q^2 from the structure functions $F_2^{\bar{\nu}p}$ and $F_2^{\nu p}$, determined by the corresponding differential cross-section on H. The measurement of S_A in particular would be sensitive to violation of isospin symmetry, charm production and strange sea $(s - \bar{s})$ asymmetries. Such measurement can also be compared to the values of S_A on carbon, for which $S_A = 0$.

- The precise calibration of the energy scale uncertainties of SAND, combined with the high discrimination capability of the $\nu/\bar{\nu}$ fluxes, will allow the detector to perform measurements of the different structure functions F_2, xF_3, F_L, F_T. On top of this, both Parton Distribution Functions (PDFs) and (non)perturbative corrections could be studied performing global QCD analysis. These can be performed over a broad range of Q^2 and Bjorken x thanks to the statistics and energies available in DUNE. The possibility of having different target materials within the STT also allows to inspect the nucleon structure and to separate valence and sea quark distributions, d and u quark distributions, and the strange quark s and $\bar{s}$ distributions.

The measurements listed above could be affected by Beyond Standard Model effects, which would manifest as unexpected deviations from the SM predictions, making SAND sensitive to new physics (NP). Moreover, SAND will be able to perform more direct NP searches, such as testing the MiniBooNE low-energy anomaly with similar L/E but different detector technology and different energies. This will be possible by searching for anomalies in the $\nu_\mu, \bar{\nu}_\mu$ and $\nu_e, \bar{\nu}_e$ CC spectra by measuring both the neutrinos and antineutrinos CC ratios and the NC/CC ratio as a function of L/E:

$$R_{e\mu}(L/E) \equiv (\nu_e N \to e^- X)/(\nu_\mu N \to \mu^- X) \tag{3.2}$$
$$\bar{R}_{e\mu}(L/E) \equiv (\bar{\nu}_e N \to e^+ X)/(\bar{\nu}_\mu N \to \mu^+ X) \tag{3.3}$$
$$R_{\nu p}(Q^2) \equiv \sigma(\nu_\mu p \to \nu_\mu p)/\sigma(\nu_\mu n \to \mu^- p) \tag{3.4}$$
$$R_{\bar{\nu}p}(Q^2) \equiv \sigma(\bar{\nu}_\mu p \to \bar{\nu}_\mu p)/\sigma(\bar{\nu}_\mu p \to \mu^+ n) \tag{3.5}$$

Lastly, SAND will provide enhanced sensitivity to searches in the Dark Sector, including searches for heavy sterile neutrinos, axion-like particles, and dark photons.

3.2 Design

3.2.1 Magnet

The KLOE magnet was designed to produce a 0.6 T magnet field over a 4.3 m long, 4.8 m diameter cylindrical volume. The coil is located inside a cryostat of

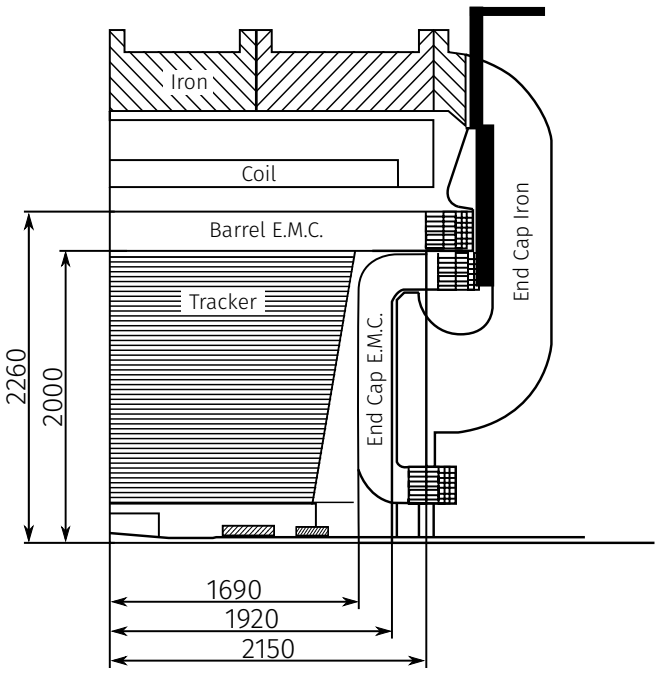

Figure 3.2: Vertical cross-section of the KLOE detector. Units are in mm. Figure readapted from [102]

4.40 m of length and with a 5.76 m of diameter positioned inside the return yoke. It is composed by a single conductor layer consisting of an (Nb-Ti) Rutherford cable co-extruded with high-purity aluminium. The coil's cooling is performed using Helium gas at 5.2 K injected at 3 bar from the cryogenic plant and liquefied into a reservoir in thermal contact with the coil. Figure 3.2 shows a lateral section of the KLOE experiment, with details of the coils and cooling system structure. Figure 3.3 shows the solenoidal longitudinal field component as measured in KLOE installation phase, compared with the simulation.

3.2.2 Electromagnetic Calorimeter

The SAND calorimeter, refurbished from the KLOE experiment[102], is a lead-scintillating fiber sampling calorimeter. Scintillating fibers offer high light transmission over several meters, sub-ns timing accuracy and very good hermeticity. The calorimeter is composed of 24 modules in a nearly cylindrical arrangement, with two endcaps consisting of 32 vertical modules each. The horizontal modules have trapezoidal shape, with 52 and 59 cm bases, a length of 4.3 m and a thickness of 23 cm. Endcaps' modules, from 0.7 to 3.9 m long, have a rectangular cross section and both ends bent in a C-like shape to allow their insertion in the

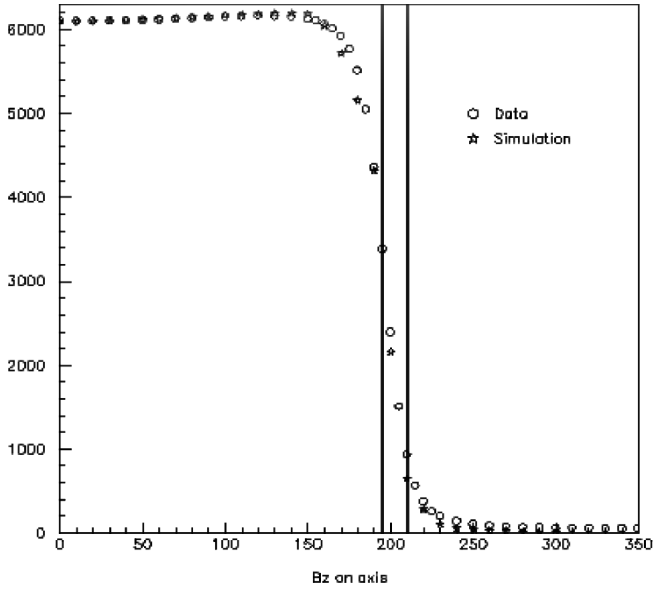

Figure 3.3: KLOE solenoid longitudinal field component (in Gauss) along the magnetic axis.

calorimeter barrel (Fig. 3.5). Each ECAL module is composed of 200 lead foils 0.5 mm thick alternated with 200 layers of cladded scintillating fibers of 1 mm diameter glued together with compatible epoxy. The end faces of each module are divided in a 5×4 grid by light guides, as shown in Fig. 3.4, and each cell is read by a phototube, for a total of 4880 phototubes. The performances of the calorimeter evaluated during the KLOE commissioning and running periods, are[102]:

$$\frac{\sigma}{E} = \frac{5\%}{\sqrt{E(\text{GeV})}} \tag{3.6}$$

$$\sigma_t = \frac{54}{\sqrt{E(\text{GeV})}} ps \tag{3.7}$$

Pictures of the KLOE calorimeter are shown in Fig. 3.5 for the horizontal and endcaps' modules.

3.2.3 Straw tube tracker

The guiding principles of the SAND inner tracker design are:

- provide a (anti)neutrino target and tracking system able to reconstruct the momentum of all charged particles.

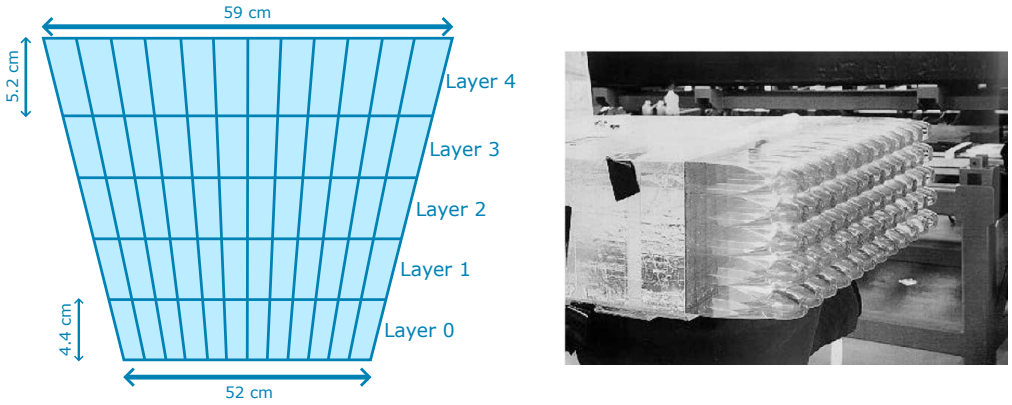

Figure 3.4: Left: schematic representation of the segmentation of one ECAL module. Right: picture of the light guides at one end of a Ecal barrel module [103].

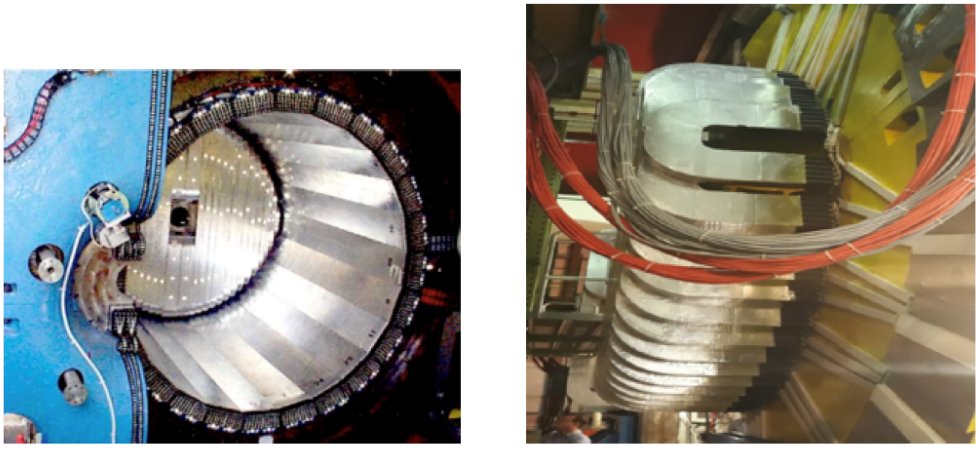

(a) (b)

Figure 3.5: Picture of the electromagnetic calorimeter of the KLOE experiment, with both the barrel and endcaps modules visible.

- provide low density and high granularity to provide high momentum, angular, and space resolutions.
- minimize secondary interactions by limiting the total thickness to about one radiation length.
- provide the possibility to change the target material during the run to study neutrino interactions on different elements.
- provide particle and charge identification for $e^{\pm}$, $\pi^{\pm}$, $K^{\pm}$, $\mu^{\pm}$, , p.
- provide a target fiducial mass of at least 5 t.

A Straw Tube Target Tracker (STT) can meet all these requirements. By separating the target material from the tracking system, the latter can be designed to be as light as possible. Moreover, with the target material distributed uniformly through the entire volume, the average density is kept low enough to achieve high-resolution measurements. The target will be arranged in thin layers of 100% chemical purity of various materials, and will account for more than 97% of the total detector mass. The STT will be organized in modules; each module can be operated and configured independently. A default configuration consists of:

- a 5 mm thick solid polypropylene (CH_2) target slab, whose thickness can be tuned in order to achieve the desired target mass and detector density;
- a polypropylene radiator composed of 105 foils 18 μm thick, alternating with air gaps 117 μm thick;
- four layers of straws arranged in an XXYY pattern, with each straw having a 5 mm diameter, 12 μm mylar walls coated with Al, and a 20 μm tungsten wire coated with gold.

The straws are filled with a Xe/CO_2 70/30 mixture, operated with an internal pressure of $\sim$1.9 atm. A section view of the default configuration is shown in Fig. 3.6.

Alternative module configurations are possible, allowing to offer great control on the chemical composition and mass of the neutrino target. This is done replacing both the radiator and the polypropylene target slab with solid targets of different materials. The most important one is graphite (pure C), which allows direct measurements of background events when selecting neutrino interaction on hydrogen in modules equipped with slab and radiator of CH_2[104]. The pure Carbon target consists of a 4 mm plate located in front of the straw layers, and its thickness can be tuned to have the same fraction of radiation length of both the

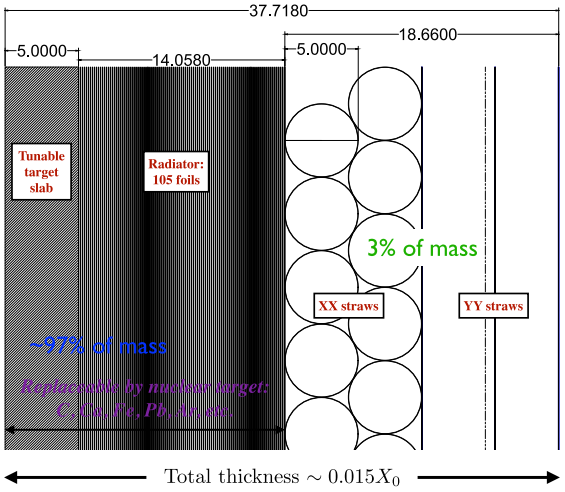

Figure 3.6: Default configuration of one STT module, with a tunable polypropylene target, a radiator, and four layers of straw with a XXYY arrangement[103].

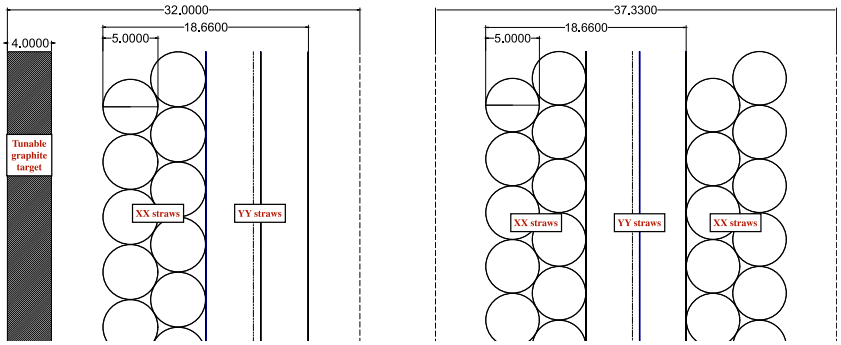

Figure 3.7: Left: STT module configuration with a solid graphite target replacing the CH_2 module and the radiator. Right: tracking STT module, with just six layers of straw in a XXYYXX arrangement[103].

CH_2 radiator and solid slab of the default configuration (Fig. 3.7, left). To guarantee the same acceptance, pure C modules are interleaved throughout the CH_2 modules. Other possible targets are Ca, Fe, and Pb, which could be installed in the upstream region of the tracker depending on the desired measurements. Lastly, a *tracking* configuration can be obtained by arranging 6 layers of straws in a XXYYXX pattern and without any target slab nor radiator (Fig. 3.7, right). The current STT design foresees 8 carbon target modules, 70 CH_2 target modules and 6 tracking module, located in the upstream and downstream regions of the STT.

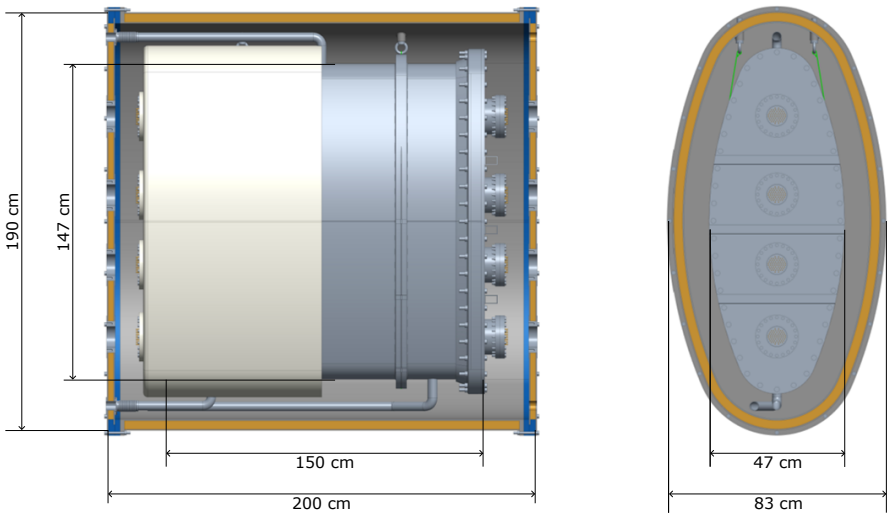

Figure 3.8: 2D rendering of GRAIN in the YX (left) and YZ (right) view.

3.2.4 GRAIN

The upstream region of SAND inner volume will be occupied by $\sim$ 1 t liquid Argon detector called GRAIN (GRanular Argon for Interaction of Neutrinos). GRAIN will supplement the ND-LAr TPCs, providing on-axis data of neutrino-argon interactions. An innovative approach based on the detection of the scintillation light in Argon is being developed. By exploiting the large light yield and fast emission time (see Chapter 4), one can limit the photon collection to few nanoseconds, and achieve high spatial resolution. GRAIN design is optimised to provide calorimetric information and spatial reconstruction of the neutrino-argon interactions To this end an optical system coupled to a fast, segmented photon detector is needed. The cryostat is composed of an inner and an outer vessel. The outer vessel is 190 cm high, 200 cm wide and with a maximum thickness along the beam direction of 83 cm. It is made of multiple layers of Aluminum alloy, honeycomb, and Carbon fiber. The inner vessel is made of Aluminium, with a height of 147 cm, a width of 150 cm and a maximum depth of 47 cm. The overall thickness of vessels - 6 mm - was kept as thin as possible to minimize the energy loss, showering and multiple scattering in the passive material. A 2D view of GRAIN is shown in Fig. 3.8, while a 3D rendering is shown in Fig. 3.9.

The light collection in GRAIN is done by instrumenting the inner vessel with Vacuum UltraViolet cameras operating at LAr temperatures (78 K). Two optical systems are currently being developed, one based on lenses, and one based on Coded Aperture Masks (the latter are discussed in detail later in Chapter 6). An example of the geometry of both cameras is shown in Fig. 3.10. Both optical systems offer advantages and present disadvantages: lenses-based cameras are bet-

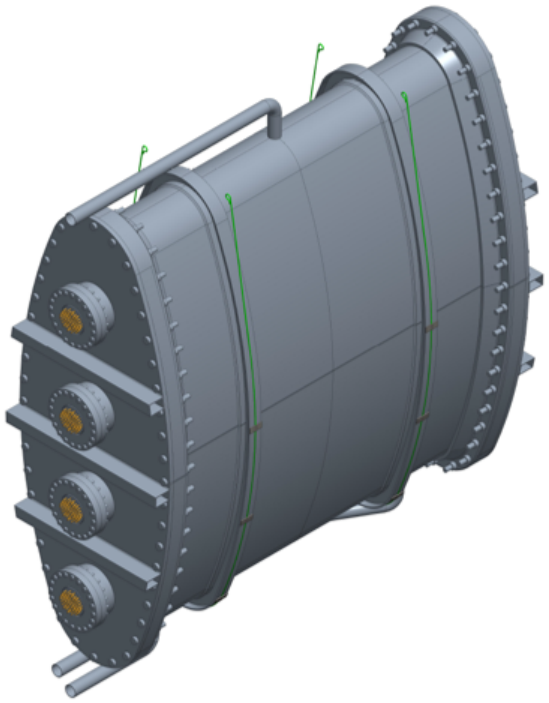

Figure 3.9: 3D rendering of GRAIN.

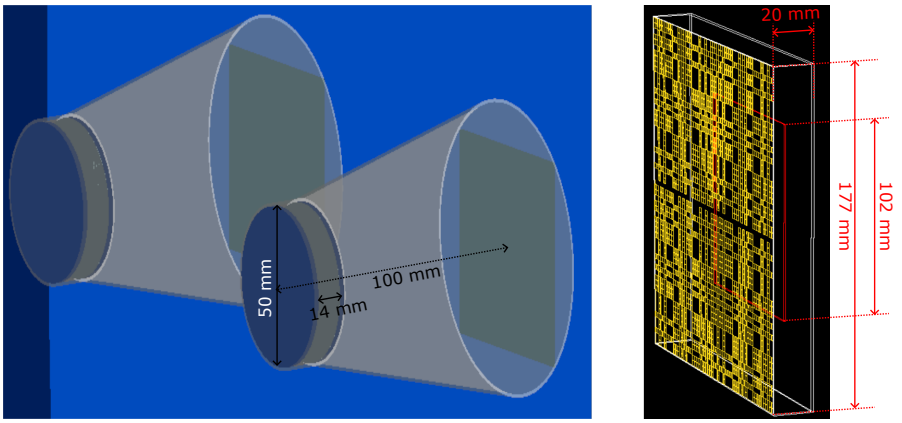

Figure 3.10: 3D models of lens- and mask-based cameras. Both models exploit a SiPM matrix as sensor beyond the optical system. The lenses are represented by blue and grey circles in the left image, while the mask is represented by the yellow squares in the right image.

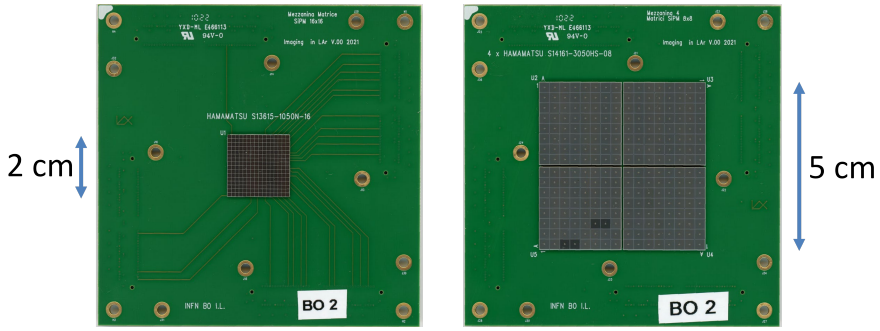

Figure 3.11: S13615 (left) and S14160 (right) Hamamatsu SiPM matrices used as sensors in the optical cameras in GRAIN.

ter known and the detected image is a direct reconstruction of the source image. However, they are difficult to build due to the cryogenics environment and because of LAr high refractive index, they have a limited Field of View and occupy a large volume. Mask-based cameras are easy to build, have a larger Depth of Field, and have a much more compact design. However, complex reconstruction algorithms are required in order to reconstruct the image of the source (Chapter 6). Both optical systems are coupled to light sensor composed of a SiPM matrix. At the time of this writing, the availability is limited to the S14160 and S13615 Hamamatsu arrays[105]. These are 8×8 and 16×16 SiPM matrices, respectively, shown in Fig. 3.11. A drawback of both SiPMs is their poor sensitivity to the 127 nm wavelength of Argon scintillation light. A wavelength-shifter (WLS) to convert UV light into visible light, where SiPMs have their optimal photon detection efficiency (PDE) is required. Tetraphenylbutadiene (TPB) is an organic compound emitting fluorescent radiation when excited by UV light. The TPB emitted spectrum is peaked at about 430 nm [106] which matches the PDE spectrum of the SiPMs (see Fig. 3.12 for S14160 model) and does not vary with the wavelength of incident light in the UV range.

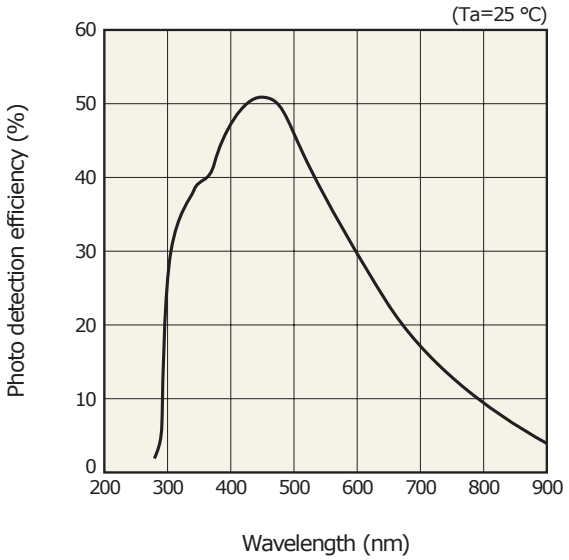

Figure 3.12: Photon detection efficiency for the S14160 SiPM model.

Chapter 4

Liquid Argon properties

Liquid argon (LAr) is one of the most common target for rare events experiments such as neutrino oscillation experiments. Liquid argon detectors exploit the scintillation light emitted by ionizing particles crossing the argon volume, often coupled with the collection of the ionizing charge as in both Far Detector's modules described in Chapter 2. Most of the challenges related to the use of liquid argon as a target are related to the very short emission wavelength, a slow decay time of the triplet component, and a short attenuation length. On the other hand, a fast decay time of the singlet component, a high light yield and a much lower cost compared to other liquid noble elements, such as xenon, make argon a widely used target. Moreover, some of the downsides of liquid argon can be mitigated with the addition of small amounts of xenon. As detailed in Chapter 2, the GRAIN detector will be completely filled with liquid argon and will use exclusively the scintillation light to perform tracks and energy reconstructions. For this reason, a deep understanding of the optical properties of liquid argon is mandatory to design the best possible GRAIN configuration. In this chapter, the emission and propagation of scintillation light in argon will be reviewed, together with a discussion on the effect of xenon doping on these processes.

4.1 Scintillation light production

An ionizing particle crossing a liquid argon volume produces both excitons (Ar*) and electron-ion pairs ($Ar^+ + e^-$). Both states can couple with other argon atoms, producing an excited molecular state (Ar_2^*) or a ionized molecule (Ar_2^+). The ionized molecules eventually get neutralized by the recombination with a thermalized electron producing again an excited argon molecule Ar_2^*. This will then decay non-radiatively to the first single and triplet states $^1\Sigma_u^+$ or $^3\Sigma_u^+$ based on the spin orientation of the excited electron in the excimer molecule[107]. Both states decay

radiatively emitting a scintillation photon of approximately the same energy of about 9.7 eV, but with very different lifetimes: 7 ns for the singlet $^1\sum_u^+$ state and 1.6 μs for the triplet $^3\sum_u^+$ one[108]. Due to their very different lifetimes, the singlet and triplet components are usually referred to as fast and slow components respectively. Equation 4.1 shows the processes of excitation and recombination just described[109]:

$$\text{Excitation: } Ar^* + Ar \rightarrow Ar_2^* \tag{4.1}$$

$$\text{Recombination: } Ar^+ + Ar \rightarrow Ar_2^+ + e^- \rightarrow Ar_2^* \tag{4.2}$$

$$\text{Radiative decay: } Ar_2^*(^{1,3}\Sigma_u^+) \rightarrow 2Ar + \gamma \tag{4.3}$$

The total number of scintillation photons emitted by argon per unit time can then be written as the sum of two exponential functions:

$$N(t) = \frac{\alpha_s}{\tau_s} e^{-\frac{t}{\tau_s}} + \frac{\alpha_3}{\tau_3} e^{-\frac{t}{\tau_3}} \tag{4.4}$$

$$\alpha_s + \alpha_3 = 1 \tag{4.5}$$

where α_s is the initial fraction of the singlet states, τ_s is the decay time of the singlet states, α_3 is the initial number of the triplet states and τ_3 is the decay time of the triplet state. Figure 4.1 shows the tipical scintillation time distribution of liquid argon for differents particles, with the narrow peaks and long tails corresponding to the fast and slow component respectively. The ratio α_s/α_3 has been measured to be strongly dependent on the particle type, as shown in Table 4.1 and Fig. 4.1. On the contrary, lifetimes, total number of emitted photons, and photons wavelength do not depend on it: the number of emitted photons depends on the total energy deposited by the ionizing particle, with a typical light yield of around 40k photons per MeV of deposited energy. The scintillation photons' wavelength has been measured multiple times by different authors[107][110] and all the measurements agree with a value around 127 nm, in the Vacuum UltraViolet range. Table 4.2 shows the emission peak wavelenght obtained for different particles, while Fig. 4.2 shows a measurement of the scintillation spectrum of liquid argon compared to the emission spectra of gaseous argon.

4.1.1 Effect of impurities on the light yield

The high light yield of 40k photons per deposited MeV does not take into account the presence of impurities which could affect this number dramatically. It is thus the best possible light yield in case of a perfectly pure argon, for which the emission of the light is governed by the processes in equation 4.1. This number can be greatly reduced when impurities are added in the argon volume and, depending on

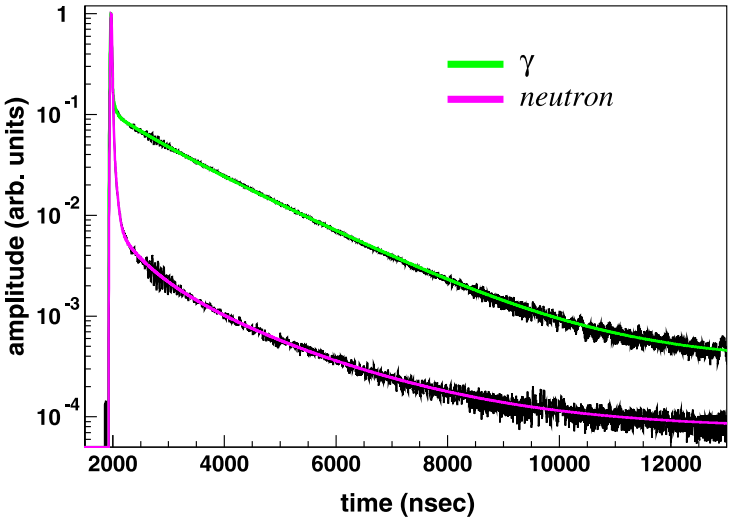

Figure 4.1: Signal shape of liquid argon scintillation light for gammas (green) and neutrons (pink). The two scintillation components are clearly visible in both cases, with the sharp peak being generated by the fast component, and the long tails being generated by the slow component[109].

Exciting particle	τ_s[ns]	τ_3[ns]	I_s/I_3	Reference
e^-	6.3 ± 0.2	1020 ± 60	0.083	[111]
	4.6	1540	0.26	[112]
	6.5	1100	0.086	[113]
	6 ± 2	1590 ± 100	0.3	[108]
γ	10 ± 5	1280 ± 20	0.30 ± 0.01	[114]
n	10 ± 5	1280 ± 20	3.5 ± 0.2	[114]
p	3.20 ± 0.02	1355.8 ± 5.8	0.28 ± 0.01	[107]

Table 4.1: Measurements' summary of the singlet and triplet lifetimes and of the singlet to triplet intensity ratio for different particles.

Exciting particle	Peak Position [nm]
p	126.8 ± 0.1
S	126.4 ± 0.1
Au	125.8 ± 0.2

Table 4.2: Summary of measurements of the emission peak position of the liquid argon scintillation light[114].

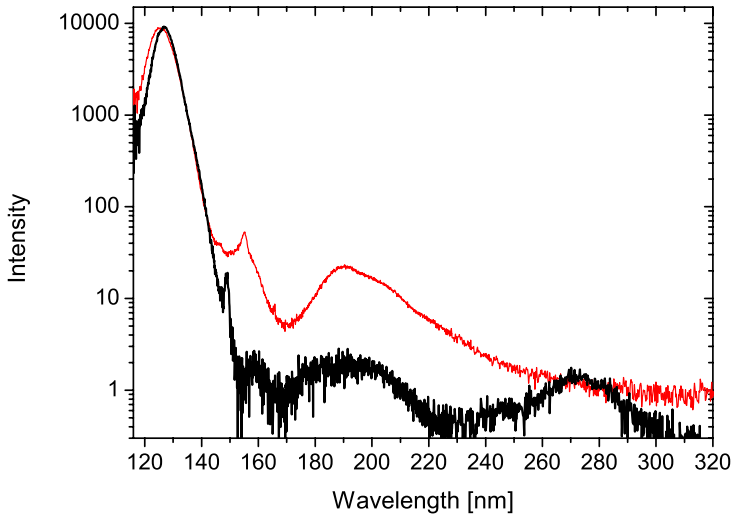

Figure 4.2: Liquid argon emission spectrum (black line) compared with the emission spectrum of gaseous argon (red line). The emission for liquid argon is dominated by a 127 nm feature, with a peak at 149 nm caused by xenon impurities and much smaller contributions up to about 300 nm. Europhys. [115]

the type of impurity, can affect the light emission by quenching and absorption. The quenching effect is a reduction of the number of Ar_2^* excited molecules by non-radiative decay. This can occur in presence of impurities such as N_2[116] or O_2[117] through the reaction

$$Ar_2^* + N_2 \rightarrow 2Ar + N_2 \tag{4.6}$$

The reaction 4.6 has the effect of decreasing the number of excited molecules, and consequently the number of emitted photons, while it does not affect the total number of impurities in the argon. It usually reduces the triplet excited states as their decay time is much longer than the singlet ones, which is too fast to be affected by few ppm impurities concentration. Equation 4.4 should then be rewritten taking into account this effect:

$$N(t) = \frac{\alpha_s^{'}}{\tau_s^{'}} e^{-\frac{t}{\tau_s^{'}}} + \frac{\alpha_3^{'}}{\tau_3^{'}} e^{-\frac{t}{\tau_3}} \tag{4.7}$$

here $\tau_j^{'}[j = s, 3]$ is the effective lifetime of each component, and $\alpha_j^{'}$ is the effective amplitude. Both depend on the nitrogen concentration $[N_2]$ and can be defined as follows[116]:

$$\frac{1}{\tau_j^{'}}([N_2]) = \frac{1}{\tau_j} + k[N_2] \tag{4.8}$$

$$\alpha_j^{'}([N_2]) = \frac{\alpha_j}{1 + \tau_j k[N_2]}. \tag{4.9}$$

Here the sum $\alpha_s^{'} + \alpha_3^{'}$ is no longer equal to one due to the quenching, and an overall quenching factor can thus be defined as:

$$Q_f = \alpha_s^{'} + \alpha_3^{'}, \quad 0 \leq Q_f \leq 1 \tag{4.10}$$

representing the fraction of the surviving excited molecules emitting a scintillation photon rather than decaying non-radiatively due to collisions with impurities. Figure 4.3 shows the quenching factor as a function of nitrogen concentration, where a fast decrease is visible up to 100 ppm. For $[N_2] > 100$ ppm, the slow component of the scintillation light is expected to completely vanish. The effect on the slow component is clearly visible in Fig. 4.4, where the light intensity spectrum for three different nitrogen concentrations is shown.

Impurities in argon could also absorb the scintillation light after its emission and during its propagation, further decreasing the light yield. In case of oxygen impurities, this effect leads to oxygen metastable states, which later decay emitting photons not transparent to the argon itself:

$$\gamma + O_2 \rightarrow O(^3P) + O(^1S) \tag{4.11}$$

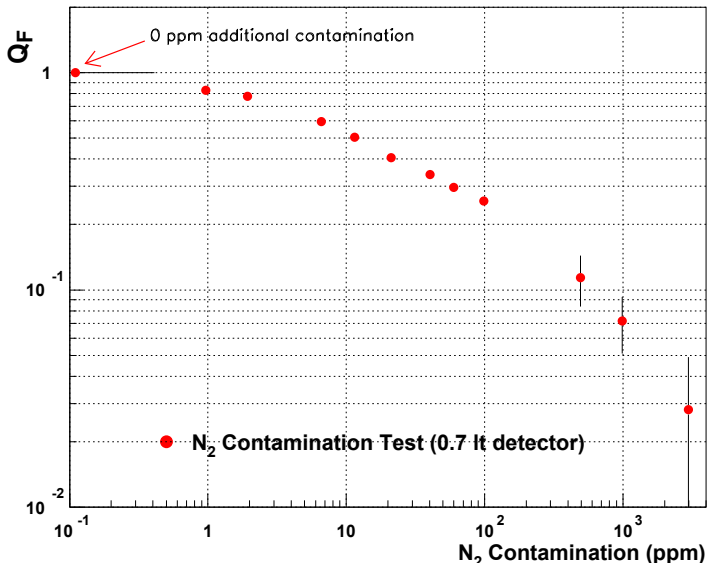

Figure 4.3: Quenching factor Q_F as a function of the nitrogen concentration. Q_F corresponds to the fraction of surviving excited argon molecules emitting scintillation photons[116].

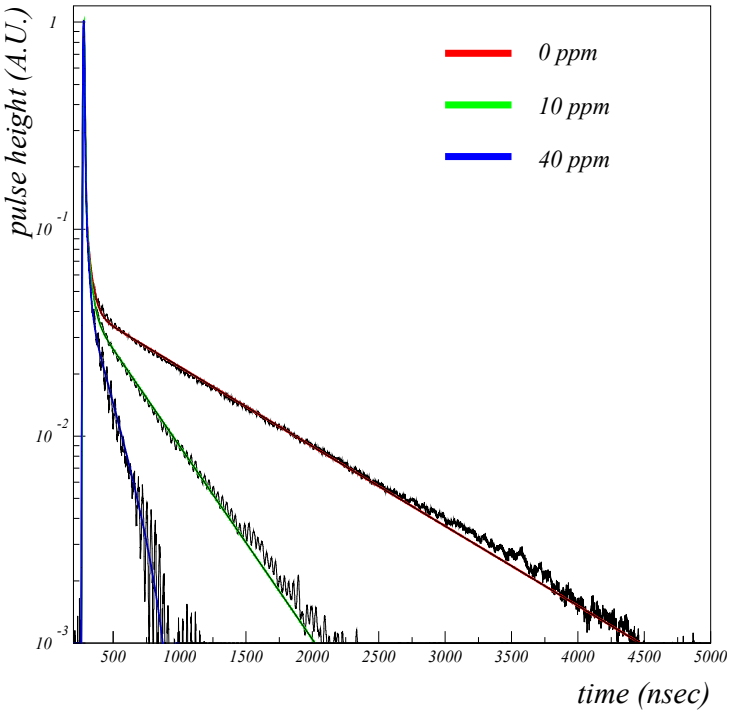

Figure 4.4: Signal shape of liquid argon scintillation light at three different nitrogen concentrations: 0, 10 and 40 ppm[116].

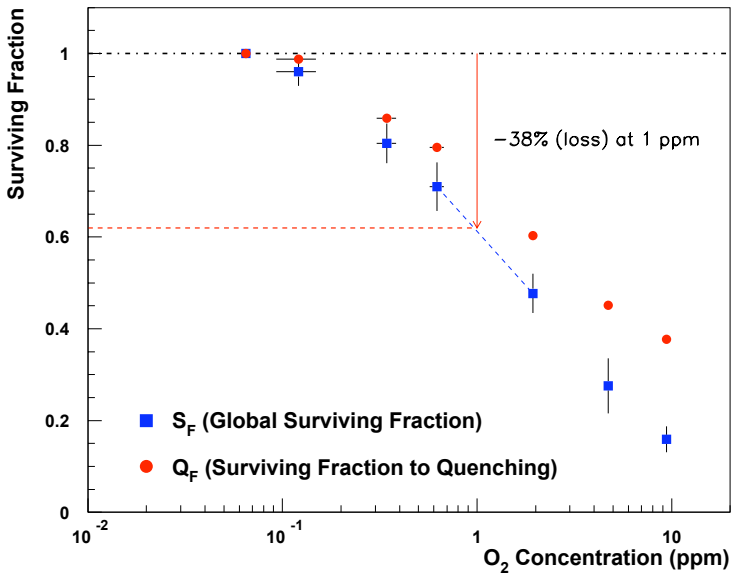

Figure 4.5: Quenching factor Q_f (blue dots) and Surviving factor S_f (red dots) as a function of the oxigen concentration. The difference between the two corresponds to the contributions of the absorption by the O_2 in argon[117].

On top of this, electro-negative molecules such as O_2 can attract free electrons generated after the argon ionization[117]:

$$e^- + O_2 \rightarrow O_2^- \tag{4.12}$$

The recombination of such electrons with ionized argon molecules produces scintillation light as described in Eq. 4.1 and their absorption with different molecules decreases the total light yield of the argon. The total light yield reduction is quantified by the survival factor S_f, which is the ratio between the total intensity of the emitted scintillation light for a given impurity concentration, and the total scintillation in case of pure liquid argon. Figure 4.5 shows the light yield decrease at different concentrations of O_2. The difference between the quenching factor and the surviving factor shows the importance of the absorption process in case of O_2 impurities.

4.2 Scintillation light propagation

Photons' interaction with matter happens via three mechanisms: photo-electric effect, elastic scattering, and Compton scattering. As the energy of a scintillation photon emitted by the argon is around 9.7 eV, it can only interact via elastic scattering, also known as Rayleigh scattering, as the first ionization potential of

Element	λ_{RS} [cm]	Ref
Ar	52.1 ± 10.4	[120]
	55 ± 5	[121]
	99.1 ± 2.3	[119]

Table 4.3: Measurements' summary of the Rayleigh scattering length for pure argon.

the argon is 15.7 eV and the Compton scattering only happens at higher energies. As already described in the previous section, scintillation photons can however be absorbed by impurities in liquid argon such as oxigen.

4.2.1 Rayleigh scattering

The Rayleigh scattering is the process describing the elastic scattering of photons on particles whose dimension is much smaller than the wavelength of the photon itself[118]. In argon, this can happen when a photon interacts with argon atoms or molecules as well as impurities, which don't affect the cross section of the process due to their similar size with the argon atoms. This process does not reduce the total light yield directly, but changes the direction of the photons, increasing the propagation length and, consequently, the absorption probability. The mean free path a photon can travel before it scatters is called Rayleigh scattering length, λ_{RS}, and is defined as follow:

$$\frac{1}{\lambda_{RS}} = \frac{16\pi^3}{6\lambda^4}[k_B T k_T \frac{(n(\lambda)^2 - 1)(n(\lambda)^2 + 2)}{3}] \tag{4.13}$$

with λ being the photon wavelength, k_B the Boltzmann's constant, T the temperature, k_T the isothermal compressibility, and n the argon refractive index. The latest measurements of the Rayleigh scattering length in argon are reported in Table 4.3. One result points to a value of about 90 cm[119], with another measurements being slightly shorter, about 50[120][121]. As the scattering length depends on the inverse of the fourth power of the photons wavelength, it is possible to increase the length by means of a wavelenght shifter. This is the case of a mixture of argon doped with a small amount of xenon. Despite some disagreements with the measured values of the scattering length, all the results suggest an increase in the scattering length, up to about several meters. More details on the effect of doping the liquid argon will be given in section 4.3.

4.2.2 Attenuation length

The attenuation length is the distance at which the light signal intensity drops to $1/e$. It depends on both the scattering length, described in the previous section, and the absorption length, which describes the absorption of the light due to the presence of impurities:

$$\frac{1}{\lambda_{Abs}} = \sigma \frac{\rho N_A}{2m_a} \tag{4.14}$$

Here ρ and m_a are the density in g/cm^3 and the atomic mass of the contaminant respectively, and N_A is the Avogadro number. The attenuation length is defined as the reciprocal sum of both the scattering and absorption lengths, and the light intensity at a distance d from the source can be defined as follow:

$$I(d) = I_0 e^{\frac{d}{\lambda_{Att}}} \tag{4.15}$$

$$\frac{1}{\lambda_{Att}} = \frac{1}{\lambda_{Abs}} + \frac{1}{\lambda_{RS}} \tag{4.16}$$

Equation 4.15 refers to a wavelength integrated value. In reality, the coefficient should be measured for each wavelength independently, as the involved attenuation processes are wavelength dependent, such as the Rayleigh scattering coefficient in Eq. 4.13. The attenuation length for different wavelengths in pure argon is thus expected to decrease for shorter wavelengths, with a consequential red-shift of the light at greater distances. Despite what just said, wavelength measurements are rarely performed due to their complicated realization. Figure 4.6 shows pure argon transmission as measured in [122], compared with the expected value for different values of Rayleigh scattering lengths. Moreover, as described in the previous section, impurities dissolved in argon could greatly increase the absorption of the emitted light, directly affecting the light propagation and the attenuation length. A summary of the absorption length measurements for pure argon and for different impurities compositions is shown in Table 4.4.

4.3 Xenon doping

While pure liquid argon is commonly used as scintillator for rare-events physics searches, its long triplet state lifetime, the low 127 nm wavelength, and the attenuation length of about 1 m are limitations that should be addressed when building a liquid argon based detector. A novel technique studied to overcome these limitations is the addition of small amount of xenon to the liquid argon[127]. Xenon-doped liquid argon (XeDLAr) features a wavelength peak at 178 nm, as the xenon molecules rapidly shift the light to the xenon scintillation light wavelength.

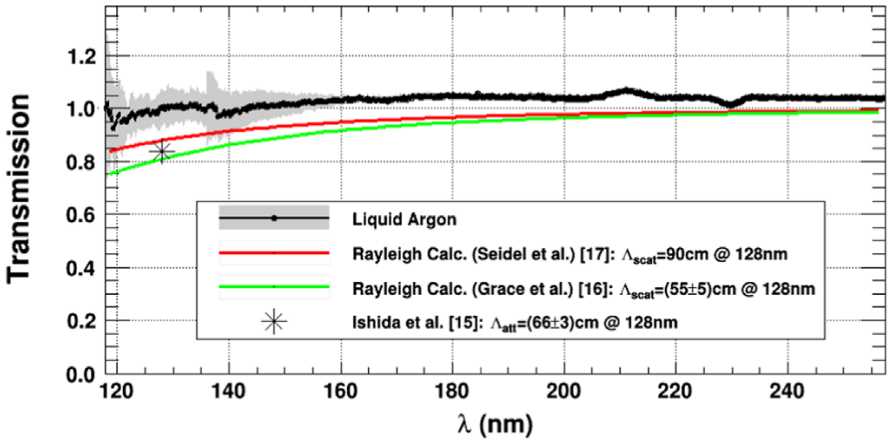

Figure 4.6: Transmission of 11.6 cm pure liquid argon, with the gray bars representing the statistical errors. The red/green solid curves show wavelength-dependent calculations of the expected transmission of 11.6 cm pure liquid argon for different values of Rayleigh scattering length[123][124]. Plot modified from [122].

		α_{abs}	Ref
Pure Ar		66 ± 3	[125]
		52 ± 7	[120]
		> 110	[122]
Impurity	Concentration	α_{abs}	Ref
N_2	2 ppm	30+2	[126]
	8 ppm	8.7 ± 0.7	
Xe	3%	170 ± 23	[125]
		118 ± 10	

Table 4.4: Summary of the absorption length measurements for pure argon and for different impurities compositions

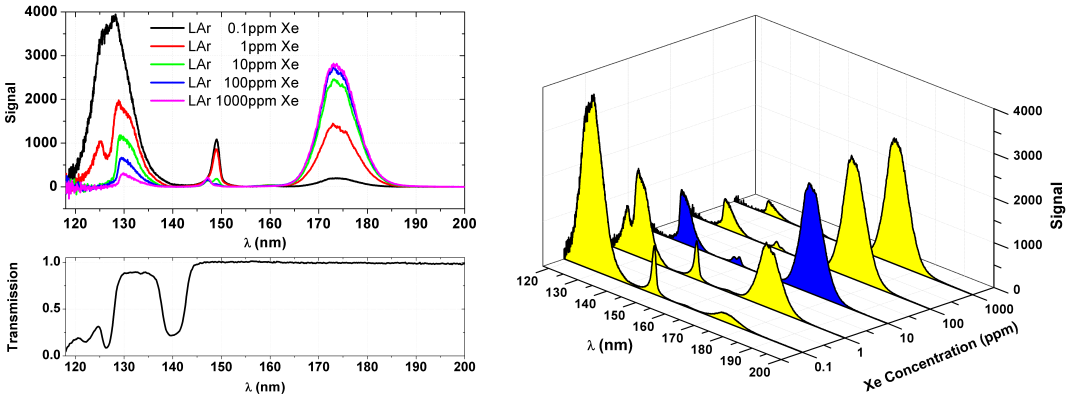

Figure 4.7: Left (upper panel) and right: emission spectrum of liquid argon doped with different xenon concentrations. The shift from the peak at 127 nm to the one at 175 nm is clearly visible as the doping increases. For concentration of 1 to 10 ppm, a peak at about 150 nm appears, decreasing again to negligible values for higher concentrations. Left (bottom panel): transmission of the argon doped with 0.1 ppm of xenon as a function of the wavelength measured with a deuterium light source and a length of the optical path of 116 mm[132].

Consequentially, the Rayleigh scattering length increases, enhancing the light collection and indirectly increasing the light yield. Furthermore, XeDLAr manifests a shorter effective triplet lifetime τ_3. The scintillation mechanisms of XeDLAr relies on the formation of argon-xenon ($ArXe^*$) and xenon-xenon excimers (Xe_2^*). This is possible as the triplet states have a long enough lifetime to transfer their energy to the xenon atoms. Starting from the processes in Eq. 4.1, the xenon-argon interactions can be described via[128][129]:

$$Ar_2^*(^3\Sigma_u^+) + Xe \rightarrow ArXe^+ + Ar \tag{4.17}$$

$$ArXe^* \rightarrow Ar + Xe + \gamma(150nm) \tag{4.18}$$

$$ArXe^* + Xe \rightarrow Xe_2^*(^{1,3}\Sigma_u^+) + Ar \tag{4.19}$$

$$Xe_2^*(^{1,3}\Sigma_u^+) \rightarrow 2Xe + \gamma(178nm) \tag{4.20}$$

On top of the 127 nm photons emitted by the de-excitation of the argon excimers, in the XeDLAr scintillation processes the emitted photons could have different wavelengths: the photons emitted by $ArXe^*$ excimers' decay have wavelenghts peaked at 150 nm[130] and decay times of 3 ns, while the ones emitted by the Xe_2^* excimers have a wavelength of about 175 nm[131] and decay times of 27 ns. Differently from the almost monochromatic scintillation spectrum of pure argon, XeDLAr spectrum has therefore up to three peaks, depending on the xenon concentration, as shown in figure 4.7. The processes described in Eq. 4.17 not

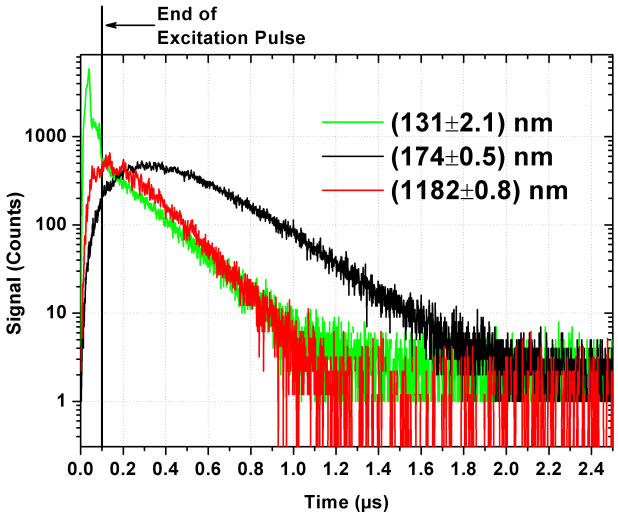

Figure 4.8: Signal shape of the scintillation light of liquid argon doped with 10 ppm of xenon. The green line shows the unshifted component at 127 nm, the black line shows the time structure of the component at 175 nm while the red line shows the contribution of an infrared component not discussed here[132].

only change the wavelength of the photons emitted by the triplet states, but also the time profile of the scintillation light[132]. This can be seen in figure 4.8, where the 127 nm photons are represented by a green line with both the fast and slow components visible, and the 175 nm photons are represented by the black line, which manifests a much slower rise time due to the transfer process between argon and xenon atoms.

An additional effect of the XeDLAr is the alteration of the photon propagation. Two opposite behaviours occur when doping liquid argon with xenon: on the one hand there is a suppression of the spectrum below 127 nm. This effect is explained by looking at figure 4.9, where the XeDLAr transmission curve at different Xe concentration is shown. One can see how the transmission is close to 0% for wavelength shorter than 128 nm, and greatly increases for wavelengths longer than 128 nm, up to almost 100% for >150 nm photons. This absorption does not depend on the Xe concentration and its characteristic length was measured to be smaller than 12 cm[133]. On the other hand, there is an enanching of the transmission of the photons emitted at higher wavelengths. This is possible not only thanks to the higher transmission efficiency just described, but also to the increased Rayleigh scattering length at 150 an 178 nm being 3.5 and 8.3 m respectively[134].

Summarizing the effect of the xenon doping, one has:

- shift of the slow 127 nm component to 150 and 178 nm depending on the

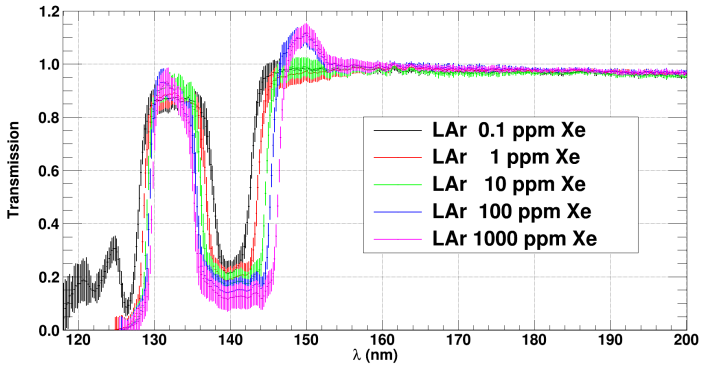

Figure 4.9: Transmission of 11.6 cm of liquid argon doped with different concentrations of xenon, from 0.1 to 1000 ppm. For xenon concentrations above 0.1 ppm the mixture is not transparent to light with wavelenght shorter than 130 nm[133].

xenon concentration

- slower rise time of the slow component due to the transfer process between argon and xenon atoms
- increased Rayleigh scattering length due to the longer 150 and 178 wavelengths, corresponding to an increased light collection at longer distances
- absorption of both the fast and slow component at 127 nm due to low transmissivity

The last two effects are visible is figures 4.11 and 4.12, where the results of measurements in the protoDUNE Dual-Phase experiment are shown[134]. In both figures the amplitude is the maximum distance from the baseline to the minimum of the signal, usually related to the amplitude of the fast component, while the charge is the integral of the signal in a 3 μs window, related to the total collected light (Fig. 4.10). Figure 4.11 shows the ratio between the signal amplitude of pure argon, XeDLAr, and XeDLAr + nitrogen (not discussed here) and the signal amplitude of pure argon. As expected from what discussed, the ratio decreases from 1 to ~ 0.65 when doping with xenon and it remains constant adding nitrogen. Figure 4.12 shows instead the signal amplitude and the total collected charge as a function of the distance from the sensors. For both measurements, the ratio between different scintillator compositions is also shown. From the left panel it is possible to see how the ratio XeDLAr/LAr is almost constant at about 0.7 for all the measured distances, in agreement with the previous result, while the total charge ratio increses with the distance, confirming a higher light yield at distances >3 m. Some studies suggest that adding greater quantities of xenon doping (>1000 ppm)

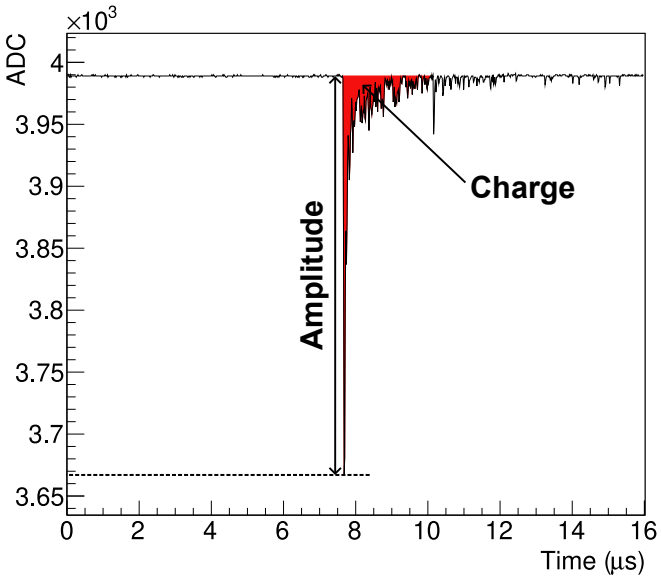

Figure 4.10: Example of a typical scintillation signal and definition of amplitude and charge as described in [134].

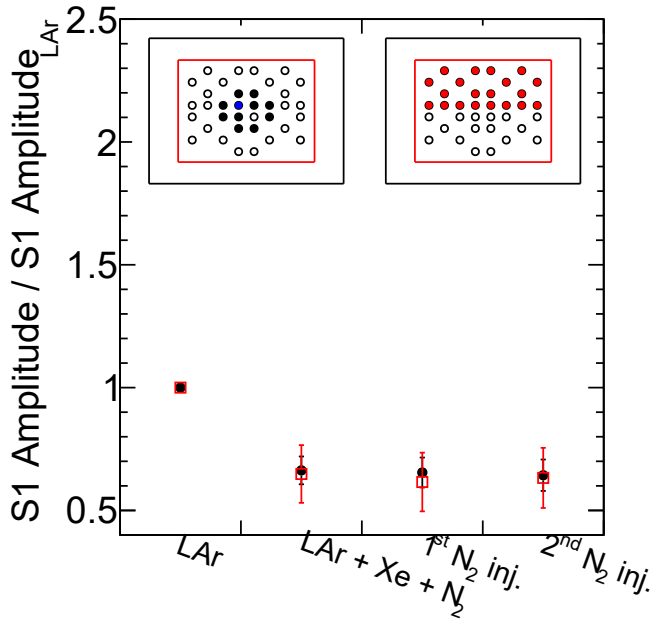

Figure 4.11: Signal amplitude ratio for different doping situations relative to pure argon. Red and black dots show the results based on different triggers, with a diagram of the PMT distribution shown in the top diagrams. More details on the trigger and PMT configurations can be found in [134].

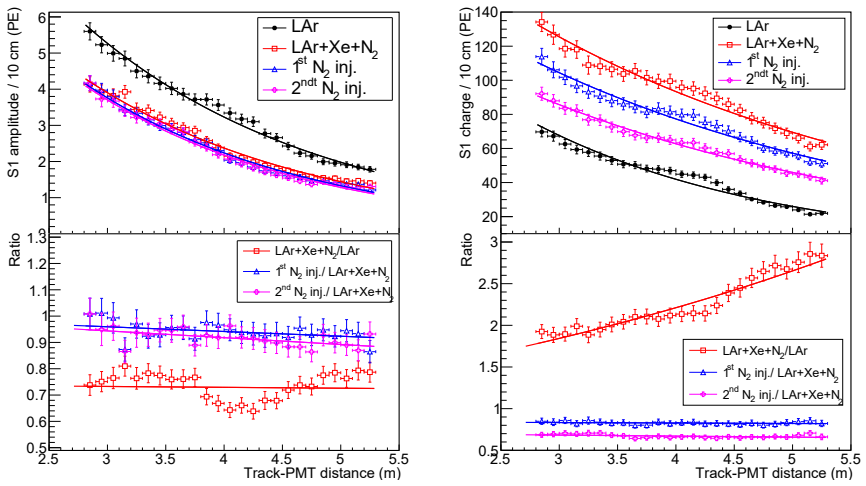

Figure 4.12: Top panels: signal amplitude (left) and charge (right) as a function of the track distance for different doping situations. Bottom panels: ratio between the data in the top panels[134].

solve the problem of the absorption of the 127 nm fast component[135]. This is possible as the larger concentration of xenon enables also the argon singlet states to interact with the xenon before de-excitation. The 127 nm component is thus completely shifted to 178 nm, as also visible in Fig. 4.7, and it is not absorbed during its propagation. It should be noted that at such large concentrations, the time profile of the fast component is modified due to the transfer process similar to what happen for the slow component.

From what discussed in this section it is clear that, while promising, the technique of xenon-doping needs careful optimization. Lower concentrations could be useful in large detector, where the light travels long distances, or in cases where the timing information of the fast component is not essential, while very large concentrations could be used when a very high argon purity is not needed, to recover the fast component information.

The application of XeDLAr in GRAIN is still under investigation. While the increased wavelength will help collecting light due to an increase in the photon detection efficiency of the SiPMs, the reduction of the fast scintillation component at low Xe concentrations, and the changes of the time profile at high concentrations are both behaviours which don't quite match the requirements of the detector. Whether or not the effect of these changes is negligible in GRAIN is not yet known and the xenon addition is not to be excluded a-priori. However, since the mask-based readout does not require the xenon doping to be effective, it is not taken into account in the following chapters.

Chapter 5

Simulation framework

In order to study the performance of SAND and GRAIN, a detailed Monte Carlo simulation was developed. The simulation framework includes several steps, from the neutrino interaction to the detector response, with a schematic view shown in Fig. 5.1. This chapter will describe in detail the most important steps of the simulation, providing the information needed to better understand the results later shown in Chapters 6 7. Section 5.1 will describe the implementation of the SAND and GRAIN geometries. The neutrino interaction simulation will be detailed in 5.2, while the liquid argon scintillation will be presented in Sec. 5.3. Details on the detector response will be given in Sec. 5.4.

5.1 SAND and GRAIN geometries

Both SAND and GRAIN geometries are implemented using the Geometry Description Markup Language (GDML). It is a format based on the XML language, commonly used to describe detector geometries in HEP frameworks such as Geant4[136] and ROOT[137]. The SAND geometry includes all the detector components described in Chapter 2, while the GRAIN geometry was developed to be as flexible as possible, with the possibility to simulate several optical cameras configurations. In both SAND and GRAIN geometries, the z axis goes along the beam direction, while the y and x axis go upward and sideways respectively.

5.1.1 SAND geometry

The SAND geometry was implemented using the General Geometry Description (*gegede*)[138], a software recommended by the DUNE collaboration to develop complex geometries. The complete geometry of SAND is visible in figures 5.2 and 5.3, showing xz and yz sections respectively. The geometry includes all the

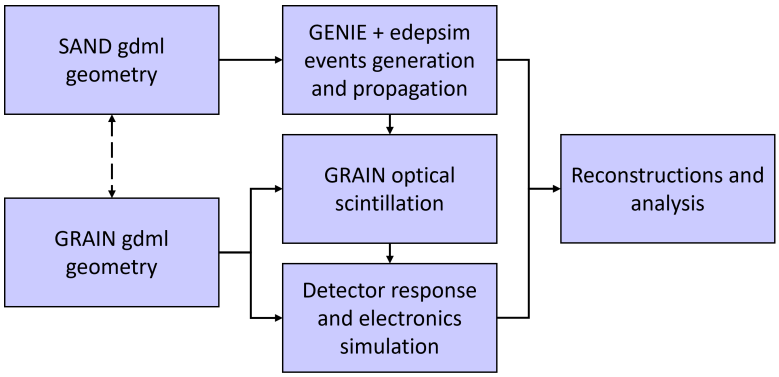

Figure 5.1: Scheme of the simulation framework. Solid arrows indicate the flow of the simulation, the output of the exiting blocks being the input for the entering blocks. The dotted line indicates a mutual influence between the two geometries. More details can be found in the text.

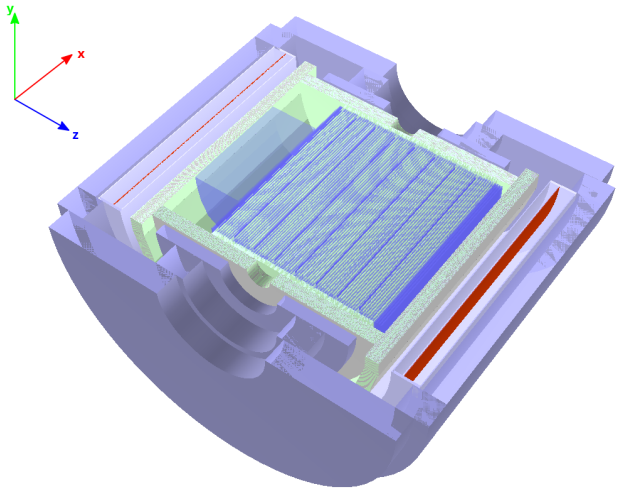

Figure 5.2: xz section of the SAND detector geometry. The inner vessel of GRAIN is not represented here.

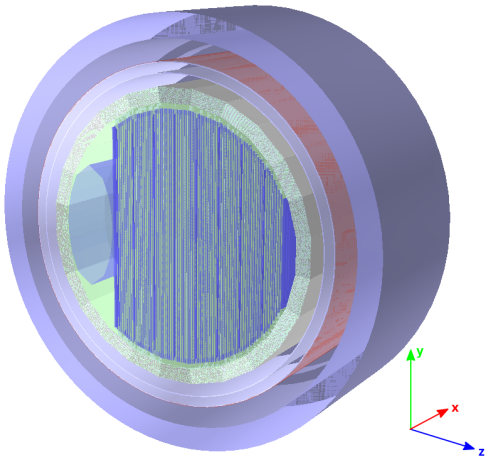

Figure 5.3: yz section of the SAND detector geometry. The inner vessel of GRAIN is not represented here.

components detailed in Chapter 2, a brief description of their implementation is given in the following:

- Electromagnetic calorimeter (ECAL): each module of the calorimeter is simulated as a trapezoidal module 4.3 m long, 23 cm thick, with minor and major bases of 52.5 and 59.6 cm respectively. The ECAL is composed by a total of 24 modules arranged along the profile of a cylinder of radius 2 m. The fine structure of the fibers and absorbers of each module is simulated alternating 0.04 cm plastic scintillator slabs and 0.07 cm thick lead slabs for a total of 418 layers. The endcaps are implemented as disks with minor radius of 21 cm and major radius of 2 m. Each endcap is 23 thick cm and subdivided in 45 vertical modules of variable width and height. A complete view of the geometry of the calorimeter is given in Fig. 5.4.

- STT modules: the Straw Tube Tracker is simulated following the design described in section 3.2.3. A total of 82 modules are implemented, alternating 1 C module every 9 CH_2 modules. Each module is composed by a slab of target material (C or CH_2), a radiator made by 105 C_3H_6 foils 18 μm thick, interleaved with air, and 4 planes of straw tubes. The first and last five STT modules are tracking modules, composed by straw tube planes without target and radiator slabs. The height of each module varies with the z position (along the beam direction), while the width is fixed at 4 m for all the modules. Figure 5.5 shows the complete geometry of the STT, together with a focus on one single module.

- GRAIN: the external vessel material is implemented as a carbon fiber-honeycomb-

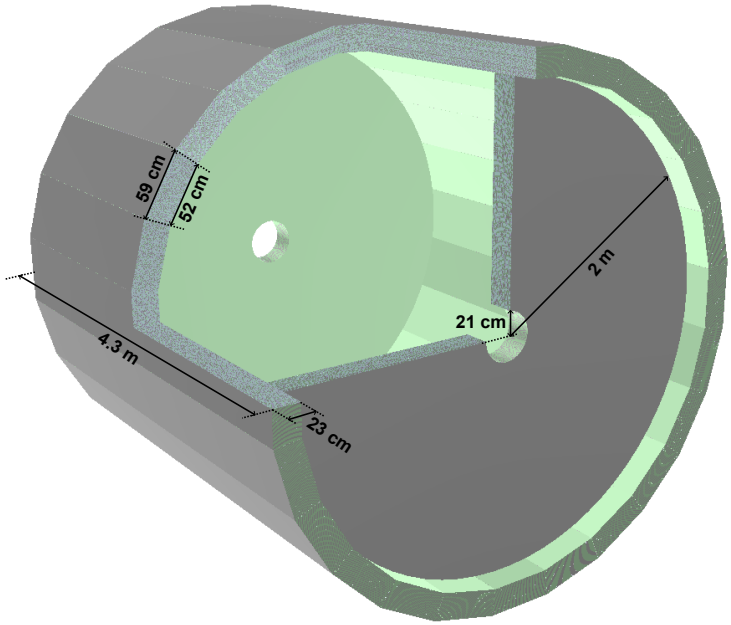

Figure 5.4: Electromagnetic calorimeter geometry with trapezoidal barrel sections and endcaps.

carbon fiber multilayer structure, for a total thickness of 62 mm. The endcaps are simulated as 16 mm steel planes. The inner vessel is entirely made of aluminum. Both vessels are implemented as elliptical modules with axis of 192.4 and 85.4 cm and length of 193.2 cm for the external vessel, and 23.75 and 72.8 cm for the inner one, with a length of 65 cm. The geometry of the cameras inside the volume of GRAIN is detailed in the next section, while a view of the GRAIN geometry is given in Fig. 5.6.

5.1.2 GRAIN geometry

To allow a greater flexibility when studying different optical cameras, the camera configuration inside GRAIN was developed independently from the event simulation inside the argon volume. Once neutrino interactions were simulated in the SAND geometry, the event sample was used to study many different readout configurations. For every configuration, the inner vessel was instrumented with multiple cameras, each of them composed of three elements:

- sensor: simulated as a 1 mm thick metallic slab with side dimension defined by the specific configuration under study, usually about 10 cm.

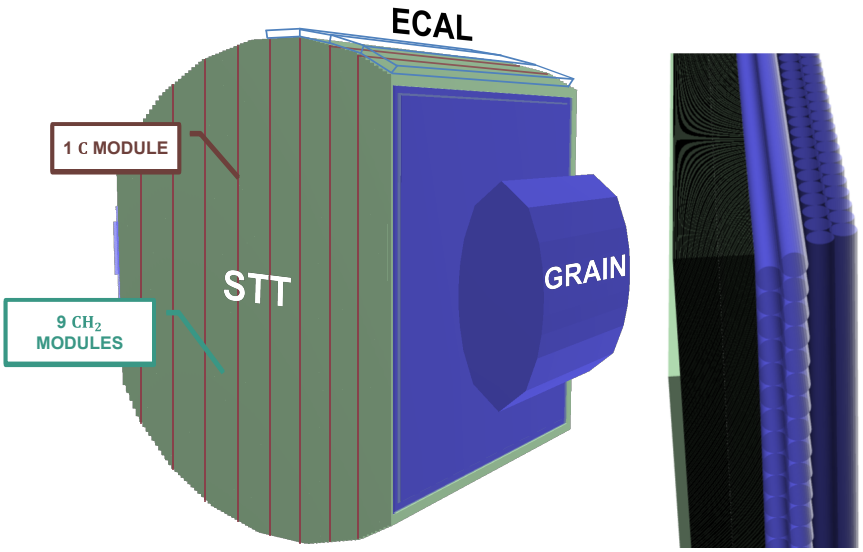

Figure 5.5: Left: Straw Tube Tracker geometry showing the alternating sequence of C and CH_2 modules, in red ad green respectively. The first and last five modules are tracking modules (blue). Right: A detail of one standard CH_2 STT module is shown on the right.

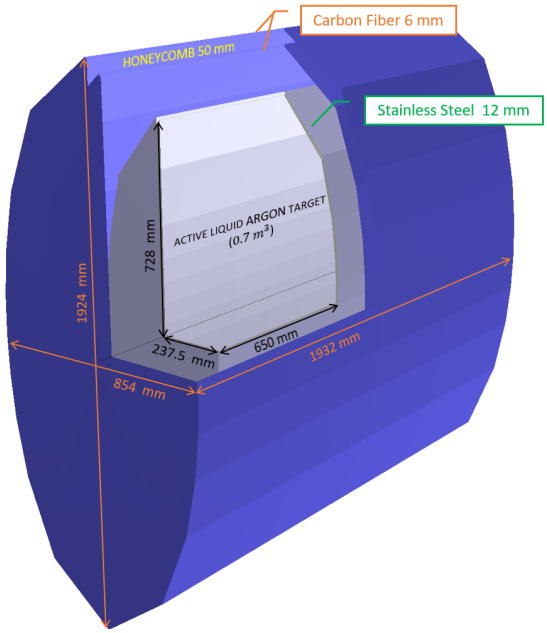

Figure 5.6: GRAIN geometry in the SAND detector. Dimensions are expressed in mm. Both vessels have elliptical shape, the polygonal representation is an effect of the viewer used to render the image.

	Percentage
^{36}Ar	0.34
^{38}Ar	0.06
^{40}Ar	99.6

Table 5.1: Argon composition as implemented in the GRAIN geometry simulation.

- mask: obtained starting from a 0.1 mm thick slab and performing boolean subtractions to obtain multiple holes. The holes are squared with dimensions and positions based on the desired configuration, usually about 3 mm. A detailed description of the masks will be provided in the next Chapter.
- body: a 1 mm thick vessel used to enclose the sensor. One face of the vessel is replaced by the mask, leaving only the holes of the mask as apertures between the inside of the body, where the sensor is located, and the outer volume.

The geometry of a single camera is shown in Fig. 5.7, while a complete geometry of GRAIN, including different camera configurations, is shown in Fig. 5.8. As described in Sec. 3.2.4, a second option for light detection is based on lens-based cameras. They are composed by three elements, with the main differences being the different optical system (lenses instead of masks) and the general geometrical shape of the cameras. More information about the use of lens-based cameras can be found in [139], and they will not be discussed further here. The inner vessel is filled with argon, simulated as a mixture of ^{36}Ar, ^{38}Ar and ^{40}Ar, as reported in table 5.1.2.

5.2 Event generation and particle propagation

The neutrino event generation is performed using the GENIE[140] event generator. GENIE is a ROOT-based[141] neutrino interaction generator widely used in the neutrino community, adopted as a reference by beamlines such as JPARC and NuMI. It is particularly used in the few-GeV range, with plans to become a generator whose validity will extend to all nuclear targets over a much wider spectrum. GENIE includes description of the main scattering mechanisms for all the neutrino flavors and target types, which can be roughly subdivided in three categories: nuclear physics models, cross section models, and hadronization models. One important aspect of the GENIE generator is the possibility to specify both a detector geometry and a neutrino flux. The software than uses these information,

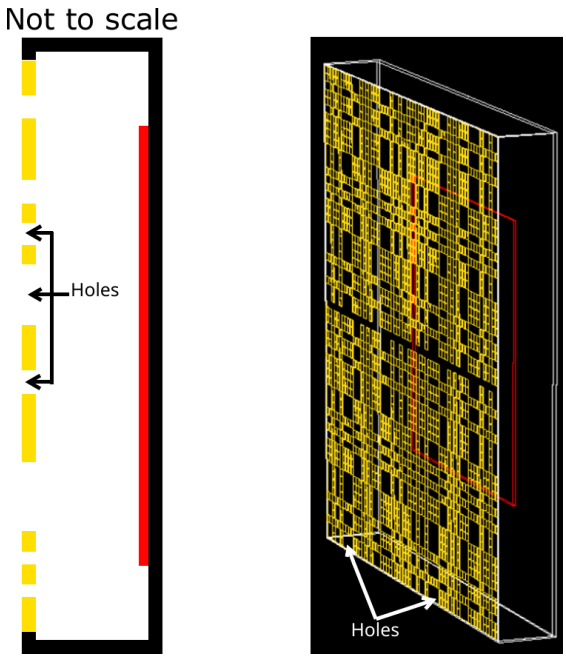

Figure 5.7: Details of a mask-based camera. The body (on the left in black, on the right in white) is simulated as 1 mm thick 100% opaque material, the sensor (in red) is placed inside the body, adjacent to the inner face of the body. The mask (in yellow) replaces the body's face on the opposite side of the sensor. Each missing region of the mask represent an hole.

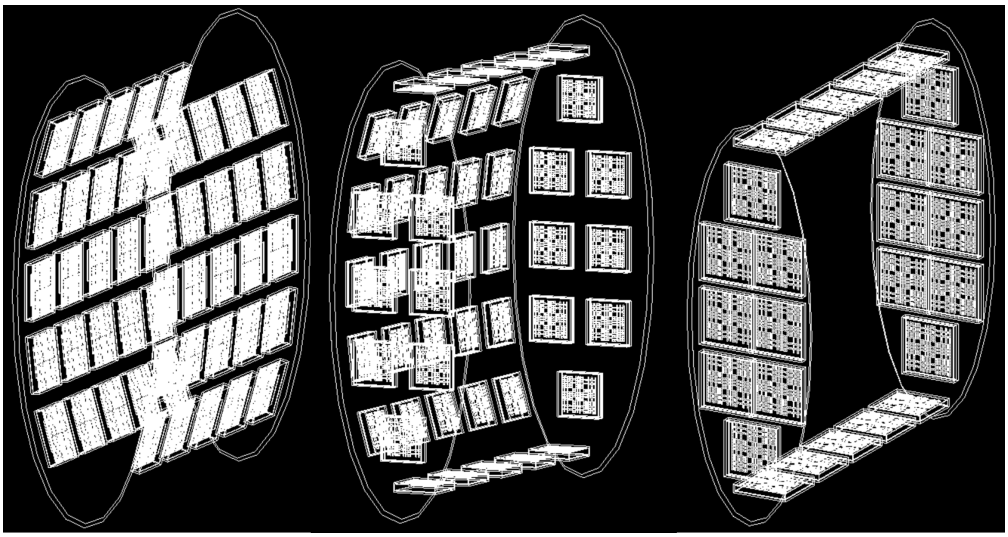

Figure 5.8: Three different configurations of the GRAIN camera geometry in the inner vessel (different position, number, and type of cameras).

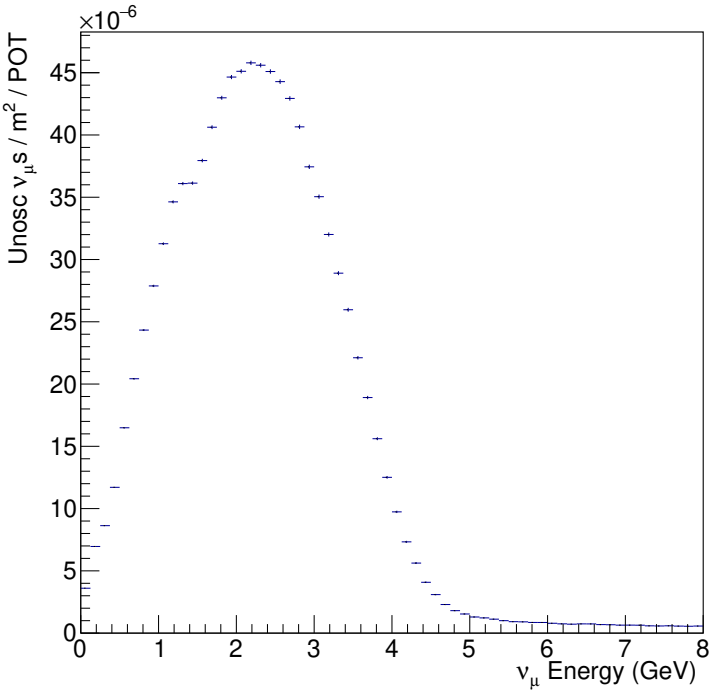

Figure 5.9: ν_μ neutrino flux used as input for the neutrino event generation in GENIE[142].

together with pre-compiled cross-section libraries, to determine the neutrino energy and interaction type. All the neutrino interactions simulated for the analysis described in the following Chapters are generated with neutrino fluxes as expected at the LBNF (Sec. 2.1.1). These are calculated at 574 m from the start of the horns and include fluxes for muon and electron neutrinos and antineutrinos[142]. Figure 5.9 shows the unoscillated calculated flux for muon neutrinos.

After the generation of the neutrino interactions, the primary particles - exiting from the interaction vertex - must be propagated in the detector geometry to simulate energy deposition and geometry issues. This step is performed with the edep-sim software[143], a wrapper around the Geant4 simulation tool. It includes a detailed energy deposition model for both ionizing and non-ionizing energy loss cases and, in case of the liquid argon, it uses the NEST (Noble Element Simulation Technique) model[144]. NEST provide data driven models to compute the scintillation and ionization yield, taking into account the energy and field dependance, as well as the intrinsic fluctuations and recombination physics. Figure 5.10 shows the charge and light yields of the liquid argon in case of electron recoil for different electric field values obtained by the latest NEST argon model.

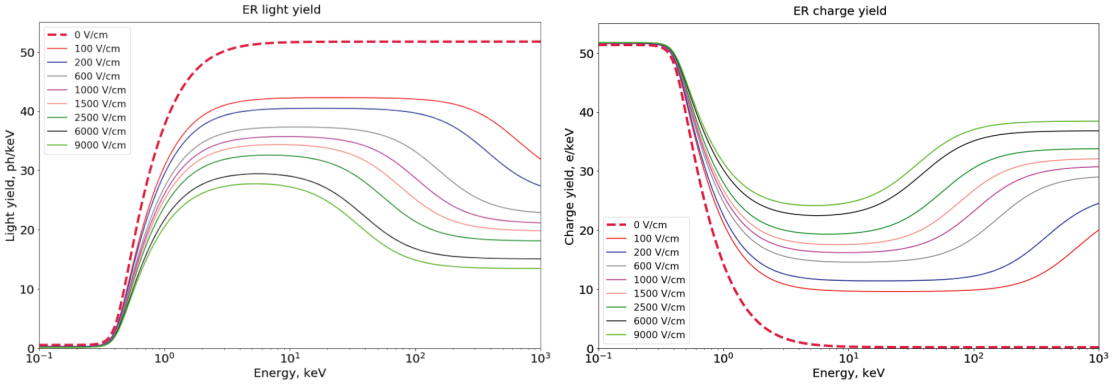

Figure 5.10: Light (left) and charge (right) yields for electron recoil in liquid argon by the latest NEST mean yield model[145].

Edep-sim processes the GENIE output file, providing information about the evolution of the neutrino interaction events. In particular, it provides information on the primary particles produced by neutrino interactions, information on all the secondary particles produced during the primaries propagation, and information on each energy deposit (hit). For the last step, it records starting and stopping position of each deposit, the particle generating the deposit as well as the parent of the depositing particle, i.e. one primary particle or the ultimate parent. These information are crucial to perform the STT and ECAL track reconstruction and to simulate the liquid argon scintillation in GRAIN, discussed in the next section. A display of one neutrino event propagated with edep-sim in the SAND geometry is shown in Fig. 5.11.

5.3 Simulation of liquid argon scintillation

The edep-sim propagation results are used to simulate the optical scintillation emission by liquid argon in GRAIN. This is done by means of a dedicated Geant4 simulation which uses the energy deposits information to emit, propagate and collect the scintillation photons in the GRAIN geometry. The most relevant Argon optical properties, such as emission spectra, singlet to triplet ratio, and Rayleigh scattering are included in the simulation and parametrized following the measurements reported in Chapter 4. Table 5.2 shows a summary of all the liquid argon properties as implemented in the simulation, which will be described in the following sections.

Light emission	
Light yield	40k ph/MeV
τ_s	7 ns
τ_3	1.6 μs
λ	127 nm
I_s/I_3	0.25 electron recoil 0.7 nuclear recoil
Light propagation	
λ_{RS}	90 cm
λ_{Abs}	5 m
Optical surface properties	
Model	glisur
Type	dielectric_dielectric
Finish	Polish
Reflectivity	0%
Absorption	100%

Table 5.2: Liquid argon and optical surfaces properties' values as implemented in the simulation.

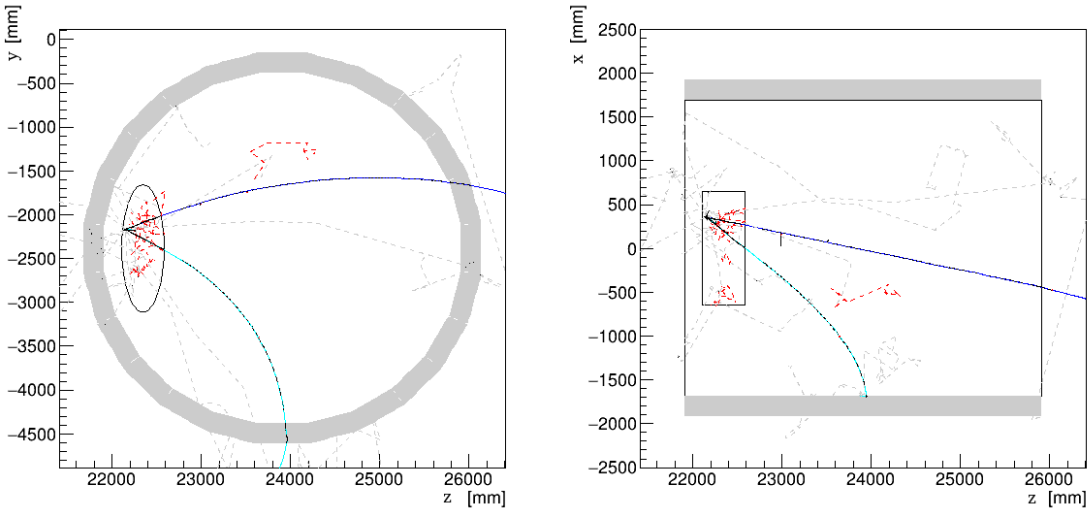

Figure 5.11: yz (left) and xz (right) views of one neutrino interaction in SAND with vertex inside GRAIN. The muon track is represented in blue, a π^- in cyan, electrons in red and neutrons in gray.

5.3.1 Photon generation

The total number of emitted photons is computed taking into account the nominal light yield of liquid argon (40 ph/keV) and the energy deposit of each hit as obtained from edep-sim. For each hit, the number of emitted photons is extracted from a Gaussian distribution whose mean is equal to the energy deposit times the argon light yield, and whose sigma is equal to the square root of the mean. For each photon, a random position and time is extracted in the range between the start and end point of the hit. The wavelength of the scintillation photons is extracted randomly from a probability distribution parameterized on the measurements shown in Fig. 4.2. Figure 5.12 shows the energy distribution of the emitted photons as obtained from the simulation. The decay time constants are fixed at the values of 7 ns and 1.6 μs for the fast and slow components respectively, while the singlet to triplet ratio is obtained from the model described in [146]. The values of the ratio as a function of the deposited energy are shown in Fig. 5.13, for both electron and nuclear recoils. In the range of energy deposition in GRAIN, the ratio is about 0.25 for the electron recoil and about 0.7 for the nuclear recoil[146].

5.3.2 Photon propagation

The propagation of the photons can be affected by both the Rayleigh scattering and the absorption by impurities, as described in section 4.1.1. They are implemented in the simulation with a constant characteristic length. The scattering length

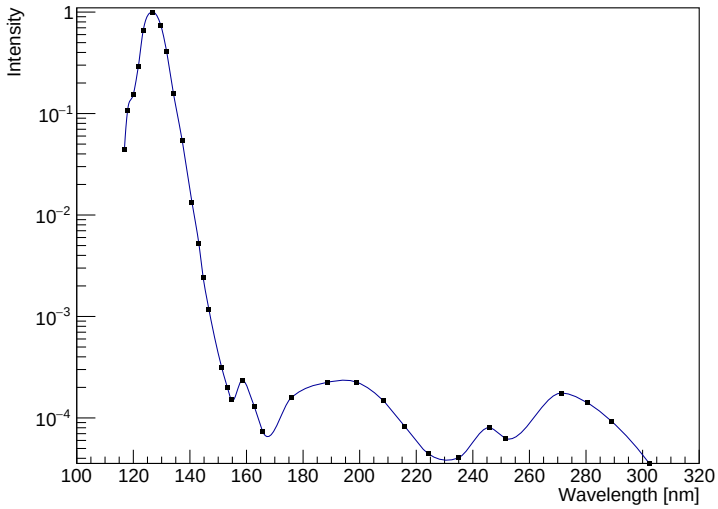

Figure 5.12: Wavelength spectrum of the scintillation photons emitted by the liquid argon as obtained from the simulation. The distribution is readapted from the results shown in Fig 4.2.

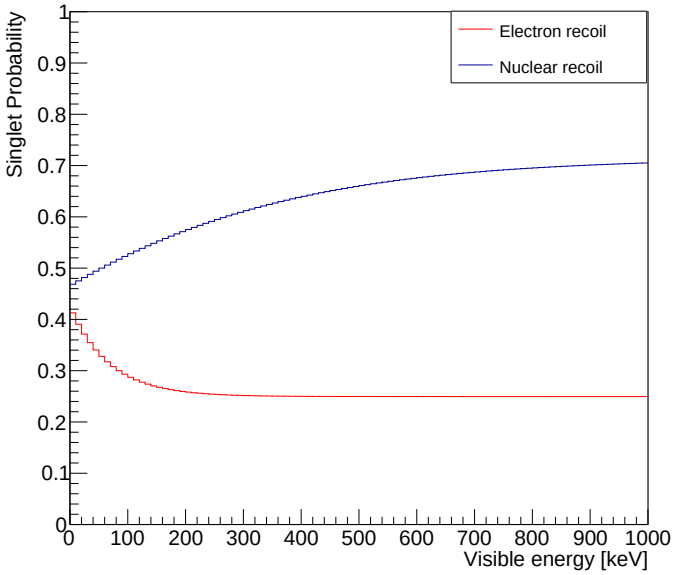

Figure 5.13: Singlet to triplet ratio as a function of the visible energy in case of electron recoil (red) and nuclear recoil (blue) as implemented in the simulation. The values are extracted from the results shown in [146].

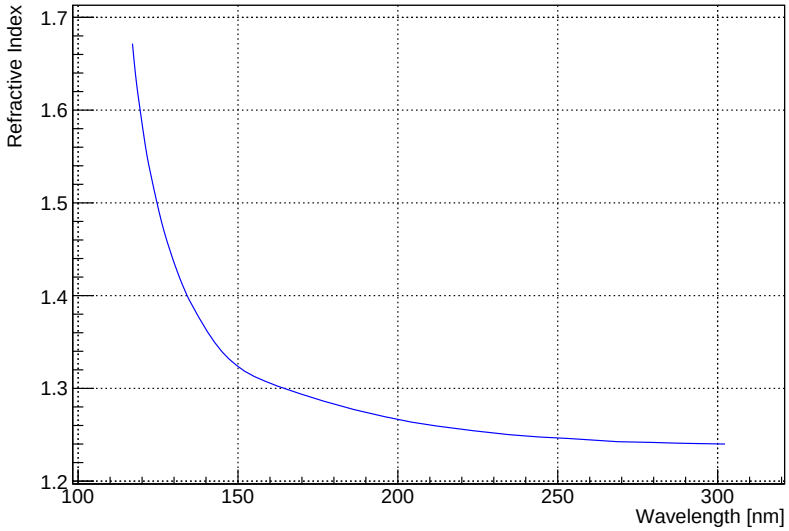

Figure 5.14: Simulated liquid argon refractive index as a function of the wavelength. Values extracted from [124].

(λ_{RS}) is set to a value of 90 cm, in the range of the values reported in Table 4.3. The absorption length (λ_{Abs}) is set to a value of 5 m. This value is slightly higher than the pure argon's values reported in Table 4.4 but, as seen in Chapter 4, the absorption length increases for very pure argon or in case of specific argon impurities (such as Xenon). Moreover, the reduction of collected light due to shorter absorption lengths could be added in following simulation steps, allowing to evaluate the effects of different lengths with one optical simulation.

The refractive index is implemented from the results obtained in [124]. The refractive index is crucial for the correct functioning of the lens-based cameras and is implemented in the range 120-300 nm (Fig. 5.14).

Optical photons could also be absorbed and reflected by the surfaces inside the inner vessel. Geant4 provides different models to simulate the behaviour of optical photons interacting with surfaces. For this analysis, the Geant4 *glisur* model with the *dielectric_dielectric* type is chosen for the simulation. This model allows to specify the details of the surface finish and the reflector coating, defining reflectivity and absorption of the surface. The *polished* finish of the surface is chosen. This finish simply applies the Snell's Law to compute the reflection angle using the refractive index, and it determines whether or not the photons are absorbed based on the reflectivity previously set. However, since the reconstruction in GRAIN is based on the imaging, the reflection of the materials inside the inner vessel must be reduced to the minimum to avoid detecting photons not coming from the source.

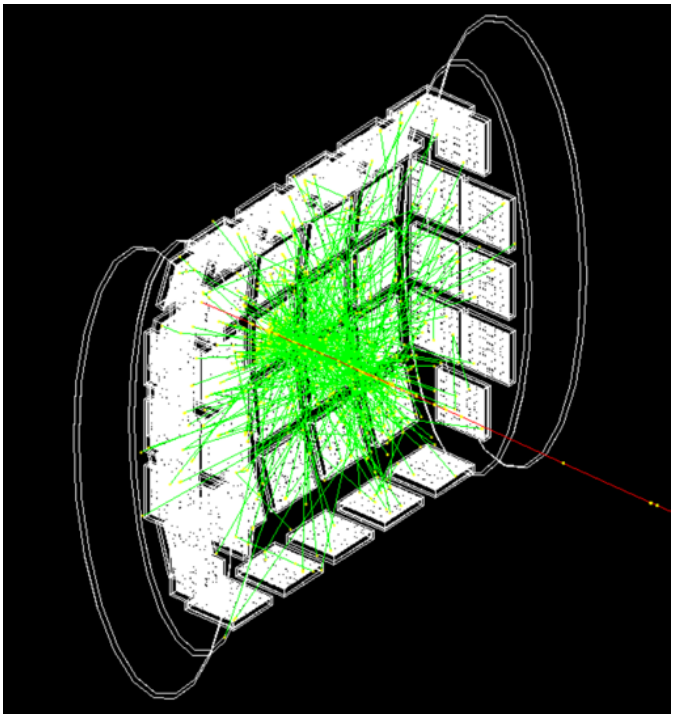

Figure 5.15: Event display of a muon (red line) crossing the GRAIN geometry. The optical photons are shown in green. The argon light yield was greatly reduced for the sake of visualization.

The surface reflection, still being simulated, is set to 0%, with 100% absorption probability. A display of a muon crossing the GRAIN geometry with emitted and propagated scintillation photons is shown in Fig. 5.15, where the muon is propagated along the beam axis and the total light yield is reduced to allow a cleaner visualization of the photons.

5.3.3 Photon collection

As described in Sec. 5.1.2, each camera in the GRAIN geometry includes a sensor volume. This volume is set as a sensitive detector in the simulation in order to collect information of each optical photon impinging on its surface. These information are the output of the simulation and are later used to simulate the detector response and the electronic. At this level, the sensors have 100% efficiency and no fine structure is simulated. This allows to simulate different sensor and electronic properties at a next step without re-running the optical simulation. The most crucial information collected by the sensors are:

- detection position on the sensor: it is the xy local coordinate of the photon

interaction point on the sensor. It is later used to compute on which pixel the photon was collected.

- detection time: it is the time of the photon collection on the sensor, with time equal to zero corresponding to the neutrino interaction vertex time.
- energy of the photon: it is later used to simulate the quantum efficiency of the sensors.

5.4 Detector response and electronic simulation

The last simulation phase, after the emission, propagation and collection of the scintillation photons, concerns the detector response. As the optical readout of GRAIN is based on SiPMs matrices (Sec. 3.2.4), the first step assigns each detected photon to the correct pixel of the matrix. The simulation then computes the number of detected photons taking into account the quantum efficiency of the simulated SiPMs, their afterpulses, dark current rate, and crosstalk. A full waveform for each photon is simulated and the final total number of photons detected on each pixel is obtained with a time over threshold measurement (Fig. 5.16, left). This procedure includes the timing information provided by the optical simulation and, for a large number of detected photons close to each other, it correctly simulates the saturation of the signals (Fig 5.16, right). This setup allows to simulate several configurations of SiPMs matrices and electronics from one single optical simulation. Differently from the size of the pixels, which is strongly related to the size of the sensor geometry in the optical simulation, the parameters describing the SiPMs noises and the electronics are kept constant, following the properties of the electonic chip under study in GRAIN [147]. In the future, with a larger number of chips available, more electonics will be simulated. The typical values of the most relevant SiPM properties, used as baseline for all the following analysis, are reported in table 5.3. More detailed information about the detector response and electronic simulation can be found in [148].

Alternatively to the full detector and electronic response just described, a simpler and faster simulation is available. This version performs the pixelization of the sensors, simulates the effect of the quantum efficiency, and includes only the crosstalk as a multiplier to the total number of detected photons. The other SiPMs noises and the waveform simulation are not included. In the following, the two detector response simulations will be referred to as *full* and *fast*.

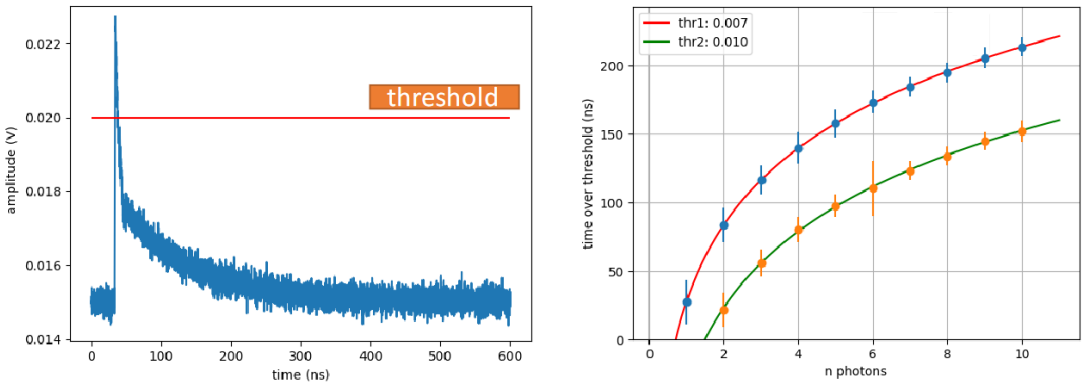

Figure 5.16: Left: example of a simulated waveform of one detected photon, with the threshold used to perform the time over threshold measurement. Right: Time over threshold measurements as a function of the number of detected photons with coincident detection times for different threshold levels.

Rise time	0.8 ns
Fall time	1.0 ns (fast) 80 ns (slow)
QE	25%
DCR	0.1 Hz/mmˆ2
Crosstalk	7%
Afterpulses	30%

Table 5.3: SiPM parameters used in the simulation of the detector response.

Chapter 6

Imaging capabilities of GRAIN

In Chapter 3, the reasons behind the need for a liquid argon target in SAND were detailed. A LAr target at the near detector complex would enable a study of the neutrino interaction topologies and cross sections which would be complementary to the measurements at the far detector, thus allowing to better constrain the systematics. In this context, GRAIN will reconstruct particle tracks exploiting the scintillation light emitted by argon and detected by multiple optical cameras, able to collect the emitted light and reconstruct the image of the source. The current design of GRAIN implies track-optical system distances up to about one meter, making necessary both a wide field of view and a large depth of field, to allow the focusing of the higher possible number of tracks. On top of this, because of the use of liquid argon, the system must be maintained at cryogenic temperature, making it even more difficult to achieve the above conditions.

To comply with these requirements, a technique already known in the X- and gamma-ray astronomy but never examined for particle physics applications, the Coded Aperture technique, is currently being studied. This technique should provide a much larger Field of View (FOV) and Depth of Field (DOF) compared to traditional optical systems, while also having a high throughput. Exploiting an optical-sensor system based on this technique, it would be possible to take a 2D picture of the tracks produced by neutrino interactions in argon. Combining multiple systems arranged in a stereo view, one could then be able to perform a complete 3D reconstruction of the event. Section 6.1 presents the idea behind this technique, detailing its working principles. Section 6.2 describes the results obtained with a simple prototype based on this technique, while Sec. 6.3 describes some results of a possible application of Coded Aperture cameras in GRAIN. Lastly, Sec. 6.4 shows an alternative reconstruction technique based on the same optical systems.

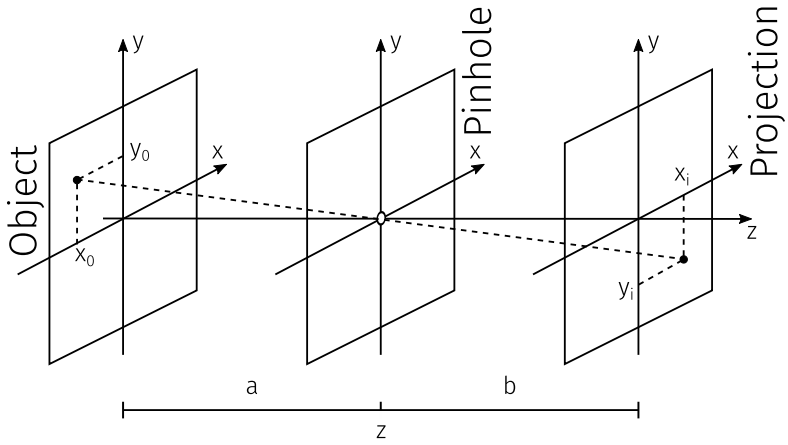

Figure 6.1: Scheme of a pinhole camera.

6.1 Coded Aperture Imaging

The Coded Aperture concept was first introduced as an imaging technique in the X- and gamma-ray astronomy in the late '70s[149][150][151]. The working principle was to expand the simpler design of a pinhole camera to overcome some of its main limitations, such as the need of long exposure time. This is done replacing the single pinhole with a pattern of holes arranged according to specific designs.

Before introducing the working principle of this technique, it is useful to start with the description of the single pinhole camera.

6.1.1 Pinhole camera

Pinhole cameras are a simple imaging device composed by a slab of opaque material with a small hole on it, and a photon sensor behind it. Ideally, with a dimensionless hole, the photons emitted from a light source in front of the opaque slab will pass through the hole along a straigth line. Each point recorded on the detector surface will then represent a point of the light source, with a 1-1 correspondence (Fig. 6.1), and the reconstructed image on the sensor will be an inverted picture of the source. In an ideal pinhole camera the response on a specific position $R(x_i, y_i)$ must then be generated by a single source point in a position (x_0, y_0), and must be proportional to its irradiance:

$$R(x_i.y_i) \propto O(x_0, y_0) \tag{6.1}$$

An ideal pinhole camera, i.e. a dimensionless pinhole coupled with an ideal detector, should provide a perfect reconstruction of the image as two point sources will always be separated on the detector. This is not true for real pinholes, for which the hole have a finite dimension w_m and a source point is represented by an

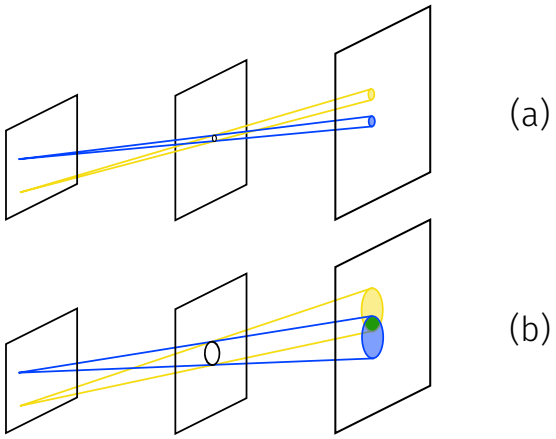

Figure 6.2: Degradation of the resolution of a pinhole camera due to the finite size of the hole. In case of infinitesimal hole (a), two point sources are projected as two, flipped, points on the detector. Finite size of the hole (b) causes the points to be projected as circles.

extended image of size:

$$w_d = \frac{a+b}{a} w_m = (1 + m_p) w_m \tag{6.2}$$

where a and b are the source-pinhole and pinhole-sensor distances respectively, and m_p is the magnification factor of the camera (Fig. 6.2). Defining the resolution as the minimum distance between two point sources such that their projections on the detector plane are separated, one obtains:

$$l \geq \frac{a}{b} w_d = \left(1 + \frac{1}{m_p}\right) w_m \tag{6.3}$$

where small values of l indicate a good resolution. From Eq.6.3 one can see how the resolution of the pinhole camera is directly limited by the size of the hole and how ideal pinholes have a perfect resolution. As a dimensionless pinhole would imply a null photon flux through the opaque slab, real pinholes must compromise between high resolution and high photon detection. This is one of the main limitations that lead to the formulation of the Coded Aperture technique: the need of a high resolution - as the one obtained with small pinholes - while maintaining a high light signal[152].

6.1.2 Coded Aperture technique

The fundamental idea of a Coded Aperture camera is to replace the single hole of a pinhole camera with a large number of smaller holes. Doing so, one can obtain

the same resolution expected by pinholes with similar hole size while maintaining a high light throughput. The holes, arranged following specific patterns, compose a so-called mask.

Detector response and image reconstruction in Coded Aperture cameras

In a Coded Aperture camera, the response of the detector at a position (x_i, y_i) generated by a source in a point (x_0, y_0) must be proportional to the irradiance $O(x_0, y_0)$ modulated by the transmission of the mask $A(x, y)$:

$$R(x_i, y_i) \propto O(x_0, y_0)A(x, y) \tag{6.4}$$

The mask is thus encoding the signal from the source due the superposition of the many shifted copies of the image produced by the holes and projected on the detector. A decoding process is thus needed to obtain the starting image. This can be performed through the correlation of the detector response with an appropriate decoding function[150]:

$$\bar{O} = R \otimes G = O * (A \otimes G) \tag{6.5}$$

where $\otimes$ indicates the correlation operator and G is a decoding array, usually referred to as *kernel*. The choice of both mask and kernel is thus crucial to correctly reconstruct the source image. Choosing a G such that:

$$A \otimes G = \delta \tag{6.6}$$

Eq. 6.5 can be reduced to:

$$\bar{O} = O * \delta = O \tag{6.7}$$

and the system has perfect image properties, as the reconstructed image corresponds to the source one. Adding a noise term to the detector response, the equations just described still hold, and the choice of the (A, G) pair does not change:

$$R \propto O * A + N \tag{6.8}$$

$$\bar{O} = O + \delta = O + N \otimes G. \tag{6.9}$$

Many possible (A, G) pairs exist, and their design and geometrical arrangement strongly affect the performance of the Coded Aperture camera.

Geometry Arrangements, Field of View and Resolution

Geometrical properties of mask and sensor directly affect the reconstruction capability of the camera. However, independently from the properties and the possible

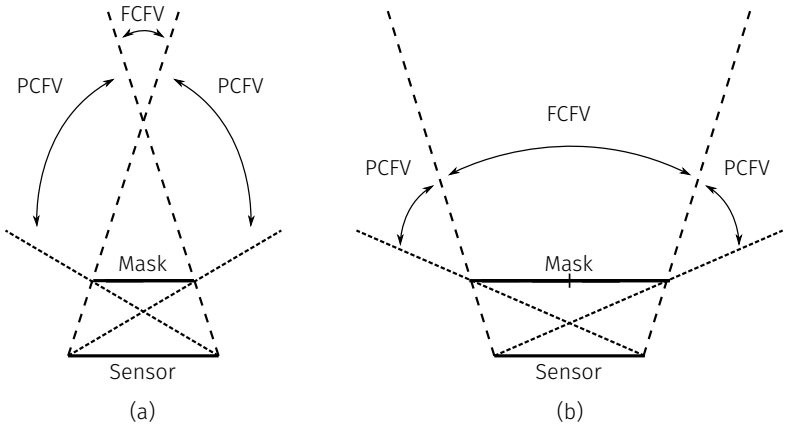

Figure 6.3: Scheme of the FCFV and PCFV for a camera with a single mask (left) and for one with a mask composed by a 2×2 mosaic (right).

arrangements, two regions of the Field of View of the camera can be defined: the Fully-Coded Field of View (FCFV), defined as the region for which a light source projects a complete shadow of the mask on the sensor, and a Partially-Coded Field of View (PCFV), for which only partial shadows are projected by the sources in this region. Both regions are shown in Fig. 6.3. To keep the condition in Eq. 6.6 valid, the full mask shadow should be projected on the sensor. The most simple mask-sensor arrangement, for which the two components have the same size, has then strong limitations, as only a source at infinite distance and on-axis with the camera will project the full mask's shadow. Increasing the size of the sensor is a possible solution to this problem, at the price of a much more expensive detector. A common alternative is then to increase the size of the mask, keeping constant the size of the sensor. This is done replicating the mask in a periodic pattern, so that a complete mask shadow is projected on the sensor, with a shift given by the periodicity of the mask pattern. A common configuration is composed by 4 masks arranged in a 2×2 mosaic, with different 2x2 mosaic configurations possible. On top of a larger FCFV, the mosaic configuration also provides an increased total Field of View of the camera compared to the single mask arrangement. This is also strictly related to the resolution of the system and to the parameters of the detector. Defining the magnification of the mask as:

$$m = 1 + \frac{a}{b} \tag{6.10}$$

one can write[152]:

$$FoV = \frac{d_d}{m-1} \tag{6.11}$$

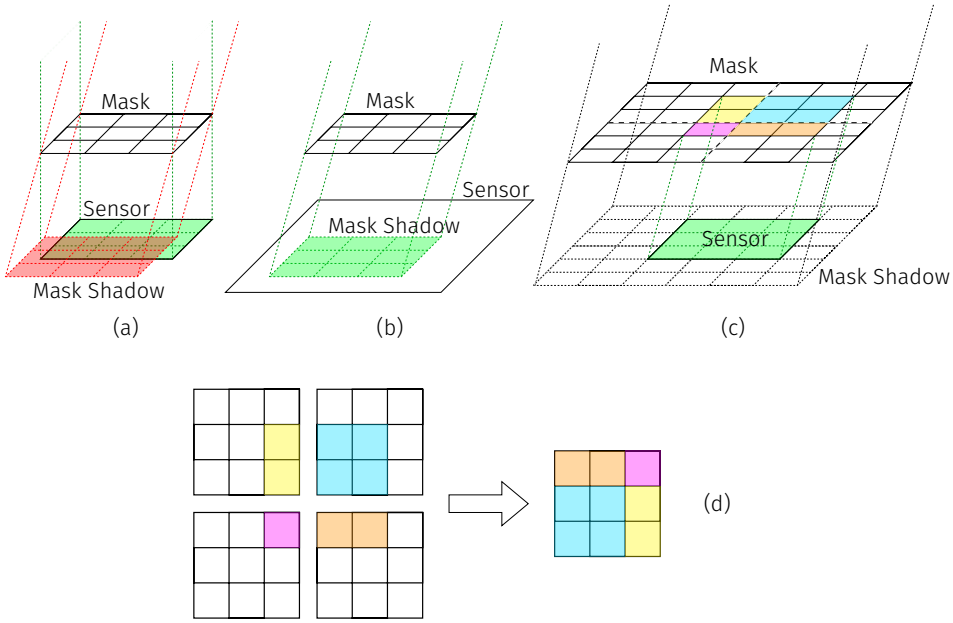

Figure 6.4: Comparison of three different coded camera arrangements. (a) Mask and detector have the same size and only the sources on the optical axis project the full mask shadow on the sensor. (b) The sensor is larger than the mask, allowing more sources to project the full mask shadow on the sensor. (c) The mask is composed by a 2×2 mosaic of the mask in (a) and (b) while the sensor has the same dimension of the one used in a). In this configuration only a part of the mask is projected on the sensor. (d) The combination of the projected parts on the sensor of the mask in (c) is the full shadow of one of the mask composing the mosaic.

with d_d being the lateral dimension of the sensor. Extending the definition of resolution of a pinhole camera, for a Coded Aperture camera it is found to be:

$$\lambda = \frac{m}{m-1} p_m \tag{6.12}$$

where p_m is the size of a single mask's hole (mask pitch). Combining Eq. 6.11 and 6.12, a relation between the FoV and the resolution can be obtained as:

$$\frac{FoV}{\lambda} = \frac{d_d}{m p_m} \tag{6.13}$$

which can be rewritten as:

$$\lambda = p_m \left(1 + \frac{FoV}{d_d}\right) \tag{6.14}$$

and implies that larger detectors, for a given FoV, provide better resolutions.

Depth of field and artifacts

Coded aperture cameras do not focus the light as more traditional optical systems, such as lenses do. Because of this, the idea of depth of field, the distance range at which objects can be focused, does not directly apply. Theoretically then, a coded camera should be able to focus images at every distance from the sensor. This is not true, as an effect similar to the defocusing seen typically in lenses is also present for the coded cameras, despite its source being different. In a coded camera, the sharpness of an image is determined by the sampling artifacts, emerging when the shadow of one mask element is projected on a non-integer number of pixels of the sensor[153]. This number can be defined as:

$$\alpha = \frac{m p_m}{p_d} = \frac{(1 + \frac{b}{a} p_m)}{p_d} \tag{6.15}$$

Light sources at distances a for which α is an integer number are then focused, with αs greater than one identifying increasing in-focus magnifications. From Eq. 6.15 it is possible to obtain the variation of α for different source-mask distances as:

$$\frac{d\alpha}{da} = -\frac{p_m b}{p_d a^2} \tag{6.16}$$

which shows how the coded cameras should provide an increasing Depth of Field at large distances from the cameras. This effect is known as sampling artifact and Fig. 6.5 shows an example of its effect when reconstructing a point source.

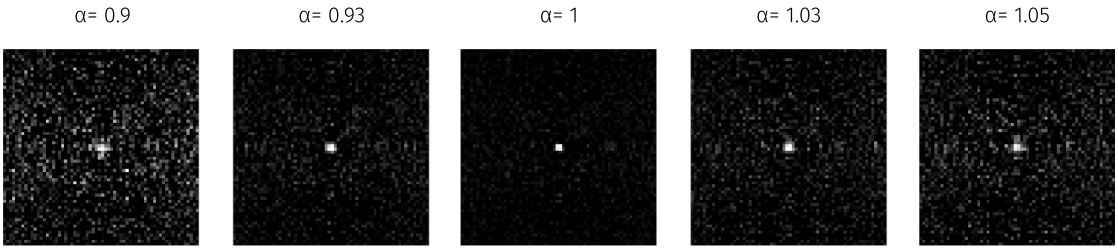

Figure 6.5: Effect of the defocusing due to the sampling artifact for a point-like light source[154].

6.1.3 MURA masks

As anticipated in Sec. 6.1.2, multiple families of masks able to satisfy the condition 6.6 exist. To quantify the ability of an (A, G) combination to reconstruct a δ function, and therefore its ability to accurately reconstruct a source, it is possible to exploit the point spread function (PSF). This is defined as the reconstruction of a perfectly centered point source at infinite distance and can be obtained as:

$$PSF = A * G \tag{6.17}$$

and should be as close as possible to a δ function.

One of the masks' designs currently considered for the GRAIN optical readout is based on the Modified Uniformly Redundant Array (MURA)[151] family. These were introduced as a modification of the Uniformly Redundant Array[150], a category of masks where the number of pairs of holes with a given separation in the pattern is the same for all possible separations. An URA mask can be defined as a binary matrix of 1s (holes) and 0s (opaque elements) generated as follow:

$$\begin{aligned} A_{i,j} = 0 \text{ if } i = 0 \\ 1 \text{ if } j = 0, i \neq 0 \\ 1 \text{ if } C_i^r C_j^s = +1 \\ 0 \text{ otherwise} \end{aligned} \tag{6.18}$$

with

$$\begin{aligned} C_i^r = +1 \text{ if } i \text{ is a quadratic residue modulo r} \\ -1 \text{ otherwise} \end{aligned} \tag{6.19}$$

with r and s being prime numbers separated by 2. For an URA mask, the kernel is defined as the mask itself. The generation of a MURA mask follow the same algorithm defined in Eq. 6.18, but a slight change in the decoding function allows to generate squared masks with any prime number p (rank), providing a much

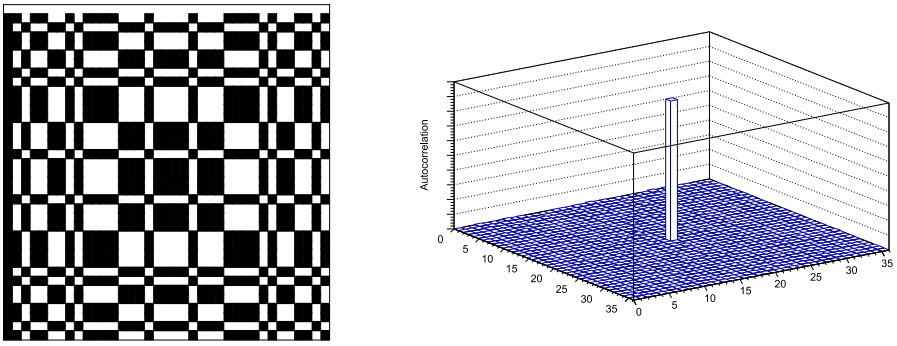

Figure 6.6: Left: MURA patter$p = 37$. Black elements indicate holes, while white elements indicate opaque regions. Right: autocorrelation of a rank 37 MURA mask.

higher flexibility in the design phase. The decoding pattern of a MURA mask can thus be defined as[151]:

$$\begin{aligned} G_{ij} = 1 \text{ if } i + j = 0 \\ 1 \text{ if } A_{i,j} = 1,\ i + j \neq 0 \\ -1 \text{ if } A_{i,j} = 0,\ i + j \neq 0. \end{aligned} \tag{6.20}$$

Figure 6.6 shows the pattern of a MURA mask of rank 37, together with its autocorrelation, and it is visible how the PSF of a MURA is close to a δ function, with a sharp peak and almost no noise around it. Another important property which should be taken into account is the mask throughput. Low values imply a reduced light collection, while in cases of high values the number of shadowed regions on the detector for a given source will be too small. The measurement of the background against which the source signal will be evaluated will then be statistically poor, degrading the S/N of the reconstructed image. For a MURA mask, the fraction of open elements (holes) compared to the total element number is defined by construction as:

$$N_{open} = \frac{p^2 - 1}{2} = \frac{N_{total} - 1}{2} \simeq 50\% \tag{6.21}$$

where p is again the rank of the mask, i.e. the prime number used to generate the mask in Eq. 6.18.

As discussed previously, periodic mosaic patterns are the most practical solution to increase the field of view and, most importantly, the FCFV of a Coded Aperture camera. With MURA masks, multiple mosaic arrangements exist[150][153]. In the following, two different 2×2 mosaic design will be studied. These will be referred to as odd and even mosaic, as defined by the final rank of the mosaic,

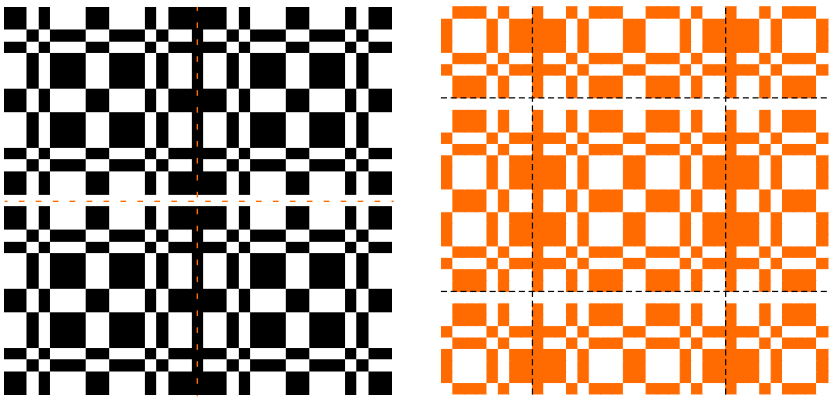

Figure 6.7: $2p-1$ odd (left) and $2p$ even (right) mosaics obtained starting from a MURA mask of rank 17. The single masks are highlighted by dotted lines in both configurations.

being $2p-1$ and $2p$ respectively. The $2p-1$ odd mosaic is obtained rotating the masks so that the (0, 0) element of each mask is located at the center of the mosaic. The two most central rows and columns are then merged in one, leaving a single column of holes and a single row of opaque elements. The final rank of the mosaic is then $2p-1$, where p is the rank of the single original mask. The $2p$ even pattern is instead obtained with a cycling permutation of both rows and column of the four masks. This operation generates a mosaic with a complete mask in the center of the pattern, with the other three spread in the remaining sectors. Both patterns for a base mask of rank 17 are shown in Fig. 6.7.

6.2 Coded Aperture demonstrator

To verify the feasibility of the Coded Aperture technique, a simple prototype was built exploiting a small SiPM matrix and two light sources obtained with a led. A simple simulation was performed to study the expected results of the prototype apparatus. The prototype exploited a SiPM matrix with a smaller rank and a smaller SiPM's dimension (pitch) than the ones which will be used in GRAIN, and was not tested at cryogenic temperatures. Its main objective was to verify the capability to read-out all the channels of the sensor at the same time, and to verify whether or not it was possible to reconstruct simple light sources with the use of a Coded Aperture camera.

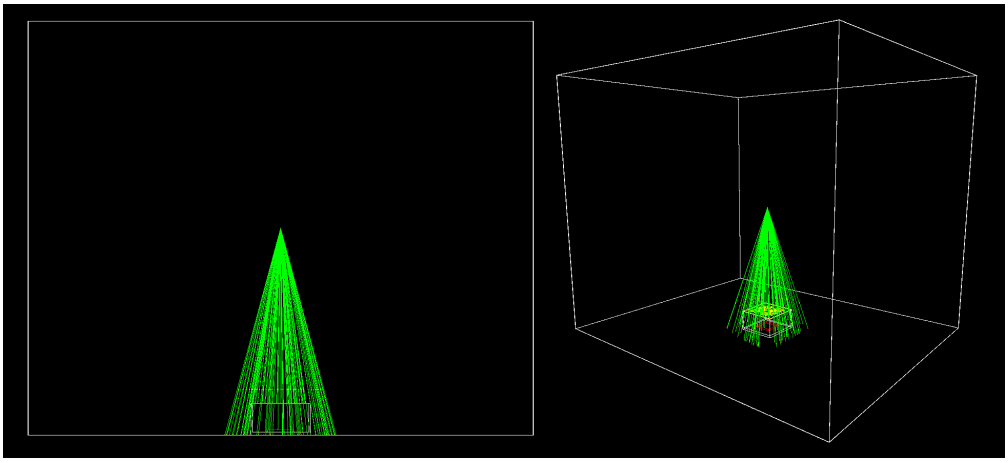

Figure 6.8: 2D (left) and 3D (right) views of the geometry used to simulate the prototype with a single light source on.

Mask rank	7
Mask pitch	1.2 mm
Mask thickness	100 μm
Mosaic configuration	2x2 odd
SiPM matrix size	8x8
SiPM pitch	1.2 mm

Table 6.1: Main parameters of mask and SiPM matrix used in the Coded Aperture prototype.

6.2.1 Prototype simulation

The Geant4 simulation developed to study the prototype differs from the general simulation described in Chap. 5, as both the propagation medium and light sources are different. Figure 6.8 shows a simple sketch of the geometry of the simulation. The leds were implemented as simple light spot, emitting photons at 403 nm. The camera geometry was implemented as described in Sec. 5.1.2, where the prototype mask and sensor parameters are reported in Table 6.1.

Using leds as light sources, it was not necessary to set a specific number of emitted photons, as it was possible to just increase the exposure time of the measurement when collecting data with the prototype. It was thus set to O(1M) emitted photons for each led. Similarly, the PDE of the SiPMs, and its intrinsic noises (crosstalk, afterpulses) were not included in the simulation. The reconstruc-

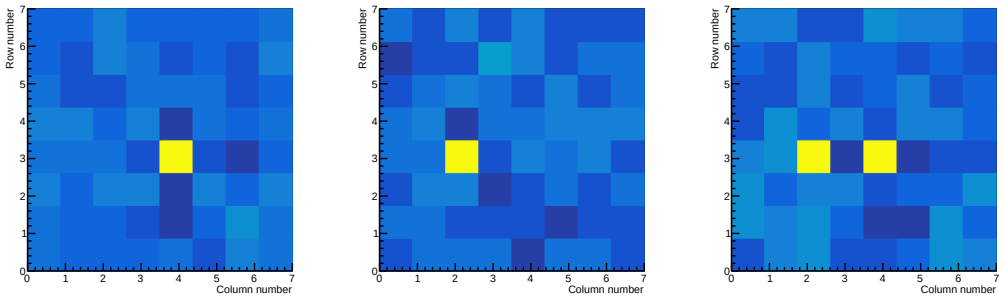

Figure 6.9: Results obtained from the prototype simulation. The first two images show the reconstruction of a single light source, while the last one is obtained with both sources turned on.

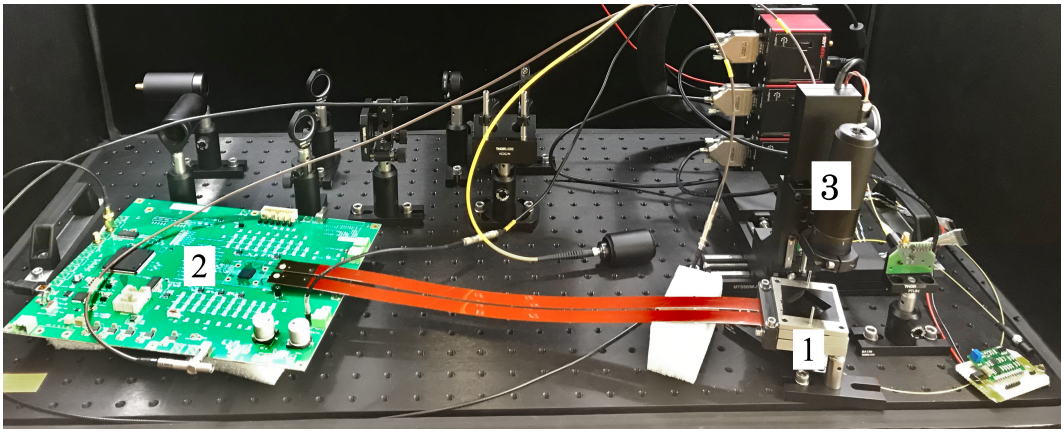

Figure 6.10: Picture of the experimental setup. Its main components are a Coded Aperture camera (1), an ASIC able to read each matrix channel individually (2), and a led light mounted on a 3-axis motor (3).

tion of the image was then performed with the deconvolution of the recorded signal exploiting a MURA decoding kernel as described in Sec. 6.1.2. Figure 6.9 shows the results of the simulation with one led on at a time and with both leds on at the same time, where the position of the light source is clearly reconstructed in all cases.

6.2.2 Experimental setup

The experimental apparatus was built inside a black box to avoid collecting light from external sources. A picture of the setup is visible in Fig. 6.10, and its main components are detailed in the following:

- SiPM matrix - an Hamamatsu S13615-1050N-08[155] SiPM matrix was used

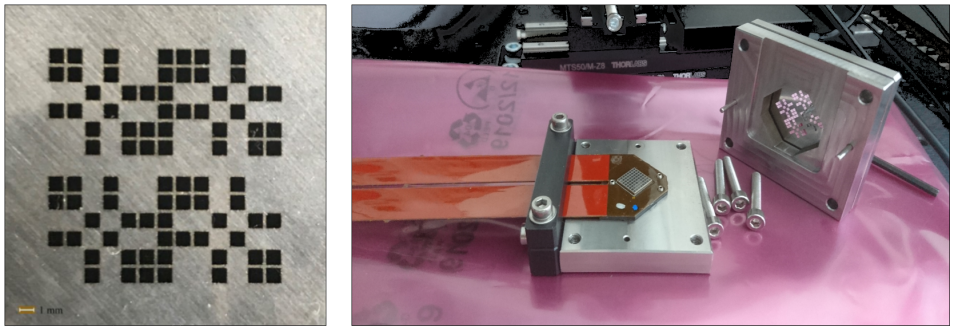

Figure 6.11: Left: details of the MURA mask obtained with the laser cut technique on a 100 μm metal slab. Right: SiPM matrix and mask mounted on the mechanical support used to keep the mask at a fixed distance from the sensor.

as sensor of the optical camera. The pitch of the matrix is 1.2 mm, with an active area of each SiPM of $1 \times 1\text{mm}^2$. The SiPM's cell have side of 50 μm and a breakdown voltage of about 53 V.

- Mask - the design of the mask is based on the MURA family. It was obtained from a metal slab 100 μm thick with the laser cut technique. To avoid reflections, the mask was painted with black paint. The mask was mounted on a mechanical support with the possibility to vary the distance between the mask and the SiPM matrix6.11.

- ASIC - the data acquisition board was a Triroc 1A [156], an ASIC specifically produced by Weeroc to read all the 64 channels of the SiPM matrix. The board is able to perform both timing and charge measurements, with a dynamic range of up to 3000 photo-electrons with a non linearity of 1% up to 2000 p.e., and a timing resolution RMS of 88 ps.

- Light source - a 405 nm laser was coupled to an optical fiber, whose endcap was used as a point source of light. The fiber was located on top of the mask and was connected to a motor able to move on three axis. This allowed to set the light source at different distances from the mask, and was used to perform gain measurements for each SiPM individually. The light sources used to actually perform the image reconstruction were composed by a led attached to the side of an optical fiber. Both ends of the fiber were then bended to point at the mask and were used as light sources, one at a time or together.

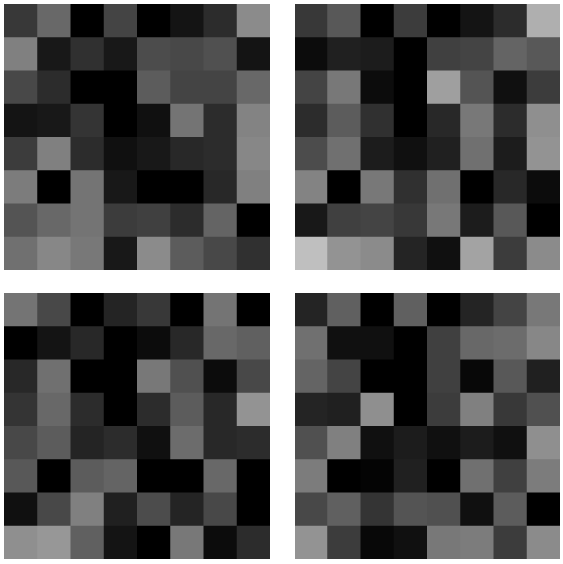

Figure 6.12: Example of raw images obtained from the data acquisitions. Each pixel of one image represents the number of detected photons, with whiter colors corresponding to a larger number of detected photons.

6.2.3 Measurements and reconstruction

To correctly measure the light detected by each SiPM, the mapping of the channels was performed exploiting the laser to probe each channel individually and compute both the SiPM gain and baseline. Multiple measurements were then performed with the LED light coupled to the optical fiber in order to study the optical system's capability to reconstruct the light source. For each acquisition, the number of detected photons on each channel was computed as

$$N_{ph} = \frac{\text{ADC counts - Baseline}}{\text{SiPM gain}} \tag{6.22}$$

The light impulses from the led were synchronized with the Triroc acquisition. For each impulse, an 8×8 image was produced, with the intensity of each pixel given by the converted number of detected photons in the corresponding SiPM of the matrix. Figure 6.12 shows some examples of the acquisitions. As expected by a coded camera, the recorded image does not resemble the source image, but is composed of a pattern of light and shadow areas generated by the projection of the mask elements.

From the different images obtained during the acquisition, the light sources have been reconstructed by means of the deconvolution technique, as described in the previous simulation step. The deconvolution is usually applied using a kernel and detector response with equal rank. This is not the case in the prototype, as

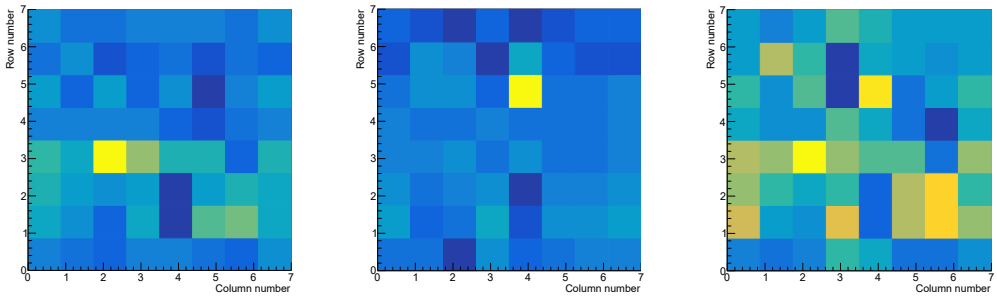

Figure 6.13: Reconstructed images of the light source. The first two images show the results obtained with one end of the fiber exposed, while the last image shows the result with both light sources. The reconstructed image of both sources shows an increased amount of artifacts, probably related to misalignment of the mask or intrinsic artifact of the Coded Aperture imaging.

the sensor is composed of an 8×8 SiPM matrix, while the MURA mask has rank 7, since the generation algorithm requires a prime number as mask rank. The reconstruction is thus performed excluding the first row and the first column of the SiPM matrix. Figure 6.13 shows the results with just one end of the fiber used as a light source, as well as having both of them turned on in the same acquisition. It is visible how the light sources were correctly reconstructed in all cases. However, compared to the simulation results, a greater number of artifacts is present, especially in the reconstruction of the two sources. This is expected as the simulation did not include any SiPM intrinsic noise, such as crosstalk and dark pulses. Moreover, mask-sensor rotation or misalignment could affect the reconstruction quality. Despite the increased number of artifacts, the results were promising, as it was proven how the Coded Aperture technique is able to reconstruct simple sources at close distances from the mask. To be able to reconstruct tracks in GRAIN, however, a much larger SiPM matrix will be needed, in order to provide a better spatial resolution and to collect more light.

6.3 Coded aperture in GRAIN

To reconstruct 3D events in GRAIN, multiple 2D images should be obtained from optical cameras arranged in a stereo view. In this context, the 2D deconvolution of images from each camera is the first step of an analytic 3D reconstruction algorithm, able to combine the decoded images to obtain a 3D view of the events.

To study the capability of Coded Aperture cameras in reconstructing particle tracks, a simulation of a setup representative of GRAIN was developed. A simplified geometry was used, with two optical cameras placed one in front of

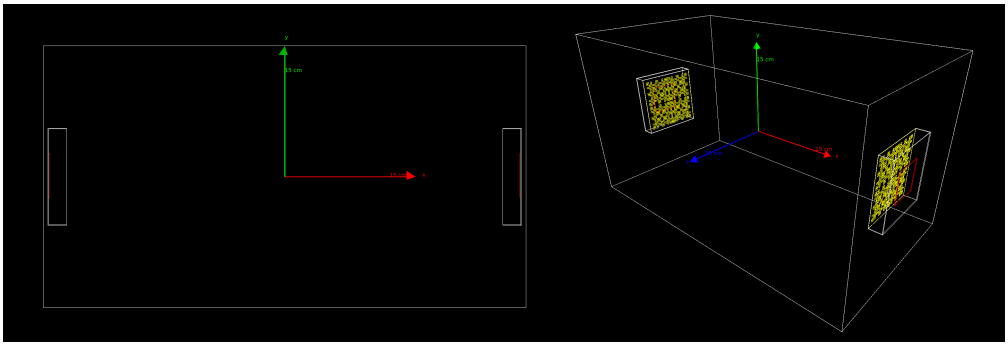

Figure 6.14: 2D (left) and 3D (right) views of the geometry used to test the Coded Aperture imaging in a GRAIN-like environment. Both cameras have an odd mosaic and are optimized to have $\alpha = 1$ in the middle of the volume, 25 cm from both masks.

Mask rank	17
Mask pitch	3.2 mm
Mask hole	2.96 mm
Mask thickness	100 μm
SiPM matrix size	16x16
SiPM pitch	3.2 mm
Mask-sensor distance	20 mm

Table 6.2: Main parameters of mask and SiPM matrix used in the simulation of GRAIN-like coded cameras.

the other, at a distance of 50 cm. The argon volume was simulated as a box of $55 \times 30 \times 30$ cm^3. Light emission, propagation, and collection, as well as the response of the electronics were performed with the standard simulation framework described in Chapter 5. The GRAIN-like coded camera parameters are reported in Table 6.2. Two different mosaics were tested in order to compare their performances: a $2 \times 2 - odd$ and a $2 \times 2 - even$, all the other parameters are fixed. Figure 6.14 shows an example of the geometry with $2 \times 2 - odd$ mosaic cameras. In this configuration, the source-mask distance for which $\alpha = 1$ is 25 cm, at equal distance from both masks.

The rank of the sensor is constrained by hardware limitations to 16, i.e. to a 16×16 SiPM matrix. The mask rank is constrained to the prime number closest to the sensor rank, i.e. 17. The single mask is thus generated with rank 17, with the two mosaics having rank 33 and 34 for the odd and even configuration respectively.

As mask and sensor ranks differ, the deconvolution technique can't be applied as it is defined in Eq. 6.5, similarly to the prototype reconstruction case. In this case, differently from the prototype, the rank of the sensor is smaller than the mask one. The missing pixels should then be added to the detector response in order to correctly reconstruct the images. This was done at software level, setting the missing amplitudes to different values. Three different sets of values were used to fill the missing pixels:

- all missing pixels set to 0;
- all missing pixels set to the mean value of detected photons of the whole sensor;
- each missing pixel set to the mean value of the closest pixels.

The results were obtained simulating muons crossing the argon volume at 45 degrees and with energy extracted from a Gaussian distribution of mean 3 GeV and sigma of $\sqrt{3}$ GeV. The argon light yield was set to be 10 times larger than the nominal one, in order to disentangle the effect of the missing pixels from the one of low light production, discussed later in this section. Figure 6.15 shows an example of the same track reconstructed with both mosaic types and with the missing pixel amplitude set to the different values just described. Several considerations can be made by looking at Fig. 6.15: first, both the even and the odd mosaics have a large artifact along one full row and column of the reconstructed image when filling the missing pixels with zeros. This is clearly visible in the even mosaic reconstruction, where the artifact is shifted near the center of the image. For both mosaic configurations, the two remaining filling procedures resulted in similar reconstructed images, with negligible differences between the two options. Comparing the results between the two mosaic configurations, larger differences are visible, with the even mosaic providing a larger contrast in the reconstructed image. On top of this, the odd mosaic shows a much larger number of artifacts, which generate fake tracks along the same direction of the true track. These artifacts, while still visible, are suppressed when using the even mosaic. These results suggested that the best solution to cope with a sensor smaller than the mask is to fill the missing pixels with either the mean or the local mean value, and that the even mosaic performs slightly better than the odd one.

The same simulation was performed with a standard argon light yield, to test the performance of the reconstruction in a more realistic GRAIN-like environment. The performances were evaluated again for diagonal muons crossing the argon volume, and with the missing pixels filled with the mean amplitude of the whole sensor. The results are shown in Fig. 6.16 for both mosaic configurations and for the two cameras in the geometry. It is clearly visible how the reconstruction

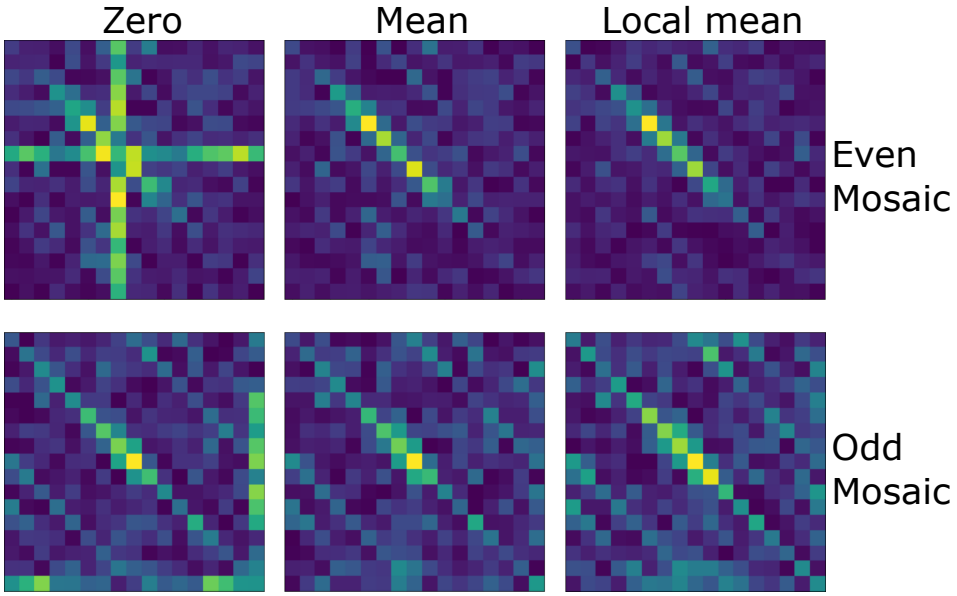

Figure 6.15: 2D track reconstructions for a muon crossing the argon volume diagonally and with both the odd (bottom) and even (top) mosaics. The 16×16 sensors matrix was extended to a 17×17 at software level, filling the missing pixel with 0s (first column), the mean value of the sensor (central column), and the local mean of pixels near the one to be filled (right column). The results were obtained with an argon light yield 10 times higher than the standard one.

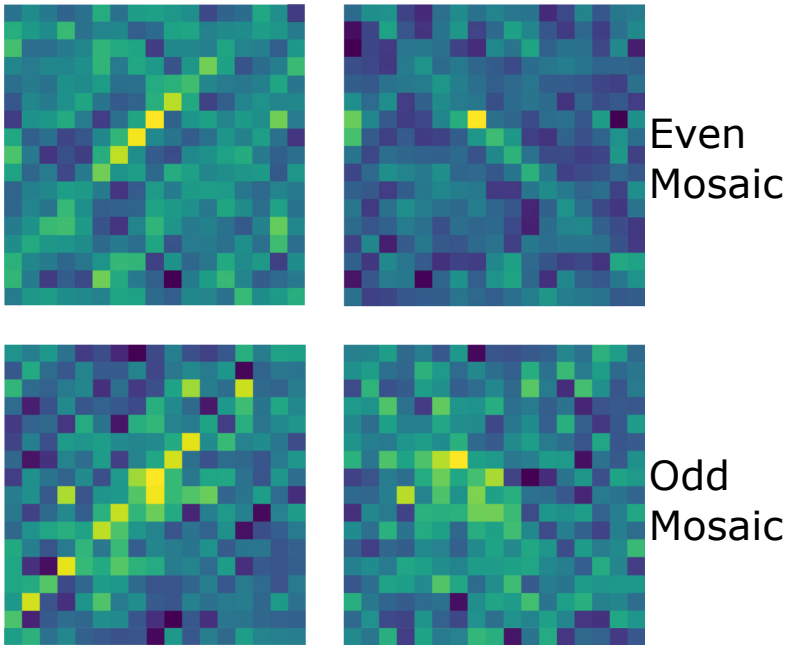

Figure 6.16: 2D track reconstructions for a muon crossing the argon volume diagonally and with both the odd (bottom) and even (top) mosaics. For both configurations, the reconstructions are shown for the two cameras in the geometry (left and right). The results were obtained with the standard argon light yield of 40k photons/MeV.

quality drops when simulating a standard light yield. This is due to the low photon density reaching the sensor plane combined with a working principle of the Coded Aperture technique: a complete shadow of the mask is required in order to correctly reconstruct the source image. With low light yield, this condition could not be satisfied, as some pixels of the sensor could detect zero photons even if they are not in a shadow region. These results limit the applicability of this technique in GRAIN, as the light produced by particles at the distances expected in its volume will not be enough to completely reconstruct a track. A possible solution is to increase the size of the SiPM in order to collect more light. This however has some limitations both in the available space in the detector, as well as on the heat load of the hardware inside the argon.

From these preliminary results, it has emerged that the Coded Aperture technique does not fit the reconstruction requirements for the full volume of GRAIN, but just in the regions close to the cameras. Possible solutions to this limitation include the use of different optical systems, able to reconstruct tracks in complementary regions of the argon volume, as well as a different reconstruction approach - still using Coded Aperture cameras - that does not depend on the full mask pattern to be projected on the sensor. This last option is briefly presented in the next section.

6.4 3D voxel reconstruction

An alternative reconstruction algorithm is currently being developed to overcome the limitations of the deconvolution reconstruction. This technique exploits a combinatorial approach to directly perform a 3D reconstruction of the images. The volume where the particles propagate is segmented in voxels. For each one an emission probability is computed projecting backward each photon detected by a camera through all the possible mask holes. Combining the projections from all the cameras, the position of the light source is related to the voxels with the higher probability. A schematic 2D view of this procedure is shown in Figure 6.17.

This technique offers different advantages compared to the deconvolution. First, it can work with a wide range of mask models, as the decoding properties are not needed. Moreover, as the photons are back-propagated individually, having a low number of detected photons does not affect the reconstruction capabilities as much as in the deconvolution procedure. On the disadvantage side, the reconstruction of a single event requires a really large number of operations, making this technique computationally heavy. At the time of writing, this reconstruction method is being actively developed and optimized. Its results are promising as can be seen in Fig. 6.18, where the reconstruction of a proton track in a GRAIN-like geometry (see 5.1.2) is shown. A comprehensive description of this technique can be found in[148].

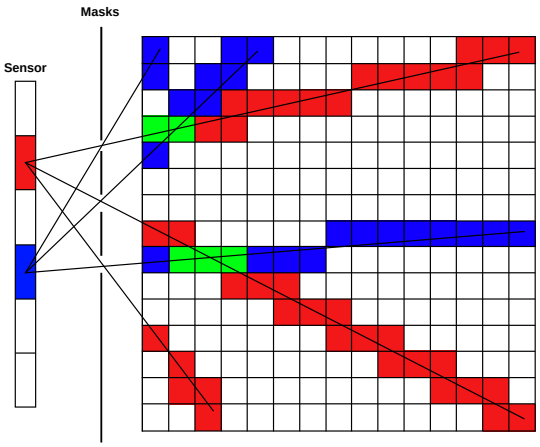

Figure 6.17: 2D view of the combinatorial approach to track reconstruction. The photons detected on each pixel of the sensor are propagated back into the segmented reconstruction volume. The intersection of their trajectories identifies the voxels most likely being the source of the photons, here highlighted in green.

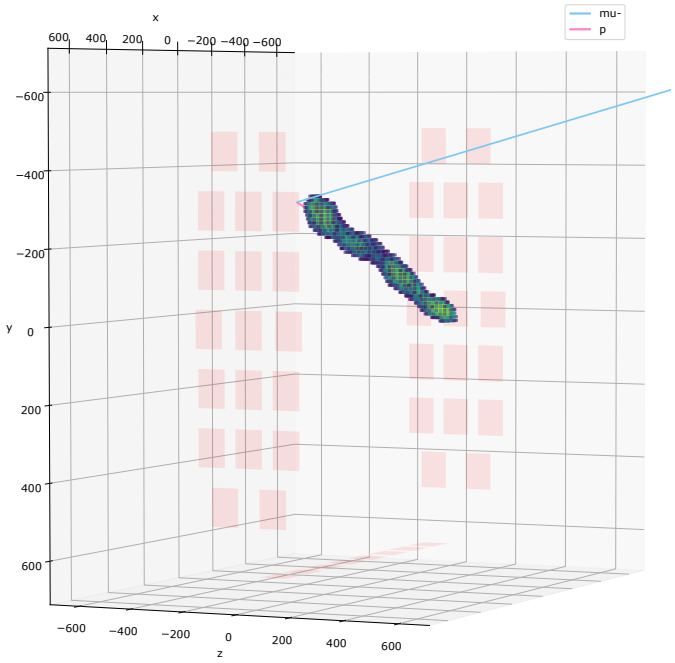

Figure 6.18: 3D reconstruction of a proton track in a GRAIN-like geometry obtained with the combinatorial approach. Only the proton is correctly reconstructed, while the technique fails to reconstruct the muon. More information can be found in [148].

Chapter 7

Analysis of $\nu_\mu + Ar$ Quasi-Elastic interactions

As previously described, GRAIN will contribute to the neutrino event reconstruction in SAND providing information about the particle trajectories inside its volume and about the neutrino interaction point position thanks to the 3D tracking technique described in Chapter 6. On top of this, it will be able to provide calorimetric information on the total energy loss in argon by secondary particles. As GRAIN uses only an optical readout, this information must be obtained from the scintillation light collected for each event, which depends on the position of the interaction points, the topology of the interaction, the secondary particles and other factors. As detailed in Chapter 3, the selection of a pure sample of neutrino-Argon interactions in SAND allows to constraint the physics response function introduced by the nuclear smearing, and allowing a better constraint of the systematic uncertainties in the neutrino oscillation analysis. This chapter will thus detail the technique used in GRAIN to reconstruct the energy deposited by particles produced in neutrino interactions, and how this information can be used together with the SAND STT and ECAL to select charged-current quasi-elastic (CCQE) neutrino interactions in the $\nu_\mu + Ar \rightarrow \mu^- + p + X$ channel. The performance of the calorimetric measurements in GRAIN will be studied looking at the improvements it will provide in the selection of a pure neutrino interaction sample in the desired channel, and in the reconstruction of the primary neutrino energy. Section 7.1 will describe a preliminary CCQE-like event selection using information from STT and ECAL, and considering GRAIN as a passive target. A report on the calorimetric measurement in GRAIN will be provided in sections 7.2 to 7.6, detailing the improvement this measurement provides in the CCQE-like selection. Lastly, a brief overview of future improvements of the analysis described in this chapter is provided in Sec. 7.7.

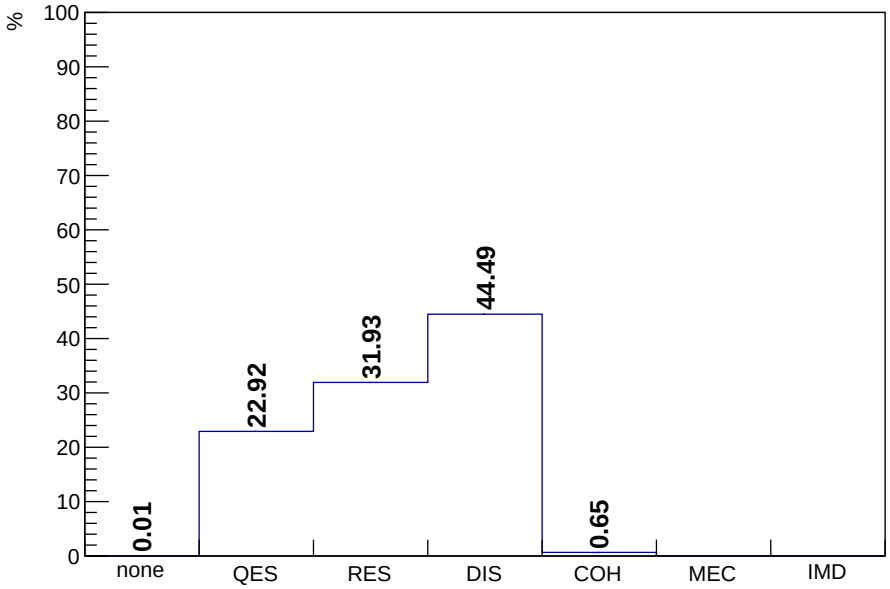

Figure 7.1: Interaction process type for all the simulated events.

7.1 GRAIN as a passive target

To study the impact of calorimetric measurements in GRAIN on the SAND performances, a preliminary evaluation exploiting the SST and the ECAL information only was performed, thus treating GRAIN as a passive liquid argon target. This was done by studying the selection performances of CCQE events in the $\nu_\mu + Ar \to \mu^- + p + X$ channel and the performances in the reconstruction of the neutrino energy. About 8 million neutrino interactions were simulated uniformly in GRAIN and propagated using edep-sim. The neutrino dataset included the main process types, with cross-sections and energy spectrum defined by GENIE as in Sec. 5.2. Figure 7.1 shows the process type composition of the simulated neutrino events. Starting from these events, 3 datasets were defined: two training datasets composed by 10% of the events each, and an analysis dataset composed of the remaining 80% of the events. Information on the propagation of the secondary particles were then reconstructed by STT and ECAL for all the three samples. At the time of writing, the STT and ECAL event reconstruction codes exploit MC-truth information at different levels and are performed separately by two algorithms:

- **STT track reconstruction** In the STT reconstruction, the algorithm performs a smearing of the MC-truth. First, a selection based on the number of

hits in the tracker is performed. To reconstruct a track, a minimum number of 4 hits in the YZ plane is required. For each track surviving the selection, the momentum, total track length, and the angles in the Y-Z and X-p_t planes are obtained from the MC-truth. A Gaussian smearing on the particle transverse momentum is then performed, with the sigma of the smearing ($\sigma(p_t)$) defined as the sum of the effect of the multiple scattering and the intrinsic momentum resolution of a particle crossing a magnetic field, described by the Gluckstern formula[157]:

$$\frac{\sigma(p_t)}{p_t} = \frac{\sigma(x) \cdot p_t}{0.3BL^2}\sqrt{720/(N+4)} \oplus 0.045\frac{1}{B\sqrt{LX_0}} \tag{7.1}$$

where $\oplus$ indicates a quadratic sum, $\sigma(x)$ is set to 2 μm, B is the magnetic field, L the total track length, N the number of hits in the STT, and X_0 is the radiation length. The particle momentum components along the x, y, and z axis are then computed starting from the smeared momentum and the Y-Z and X-p_t angles. Both angles were smeared with a Gaussian distribution, with the sigma again defined as the expected resolution of the angles. This is affected by the multiple scattering equation at small angles and is defined as[158]:

$$\sigma = \frac{0.0136 \text{ GeV}}{p}\sqrt{\frac{L}{X_0}}\left(1 + 0.038 \log\left(\frac{L}{X_0}\right)\right) \tag{7.2}$$

The smeared momentum, together with some other particle properties extracted from the MC-truth, such as the particle type and the number of hits, are provided as output of the STT reconstruction step.

- **ECAL cluster reconstruction** To reconstruct clusters produced by particles crossing the SAND electromagnetic calorimeter, first the digitization of the signals is performed. This is used to reproduce the segmentation of the calorimeter and simulate the output expected from the DAQ system. To do so, each calorimeter module is divided in a 12 $\times$ 5 grid, as described in Sec. 3.2.2. As each cell will be read by a PMT on each side of the module, the number of photo-electrons, N_{pe}, is computed on both sides of one module. This procedure takes into account the light attenuation length of the fibers and the energy deposit conversion into photo-electrons. N_{pe} is thus extracted from a Poisson distribution with mean value μ_{pe} given by:

$$\mu_{pe} = dE \cdot A_l E_{pe} \tag{7.3}$$

$$A_l = p_1 \cdot \exp\left(-\frac{d_B}{alt_1}\right) + (1-p_1) \cdot \exp\left(-\frac{d_B}{alt_2}\right) \tag{7.4}$$

with A_l being the fiber attenuation length, E_{pe} the energy to photo-electrons conversion factor, d_B the distance between the hit position and the PMT

reading the cell. The value of alt_1 is kept constant at 50 cm, while alt_2 changes depending on the cell's layer, from 330 cm for the inner layers, to 430 cm for the most outer ones. E_{pe} is taken from the results of the KLOE experiment and its value is set to 18.5 eV[102]. For each photon produced in the fiber, an arrival time on the PMT is obtained as:

$$t_{pe} = t_{cross} + t_{decay} + d_B/v_{ph} + G(1 \text{ ns}) \tag{7.5}$$

where t_{cross} is the time of the hit from the MC truth, t_{decay} is the decay time of the scintillator, and d_B/v_{ph} is the time of propagation of the photons along the fiber. G(1 ns) is a Gaussian smearing corresponding to the photo sensor time uncertainty. After the digitization, the algorithm performs an iterative procedure starting from cells with hits on both sides, and creates a cluster composed by the hit cells found around the starting ones. Groups of cells whose time differs of more than 5 ns are then split in different clusters while clusters within 40 cm and 2.5 ns one from the other are merged in a single one. For each cluster the energy, position, time and direction are computed, while information on the particle generating it are stored from the MC-truth. More information on the clustering algorithm can be found in [159].

The selection of a CCQE-like event sample was then performed selecting all the events which satisfied two conditions:

- Exactly one muon and one proton must be reconstructed by the STT;
- All the clusters in the ECAL should be matched with the muon or the proton reconstructed by the STT, with no clusters remaining unmatched.

The results of this selection on the analysis dataset are shown in Fig. 7.2 and reported in Table 7.1: exploiting only the information of STT and ECAL, a selection efficiency of 25.3% is obtained, with a purity of 73.3%. The low selection efficiency can be explained looking at Fig. 7.3, where the YZ position of all the simulated CCQE events in the $\nu_\mu + Ar \to \mu^- + p + X$ channel is shown in left panel, while the position of the selected events in the same plane is shown on the right panel. Here the position is reconstructed analytically as the intersection point between the muon and proton tracks reconstructed by the STT. Despite the events being generated uniformly in the GRAIN volume, the selection criteria strongly favors events in the downstream region, close to the edge of the argon volume. This is a consequence of the requirement of a reconstructed proton in the STT. Events whose interaction point is farther upstream from the downstream edge of GRAIN have the proton stopping inside the argon. These events don't survive the cut and the selection efficiency drops as a consequence. The low purity of the selection can instead be explained looking at the composition of the events surviving the

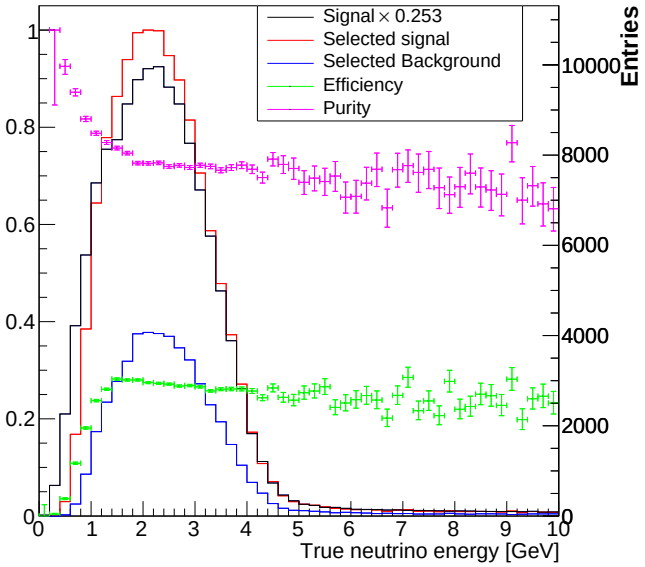

Figure 7.2: Selection efficiency (green) and purity (magenta) for CCQE-like events in the $\nu_\mu + Ar \rightarrow \mu + p + X$. The spectrum of the full signal sample (black), the selected signal (red), and the selected background (blue) are also shown. The selection is performed exploiting the STT and ECAL reconstruction, while GRAIN was considered a passive target.

Total Events	6170000
Signal Events	574974
Selected Events	198233
Selected Signal	145335
Selected Bkg	52898
Selection Eff	25.3%
Selection Purity	73.3%

Table 7.1: Performances of the event selection in the $\nu_\mu + Ar \rightarrow \mu^- + p + X$ channel exploiting the STT and ECAL event reconstructions.

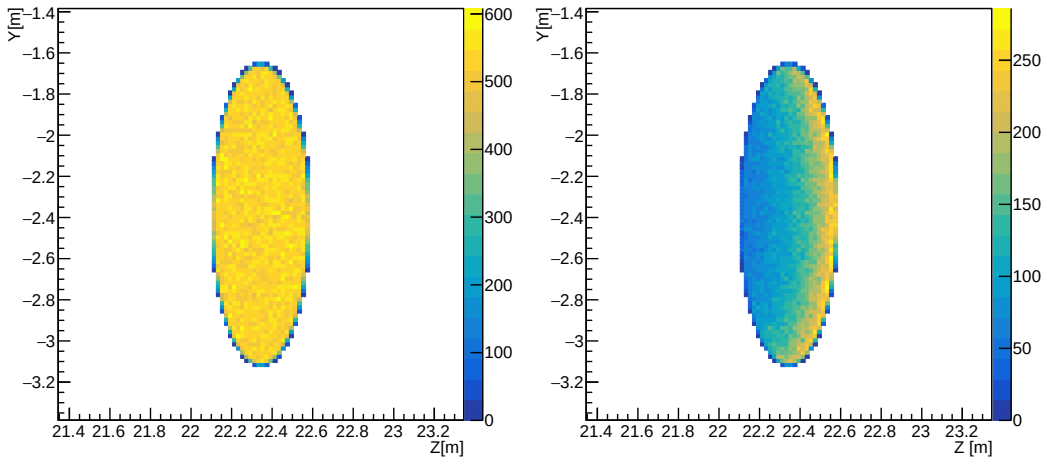

Figure 7.3: Left: reconstructed position in the YZ plane of GRAIN for all the simulated CCQE events in the $\nu_\mu + Ar \rightarrow \mu + p + X$ channel. Right: reconstructed position in the YZ plane of GRAIN for all the events surviving the selection criteria.

cuts, shown in Fig. 7.4 and 7.5. The majority of the misidentified events are either CCQE events with more than a single proton produced in the interaction, or resonance events with multiple secondary particles produced. As none of these particles are seen in the STT nor in the ECAL, they must be particles which stop inside the GRAIN volume. From the deposited energy in the electromagnetic calorimeter and the reconstructed momentum in the STT, it is then possible to reconstruct the energy of the primary neutrinos. The results are visible in Fig. 7.6, where both the reconstructed energy as a function of the true neutrino energy and the ratio between the two quantities are shown. From both plots of Fig. 7.6 one can see how the reconstructed energy has a bias towards underestimated energies. On top of this, the ratio distribution is asymmetrical, with events for which the reconstructed energy is even more underestimated. The distribution's bias is expected, as the energy reconstruction with just STT and ECAL does not take into account the deposited energy in argon by the secondary particles. This effect is enhanced for background events as there are more particles depositing energy in argon not included in the neutrino energy reconstruction. Calorimetric measurements in GRAIN should then improve these results. Including the information on the deposited energy in argon, the bias of the distribution should decrease, while it should be possible to filter the background events as their deposited energy will be higher than what is expected from just a muon and a proton. A selection based on the deposited energy in argon should then increase the purity of the selection and improve the neutrino energy reconstruction.

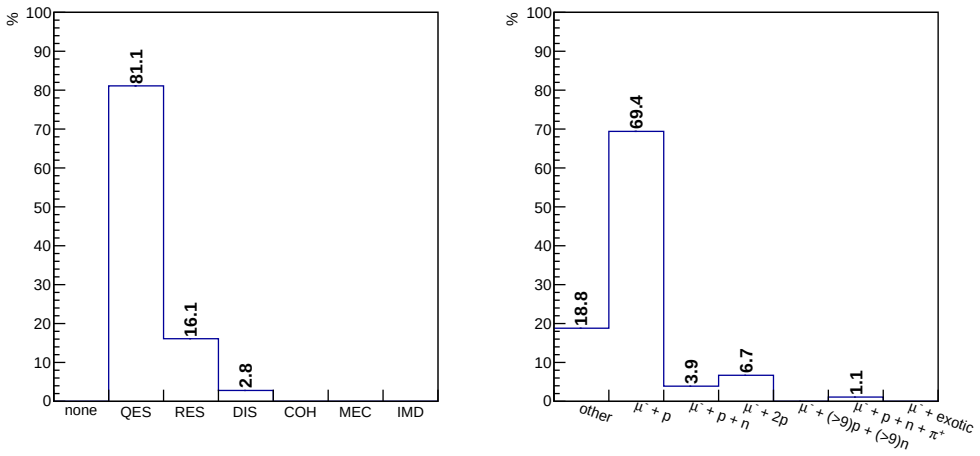

Figure 7.4: Left: interaction process type for all the selected events. Right: true final composition of all the selected events.

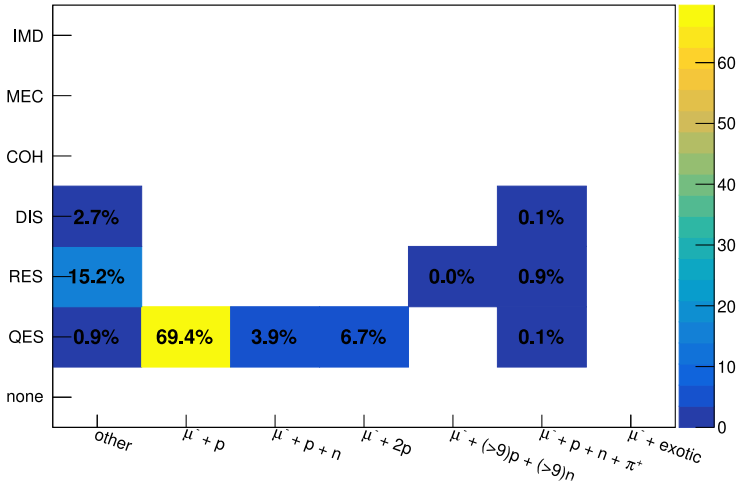

Figure 7.5: Interaction process type and true final composition of all the selected events. Events were selected exploiting the STT and ECAl reconstruction, while GRAIN was considered a passive target.

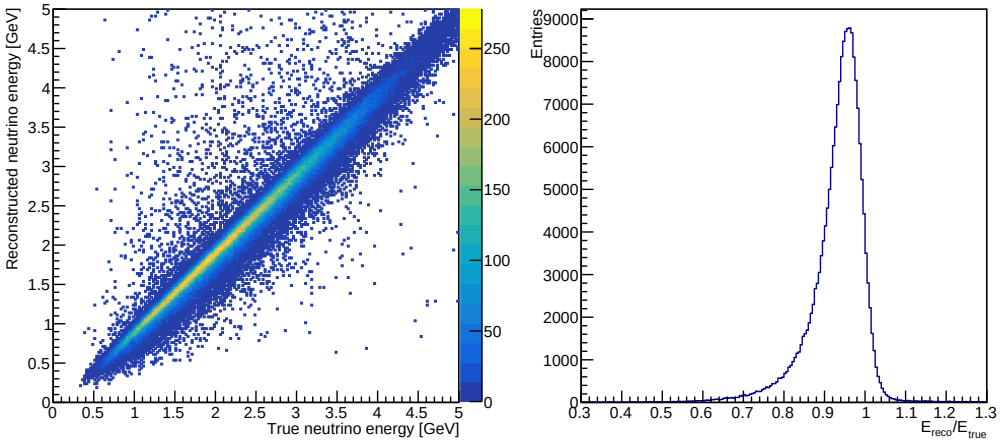

Figure 7.6: Left: distribution of the true and reconstructed neutrino energy using only information from STT and ECAL. Right: Reconstructed neutrino energy as a function of the true neutrino energy.

7.2 Preliminary study on the calorimetry requirements

A preliminary study was carried on to better understand the requirements needed to perform calorimetric measurements in GRAIN. This was done with a relatively small set of neutrino interactions with interaction point inside the argon volume. The aim of the study was to verify whether or not it is possible to obtain a calibration coefficient to reconstruct the deposited energy in argon from the total number of detected photons, and find out possible limitations that should be addressed in doing so.

7.2.1 Neutrino datasets and geometry configuration

Neutrino events were simulated following the simulation framework described in Chap. 5, with two spatial distributions: uniformly in GRAIN and limited in a smaller volume of $5 \times 5 \times 5$ cm^3 (a voxel) in the center of GRAIN. Both dataset were composed by 10k ν_μ CCQE events, with energies extracted from the expected flux at LBNF (Sec. 2.1.1). In the following, the two datasets will be referred to as uniform and voxel distributions. The GRAIN and camera geometries were simulated as described in Sec. 5.1.2, with the argon volume instrumented with 76 optical cameras: 8 on each face on the side of the cryostat, 5 on the top and bottom region of the cryostat, and 25 on each curved face, arranged in a 5×5 grid

Parameter	Value
Rank	31
Mask pitch	2.91 mm
Mask hole	2.71 mm
Configuration	2x2 mosaic
Sensor side	102.4 mm
Sensor-mask distance	20 mm

Table 7.2: Main parameters of the optical cameras simulated in the GRAIN geometry.

and following the curvature of the face. The model of the camera was shared by all 76 cameras and the value of their most important parameters are reported in Table 7.2. The distribution of the cameras in the GRAIN geometry is visible in Fig. 7.7, while Fig. 7.8 shows the volume of the voxel were the neutrino events were generated inside GRAIN. The GRAIN geometry just described will be used as the default geometry for the remainder of this chapter.

7.2.2 Energy and position dependances

For all the simulated events, the total number of detected scintillation photons was evaluated with the full electronic response described in Sec. 5.4. Figure 7.9 (top) shows this number, for the uniform distribution, as a function of the energy deposited by the secondary particles produced in the neutrino interaction. Here the deposited energy was obtained from the edepsim MC files. It is clear that, despite a linear relation between the two quantities is visible, there is a wide spread on the number of detected photons for a specific value of deposited energy. This is expected as events with similar quantities of energy deposition, but in different positions inside GRAIN, could be seen by a different number of optical cameras, directly affecting the total number of collected photons. This spacial dependency of the number of collected photons is clearly visible comparing the results obtained with the uniform distribution and the one obtained with the voxel distribution. These results are shown in the bottom plot of Fig. 7.9 , where is visible how the spread of the detected light is much smaller. To justify this behavior, one can evaluate how much of the cameras' sensors is visible from a specific position inside the argon volume. Both the distance of each sensor from the position under investigation and the obstruction effect of the masks should be taken into account when performing this evaluation. This is done computing the

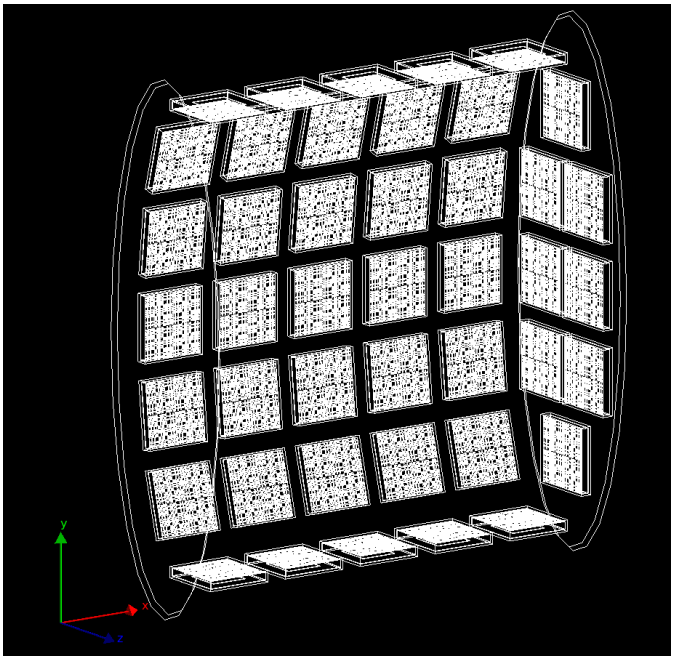

Figure 7.7: GRAIN geometry instrumented with optical cameras. To better visualize the camera disposition, the cameras in one lateral face and one curved face are excluded from the image.

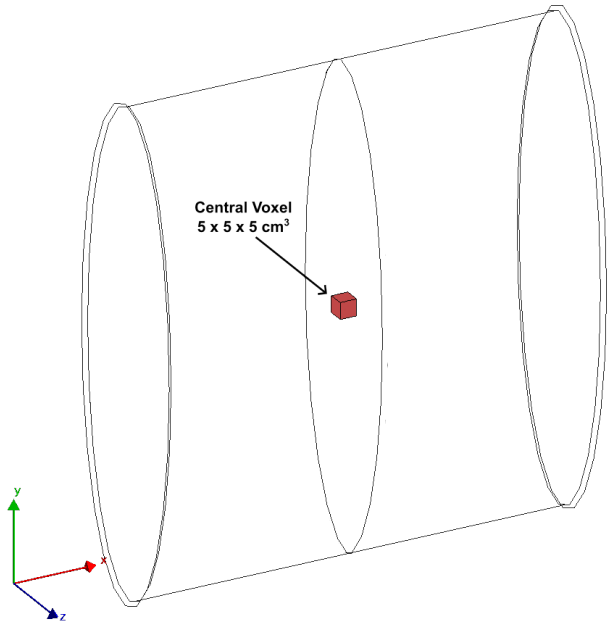

Figure 7.8: Sketch of the GRAIN and voxel volumes where the two set of neutrino interactions were simulated.

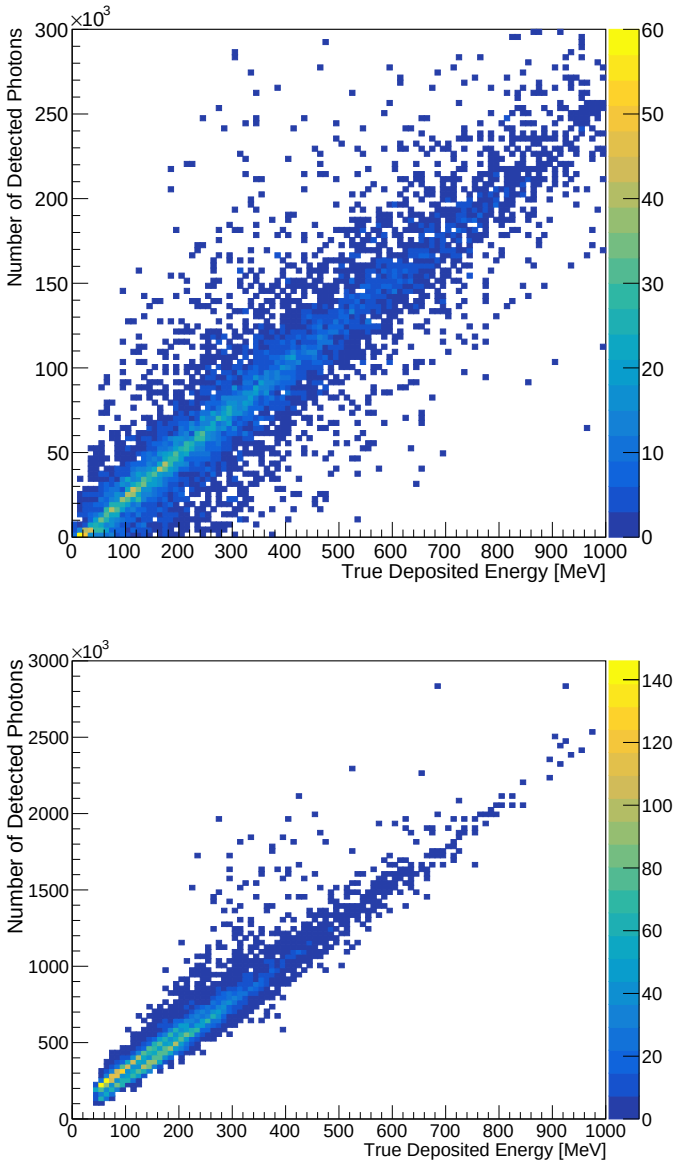

Figure 7.9: Number of detected photons as a function of the true deposited energy in GRAIN for events with interaction point uniformly distributed in GRAIN (top) and for events with interaction point in the central voxel (Sec. 7.2.2, bottom). The number of detected photons is computed as the sum of the counts by the 76 optical cameras of the GRAIN geometry in Fig. 7.7, while the true energy is obtained from the edepsim MC file.

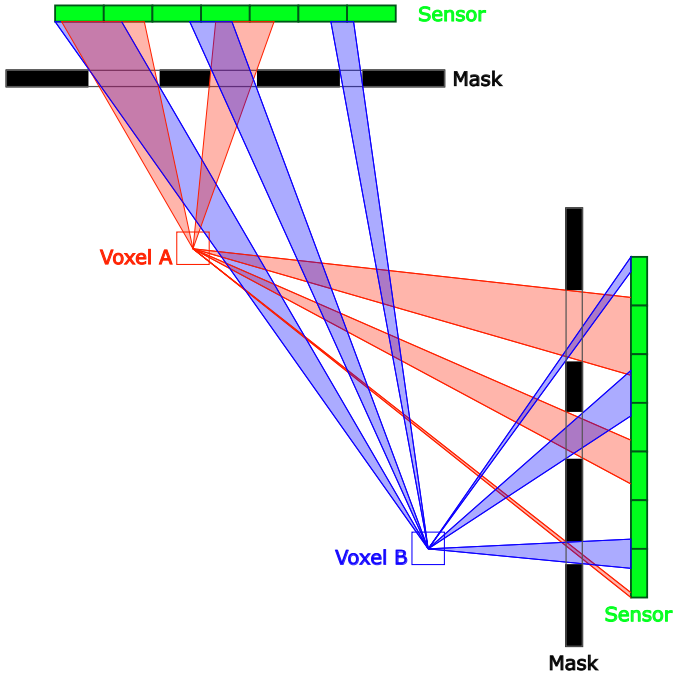

Figure 7.10: Sketch of the total solid angle computation for two different voxels with two optical cameras. The visible pixels from each voxel are highlighted with shaded areas. The higher the total shaded area is for one voxel, the higher is the number of photons generated from that voxel that can be detected.

total solid angle covered by all the sensors' area visible through the holes of all the masks from a specific position. This value directly relates to the total number of detected photons, as higher values imply a larger available detecting area for photons produced in that position. Figure 7.10 shows a sketch of this process, while Fig. 7.11 shows the total solid angle for different positions of 1/4th of the GRAIN volume. As it is visible, the values of the central region are quite uniform and do not have a strong position dependance. This justifies the narrow band of total number of detected photons for events produced in these regions, such as the ones simulated in the voxel in the center of GRAIN. On the other hand, regions on the borders of the volume and close to the cameras have values with a much larger spread. This directly affects the total number of detected photons for events of the uniform dataset, for which a larger spread is thus expected, as already seen in Fig. 7.9.

The linear dependency seen for the voxel distribution suggests the possibility to obtain a calibration coefficient to convert the total number of detected photons back to the total deposited energy in argon. However, this coefficient should not be computed for the complete volume, but should instead be computed locally,

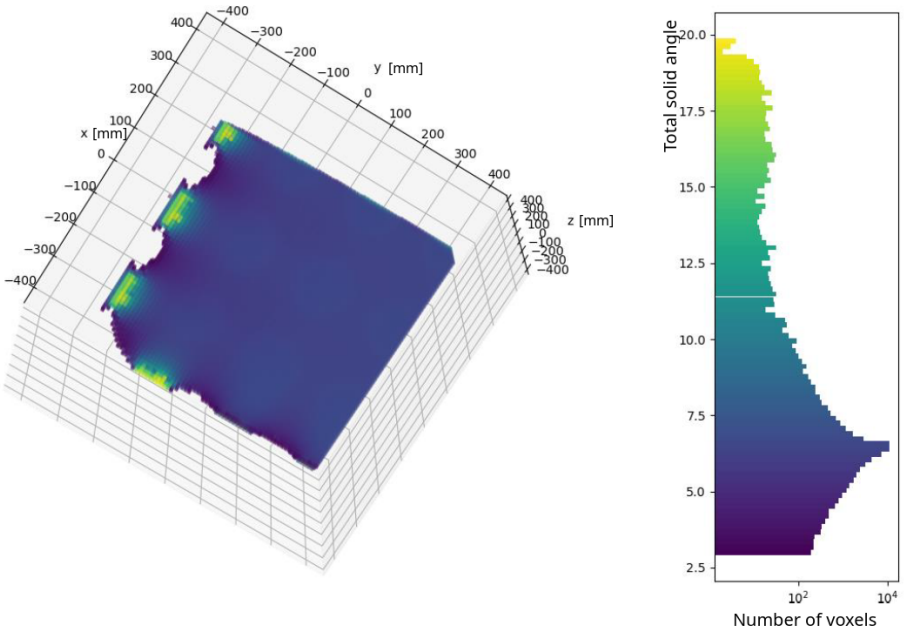

Figure 7.11: Left: total solid angle for 1/4th of the GRAIN volume. The color scale indicates the value of each voxel. Right: color scale and frequency of each solid angle value in the left plot. It is visible how most of the voxels have a value of ~ 7 (x log scale), suggesting a negligible spatial dependance.

obtaining a coefficient for each region in which the spatial dependance is negligible. It should be noted that the uniformity of the solid angle values seen in Fig. 7.11 is a consequence of the high number of cameras in the geometry, and their symmetrical arrangement along all the faces of the detector. A different configuration of cameras will greatly affect the collected light and the uniformity of the measured total solid angle, greatly enhancing the spatial dependency.

7.2.3 Light yield dependance

Neutrino events were simulated with the standard liquid argon light yield of 40k emitted photons per MeV of deposited energy. However, the optical simulation used to propagate and collect the light, and the simulation of the detector response and electronics, are computationally heavy, making difficult to generate datasets much larger than the one used in this study. A solution to this problem was to simulate the liquid argon with a reduced light yield, fastening both optical and detector simulations, and scale back the results to the expected values at nominal light yield. The results of the previous section were thus obtained and compared for the same events at different light yield values. The used light yields were 2.5%, 10%, and 25% of the nominal liquid argon light yield, corresponding to 1k, 4k, and 10k photons per deposited MeV respectively. Figure 7.12 (top) shows the distribution of the total number of detected photons for the four simulated light yields, scaled to 40k photons per MeV. The bottom part of the Fig. 7.12 shows instead the ratio between the three scaled distributions and the nominal one. Similar results are shown in Fig. 7.13, where the mean number of detected photons is shown as a function of the deposited energy.

For a light yield of 10k photons/MeV, the results agree within 10%, suggesting that reducing the liquid argon light yield is a viable solution to reduce the computational time of the simulation. In the following, the light yield is thus kept constant at a value of 10k photons per deposited MeV.

7.3 Spill simulation and pileup removal

Before computing the calibration coefficients needed to reconstruct the deposited energy in GRAIN, the effect of the spill structure and the backgrounds should be taken into account. Because of the event pileup in GRAIN, and the slow time decay of the triplet component of liquid argon, an almost permanent light background is expected in GRAIN during a spill. A signal event in GRAIN could then have a light contribution coming from background events that crossed the argon volume before it. These contributions will increase the light collected and, if included with the light emission of the event itself, will generate a bias in the

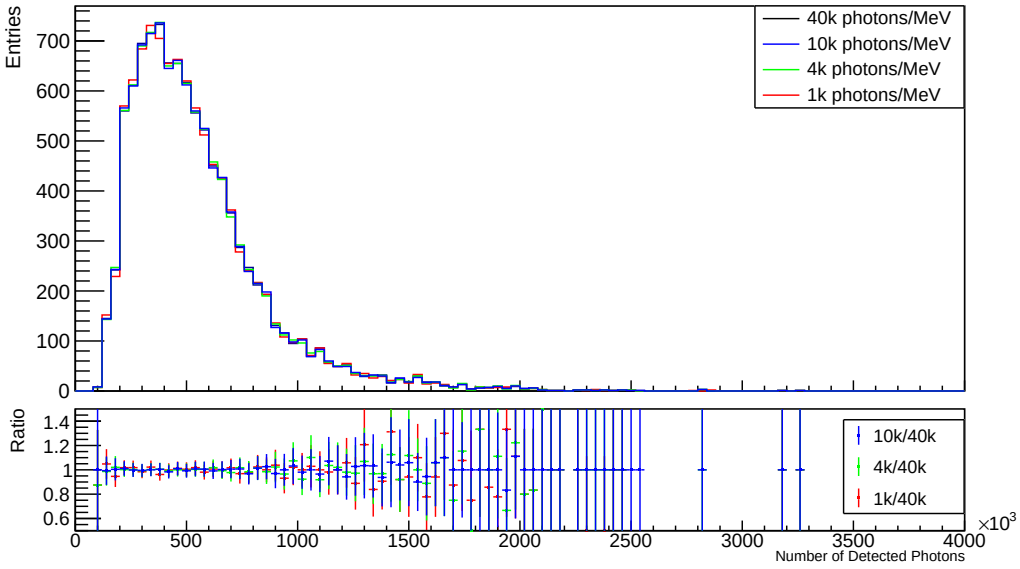

Figure 7.12: Top: total number of detected photons' distribution for different light yield scaled to the nominal one of 40k photons/MeV. Bottom: ratio of the scaled distributions over the 40k distribution.

reconstructed energy. The light generated from the particles produced in the signal neutrino interactions should then be separated from the light coming from the background. Before studying this effect on the CCQE-like neutrino sample selected in the previous section, a dedicated procedure to identify, fit, and separate the contribution of each event in a spill was developed. First, a dedicated dataset was simulated. This was generated following the usual simulation framework, with the difference of providing GENIE the time structure of the beam and the whole geometry of SAND, thus not including the geometry of the other detectors in the Near Detector hall, nor the rocks around the detector. The dataset was composed by 900 spills, with Fig. 7.14 showing an example of the time profile of all the photons collected in GRAIN during one spill. A structure with multiple peaks is visible, with each peak corresponding to the liquid argon fast component of one event, and the long tails corresponding to the triplet component. Most of the time, the events in one spill are background events generated by neutrino interacting outside the volume of GRAIN and for which the secondary particles produced in the interaction cross the argon volume. It is clear how, depending on the intensity and temporal distance of the events in the spill, the total collected light for a specific event could be largely overestimated due to the contribution of the slow component of the previous events. To separate the contribution of

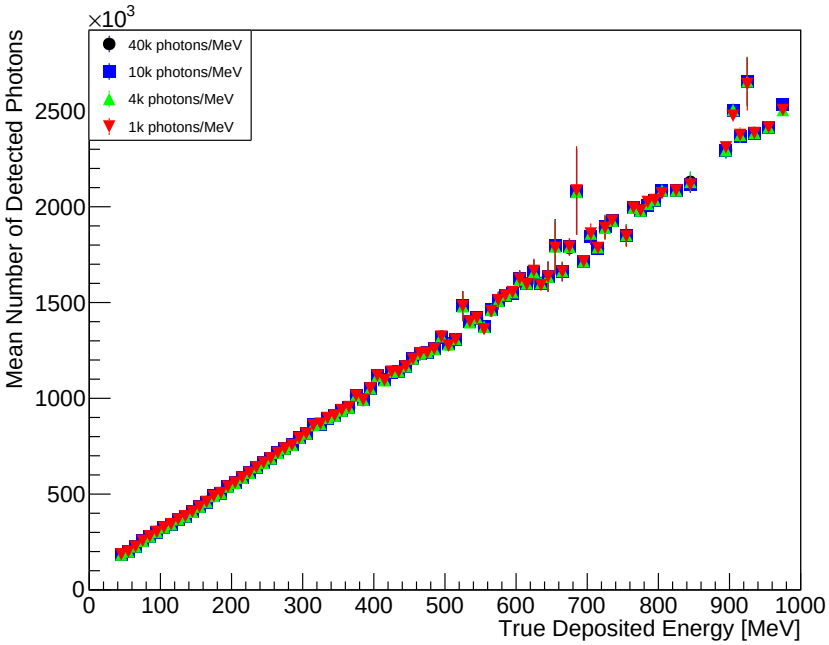

Figure 7.13: Mean value of the total number of detected photons as a function of the true deposited energy for different light yields scaled to the nominal one of 40k photons/MeV. Where not visible, error bars are within the markers.

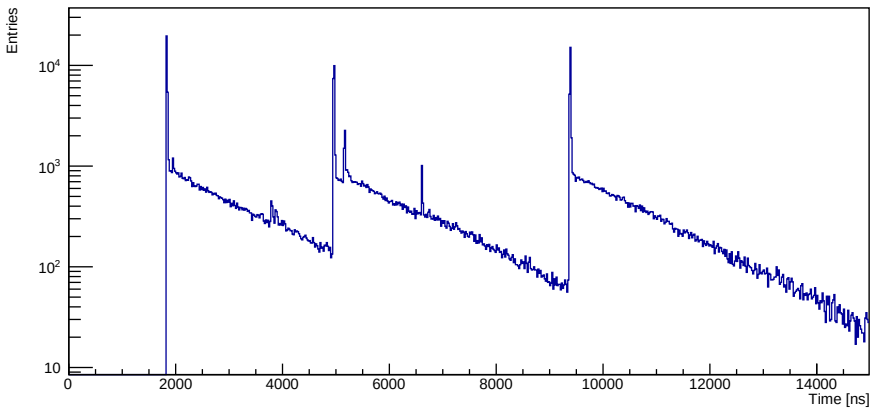

Figure 7.14: Time profile of the detected photons for one of the simulated spills. Each entry is one detected photons on one of the 76 optical cameras. Each peak corresponds to the fast component of one event, while the long tail correspond to its slow component.

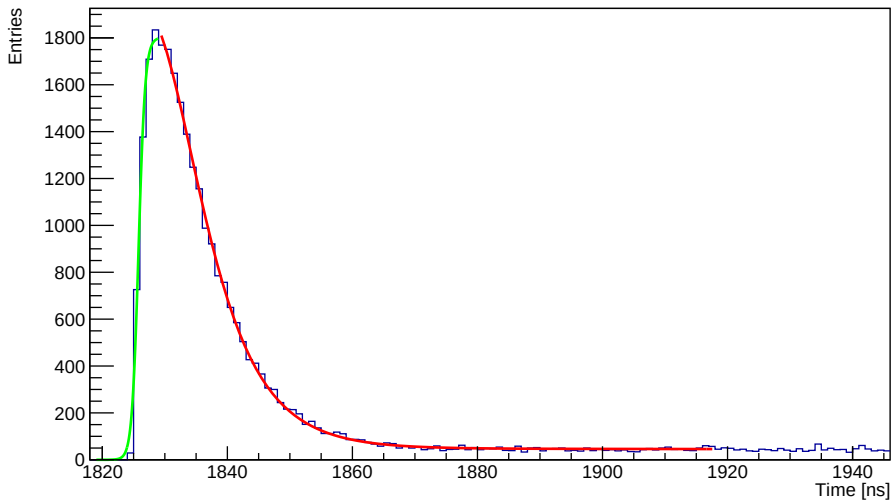

Figure 7.15: Waveform of a single event of one spill with fitted functions described in 7.6 and 7.7 overlaid in red and green respectively.

each event, its waveform was first fitted with two different functions, one for the rising edge and one for the tail. The tail was modeled as a sum of exponentials to characterize the scintillation time, convoluted with a Gaussian to represent the detector response[160]:

$$f(t) = \sum_{j=f,s} \frac{A_j}{2\tau_j} \exp\left[\frac{1}{2}\left(\frac{\sigma}{\tau_j}\right)^2 - \left(\frac{t-t_m}{\tau_j}\right)\right]\left[1 - \mathrm{erf}\left(\frac{1}{\sqrt{2}}\left(\frac{\sigma}{\tau_j} - \frac{(t-t_m)}{\sigma}\right)\right)\right] \quad (7.6)$$

where j refers to the two exponential components (f fast and s slow), A_j are normalization constants, t_m and σ are the Gaussian mean and width respectively and τ_j are the parameter characterizing the exponential fall-offs. The rising edge was instead modeled as a Sigmoid function:

$$f(t) = \frac{1}{1+e^{-t}} \quad (7.7)$$

Figure 7.15 shows the waveform of one event with the fitted functions superimposed. After fitting one peak in one spill, its contribution can be removed from the total spill waveform, leaving the following peaks free from background light. The same procedure can then be applied iteratively to all the the events in the spill. Figure 7.16 shows an example of this procedure for two consecutive peaks of one spill. It should be noted that, while it is possible to obtain the waveform in Fig. 7.14 after the full detector response (Sec. 5.4), the need of information on the

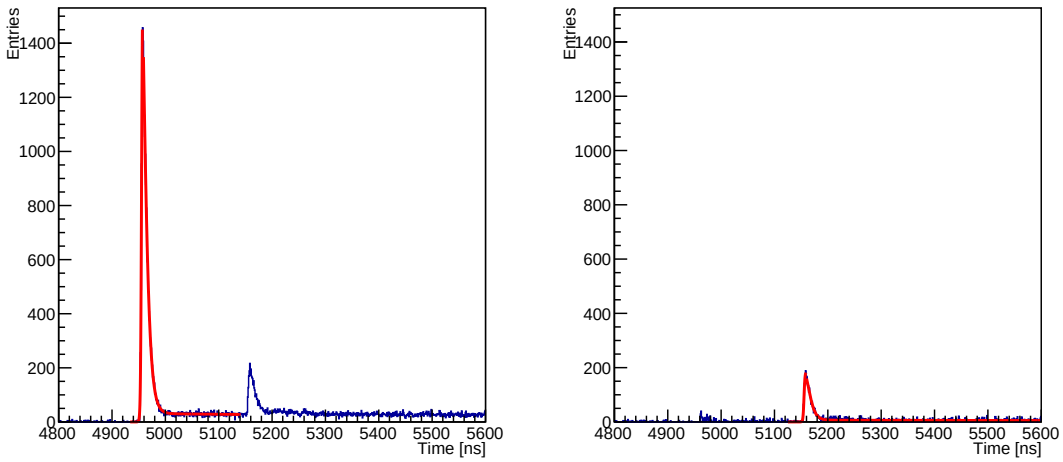

Figure 7.16: Example of removal procedure for an event in one spill. Both plots show the time profile of the detected photons in GRAIN. Left: the first peak of the waveform is fitted with the two functions described in Eq. 7.6 and 7.7. Its contribution is later removed along the whole wavefrom. Right: the second event is fitted with the same two functions. The number of detected photons is now correctly computed as the event is free from the contribution of the previous one.

photons count on each sensor's pixel is not crucial in this analysis. This step is thus skipped, leaving only the simulation of the PDE and crosstalk obtained with the fast response. With each event isolated from the background light, the total number of photons detected for each event is computed as the integral of the waveform in the first 200 ns from the rising edge of the event. This procedure was applied to each event of the 900 simulated spills, and Fig. 7.17 shows the distribution of the number of collected photons obtained including the backgrounds as a function of the number of collected photons obtained after the removal of the background light. From Fig. 7.17 one can see how the photons count is often overestimated due to the background. This procedure is thus critical to correctly reconstruct the total number of collected photons and, consequentially, the energy deposited in GRAIN by a neutrino interaction during a spill. Detailed description of the different steps performed during this procedure, and on the performance of the algorithm, can be found in Appendix A. With the spill fitting procedure defined, it was possible to compute the total number of detected photons for all the events in the CCQE-like sample. However, as all the neutrino interactions were generated as isolated events, the spill structure was simulated in a separated step for each event. To do so, about 50k background events were generated. These events were obtained simulating events uniformly in SAND and selecting the ones with energy

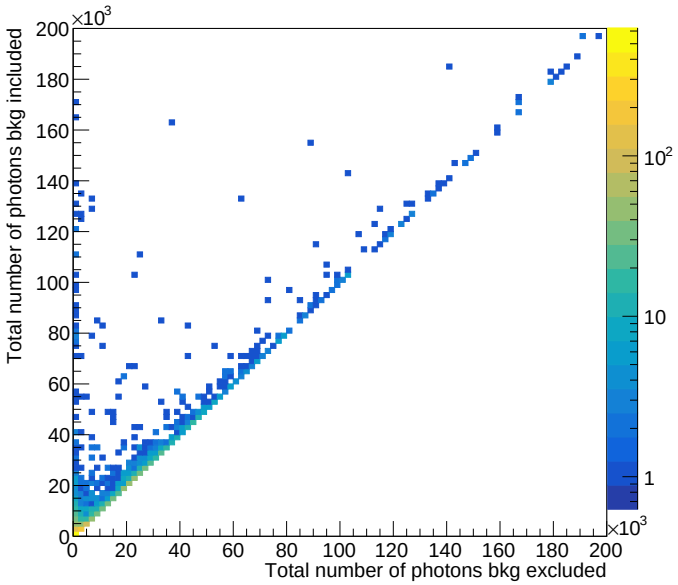

Figure 7.17: Number of detected photons before removing the contributions from background light as a function of the number of detected photons obtained after their removal.

deposits in GRAIN. The contributions from other detectors and the sorrounding rocks were again not included in the simulation of the background events. For each signal event of the CCQE-like sample, a random number of associated background events was extracted from the background dataset. The expected number of background events in GRAIN per spill was obtained from a separate study, and was found to be 4 background events per spill. The number of events was then extracted from a Poisson distribution with MPV = 4. All the events, both signal and background, were then shifted at random times in the spill time windows. Figure 7.18 shows some examples of simulated spills obtained with this procedure. After the generation of the spills, the fit procedure just described was applied to each one and the number of collected photons was computed for each event in one spill. Calibration coefficients were thus computed starting from this number, as described in the next sections.

7.4 Computation of the calibration coefficients

The calibration coefficients were computed starting from one of the two training datasets obtained from the whole 8×10^6 simulated neutrino interactions, exploiting the total number of detected photons as obtained in the previous section. The

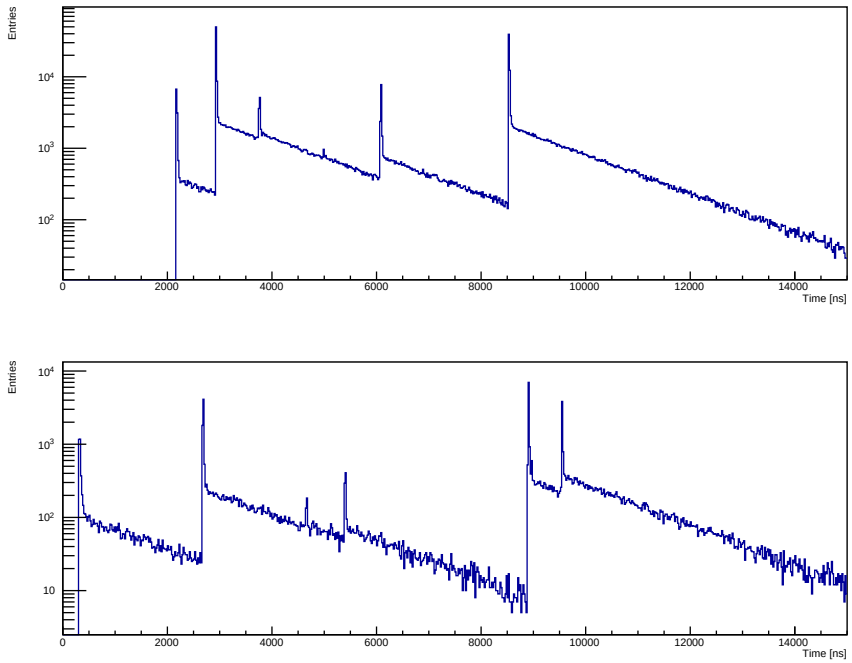

Figure 7.18: Examples of simulated spills composed by one signal event from the CCQE-like events and multiple events from the background dataset. The number of background events is extracted from a Piosson distribution with mean 4, while the time of each event (signal and background) is extracted randomly in the spill time windows.

preliminary study of Sec. 7.2. showed how the differences in the total solid angle for the positions in the central region of GRAIN are small, while the regions closer to the borders have differences in the solid angle values which affect the total number of detected photons. Because of this, the calibration coefficients were computed separately for the inner region and the ones at the border. A total of 7 regions were defined:

- inner region, covering the central part of the volume, 20 cm from both the top, bottom and side faces and 10 cm from the borders along the Z axis;
- central up- and downstream regions, covering the first and last 10 cm of the argon volume along the up- and downstream curved faces;
- north up- and downstream regions, covering the up- and downstream half volume along the Z direction respectively, and the external 20 cm of the X axis along the negative direction.
- south up- and downstream regions, covering the up- and downstream half volume along the Z direction respectively, and the external 20 cm of the X axis along the positive direction.

Figure 7.19 shows an exploded view of all the regions for which the calibration coefficients were computed. Due to the optical cameras position, the top and bottom regions of the argon volume are behind the optical cameras themself. These regions are thus excluded from the computation of the calibration coefficients. For all the regions, the coefficients were obtained with one of the two training datasets, starting from the distribution of total detected photons as a function of the deposited energy and exploiting two different techniques. A cut on the number of detected photons was also performed on all the events, excluding all the ones for wich less than 1000 photons were detected. It should also be noted how this calibration process strongly depends on the interaction process and on the number and type of secondary particles produced in the neutrino interaction. To fully calibrate the detector, the procedure described in the following should be performed for each possible interaction process or for each possible secondary particle, as the time profile of the emitted scintillation light depends on the exciting particle (Table 4.1).

7.4.1 Linear Fit

For each region, the mean deposited energy for different values of detected photons was computed from the MC truth files. The calibration coefficients were then obtained with a linear fit (LF) of the mean deposited energy distribution, and it is

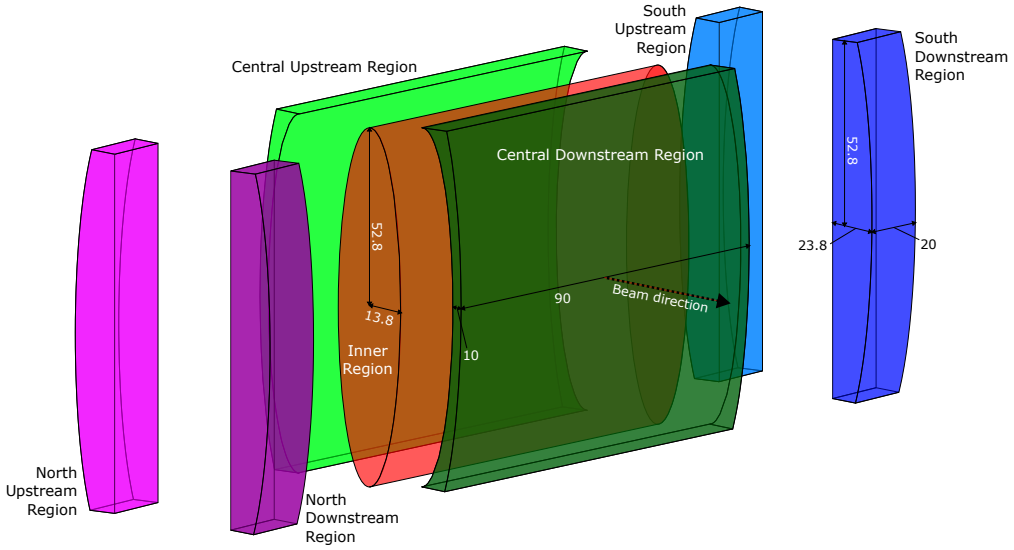

Figure 7.19: Exploded view of the regions for which the calibration coefficients were computed. Units are in cm.

Range	Slope	Intercept
$0 - 400$	0.712 ± 0.005	27 ± 1
$100 - 600$	0.751 ± 0.006	1 ± 1
$0 - 1000$	0.868 ± 0.001	6 ± 1

Table 7.3: Results of the three different linear fits in Fig. 7.20.

expressed as the slope and the intercept of the fit. Figure 7.20 shows an example of this process for the inner region of the argon volume. From Fig. 7.20 one can identify different limitations of this technique. Firstly, the extracted coefficient depends on the range of the fit. This can be seen in the right side of Fig. 7.20 where three fits with three different ranges are shown. The parameters of the fits are also reported in Table 7.3. It can be seen how changes in the range could affect the results and, consequentially, the reconstructed energy. It is also visible how, for increasing values of deposited energies, the statistics starts to decrease, making it difficult to correctly fit the distribution. The correct identification of the range over which one should fit the distribution in Fig. 7.20 is thus crucial to compute the correct calibration coefficient. Such range however is different across the voxels, as their exposure to the optical cameras, and consequentially the total number of detected photons, depends on the position inside the argon volume. The automatic identification of the optimal fitting range for each region is not yet

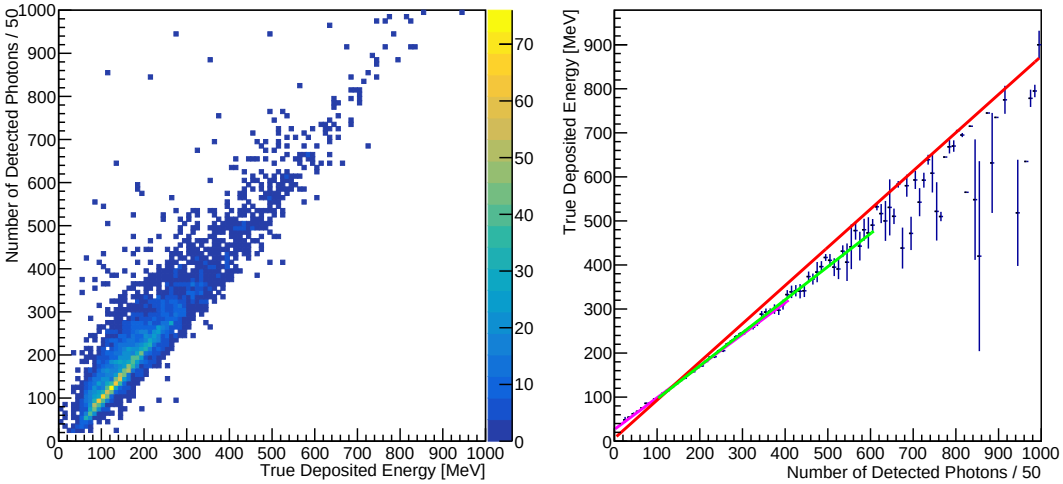

Figure 7.20: Left: Number of detected photons as a function of the true deposited energy for the events with interaction point in the voxel at the center of GRAIN. Right: mean value of the true deposited energy as a function of the number of detected photons with superimposed linear fits performed over different ranges.

implemented in the algorithm, and the different ranges are set manually for each region.

7.4.2 Hough transform

Starting from the same photons distribution of the previous paragraph, the calibration coefficients were computed by means of the Hugh Transform (HT). HT is a common technique of line detection, first proposed to detect straight lines in photographs from bubble chambers and later extended to detect lines in digital images [161][162]. The idea behind HT is to vote the evidence of the desired shape in the image domain to a parametric domain. Local maxima in the parameter space represent the identified shapes in the source image. A convenient parameterization of a straight line is:

$$x \cos\theta + y \sin\theta = r \tag{7.8}$$

with x and y belonging to the line, r being the length of a normal from the origin to this line, and θ the angle between r and the x-axis (Fig. 7.21). As the value of r and θ are the same for all the points of a line, the point (r, θ) in the parameters space will rapidly become an accumulator point corresponding to the line in the image space. Usually, a scan of theta over the [0°, 180°] or [−90°, 90°] range is performed for each point of the image, calculating r for each value of θ as per

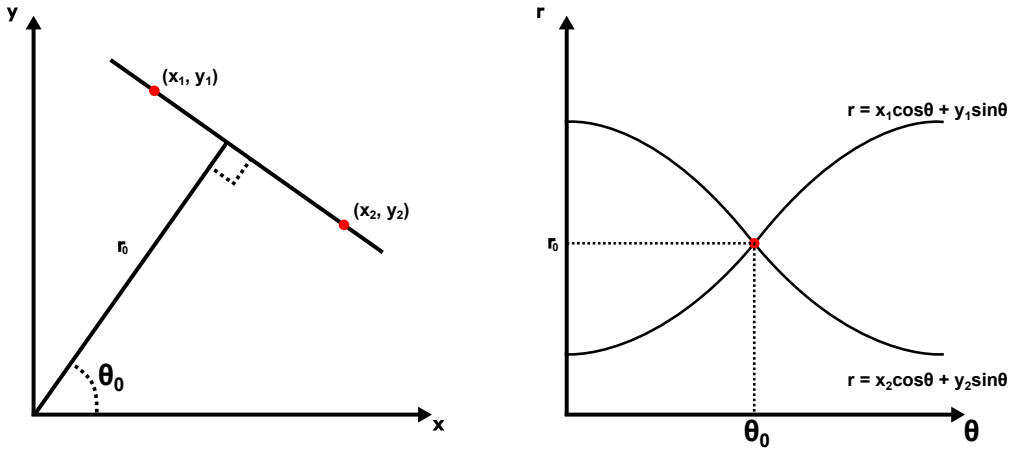

Figure 7.21: Definition of the r and θ parameters used to represent tracks in the HT parameters space.

θ step	r step	max θ	max r
2°	2	135°	1.0
0.5	1	134.75	0.995
0.125	1	135.06	0.0
0.125	0.125	135.06	0.06
0.0625	0.0625	135.03	0.03

Table 7.4: Results of the Hough Transform with different step size of θ and r for the distribution in Fig. 7.22 left.

Eq. 7.8 and increasing the value of the corresponding parameters point. The HT was applied to the distribution of detected photons as a function of the deposited energy and the result is shown on the right side of Fig. 7.22. The scanning intervals of θ and r affect the precision at which one can reconstruct the line parameters. Large intervals provide more approximative results, while decreasing them too much could result in multiple local maxima with comparable intensity in the parameters space for one single line. Table 7.4 shows the results obtained performing the HT using different step values of (θ, r). It is visible how, differently from the results obtained with the linear fit, the results don't differ much one from the other, with θ rapidly converging to the value of about 135 degrees, and r converging to a value of zero. As the scanning must be performed for each pixel of the image, decreasing the step size rapidly increases the computational time. In the following, all the coefficients obtained with the HT will be obtained with step

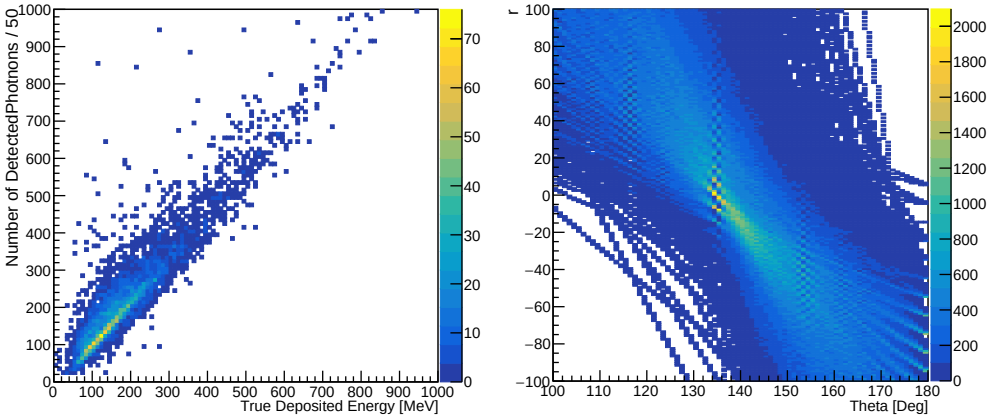

Figure 7.22: Left: Number of detected photons as a function of the true deposited energy for the events with interaction point in the voxel at the center of GRAIN. Right: Hough Transform's parameter space for the distribution on the left side.

sizes of 0.125 degrees and 0.125 for θ and r respectively.

7.5 Reconstruction of energy deposits in GRAIN

With both the number of detected photons and a coefficient for each region of GRAIN, the position of the neutrino interaction was used to get the correct coefficient and reconstruct the deposited energy. Here, the position of the events inside the volume is reconstructed again analytically from the intersection of the muon and proton tracks, and the identification of the signal event between the events of one spill is assumed to be known. The values of $(E_{true} - E_{reco})/E_{true}$ are shown in Fig. 7.23. The top row shows the results obtained with the coefficients computed with the linear fit, while the bottom row shows the results obtained applying the HT. In both cases, the left column shows results with events having the interaction point in the inner region, while the results on the right column are instead obtained with events having positions in the central downstream region. For each distribution, the most probable value was obtained as the center of the maximum bin. These values are reported in Table 7.5, where the errors are obtained as the standard deviation of an uniform distribution in the bin range. From these results it is clear how the procedure used to reconstruct the deposited energy, as it is, is not suitable to perform precise calorimetric measurements. However, multiple observations can be made looking at the distributions of Fig. 7.23. Firstly, both distributions obtained with the LF technique have the most probable value with a strong bias towards lower values of reconstructed energy. This is expected re-

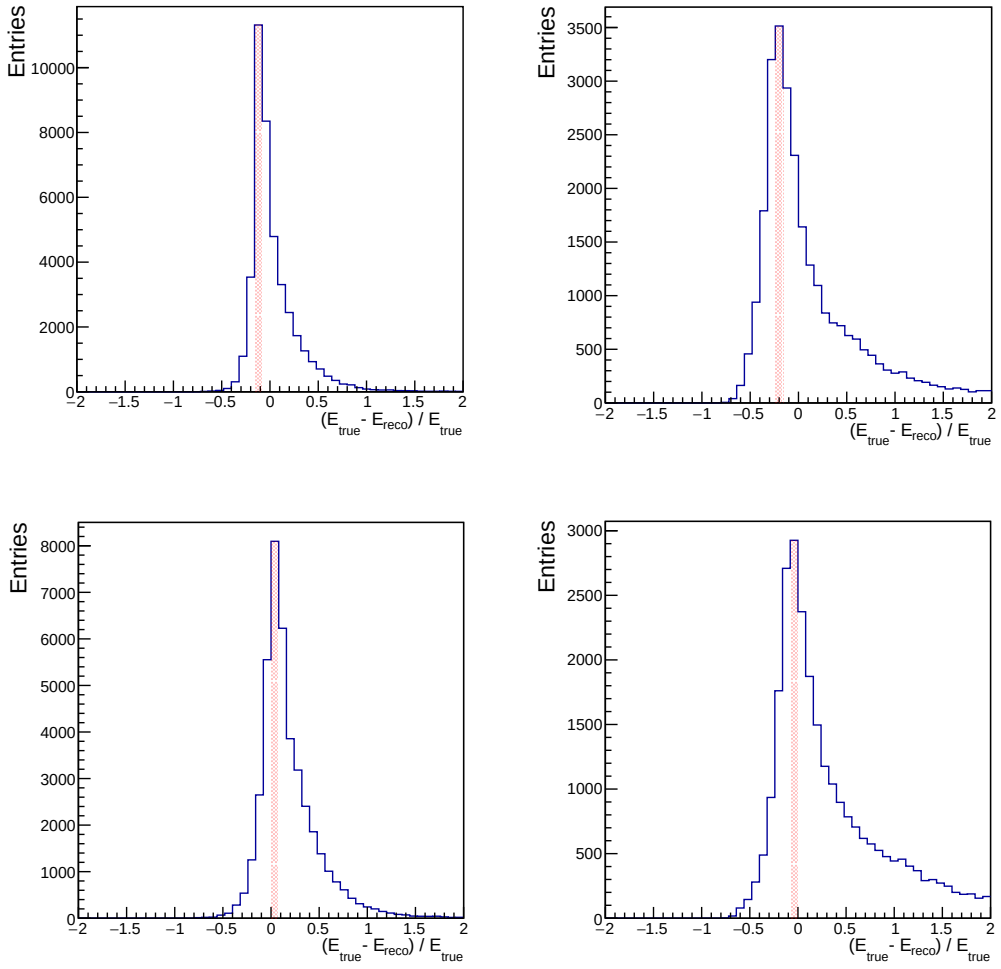

Figure 7.23: $(E_{true} - E_{reco})/E_{true}$ for all the events in the CCQE-like dataset. The reconstructed energy is computed exploiting the calibration coefficient for the position of the interaction point. Top row shows the results obtained with the calibration coefficient computed with the linear fit, while bottom row shows the results for the calibration obtained with the HT. Both plots in the left column show the results for events with interaction point in a central region of the GRAIN volume, while the plots on the right column show the results for events in the central downstream region of GRAIN (Fig. 7.19).

	Linear Fit	Hough Trasform
Central	-0.12 ± 0.02	0.04 ± 0.02
Downstream	-0.20 ± 0.02	-0.04 ± 0.02

Table 7.5: Result of the fits in Fig. 7.23 for the two investigated regions and the two techniques used to compute the calibration coefficients.

calling the linear fit procedure: as the fit is performed on the distribution of the mean values of deposited energy as a function of the total number of detected photons, the strong asymmetry of the distribution in Fig. 7.20 makes the mean value and the most probable value not equals. Consequentially, the reconstructed energy distribution should manifest a bias of the most probable value, as clearly visible in the top row of Fig. 7.23. The same offset is instead not present for the results obtained with the HF, as it identifies the line with the highest number of events to extract the calibration coefficient, instead of the mean value. The ratios of Fig. 7.23 (bottom) should thus have the most probable value closer to 1, as clearly visible in both distributions. Moreover, both results obtained in the downstream region show a larger tail of events with underestimated energies compared to the events in the central region. This can be explained as the events close to the borders could have interaction point in regions with really low camera exposure, which corresponds to a much lower light collection. This effect suggests the necessity of computing calibration coefficients with a finer granularity near the borders, as the current region definition includes regions with large differences of exposure. This effect is not visible in the results for the inner region as the changes of the exposure in this region are negligible (Sec. 7.2.2). As the number of simulated events close to the borders is not enough to compute calibration coefficients for the underexposed regions, a cut on the fiducial volume of 5 cm from the borders was made to try to remove the tail of underestimated reconstructed energies. Lastly, all the results show an important tail of events which reconstructed energy is up to three times higher than the true deposited energy. As the effect is present for all the analyzed regions, it should not depend on the position of the events inside the volume. The source of this effect was instead found to be related to dazzled cameras, which will be described in the next section.

7.5.1 Effect of dazzled cameras on the energy reconstruction

As particles propagate through the liquid argon volume, they could cross the inner volume of one or more cameras. This is the volume confined by the body and the

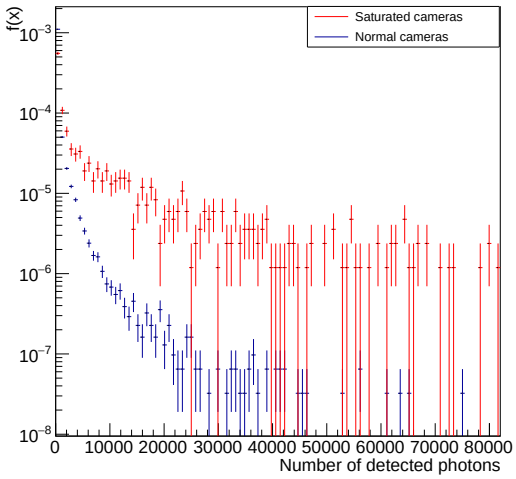

Figure 7.24: Probability density distributions for both normal and dazzled cameras.

mask of a camera, where the sensor is located. When this happens, the sensor of such camera detects a much larger number of photons compared to the usual amount. This can be seen in Fig. 7.24, where the probability density distribution of the number of collected photons by one single camera is shown. These cameras are usually referred to as dazzled cameras. Often, events with dazzled cameras have a total collected light much higher than events with similar energy depositions, but no dazzled cameras. This effect is clearly visible looking again at the distribution of total collected photons as a function of the deposited energy in GRAIN, where it is now possible to explain the origin of the asymmetrical distribution as generated by the events with dazzled cameras. To prove this hypothesis, all the dazzled cameras in the neutrino events selected with STT and ECAL were removed exploiting the MC-truth of the optical simulation. The result is shown in Fig. 7.25, where such distribution is compared to the one obtained after removing the dazzled cameras. It should be noted how the removal of all the dazzled cameras, while reducing the asymmetry of the distribution, introduces a bias toward a smaller number of detected photons, as this procedure completely removes the info from some of the cameras. A better solution should exploit the information of the dazzled cameras without removing their contribution. Removing the dazzled cameras, the spread of the distribution narrows, and its asymmetrical tail is largely suppressed. This result suggests that removing these cameras, the tail of events with overestimated reconstructed energy seen in Fig. 7.23 should be reduced. New calibration coefficients were thus computed following the same procedure described in the previous section, but starting from the distribution without the dazzled

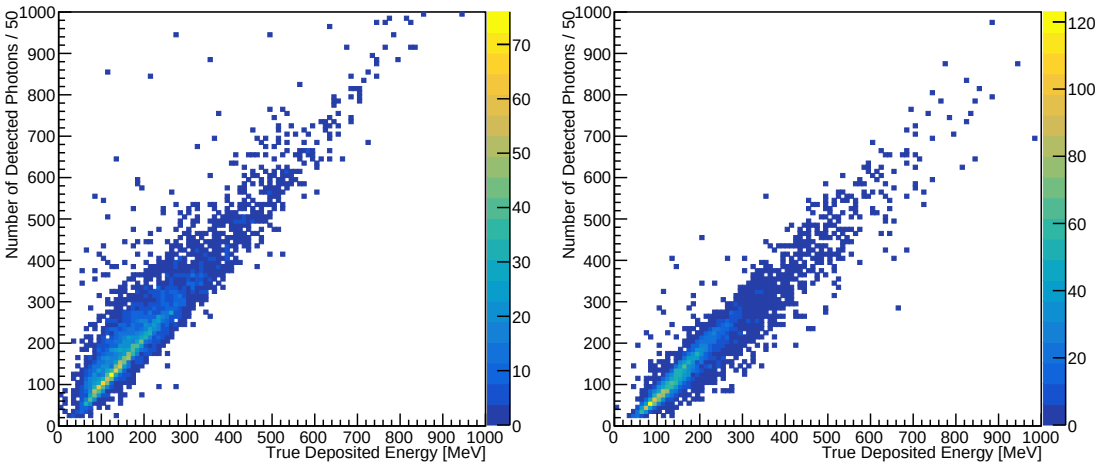

Figure 7.25: Left: distribution of the total number of collected photons as a function of the deposited energy in the volume argon. The total number is computed including all the 76 cameras in the GRAIN geometry. Right: same distribution of the left panel with the number of detected photons computed excluding all the dazzled cameras.

cameras. The values of $(E_{true} - E_{reco})/E_{true}$ obtained with the same dataset of events, a 5 cm cut of the fiducial volume from the borders, and with the new calibration coefficients are shown in Fig. 7.26. The most probable values were obtained again as the central value of the maximum bin. Both tails of under- and overestimated reconstructed energy are now suppressed. Moreover, due to the suppression of the asymmetrical structure of the distribution in Fig. 7.25, the bias of the distributions obtained using the linear fit is now compatible with the bias of the distribution obtained with the HT, and for all cases the maximum bin was the closest bin to zero. Despite a more fine calibration process is possible, these results suggest that the reconstruction of the deposited energy in argon exploiting exclusively the scintillation light and multiple optical systems based on Coded Aperture Cameras is possible. In the following, the calibration coefficients obtained with the Hough Transform technique will be the ones used to reconstruct the deposited energy,

7.6 GRAIN as an active target

With the deposited energy in GRAIN reconstructed, it is now possible to evaluate the improvements this information provides in the selection of events in the $\nu_\mu + Ar \rightarrow \mu^- + p + X$ channel. For each event, the expected deposited energy

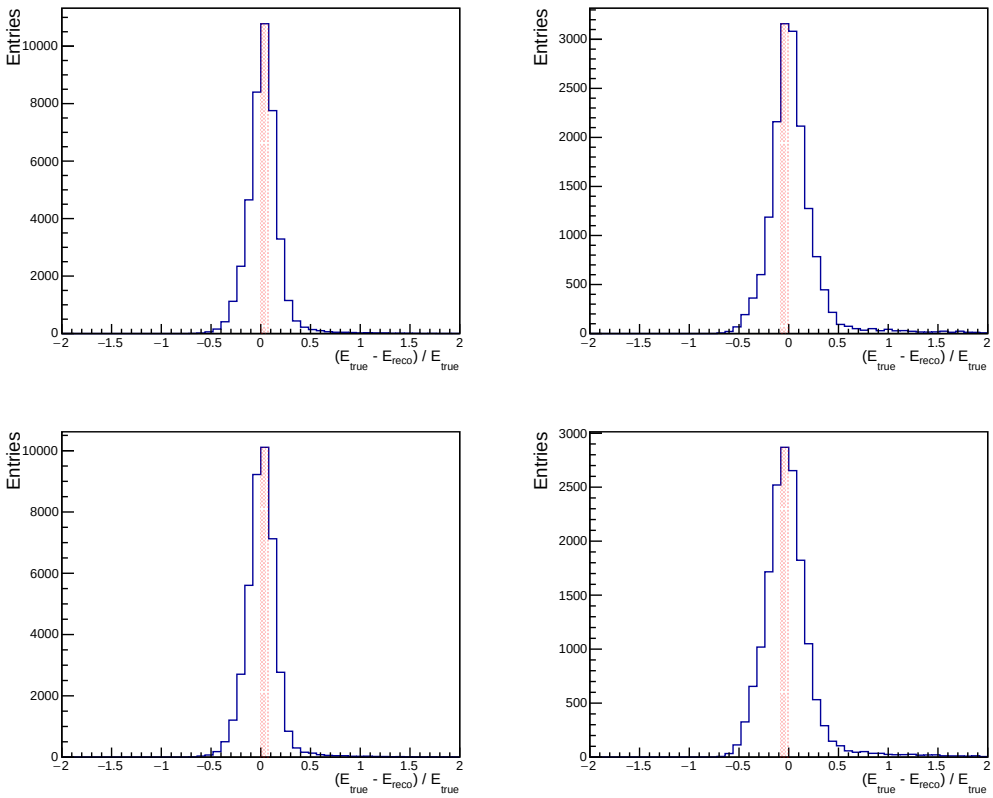

Figure 7.26: $(E_{true} - E_{reco})/E_{true}$ values for all the events in the CCQE-like dataset excluding the dazzled cameras. The reconstructed energy is computed exploiting the calibration coefficient of the position of the interaction point. Top row shows the results obtained with the calibration coefficient computed with the linear fit, while bottom row shows the results for the calibration obtained with the HT. Both plots in the left column show the results for events with interaction point in a central region of the GRAIN volume, while the plots on the right column show the results for events in the central downstream region of GRAIN (Fig. 7.19).

was obtained from the secondary particles' path length inside the argon volume and an energy loss defined as dE/dx = 2.72 MeV/cm. The path length was computed analytically from the vertex position to the exiting point from the GRAIN volume, while the energy loss value was obtained from the MC-truth as the mean deposited energy by a proton and a muon in GRAIN. The expected deposited energy and the reconstructed one were then used to define the best cut to separate background events from signal ones. This was done on the second training dataset extracted from the CCQE-like event sample, and computing the difference between the expected and reconstructed energy for background and signal events. Figure 7.27 shows the distribution of the residual energies for both types of events. The cut value was chosen as the value for which the signal over background ratio was maximal, and was found to be 0 MeV. With the best-cut value defined, a third selection criterion was added to the two described in Sec 7.1:

- Exactly one muon and one proton must be reconstructed by the STT;
- All the clusters in the ECAL should be matched with the muon or the proton reconstructed by the STT, with no clusters remaining unmatched.
- The residual between the reconstructed energy and the expected deposited energy in argon must be equal to or less than 0 MeV.

The selection and reconstruction performances are thus evaluated again on the analysis dataset and in the fiducial volume previously defined (5 cm from the borders and excluding the top and bottom regions as in Sec. 7.4). The CCQE events selection results are reported in Table 7.6 both with and without the use of the calorimetric information from GRAIN: with the third requirement based on the reconstructed energy in GRAIN, the selection purity increases from about 71% to 92% when selecting events in the fiducial volume (Fig. 7.28), while the selection efficiency drop to less than half due to the cut performed on the residual energy. The effect of the energy cut can be also seen in Fig. 7.29, where the final composition of the events surviving the cut is shown.

Calorimetric information from GRAIN can now be used together with the STT and ECAL reconstructions to obtain the energy of the primary neutrinos, as already done in Sec. 7.1. Figure 7.30 shows the results for the selected events in the fiducial volume, both with and without the contribution of the calorimetric information provided by GRAIN. It is clearly visible how, when calorimetric information are included, the tail of underestimated reconstructed energies is suppressed, and the bias of the $(E_{reco} - E_{true})/E_{true}$ distribution has a mean value closer to 0. In the reconstruction of the neutrino energy, the contribution of the energy deposited in the passive material of the cryostat was found to be negligible. Despite the improvement, a tail of overestimated reconstructed energies is still

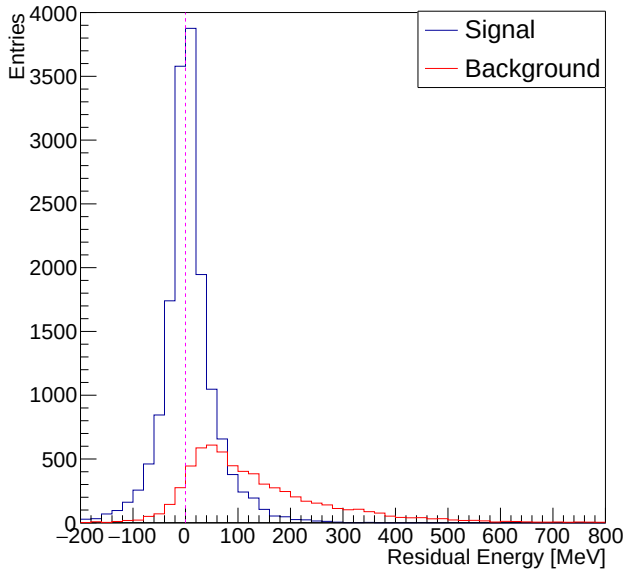

Figure 7.27: Residual energy for both the signal (blue) and background (red) events. The magenta line represents the cut value used to select CCQE candidates.

	Fiducial volume	
GRAIN	Passive	Active
Total Events	85574	
Signal Events	60697	
Selected Events	85574	29695
Selected Signal	60697	27452
Selected Bkg	24877	2243
Selection Eff	100%	45.2%
Selection Purity	70.9%	92.4%

Table 7.6: Performances of the event selection in the $\nu_\mu + Ar \rightarrow \mu^- + p + X$ channel exploiting the STT and ECAL event reconstructions and GRAIN both as a passive or active target.

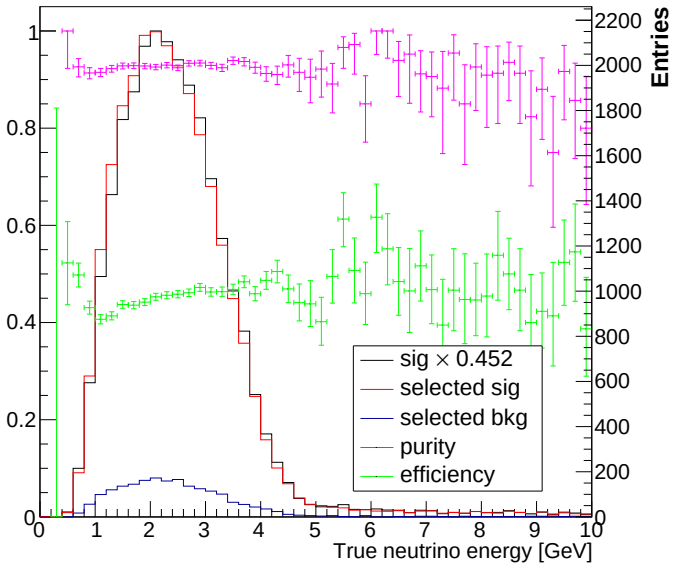

Figure 7.28: Selection efficiency (green) and purity (magenta) for CCQE-like events in the $\nu_\mu + Ar \rightarrow \mu + p + X$. The spectrum of the full signal sample (black), the selected signal (red), and the selected background (blue) are also shown. The selection is performed exploiting the STT, ECAL, and GRAIN reconstructions.

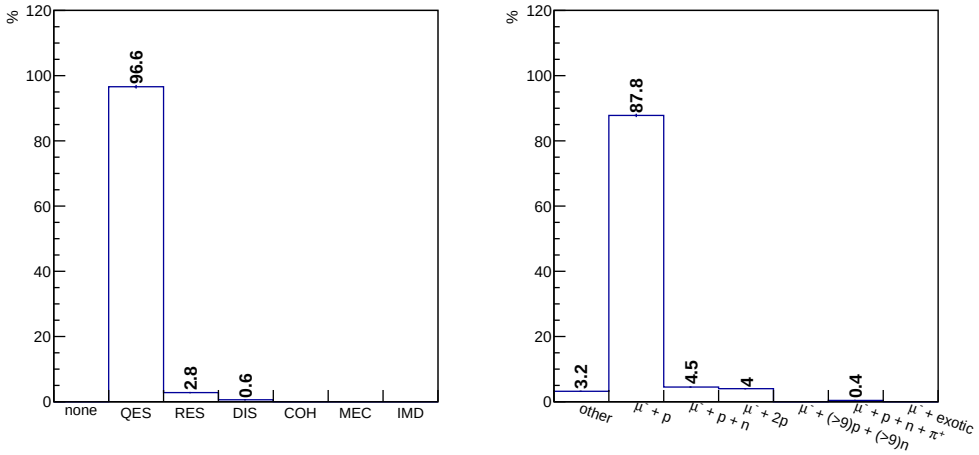

Figure 7.29: Left: interaction process type for all the selected events. Right: true final composition of all the selected events. Events were selected exploiting the STT, ECAL, and GRAIN reconstruction.

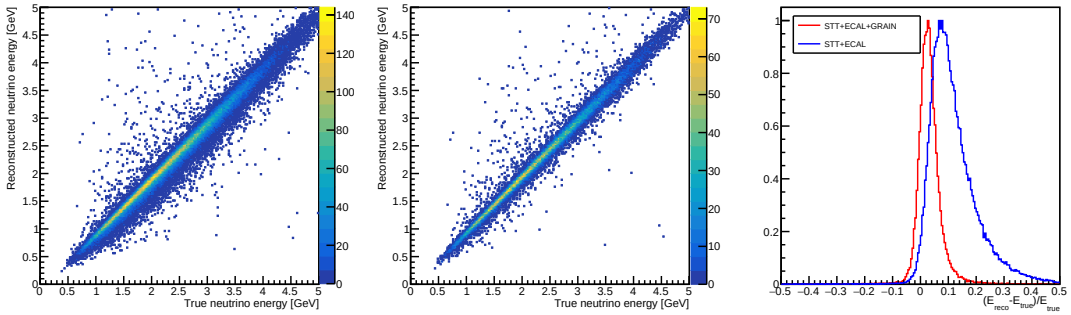

Figure 7.30: Left: Reconstructed neutrino energy as a function of the true one for the selected events in the fiducial volume exploiting the reconstructed information of STT and ECAL only. Center: Reconstructed neutrino energy as a function of the true one for the selected events in the fiducial volume exploiting the reconstructed information of STT, ECAL, and GRAIN. Right: distribution of the $(E_{true} - E_{reco})/E_{true}$ value with (red line) and without (blue line) the calorimetric information of GRAIN.

present. At the time of writing the origin of such tail is not yet understood, and further studies will be needed to fully address it.

Lastly, it was possible to compute the SAND energy resolution as a function of the true neutrino energy of CCQE events in the $\nu_\mu + Ar \rightarrow \mu + p + X$ channel. Figure 7.31 shows the result for the selected events in the fiducial volume, where the distribution was fitted with the general energy resolution equation of electromagnetic calorimeters:

$$\frac{\sigma}{E} = \frac{a}{\sqrt{E}} \oplus \frac{b}{E} \oplus c \tag{7.9}$$

where $\oplus$ indicates a quadratic sum. The first term of Eq. 7.9 was found to be negligible, and the energy resolution can be written as:

$$\frac{\sigma}{E} = \frac{8\%}{E} \oplus 1\% \tag{7.10}$$

.

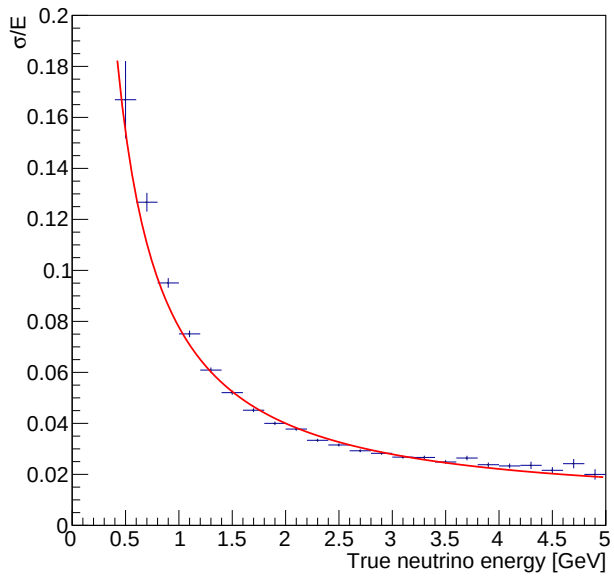

Figure 7.31: SAND energy resolution as a function of the true neutrino energy for CCQE $\nu_\mu + Ar \rightarrow \mu^- + p + X$ events in the fiducial volume.

7.7 Future prospects

As it is now, the procedure described in this chapter exploits MC-truth multiple times. Moreover, some of the reconstructions algorithms are still preliminary and in active development. Different changes can be made to avoid relying on the MC-truth, and to better simulate the expected detector response and complications that could arise when building GRAIN.

STT reconstruction The current algorithm for the STT reconstruction performs a smearing of the MC values without taking into account possible detector and DAQ effects. These quantities are later used to reconstruct information about the events, such as the identification of the particle type and charge, and their momentum. In the future, a more advanced algorithm should be developed to properly take into account all the detector effects currently being neglected, while also performing an event reconstruction starting from the recorded hits. Doing so, the improvements GRAIN provides in the selection of a pure neutrino sample should not change, as STT information are exploited only in the reconstruction of the vertex position, which will be provided instead directly by the track reconstruction in GRAIN.

GRAIN track reconstruction Both reconstruction algorithms described in sections 6.1 and 6.4 are still under active development. Both methods should be able to provide information about the particles' trajectory inside the argon volume, without the need for information from other SAND components. The reconstructed tracks could then be used to identify the vertex position inside the argon volume, which can then be used to select the proper calibration coefficient. The track reconstruction in GRAIN will also improve the selection efficiency of the procedure, as it will be possible to select events without the need of multiple hits in the STT. This will allow to select the events for which the proton stops inside the argon volume, and were not selected in this analysis.

Calibration coefficients A much more fine segmentation of the volume will provide calibration coefficients for the regions in which the spatial dependency is not negligible. Doing so, the fiducial volume will increase, as the regions closer to the edges which were excluded in this analysis would instead be included. Moreover, by combining the information from the track reconstruction in GRAIN with the calibration coefficients, it would be possible to reconstruct the deposited energy along all the voxels crossed by the particles, instead of exploiting a single coefficient from the position of the vertex.

Dazzled cameras A proper algorithm can be developed to identify the dazzled cameras. These have a distinct pattern recorded on the sensor compared to the standard cameras, and a Convolutional Neural Networks can be trained to identify them. With the dazzled cameras identified, a dedicated algorithm can be implemented to exploit their information, instead of discarding them, providing thus a more accurate energy reconstruction.

Different interaction channels The same procedure can be replicated selecting different interaction channels and process types. To do so, one should first verify whether or not the calibration coefficients depend on the interaction channel and if so, compute them again for the channels under study. To separate events of different interaction channels, a proper particle identification algorithm should also be implemented. The increased sample of calibrated channels will then allow SAND to pursue its physics program with a much larger event statistics.

Conclusions

The discovery of the neutrino oscillation phenomenon provided a clear evidence of the need of an extension of the Standard Model. Neutrino oscillation studies are thus crucial as they could provide information on some of the still open questions about neutrino nature. DUNE, a dual-site neutrino oscillation experiment, aims to measure the parameters that govern the oscillation phenomenon with unprecedented levels of precision. It will employ a Far Detector composed of four LAr TPC, and a Near Detector complex composed of three different detectors. SAND will permanently be located on-axis and will provide measurements to constrain systematic uncertainties, monitor the beam, and pursue a dedicated physics program. SAND will be equipped with a 1-ton liquid argon target, GRAIN, which will provide important information about neutrino-argon interactions. GRAIN will exploit a novel approach, never studied in a particle physics scenario before, to image the scintillation light emitted by liquid Argon and provide event information on a nanosecond timescale.

In this thesis, the first results about the GRAIN capabilities to reconstruct tracks by the use of optical cameras based on the Coded Aperture Technique are obtained. A detailed simulation of the liquid Argon scintillation, the light propagation, and its collection was developed, together with a detailed implementation of the cameras' geometry and the simulation of the sensor response. The results from the simulation were compared with the ones obtained with a small scale prototype composed by single coded camera, and showed how this technique can be used to reconstruct simple light sources. The same simulation was used to reconstruct muon tracks in a configuration closer to the GRAIN one, highlighting the limitation the Coded Aperture technique suffers from environments with a low light yield, such as in GRAIN. This result suggested the need for a different approach to the track reconstruction, or for the combination of Coded Aperture cameras with cameras based on a different optical system, able to reconstruct tracks in regions where the coded cameras cannot.

The GRAIN contribution to the SAND performances in the selection of $\nu_\mu + Ar \rightarrow \mu^- + p + X$ events and the reconstruction of neutrino energy was also evaluated. This was done by reconstructing the deposited energy in Argon by

secondary particles produced in the neutrino interactions. A calibration process was implemented in order to reconstruct the deposited energy from the total number of detected photons in GRAIN. The calibration process was found suitable to reconstruct the energy deposited in argon in a reduced fiducial volume. This information was used together with the other SAND components to reconstruct the energy of the primary neutrino, exploiting GRAIN both as a passive target and as a homogeneous calorimeter. The results were compared to verify the effect calorimetric measurements in GRAIN have on SAND performance. The selection efficiency of CCQE events in the desired channel improved from 25% when using GRAIN as a passive target, to 45% when exploiting it as a homogeneous calorimeter. Similarly, the purity of the selected sample increased from 72% to 92%, showing how the information GRAIN can provide is crucial to select a pure sample of neutrino interactions in SAND. The resolution on the neutrino energy was thus computed from the results obtained including GRAIN, and was found to be $\sigma/E = 8\%/E \oplus 1\%$.

Both the tracking and calorimetric reconstructions in GRAIN are still being developed. In the future, multiple improvements can be made on the reconstruction algorithms, aiming to reduce the MC information currently included, and better use the information provided by the optical systems. Eventually, both track and calorimetric reconstructions will be combined to provide a complete event reconstruction based only the argon scintillation light. This ongoing simulation effort is informing the design of the GRAIN detector and will be validated by the planned prototyping campaign.

Appendix A

Spill fitting algorithm

This appendix will describe more in detail the spill fitting procedure introduced in Chapter 7, used to obtain the total number of detected photons in GRAIN. This procedure is needed as background events could generate light in the argon volume that, if measured together with the light produced by the signals, will affect the reconstruction of the deposited energy.

For each spill, the detector response is obtained as the sum of the detected photons by all the optical cameras in the detector (see Sec. 7.2). After obtaining the response, the first step of the procedure is the identification of the peaks in the time profile of a spill. These correspond to the signal produced by the fast component of the scintillation light, produced by one ore more secondary particles of a neutrino interaction. Each peak thus corresponds to one interaction, with interaction vertex either in argon (signal) or in some other component of the SAND detector (background). This is done looking for local maxima along the time spectrum. Due to the statistical noise of the waveform, common techniques used to search for local maxima often find peaks where there should be none. To avoid this problem, multiple operations where applied to the waveform: first, a nearest neighbor smoothing kernel[163] was applied to smooth each bin based on the content of its closest bins. The dilation and erosion morphological operators[164] where then applied to the smoothed waveform. These steps flatten the statistical noise, enanching the signal/noise ratio. The peaks where then identified computing the first derivate between two consecutive bins, and selecting the bins with derivate's value higher than a threshold. The effect of each operation on the waveform is shown in Figure A.1.

With the peaks of the waveform identified, the first identified peak was fitted and its contributions were removed from all the following peaks. Usually, the light emission profile of the liquid Argon is fitted with a Gaussian function convoluted with an exponential for both the singlet and triplet component[109][160]. This was

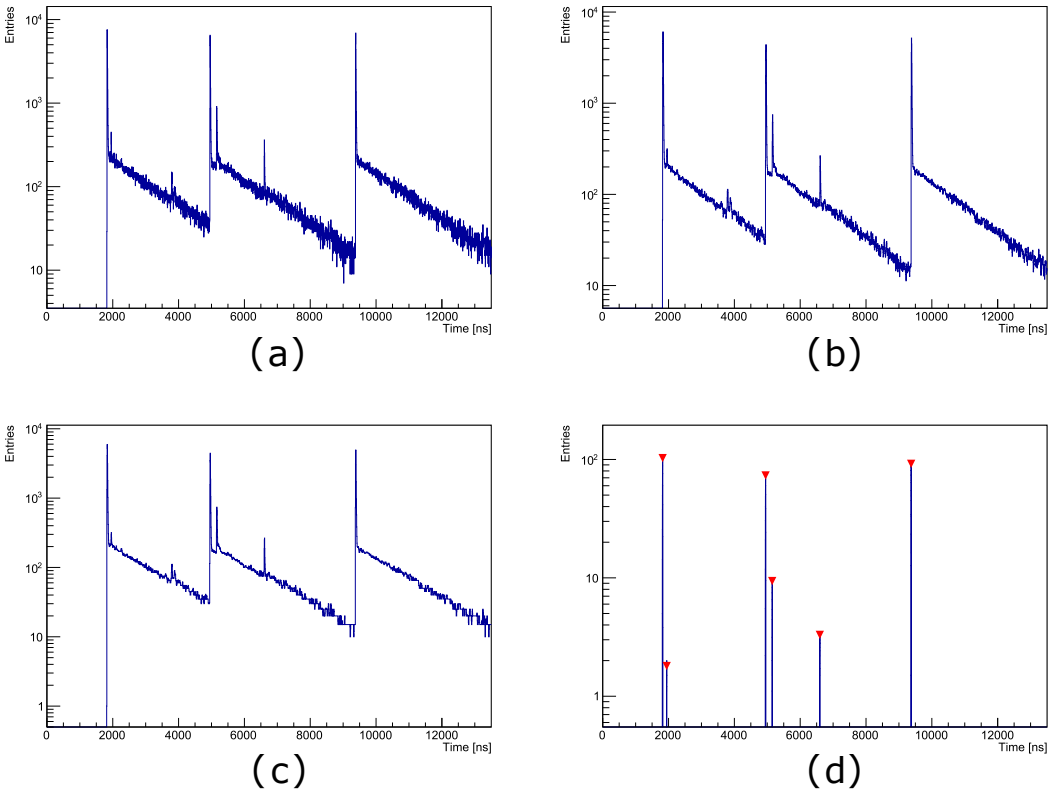

Figure A.1: a) Time spectrum of the detected photons for one simulated spill in GRAIN. At least 7 peaks are visible, corresponding to 7 different neutrino interactions. No separation between signal and background events is made at this level. b) smoothed waveform after applying the nearest neighbor smoothing kernel. c) result of the application of both the dilation and erosion operators on the waveform in *b*. d) Surviving bins after requiring the bin content to be > 1. Six out of the seven peaks of the original waveform were selected, with at least one peak close to 4000 ns not surviving the cut.

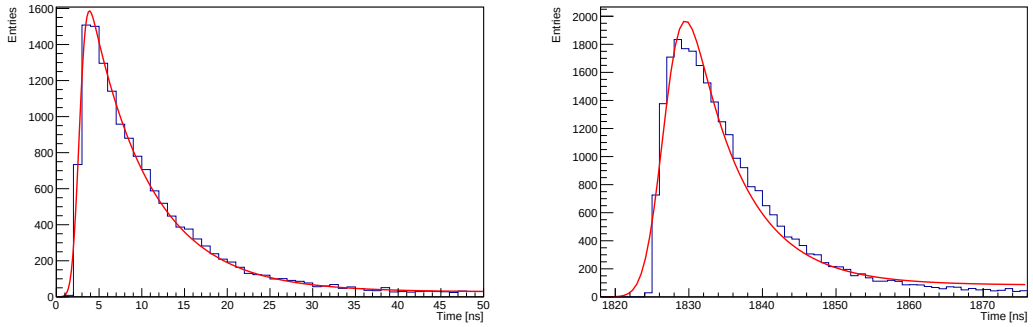

Figure A.2: Time profile of the detected photons by a single camera (left), and by all the available cameras(right). It is visible how the first case is correctly described by Eq. A.1, while it fails for the second case.

already described in Eq. 7.6 and it is reported again here for convenience:

$$f(t) = \sum_{j=f,s} \frac{A_j}{2\tau_j} \exp\left[\frac{1}{2}\left(\frac{\sigma}{\tau_j}\right)^2 - \left(\frac{t-t_m}{\tau_j}\right)\right]\left[1 - \mathrm{erf}\left(\frac{1}{\sqrt{2}}\left(\frac{\sigma}{\tau_j} - \frac{(t-t_m)}{\sigma}\right)\right)\right] \quad \text{(A.1)}$$

However, due to the spectrum being obteined as the sum of multiple cameras, the same function is not suited to fit the full peak. The different propagation times from the light source to the cameras generate a slower rising time and a widening of the peak. Despite the time differences in GRAIN are limited to value < 10 ns, Eq. A.1 fails to describe the peak. This is clearly visible in Fig. A.2, where the same function is exploited to fit the time profile of the detected photon of a single camera and the sum of all the detected photon by the available cameras. One possible solution is to fit the time profile of each camera individually, and later combine the results of the fitting procedure. Fitting the waveform of a single camera, however, is not always possible, as cameras often detected a number of photons to low to correctly be fitted by Eq. A.1. Excluding such cameras is possible, but the calibration process could be affected, as the number of detected photons will have an additional dependancy on the number and position of the excluded cameras. Summing over all the detected photons overcome this limitation, but requires a different fitting function to describe the peaks. Each peaks is thus described by two different functions. The tail of one peak is described by Eq. A.1, while the rising edge is described by a Sigmoid function as described in Eq. 7.7: Each peak is fitted from 20 ns before its local maximum and 50 ns before the local maximum of the next peak, with the local maximum also defining the end of the rising edge and the start of the tail of each peak. Figure 7.15, showed here again for convenience (A.3), shows one peak with both fitting functions overimposed. With the first peak

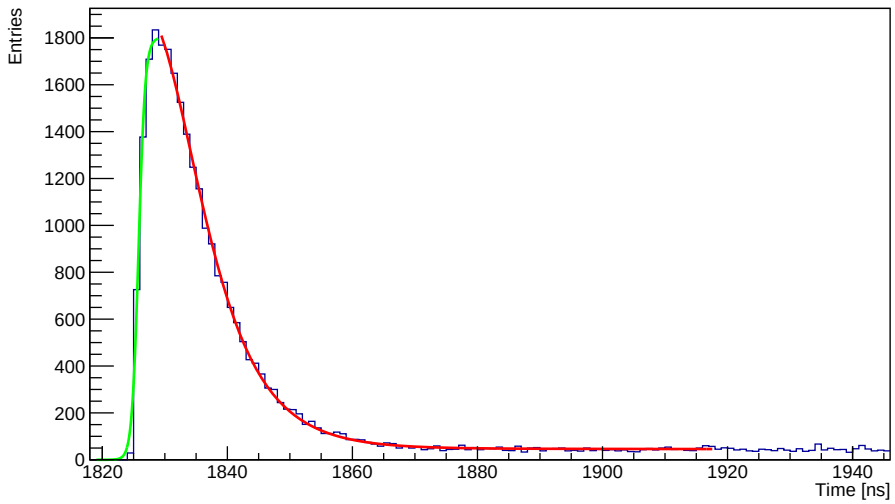

Figure A.3: Waveform of a single event of one spill with fitted functions described in A.1 and 7.7 overlaid in red and green respectively..

of the waveform fitted, it was possible to remove its contribution from the whole spill, thus removing the possible background light from the following events. Each remaining peaks was then fitted and its contribution removed following the same procedure. This is visible in Fig. A.4, where an example of the procedure with two peaks is shown. The number of detected photons for each peak was then computed as the integral of the waveform in the first 200 ns from its rising edge. The total number of detected photons before the removal of the backgroun is shown as a function of the total number of detected photons after this procedure in Fig. A.5.

The performance of this algorithm were evaluated looking at the number of peaks found where there should be none (false positive), and at the number of missed peaks (false negative), for a sample of 900 spills. As the MC-truth do not preserve the information of the single peak in the spill, this was done looking at the timing information of the energy deposits (hits). A false positive is defined as an identified peak for which no energy deposition is found within ± 50 ns from its rising edge. A false negative is instead defined as an energy deposition with no associated peaks within the same timing range. It should be noted that this is a conservative definition, as deposits generated by events could be still considered false negative if their time difference with the peak rising edge is larger than the range of the check. A total of 3.9% false positive was found. The distribution of the total number of detected photons obtained for these events is shown in Fig. A.6 and it is compared to the total number of detected photons of peaks for which an energy

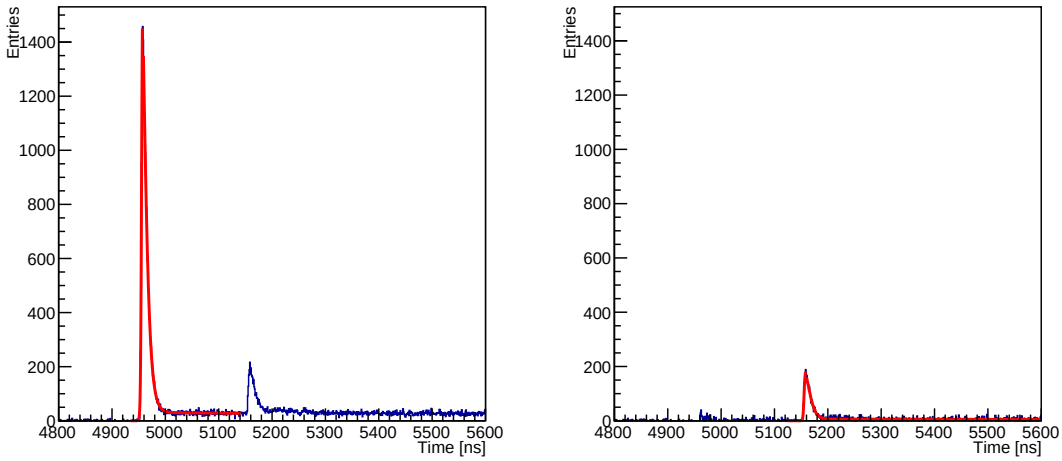

Figure A.4: Example of removal procedure for an event in one spill. Both plots show the time profile of the detected photons in GRAIN. Left: the first peak of the waveform is fitted with the two functions described in Eq. 7.6 and 7.7. tts contribution is later removed along the whole wavefrom. Right: the second event is fitted with the same two functions. The number of detected photons is now correctly computed as the event is free from the contribution of the previous one.

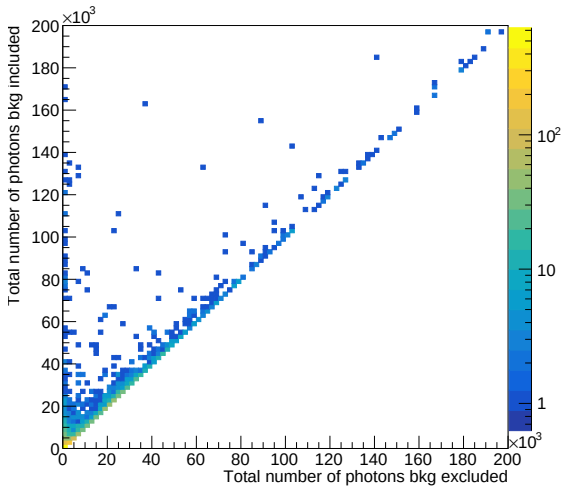

Figure A.5: Number of detected photons before removing the contributions from background light as a function of the number of detected photons obtained after their removal.

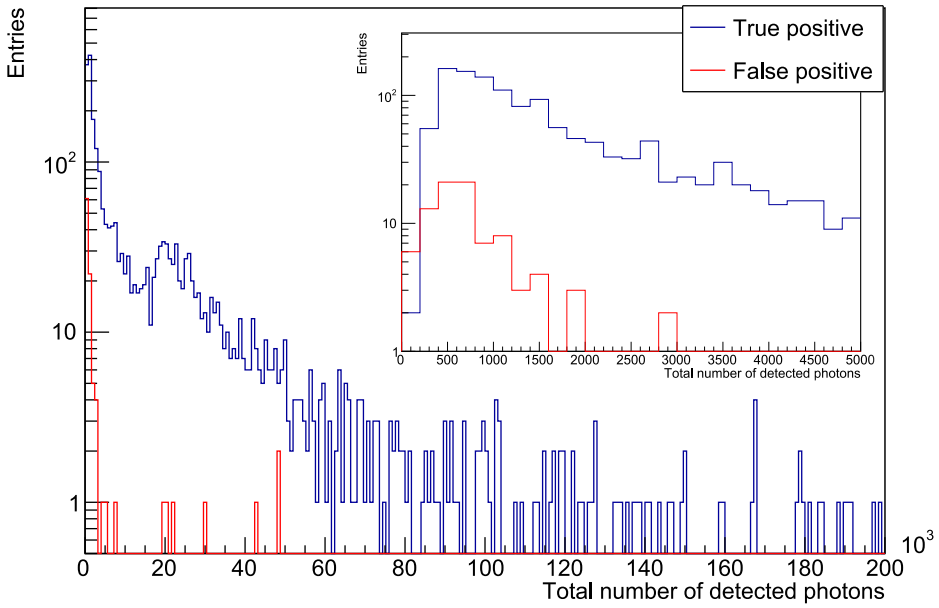

Figure A.6: Distribution of the total number of detected photons for both the true positive peaks (peaks with an energy deposition within ±50 ns from its rising edge) and the false positive (peaks without an energy deposition within ±50 ns from its rising edge).

deposition was instead found within the required timing range (true positive). As false positive events correspond to a fit of the statistical noise, their total number of detected photons is low, and the removal of their contributions from the following peaks was considered to be negligible. Figure A.7 shows instead the number of energy deposits not associated with any peaks as a function of the deposited energy by the single hit, together with the fraction of the correctly identified hits. It is visible how the identification efficiency is $> 90\%$ for energy deposits larger than 0.7 MeV, and increase to over 95% for energy deposits larger than 1.5 MeV. The low efficiency at low values of deposited energy was not considered critical. Hits in this region either belong to identified peaks, and are thus included in their fit, or belong to an event with really low energy deposition and light emission, which are excluded from the analysis of this thesis.

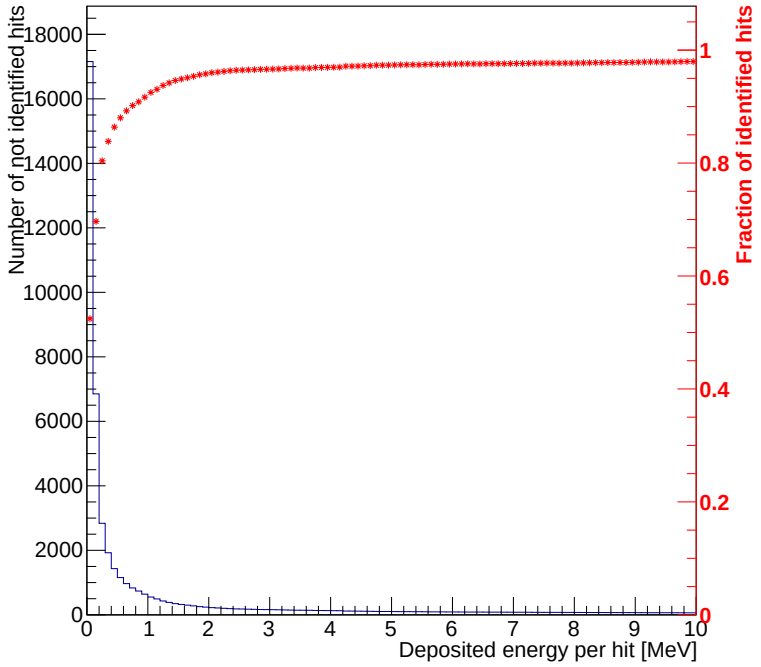

Figure A.7: Number of hits with no identified peaks within ±50 ns (blue) and ratio of identified hits over the total number of hits (red) as a function of the deposited energy per hit.

Bibliography

[1] KATRIN Collaboration. "Direct neutrino-mass measurement with sub-electronvolt sensitivity". In: *Nat. Phys.* 18 (2022), pp. 160–166. DOI: 10.1038/s41567-021-01463-1.

[2] V. N. Aseev et al. "An upper limit on electron antineutrino mass from Troitsk experiment". In: *Phys. Rev.* D84 (2011), p. 112003. DOI: 10.1103/PhysRevD.84.112003. arXiv: 1108.5034 [hep-ex].

[3] Ch. Kraus et al. "Final results from phase II of the Mainz neutrino mass search in ium beta decay". In: *Eur. Phys. J.* C40 (2005), pp. 447–468. DOI: 10.1140/epjc/s2005-02139-7. arXiv: hep-ex/0412056 [hep-ex].

[4] Planck Collaboration. "Planck 2018 results - VI. Cosmological parameters". In: *A&A* 641 (2020), A6. DOI: 10.1051/0004-6361/201833910.

[5] S.M. Bilenky and B. Pontecorvo. "Lepton mixing and neutrino oscillations". In: *Physics Reports* 41.4 (1978), pp. 225–261. ISSN: 0370-1573. DOI: https://doi.org/10.1016/0370-1573(78)90095-9.

[6] Ziro Maki, Masami Nakagawa, and Shoichi Sakata. "Remarks on the Unified Model of Elementary Particles". In: *Progress of Theoretical Physics* 28.5 (Nov. 1962), pp. 870–880. ISSN: 0033-068X. DOI: 10.1143/PTP.28.870. eprint: https://academic.oup.com/ptp/article-pdf/28/5/870/5258750/28-5-870.pdf.

[7] C. Giganti, S. Lavignac, and M. Zito. "Neutrino oscillations: The rise of the PMNS paradigm". In: *Progress in Particle and Nuclear Physics* 98 (2018), pp. 1–54. ISSN: 0146-6410. DOI: https://doi.org/10.1016/j.ppnp.2017.10.001.

[8] A. De Rújula et al. "A fresh look at neutrino oscillations". In: *Nuclear Physics B* 168.1 (1980), pp. 54–68. ISSN: 0550-3213. DOI: https://doi.org/10.1016/0550-3213(80)90276-X.

[9] V. Barger, K. Whisnant, and R. J. N. Phillips. "CP Nonconservation in Three-Neutrino Oscillations". In: *Phys. Rev. Lett.* 45 (26 Dec. 1980), pp. 2084–2088. DOI: 10.1103/PhysRevLett.45.2084.

[10] C. Jarlskog. "A basis independent formulation of the connection between quark mass matrices, CP violation and experiment". In: *Z. Phys. C - Particles and Fields* 29 (1985), pp. 491–497. DOI: doi.org/10.1007/BF01565198.

[11] V. Barger et al. "Matter effects on three-neutrino oscillations". In: *Phys. Rev. D* 22 (11 Dec. 1980), pp. 2718–2726. DOI: 10.1103/PhysRevD.22.2718.

[12] Carlo Giunti and Marco Laveder. "Neutrino mixing". In: (Oct. 2003). arXiv: hep-ph/0310238.

[13] Mattias Blennow and Alexei Yu. Smirnov. "Neutrino Propagation in Matter". In: *Advances in High Energy Physics* 2013 (Mar. 2013), p. 972485. ISSN: 1687-7357. DOI: 10.1155/2013/972485.

[14] A. Cervera et al. "Golden measurements at a neutrino factory". In: *Nuclear Physics B* 579.1 (2000), pp. 17–55. ISSN: 0550-3213. DOI: https://doi.org/10.1016/S0550-3213(00)00221-2.

[15] A. Cervera et al. "Erratum to "Golden measurements at a neutrino factory": [Nucl. Phys. B 579 (2000) 17]". In: *Nuclear Physics B* 593.3 (2001), pp. 731–732. ISSN: 0550-3213. DOI: https://doi.org/10.1016/S0550-3213(00)00606-4.

[16] K. Abe et al. "A Long Baseline Neutrino Oscillation Experiment Using J-PARC Neutrino Beam and Hyper-Kamiokande". In: Dec. 2014. arXiv: 1412.4673 [physics.ins-det].

[17] R.B. Patterson. "Prospects for Measurement of the Neutrino Mass Hierarchy". In: *Annual Review of Nuclear and Particle Science* 65.1 (2015), pp. 177–192. DOI: 10.1146/annurev-nucl-102014-021916. eprint: https://doi.org/10.1146/annurev-nucl-102014-021916.

[18] Bruce T. Cleveland et al. "Measurement of the Solar Electron Neutrino Flux with the Homestake Chlorine Detector". In: *The Astrophysical Journal* 496.1 (Mar. 1998), p. 505. DOI: 10.1086/305343.

[19] J. N. Abdurashitov et al. "Measurement of the solar neutrino capture rate with gallium metal. III. Results for the 2002–2007 data-taking period". In: *Phys. Rev. C* 80 (1 July 2009), p. 015807. DOI: 10.1103/PhysRevC.80.015807.

[20] W. Hampel et al. "GALLEX solar neutrino observations: Results for GALLEX IV". In: *Phys. Lett. B* 447 (1999), pp. 127–133. DOI: 10.1016/S0370-2693(98)01579-2.

[21] M. Altmann et al. "Complete results for five years of GNO solar neutrino observations". In: *Physics Letters B* 616.3 (2005), pp. 174–190. ISSN: 0370-2693. DOI: https://doi.org/10.1016/j.physletb.2005.04.068.

[22] W.C. Haxton, R.G. Hamish Robertson, and Aldo M. Serenelli. "Solar Neutrinos: Status and Prospects". In: *Annual Review of Astronomy and Astrophysics* 51.1 (2013), pp. 21–61. DOI: 10.1146/annurev-astro-081811-125539.

[23] K.S. Hirata et al. "Experimental study of the atmospheric neutrino flux". In: *Physics Letters B* 205.2 (1988), pp. 416–420. ISSN: 0370-2693. DOI: https://doi.org/10.1016/0370-2693(88)91690-5.

[24] T. Kajita, E. Kearns, and M. Shiozawa. "Establishing atmospheric neutrino oscillations with Super-Kamiokande". In: *Nucl. Phys. B* 908 (2016), pp. 14–29. DOI: 10.1016/j.nuclphysb.2016.04.017.

[25] Y. Fukuda et al. "Solar Neutrino Data Covering Solar Cycle 22". In: *Phys. Rev. Lett.* 77 (9 Aug. 1996), pp. 1683–1686. DOI: 10.1103/PhysRevLett.77.1683.

[26] K. Abe et al. "Solar neutrino measurements in Super-Kamiokande-IV". In: *Phys. Rev. D* 94 (5 Sept. 2016), p. 052010. DOI: 10.1103/PhysRevD.94.052010.

[27] J Boger et al. "The Sudbury Neutrino Observatory". In: *Nuclear Instruments and Methods in Physics Research Section A: Accelerators, Spectrometers, Detectors and Associated Equipment* 449.1 (2000), pp. 172–207. ISSN: 0168-9002. DOI: https://doi.org/10.1016/S0168-9002(99)01469-2.

[28] B. Aharmim et al. "Combined analysis of all three phases of solar neutrino data from the Sudbury Neutrino Observatory". In: *Phys. Rev. C* 88 (2 Aug. 2013), p. 025501. DOI: 10.1103/PhysRevC.88.025501.

[29] G. Alimonti et al. "The Borexino detector at the Laboratori Nazionali del Gran Sasso". In: *Nucl. Instrum. Meth. A* 600 (2009), pp. 568–593. DOI: 10.1016/j.nima.2008.11.076. arXiv: 0806.2400 [physics.ins-det].

[30] G. Bellini et al. "Precision Measurement of the ^{7}Be Solar Neutrino Interaction Rate in Borexino". In: *Phys. Rev. Lett.* 107 (14 Sept. 2011), p. 141302. DOI: 10.1103/PhysRevLett.107.141302.

[31] G. Bellini et al. "First evidence of pep solar neutrinos by direct detection in Borexino". In: *Phys. Rev. Lett.* 108 (2012), p. 051302. DOI: 10.1103/PhysRevLett.108.051302. arXiv: 1110.3230 [hep-ex].

[32] K. Eguchi et al. "First results from KamLAND: Evidence for reactor antineutrino disappearance". In: *Phys. Rev. Lett.* 90 (2003), p. 021802. DOI: 10.1103/PhysRevLett.90.021802. arXiv: hep-ex/0212021.

[33] A. Gando et al. "Reactor on-off antineutrino measurement with KamLAND". In: *Phys. Rev. D* 88 (3 Aug. 2013), p. 033001. DOI: 10.1103/PhysRevD.88.033001.

[34] D. Casper et al. “Measurement of atmospheric neutrino composition with the IMB-3 detector”. In: *Phys. Rev. Lett.* 66 (20 May 1991), pp. 2561–2564. DOI: 10.1103/PhysRevLett.66.2561.

[35] M Ambrosio et al. “Measurement of the atmospheric neutrino-induced upgoing muon flux using MACRO”. In: *Physics Letters B* 434.3 (1998), pp. 451–457. ISSN: 0370-2693. DOI: https://doi.org/10.1016/S0370-2693(98)00885-5.

[36] W.W.M. Allison et al. “Measurement of the atmospheric neutrino flavour composition in Soudan 2”. In: *Physics Letters B* 391.3 (1997), pp. 491–500. ISSN: 0370-2693. DOI: https://doi.org/10.1016/S0370-2693(96)01609-7.

[37] Y. Fukuda et al. “The Super-Kamiokande detector”. In: *Nucl. Instrum. Meth. A* 501 (2003). Ed. by V. A. Ilyin, V. V. Korenkov, and D. Perret-Gallix, pp. 418–462. DOI: 10.1016/S0168-9002(03)00425-X.

[38] Oleg Kalekin and (on behalf ofthe ANTARES collaboration). “The ANTARES underwater neutrino telescope”. In: *Journal of Physics: Conference Series* 160.1 (Apr. 2009), p. 012036. DOI: 10.1088/1742-6596/160/1/012036.

[39] A. Achterberg et al. “First year performance of the IceCube neutrino telescope”. In: *Astroparticle Physics* 26.3 (2006), pp. 155–173. ISSN: 0927-6505. DOI: https://doi.org/10.1016/j.astropartphys.2006.06.007.

[40] M. G. Aartsen et al. “Measurement of Atmospheric Neutrino Oscillations at 6–56 GeV with IceCube DeepCore”. In: *Phys. Rev. Lett.* 120 (7 Feb. 2018), p. 071801. DOI: 10.1103/PhysRevLett.120.071801.

[41] P. Adamson et al. “Measurement of Neutrino and Antineutrino Oscillations Using Beam and Atmospheric Data in MINOS”. In: *Phys. Rev. Lett.* 110.25 (2013), p. 251801. DOI: 10.1103/PhysRevLett.110.251801. arXiv: 1304.6335 [hep-ex].

[42] K. Abe et al. “Combined Analysis of Neutrino and Antineutrino Oscillations at T2K”. In: *Phys. Rev. Lett.* 118.15 (2017), p. 151801. DOI: 10.1103/PhysRevLett.118.151801. arXiv: 1701.00432 [hep-ex].

[43] P. Adamson et al. “Measurement of the neutrino mixing angle θ_{23} in NOvA”. In: *Phys. Rev. Lett.* 118.15 (2017), p. 151802. DOI: 10.1103/PhysRevLett.118.151802. arXiv: 1701.05891 [hep-ex].

[44] M. H. Ahn et al. “Measurement of neutrino oscillation by the K2K experiment”. In: *Phys. Rev. D* 74 (7 Oct. 2006), p. 072003. DOI: 10.1103/PhysRevD.74.072003.

[45] P. Adamson et al. "Combined Analysis of ν_μ Disappearance and $\nu_\mu \to \nu_e$ Appearance in MINOS Using Accelerator and Atmospheric Neutrinos". In: *Phys. Rev. Lett.* 112 (19 May 2014), p. 191801. DOI: 10.1103/PhysRevLett.112.191801.

[46] M. H. Ahn et al. "Measurement of Neutrino Oscillation by the K2K Experiment". In: *Phys. Rev. D* 74 (2006), p. 072003. DOI: 10.1103/PhysRevD.74.072003. arXiv: hep-ex/0606032.

[47] Y. Fukuda et al. "Measurements of the solar neutrino flux from Super-Kamiokande's first 300 days". In: *Phys. Rev. Lett.* 81 (1998). [Erratum: Phys.Rev.Lett. 81, 4279 (1998)], pp. 1158–1162. DOI: 10.1103/PhysRevLett.81.1158. arXiv: hep-ex/9805021.

[48] D. G. Michael et al. "Observation of muon neutrino disappearance with the MINOS detectors and the NuMI neutrino beam". In: *Phys. Rev. Lett.* 97 (2006), p. 191801. DOI: 10.1103/PhysRevLett.97.191801. arXiv: hep-ex/0607088.

[49] N. Agafonova et al. "Discovery of τ Neutrino Appearance in the CNGS Neutrino Beam with the OPERA Experiment". In: *Phys. Rev. Lett.* 115 (12 Sept. 2015), p. 121802. DOI: 10.1103/PhysRevLett.115.121802.

[50] Lukas Berns. "Recent Results from T2K". In: *55th Rencontres de Moriond on Electroweak Interactions and Unified Theories*. May 2021. arXiv: 2105.06732 [hep-ex].

[51] Ivan Esteban et al. "The fate of hints: updated global analysis of three-flavor neutrino oscillations". In: *JHEP* 09 (2020), p. 178. DOI: 10.1007/JHEP09(2020)178. arXiv: 2007.14792 [hep-ph].

[52] F. Ardellier et al. "Double Chooz: A Search for the neutrino mixing angle theta(13)". In: (June 2006). arXiv: hep-ex/0606025.

[53] J. K. Ahn et al. "RENO: An Experiment for Neutrino Oscillation Parameter θ_{13} Using Reactor Neutrinos at Yonggwang". In: (Mar. 2010). arXiv: 1003.1391 [hep-ex].

[54] F.P. An et al. "The detector system of the Daya Bay reactor neutrino experiment". In: *Nuclear Instruments and Methods in Physics Research Section A: Accelerators, Spectrometers, Detectors and Associated Equipment* 811 (2016), pp. 133–161. ISSN: 0168-9002. DOI: https://doi.org/10.1016/j.nima.2015.11.144.

[55] F. P. An et al. "Measurement of electron antineutrino oscillation based on 1230 days of operation of the Daya Bay experiment". In: *Phys. Rev. D* 95 (7 Apr. 2017), p. 072006. DOI: 10.1103/PhysRevD.95.072006.

[56] A. Meregaglia. "Multi detector results from the Double Chooz experiment". In: *52nd Rencontres de Moriond on EW Interactions and Unified Theories*. 2017, pp. 359–366.

[57] S. H. Seo et al. "Spectral measurement of the electron antineutrino oscillation amplitude and frequency using 500 live days of RENO data". In: *Phys. Rev. D* 98 (1 July 2018), p. 012002. DOI: 10.1103/PhysRevD.98.012002.

[58] Yasaman Farzan and Mariam Tórtola. "Neutrino Oscillations and Non-standard Interactions". In: *Frontiers in Physics* 6 (2018). ISSN: 2296-424X. DOI: 10.3389/fphy.2018.00010.

[59] P. F. De Salas et al. "Neutrino Mass Ordering from Oscillations and Beyond: 2018 Status and Future Prospects". In: *Front. Astron. Space Sci.* 5 (2018), p. 36. DOI: 10.3389/fspas.2018.00036. arXiv: 1806.11051 [hep-ph].

[60] D. V. Forero, M. Tórtola, and J. W. F. Valle. "Neutrino oscillations refitted". In: *Phys. Rev. D* 90 (9 Nov. 2014), p. 093006. DOI: 10.1103/PhysRevD.90.093006.

[61] Ivan Esteban et al. *NuFIT 5.2 (2022)*. http://www.nu-fit.org/, Last accessed on 2022-12-08.

[62] A. Aguilar et al. "Evidence for neutrino oscillations from the observation of $\overline{\nu}_e$ appearance in a $\overline{\nu}_\mu$ beam". In: *Phys. Rev. D* 64 (11 Nov. 2001), p. 112007. DOI: 10.1103/PhysRevD.64.112007.

[63] A. A. Aguilar-Arevalo et al. "Significant Excess of ElectronLike Events in the MiniBooNE Short-Baseline Neutrino Experiment". In: *Phys. Rev. Lett.* 121.22 (2018), p. 221801. DOI: 10.1103/PhysRevLett.121.221801. arXiv: 1805.12028 [hep-ex].

[64] G. Mention et al. "Reactor antineutrino anomaly". In: *Phys. Rev. D* 83 (7 Apr. 2011), p. 073006. DOI: 10.1103/PhysRevD.83.073006.

[65] Joachim Kopp et al. "Sterile neutrino oscillations: the global picture". In: *Journal of High Energy Physics* 2013.5 (May 2013), p. 50. ISSN: 1029-8479. DOI: 10.1007/JHEP05(2013)050.

[66] M. A. Acero et al. "White Paper on Light Sterile Neutrino Searches and Related Phenomenology". In: (Mar. 2022). arXiv: 2203.07323 [hep-ex].

[67] N. Agafonova et al. "Search for $\nu\mu\rightarrow$ νeoscillations with the OPERA experiment in the CNGS beam". In: *Journal of High Energy Physics* 2013.7 (July 2013), p. 4. ISSN: 1029-8479. DOI: 10.1007/JHEP07(2013)004.

[68] M. Antonello et al. "Experimental search for the "LSND anomaly" with the ICARUS detector in the CNGS neutrino beam". In: *The European Physical Journal C* 73.3 (Mar. 2013), p. 2345. ISSN: 1434-6052. DOI: 10.1140/epjc/s10052-013-2345-6.

[69] P. Astier et al. "Search for nu(mu) —> nu(e) oscillations in the NOMAD experiment". In: *Phys. Lett. B* 570 (2003), pp. 19–31. DOI: 10.1016/j.physletb.2003.07.029. arXiv: hep-ex/0306037.

[70] B. Armbruster et al. "Upper limits for neutrino oscillations $\overline{\nu}_\mu \to \overline{\nu}_e$ from muon decay at rest". In: *Phys. Rev. D* 65 (11 June 2002), p. 112001. DOI: 10.1103/PhysRevD.65.112001.

[71] Mona Dentler et al. "Updated Global Analysis of Neutrino Oscillations in the Presence of eV-Scale Sterile Neutrinos". In: *JHEP* 08 (2018), p. 010. DOI: 10.1007/JHEP08(2018)010. arXiv: 1803.10661 [hep-ph].

[72] Mikhail Danilov. "Review of sterile neutrino searches at very short-baseline reactor experiments". In: *Phys. Scripta* 97.9 (2022), p. 094001. DOI: 10.1088/1402-4896/ac81fd. arXiv: 2203.03042 [hep-ex].

[73] I. Alekseev et al. "DANSS: Detector of the reactor AntiNeutrino based on Solid Scintillator". In: *Journal of Instrumentation* 11.11 (Nov. 2016), P11011. DOI: 10.1088/1748-0221/11/11/P11011.

[74] Z. Atif et al. "Search for sterile neutrino oscillations using RENO and NEOS data". In: *Phys. Rev. D* 105.11 (2022), p. L111101. DOI: 10.1103/PhysRevD.105.L111101. arXiv: 2011.00896 [hep-ex].

[75] The MicroBooNE collaboration. "Search for a Sterile Neutrino in a 3+1 Framework using the Wire-Cell Inclusive Charged-Current ν_e Selection from MicroBooNE". In: (2022). DOI: MICROBOONE-NOTE-1116-PUB. arXiv: 2011.00896 [hep-ex].

[76] M. Ball et al. "The PIP-II Conceptual Design Report". In: (Mar. 2017). Ed. by Valeri Lebedev. DOI: 10.2172/1346823.

[77] Babak Abi et al. "Deep Underground Neutrino Experiment (DUNE), Far Detector Technical Design Report, Volume II: DUNE Physics". In: (Feb. 2020). arXiv: 2002.03005 [hep-ex].

[78] James Strait et al. "Long-Baseline Neutrino Facility (LBNF) and Deep Underground Neutrino Experiment (DUNE): Conceptual Design Report, Volume 3: Long-Baseline Neutrino Facility for DUNE June 24, 2015". In: (Jan. 2016). arXiv: 1601.05823 [physics.ins-det].

[79] Babak Abi et al. "Deep Underground Neutrino Experiment (DUNE), Far Detector Technical Design Report, Volume III: DUNE Far Detector Technical Coordination". In: *JINST* 15.08 (2020), T08009. DOI: 10.1088/1748-0221/15/08/T08009. arXiv: 2002.03008 [physics.ins-det].

[80] C. Brizzolari et al. "Enhancement of the X-Arapuca photon detection device for the DUNE experiment". In: *JINST* 16.09 (2021), P09027. DOI: 10.1088/1748-0221/16/09/P09027. arXiv: 2104.07548 [physics.ins-det].

[81] Babak Abi et al. "Deep Underground Neutrino Experiment (DUNE), Far Detector Technical Design Report, Volume I Introduction to DUNE". In: *JINST* 15.08 (2020), T08008. DOI: 10.1088/1748-0221/15/08/T08008. arXiv: 2002.02967 [physics.ins-det].

[82] Sabrina Sacerdoti. "A LArTPC with Vertical Drift for the DUNE Far Detector". In: *PoS* NuFact2021 (2022), p. 173. DOI: 10.22323/1.402.0173.

[83] Adam Abed Abud et al. "Deep Underground Neutrino Experiment (DUNE) Near Detector Conceptual Design Report". In: *Instruments* 5.4 (2021), p. 31. DOI: 10.3390/instruments5040031. arXiv: 2103.13910 [physics.ins-det].

[84] B. Abi et al. "Long-baseline neutrino oscillation physics potential of the DUNE experiment". In: *Eur. Phys. J. C* 80.10 (2020), p. 978. DOI: 10.1140/epjc/s10052-020-08456-z. arXiv: 2006.16043 [hep-ex].

[85] M. Bass et al. "Baseline Optimization for the Measurement of CP Violation, Mass Hierarchy, and θ_{23} Octant in a Long-Baseline Neutrino Oscillation Experiment". In: *Phys. Rev. D* 91.5 (2015), p. 052015. DOI: 10.1103/PhysRevD.91.052015. arXiv: 1311.0212 [hep-ex].

[86] A. Abed Abud et al. "Snowmass Neutrino Frontier: DUNE Physics Summary". In: (Mar. 2022). arXiv: 2203.06100 [hep-ex].

[87] L. Hüdepohl et al. "Neutrino Signal of Electron-Capture Supernovae from Core Collapse to Cooling". In: 104.25, 251101 (June 2010), p. 251101. DOI: 10.1103/PhysRevLett.104.251101.

[88] Lorenz Hudepohl. "Neutrinos from the Formation, Cooling and Black Hole Collapse of Neutron Stars". PhD thesis. Munich, Tech. U., Oct. 2013.

[89] A. Roeth. *Supernova Neutrino Pointing with DUNE*. https://indico.cern.ch/event/868940/contributions/3813598/attachments/2081577/3496427/Point_Res_ICHEP_2020_07_AJRoeth.pdf. 2020.

[90] Kate Scholberg. "Supernova Signatures of Neutrino Mass Ordering". In: *J. Phys. G* 45.1 (2018), p. 014002. DOI: 10.1088/1361-6471/aa97be. arXiv: 1707.06384 [hep-ex].

[91] Francesco Capozzi et al. "DUNE as the Next-Generation Solar Neutrino Experiment". In: *Phys. Rev. Lett.* 123.13 (2019), p. 131803. DOI: 10.1103/PhysRevLett.123.131803. arXiv: 1808.08232 [hep-ph].

[92] Y. Farzan and M. Tortola. "Neutrino oscillations and Non-Standard Interactions". In: *Front. in Phys.* 6 (2018), p. 10. DOI: 10.3389/fphy.2018.00010. arXiv: 1710.09360 [hep-ph].

[93] Valentina De Romeri, Kevin J Kelly, and Pedro A N Machado. "Hunting for light dark matter with DUNE PRISM". In: *Journal of Physics: Conference Series* 1468.1 (Feb. 2020), p. 012061. DOI: 10.1088/1742-6596/1468/1/012061.

[94] Lina Necib et al. "Boosted Dark Matter at Neutrino Experiments". In: *Phys. Rev. D* 95.7 (2017), p. 075018. DOI: 10.1103/PhysRevD.95.075018. arXiv: 1610.03486 [hep-ph].

[95] B. Abi et al. "Prospects for beyond the Standard Model physics searches at the Deep Underground Neutrino Experiment". In: *Eur. Phys. J. C* 81.322 (2021). DOI: doi.org/10.1140/epjc/s10052-021-09007-w.

[96] R. Acciarri et al. "Long-Baseline Neutrino Facility (LBNF) and Deep Underground Neutrino Experiment (DUNE): Conceptual Design Report, Volume 2: The Physics Program for DUNE at LBNF". In: (Dec. 2015). arXiv: 1512.06148 [physics.ins-det].

[97] S. Alekhin, S. A. Kulagin, and R. Petti. "Modeling Lepton-Nucleon Inelastic Scattering from High to Low Momentum Transfer". In: *AIP Conference Proceedings* 967.1 (2007), pp. 215–224. DOI: 10.1063/1.2834481. eprint: https://aip.scitation.org/doi/pdf/10.1063/1.2834481.

[98] A. B. Arbuzov, D. Yu. Bardin, and L. V. Kalinovskaya. "Radiative corrections to neutrino deep inelastic scattering revisited". In: *JHEP* 06 (2005), p. 078. DOI: 10.1088/1126-6708/2005/06/078. arXiv: hep-ph/0407203.

[99] S. A. Kulagin and R. Petti. "Neutrino inclusive inelastic scattering off nuclei". In: *Phys. Rev. D* 76 (9 Nov. 2007), p. 094023. DOI: 10.1103/PhysRevD.76.094023.

[100] William J. Marciano and Zohreh Parsa. "Neutrino electron scattering theory". In: *J. Phys. G* 29 (2003), pp. 2629–2645. DOI: 10.1088/0954-3899/29/11/013. arXiv: hep-ph/0403168.

[101] Stephen L. Adler. "Tests of the Conserved Vector Current and Partially Conserved Axial-Vector Current Hypotheses in High-Energy Neutrino Reactions". In: *Phys. Rev.* 135 (1964), B963–B966. DOI: 10.1103/PhysRev.135.B963.

[102] M Adinolfi et al. "The KLOE electromagnetic calorimeter". In: *Nuclear Instruments and Methods in Physics Research Section A: Accelerators, Spectrometers, Detectors and Associated Equipment* 482.1 (2002), pp. 364–386. ISSN: 0168-9002. DOI: https://doi.org/10.1016/S0168-9002(01)01502-9.

[103] G. Adamov et al. "A Proposal to enhance the DUNE Near-Detector Complex". In: *DUNE Document Database* DUNE-doc-13262 (2019).

[104] H. Duyang et al. "A Novel Approach to Neutrino-Hydrogen Measurements". In: (Sept. 2018). arXiv: 1809.08752 [hep-ph].

[105] Hamamatsu Photonics. *MPPC S14160-3050HS*. https://www.hamamatsu.com/jp/en/product/optical-sensors/mppc/mppc_mppc-array/S14160-3050HS.html, Last accessed on 2023-01-26.

[106] Powell BA. Burton WM. "Fluorescence of tetraphenyl-butadiene in the vacuum ultraviolet". In: *Appl Opt.* 12 (1973), pp. 87–89. DOI: doi:10.1364/AO.12.000087.

[107] M. Hofmann et al. "Ion-beam excitation of liquid argon". In: *Eur. Phys. J. C* 73.2618 (2013). DOI: doi.org/10.1140/epjc/s10052-013-2618-0.

[108] Akira Hitachi et al. "Effect of ionization density on the time dependence of luminescence from liquid argon and xenon". In: *Phys. Rev. B* 27 (9 May 1983), pp. 5279–5285. DOI: 10.1103/PhysRevB.27.5279.

[109] Ettore Segreto. "Properties of Liquid Argon Scintillation Light Emission". In: *Phys. Rev. D* 103.4 (2021), p. 043001. DOI: 10.1103/PhysRevD.103.043001. arXiv: 2012.06527 [physics.ins-det].

[110] Joshua Jortner et al. "Localized Excitations in Condensed Ne, Ar, Kr, and Xe". In: *The Journal of Chemical Physics* 42.12 (1965), pp. 4250–4253. DOI: 10.1063/1.1695927. eprint: https://doi.org/10.1063/1.1695927.

[111] S Kubota, M Hishida, and J Raun. "Evidence for a triplet state of the self-trapped exciton states in liquid argon, krypton and xenon". In: *Journal of Physics C: Solid State Physics* 11.12 (June 1978), p. 2645. DOI: 10.1088/0022-3719/11/12/024.

[112] M.J. Carvalho and G. Klein. "Luminescence decay in condensed argon under high energy excitation". In: *Journal of Luminescence* 18-19 (1979), pp. 487–490. ISSN: 0022-2313. DOI: https://doi.org/10.1016/0022-2313(79)90167-4.

[113] Shinzou Kubota et al. "Liquid and solid argon, krypton and xenon scintillators". In: *Nuclear Instruments and Methods in Physics Research* 196.1 (1982), pp. 101–105. ISSN: 0167-5087. DOI: https://doi.org/10.1016/0029-554X(82)90623-1.

[114] P Peiffer et al. “Pulse shape analysis of scintillation signals from pure and xenon-doped liquid argon for radioactive background identification”. In: *Journal of Instrumentation* 3.08 (Aug. 2008), P08007. DOI: 10.1088/1748-0221/3/08/P08007.

[115] T. Heindl et al. “The scintillation of liquid argon”. In: *Europhysics Letters* 91.6 (Oct. 2010), p. 62002. DOI: 10.1209/0295-5075/91/62002.

[116] R Acciarri et al. “Effects of Nitrogen contamination in liquid Argon”. In: *Journal of Instrumentation* 5.06 (June 2010), P06003. DOI: 10.1088/1748-0221/5/06/P06003.

[117] R. Acciarri et al. “Oxygen contamination in liquid Argon: Combined effects on ionization electron charge and scintillation light”. In: *JINST* 5 (2010), P05003. DOI: 10.1088/1748-0221/5/05/P05003. arXiv: 0804.1222 [nucl-ex].

[118] Lord Rayleigh F.R.S. “XXXIV. On the transmission of light through an atmosphere containing small particles in suspension, and on the origin of the blue of the sky”. In: *The London, Edinburgh, and Dublin Philosophical Magazine and Journal of Science* 47.287 (1899), pp. 375–384. DOI: 10.1080/14786449908621276. eprint: https://doi.org/10.1080/14786449908621276.

[119] M. Babicz et al. “A measurement of the group velocity of scintillation light in liquid argon”. In: *JINST* 15.09 (2020), P09009. DOI: 10.1088/1748-0221/15/09/P09009. arXiv: 2002.09346 [physics.ins-det].

[120] J. Calvo et al. “Measurement of the attenuation length of argon scintillation light in the ArDM LAr TPC”. In: *Astroparticle Physics* 97 (2018), pp. 186–196. ISSN: 0927-6505. DOI: https://doi.org/10.1016/j.astropartphys.2017.11.009.

[121] Emily Grace et al. “Index of refraction, Rayleigh scattering length, and Sellmeier coefficients in solid and liquid argon and xenon”. In: *Nuclear Instruments and Methods in Physics Research Section A: Accelerators, Spectrometers, Detectors and Associated Equipment* 867 (2017), pp. 204–208. ISSN: 0168-9002. DOI: https://doi.org/10.1016/j.nima.2017.06.031.

[122] A. Neumeier et al. “Attenuation measurements of vacuum ultraviolet light in liquid argon revisited”. In: *Nuclear Instruments and Methods in Physics Research Section A: Accelerators, Spectrometers, Detectors and Associated Equipment* 800 (2015), pp. 70–81. ISSN: 0168-9002. DOI: https://doi.org/10.1016/j.nima.2015.07.051.

[123] G. M. Seidel, R. E. Lanou, and W. Yao. “Rayleigh scattering in rare gas liquids”. In: *Nucl. Instrum. Meth. A* 489 (2002), pp. 189–194. DOI: 10.1016/S0168-9002(02)00890-2. arXiv: hep-ex/0111054.

[124] Emily Grace and James A. Nikkel. "Index of refraction, Rayleigh scattering length, and Sellmeier coefficients in solid and liquid argon and xenon". In: *Nucl. Instrum. Meth. A* 867 (2017), pp. 204–208. DOI: 10.1016/j.nima.2017.06.031. arXiv: 1502.04213 [physics.ins-det].

[125] N. Ishida et al. "Attenuation length measurements of scintillation light in liquid rare gases and their mixtures using an improved reflection suppresser". In: *Nuclear Instruments and Methods in Physics Research Section A: Accelerators, Spectrometers, Detectors and Associated Equipment* 384.2 (1997), pp. 380–386. ISSN: 0168-9002. DOI: https://doi.org/10.1016/S0168-9002(96)00740-1.

[126] B J P Jones et al. "A measurement of the absorption of liquid argon scintillation light by dissolved nitrogen at the part-per-million level". In: 8.07 (July 2013), P07011. DOI: 10.1088/1748-0221/8/07/P07011.

[127] C. Vogl et al. "Scintillation and optical properties of xenon-doped liquid argon". In: *JINST* 17.01 (2022), p. C01031. DOI: 10.1088/1748-0221/17/01/C01031. arXiv: 2112.07427 [physics.ins-det].

[128] A. Buzulutskov. "Photon emission and atomic collision processes in two-phase argon doped with xenon and nitrogen". In: *Europhysics Letters* 117.3 (Mar. 2017), p. 39002. DOI: 10.1209/0295-5075/117/39002.

[129] C. Galbiati et al. "Pulse shape study of the fast scintillation light emitted from xenon-doped liquid argon using silicon photomultipliers". In: *Journal of Instrumentation* 16.02 (Feb. 2021), P02015. DOI: 10.1088/1748-0221/16/02/P02015.

[130] G Nowak and J Fricke. "The heteronuclear excimers ArKr*, ArXe* and KrXe*". In: *Journal of Physics B: Atomic and Molecular Physics* 18.7 (Apr. 1985), p. 1355. DOI: 10.1088/0022-3700/18/7/016.

[131] Keiko Fujii et al. "High-accuracy measurement of the emission spectrum of liquid xenon in the vacuum ultraviolet region". In: *Nuclear Instruments and Methods in Physics Research Section A: Accelerators, Spectrometers, Detectors and Associated Equipment* 795 (2015), pp. 293–297. ISSN: 0168-9002. DOI: https://doi.org/10.1016/j.nima.2015.05.065.

[132] A. Neumeier et al. "Intense Vacuum-Ultraviolet and Infrared Scintillation of Liquid Ar-Xe Mixtures". In: *EPL* 109.1 (2015), p. 12001. DOI: 10.1209/0295-5075/109/12001. arXiv: 1511.07723 [physics.ins-det].

[133] A. Neumeier et al. "Attenuation of vacuum ultraviolet light in pure and xenon-doped liquid argon —An approach to an assignment of the near-infrared emission from the mixture". In: *EPL* 111.1 (2015), p. 12001. DOI: 10.1209/0295-5075/111/12001. arXiv: 1511.07725 [physics.ins-det].

[134] Jose Alfonso Soto Oton. "Scintillation light detection techniques in a 750-ton liquid argon TPC for the Deep Underground Neutrino Experiment". In: (2022). Presented 13 Jun 2022.

[135] D. Akimov et al. "Fast component re-emission in Xe-doped liquid argon". In: *Journal of Instrumentation* 14.09 (Sept. 2019), P09022. DOI: 10.1088/1748-0221/14/09/P09022.

[136] J. Allison et al. "Geant4 developments and applications". In: *IEEE Transactions on Nuclear Science* 53.1 (2006), pp. 270–278. DOI: 10.1109/TNS.2006.869826.

[137] Rene Brun and other. *root-project/root: v6.18/02*. Version v6-18-02. Aug. 2019. DOI: 10.5281/zenodo.3895860.

[138] B. Viren. *gegede*. URL: https://github.com/brettviren/gegede.

[139] M. Vicenzi. "A GRAIN of SAND for DUNE: Development of Simulations and Reconstruction Algorithms for the Liquid Argon Target of the SAND Detector in DUNE." In: (2023). DOI: doi.org/10.15167/vicenzi-matteo_phd2023-01-20.

[140] C. Andreopoulos et al. "The GENIE Neutrino Monte Carlo Generator". In: *Nucl. Instrum. Meth.* A614 (2010), pp. 87–104. DOI: 10.1016/j.nima.2009.12.009. arXiv: 0905.2517 [hep-ph].

[141] Rene Brun and Fons Rademakers. "ROOT — An object oriented data analysis framework". In: *Nuclear Instruments and Methods in Physics Research Section A: Accelerators, Spectrometers, Detectors and Associated Equipment* 389.1 (1997). New Computing Techniques in Physics Research V, pp. 81–86. ISSN: 0168-9002. DOI: https://doi.org/10.1016/S0168-9002(97)00048-X. URL: https://www.sciencedirect.com/science/article/pii/S016890029700048X.

[142] Laura Fields. *DUNE Fluxes*. https://glaucus.crc.nd.edu/DUNEFluxes/, Last accessed on 2023-01-27.

[143] Clark D. McGrew. *edep-sim*. https://github.com/ClarkMcGrew/edep-sim, Last accessed on 2023-01-27.

[144] M. Szydagis, J. Balajthy, et al. *Noble Element Simulation Technique v2.0*. Version v2.0.0. July 2018. DOI: 10.5281/zenodo.1314669.

[145] E. Kozlova J. Mueller et al. "NEST liquid argon mean yields note". In: ().

[146] P. Agnes et al. "Simulation of argon response and light detection in the DarkSide-50 dual phase TPC". In: *JINST* 12.10 (2017), P10015. DOI: 10.1088/1748-0221/12/10/P10015. arXiv: 1707.05630 [physics.ins-det].

[147] R. Kugathasan. "Integrated front-end electronics for single photon time-stamping in cryogenic dark matter detectors". In: *Journal of Instrumentation* 15.05 (May 2020), p. C05019. DOI: 10.1088/1748-0221/15/05/C05019.

[148] V. Cicero. "Study of the tracking performance of a liquid Argon detector based on a novel optical imaging concept". In: *Ph. D. Thesis* (2023).

[149] Michał J. Cieślak, Kelum A.A. Gamage, and Robert Glover. "Coded-aperture imaging systems: Past, present and future development – A review". In: *Radiation Measurements* 92 (2016), pp. 59–71. ISSN: 1350-4487. DOI: https://doi.org/10.1016/j.radmeas.2016.08.002.

[150] E. E. Fenimore and T. M. Cannon. "Coded aperture imaging with uniformly redundant arrays". In: *Appl. Opt.* 17.3 (Feb. 1978), pp. 337–347. DOI: 10.1364/AO.17.000337.

[151] Stephen R. Gottesman and E. E. Fenimore. "New family of binary arrays for coded aperture imaging". In: *Appl. Opt.* 28.20 (Oct. 1989), pp. 4344–4352. DOI: 10.1364/AO.28.004344.

[152] R. Accorsi. "Design of a near-field coded aperture cameras for high-resolution medical and industrial gamma-ray imaging". In: (Aug. 2005).

[153] M. Andreotti et al. "Coded masks for imaging of neutrino events". In: *Eur. Phys. J. C* 81.11 (2021), p. 1011. DOI: 10.1140/epjc/s10052-021-09798-y. arXiv: 2105.10820 [physics.ins-det].

[154] Valerio Pia. "Study of a novel VUV-imaging system in liquid argon for neutrino oscillation experiments". PhD thesis.

[155] Hamamatsu Photonics. *MPPC S13615*. Last accessed on 2023-01-26. URL: https://www.hamamatsu.com/content/dam/hamamatsu-photonics/sites/documents/99_SALES_LIBRARY/ssd/s13615_series_kapd1062e.pdf.

[156] Weeroc. *Triroc-1A*. https://www.weeroc.com/products/sipm-read-out/triroc-1a, Last accessed on 2023-01-26.

[157] R.L. Gluckstern. "Uncertainties in track momentum and direction, due to multiple scattering and measurement errors". In: *Nuclear Instruments and Methods* 24 (1963), pp. 381–389. ISSN: 0029-554X. DOI: https://doi.org/10.1016/0029-554X(63)90347-1.

[158] Virgil L. Highland. "Some practical remarks on multiple scattering". In: *Nuclear Instruments and Methods* 129.2 (1975), pp. 497–499. ISSN: 0029-554X. DOI: https://doi.org/10.1016/0029-554X(75)90743-0.

[159] Irene Cagnoli. "Electromagnetic shower identification in the SAND Calorimeter of the DUNE Near Detector". PhD thesis.

[160] B. Aimard et al. “Study of scintillation light collection, production and propagation in a 4 tonne dual-phase LArTPC”. In: *Journal of Instrumentation* 16.03 (Mar. 2021), P03007. DOI: 10.1088/1748-0221/16/03/P03007.

[161] P V.C. Hough. “METHOD AND MEANS FOR RECOGNIZING COMPLEX PATTERNS”. In: (Dec. 1962).

[162] Richard O Duda and Peter E Hart. “Use of the Hough transformation to detect lines and curves in pictures”. In: *Communications of the ACM* 15.1 (1972), pp. 11–15.

[163] N. S. Altman. “An Introduction to Kernel and Nearest-Neighbor Nonparametric Regression”. In: *The American Statistician* 46.3 (1992), pp. 175–185. DOI: 10.1080/00031305.1992.10475879. eprint: https://www.tandfonline.com/doi/pdf/10.1080/00031305.1992.10475879.

[164] E.R. Dougherty. *An Introduction to Morphological Image Processing*. Books in the Spie Tutorial Texts Series. SPIE Optical Engineering Press, 1992. ISBN: 9780819408457.